FIBROUS CATALYSTS FOR AIR POLLUTION CONTROL

by Eng. RODRIGUEZ Maximiliano

IN FULFILLMENT OF THE REQUIREMENTS FOR THE DEGREE OF DOCTOR IN AGRONOMIC SCIENCES AND BIOLOGICAL ENGINEERING (UCL) / CHEMICAL ENGINEERING (UNL)

THESIS COMMITTEE

Prof. Viviana Milt (UNL, Argentina)	Supervisor
Prof. Eric Gaigneaux (UCLouvain, Belgium)	Supervisor
Prof. Michel Devillers (UCLouvain, Belgium)	Chairperson
Prof. Damien Debecker (UCLouvain, Belgium)	Secretary
Prof. Carlos Vera (UNL, Argentina)	
Prof. Oihane Sanz (UPV/EHU, Spain)	
Prof. Stéphanie Lambert (ULiège, Belgium)	

April 2025

“If there is no struggle, there is no progress”

- Frederick Douglass

ACKNOWLEDGEMENTS

The writing of this thesis could not have been possible without the contribution and support from many people that crossed my path during all these years. They were essential to me in the workplace but outside the lab as well.

First of all, I would like to thank my supervisors: Vivi and Eric, for the guidance, support, lessons and discussions that enriched my PhD journey.

I was fortunate enough to have had the opportunity to spend two years of work time overseas, in a foreign institute in Belgium. In this regard, I owe a lot to UCL and the CAI fellowship for giving me the opportunity to live a unique experience.

In this adventure, I met incredible people with whom I shared beautiful moments. They also gave me a hand whenever I found myself in trouble. From this side of the pond, a huge thanks to:

The C3: Ali, Isaac, Fanny, Hippo, François, Plaifa, Gio, Margot, Denis, Marty, Feilong, Yingrui, Sebas, Diego, Gabo, Alix, Jean-Charles, Nathalie, and all Master students as well. I was extremely fortunate to have landed in such a great group.

Briggite and Luc: for giving me a room during my most difficult time and making me feel at home.

Gabriela y Danilo: por ayudarme desde el comienzo (incluso desde antes de pisar Bélgica), por sus invitaciones, comidas, largas charlas y hacerme sentir parte de su familia.

Fernando, Paola, Marjan: por las salidas, los viajes y dejarme compartir momentos con ustedes.

Xime: por haberte cruzado en mi camino, por brindarme un cariño inigualable y un apoyo incondicional. Por nuestras escapaditas inolvidables y hacerme una mejor persona. Este doctorado hubiese sido mucho más complicado sin vos.

Del lado argento, mil gracias a (l):

Agencia (ANPCYT), CONICET e INCAPE: por darme la oportunidad de hacer un doctorado.

Grupo de Fisicoquímica: por recibirme con los brazos abiertos, hacerme sentir a gusto, cuidado, y por todos los momentos compartidos juntos. Hay un sentido de unidad, de familia, que ojalá nunca se pierda.

Grupo Soot: por aceptarme y la ayuda brindada en todo momento, sobre todo Sabri y Nico en mis comienzos preparando papeles, y más adelante Naty con el equipo. Fue placentero aprender y compartir con ustedes.

Cabe: mi codirector “off the record”, por dedicarme tanto tiempo, por la paciencia, aprendizajes y los chistes para distender un poco.

Aulita: por darme un lugarcito, por su calidez, la amistad, las anécdotas, las risas y los cafecitos.

Gabo: por estar siempre presente, incluso (y sobre todo) a la distancia, por las juntadas, las charlas y compartir ese amor por la guitarra.

Flor: por ser tan buena compañera y amiga cuando empezamos juntos el doctorado y los cursos daban miedo.

Mis amigos, “los chicos”, los de siempre: que aunque ya no nos veamos tan seguido como antes, siempre que nos juntamos es como si nada hubiera pasado. Eso quiere decir muchísimo.

Por último y más importante, a mi familia: que siempre está presente y son mi sostén, ya sea si estoy a miles de kilómetros o a unos pocos metros molestando en casa. No hubiese llegado hasta este punto de no haber sido por ustedes. Son lo más valioso que tengo. Estoy y estaré eternamente agradecido. Los amo inmensamente.

ABSTRACT

This thesis dives into the application of supported fibrous catalysts for air pollution control since atmospheric contamination is responsible for severely damaging the environment and harming all living beings on this planet.

Fiber-based catalysts are an attractive option in catalysis since fibers can enhance heat and mass transfer, reduce the pressure drop, and provide versatility in terms of materials, sizes and shapes. In order to obtain fibrous supports, a biotemplating synthesis route was adopted to produce different types of ceramic supports.

Two different deposition methods were used to incorporate active oxide phases for oxidation reactions: the traditional wet impregnation technique and a novel approach by performing a glidarc plasma precipitation-deposition.

The abatement of three different air contaminants was studied through catalytic oxidation reactions: a solid reactant, representative of particulate matter, along with two different gaseous reactants, one of them coming from the incomplete combustion of hydrocarbons, and the second one, from the volatile organic compound family.

A wide array of characterization techniques was applied to understanding the main physicochemical, morphological and textural properties of the catalysts. Great effort was put into trying to correlate catalytic activity with characterization results.

This work contributes to gaining insight into the synthesis of fibrous catalysts, on how their properties are affected by following different deposition paths, and their influence on the catalytic activity towards the oxidation of three different air pollutants.

TABLE OF CONTENTS

GENERAL

INTRODUCTION

1 Introduction

1.1 Catalysis

Catalysis is at the core of this thesis. But what is catalysis? What is a catalyst? Why is catalysis important? Addressing these fundamental questions is the best starting point for better comprehending the rest of the document.

The most commonly encountered definition of a catalyst is the following: "A material that converts reactants into products, through a series of elementary steps, in which the catalyst participates while being regenerated at the end of the cycle. More importantly, a catalyst makes a reaction proceed faster" [1].

In a simplified way, the function of a catalyst is to speed up a reaction. It offers an alternative path of reaction, more complex but energetically more favorable than the non-catalytic mechanism, allowing processes to be carried out at milder conditions of pressure and temperature, achievable in industrial facilities.

A catalyst changes the kinetics of the reaction but does not change the thermodynamics. It reduces the global activation energy of chemical reactions and thereby increases their rates. This is clearly exemplified in Fig. i.1 for a generic reaction between two molecules A and B to produce P [2]. The catalytic path requires less energy than the non-catalytic one, while the starting and ending points remain the same for both reactions routes.

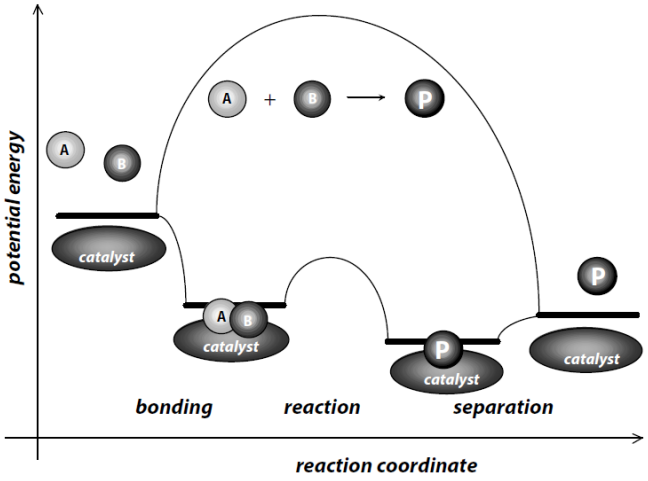

Fig. i.1 - Potential energy diagram for a generic reaction A + B → P [2].

Another important property of a catalyst is the ability to favor the formation of a specific product, minimizing the formation of unwanted by-products. This property is known as selectivity, and it is crucial for producing desired products by preferentially favoring specific reaction pathways.

It is estimated that 85-90% of the products made by the chemical industry require the use of catalysts [1]. Among the catalytic processes, three distinct areas can be differentiated: biocatalysis, homogeneous catalysis, and heterogeneous catalysis, where the latter makes the greatest contribution in terms of industrial processes (Fig. i.2) [3].

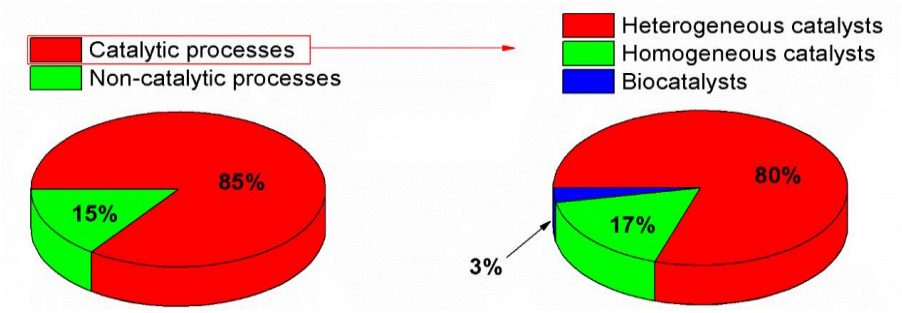

Fig. i.2 - Relative contribution of catalytic processes to the chemical industry (left) and comparison between types of catalysts used (right) [3].

Heterogeneous catalysis corresponds to processes that use a catalyst that is in a different phase than the reactant(s), i.e. the catalyst is usually in solid phase and the reactant is in gaseous or liquid phase [3]. The main advantage of using heterogeneous catalysis over their homogeneous counterpart is the easy separation of the solid from the liquid and/or gas reactants and products.

Heterogeneous catalysts have numerous industrial applications in several sectors such as chemical, food, pharmaceutical, automobile, and petrochemical [1]. It is also directly related to solving environmental problems. It is a means to minimize the emissions of several pollutants to the atmosphere by transforming them into more benign products. The most typical case that the average person associates catalysis with is the automotive exhaust converter. However, the scope is much wider when considering pollution abatement via catalysis. An illustration of the environmental scope involving heterogeneous catalysis is shown in Fig. i.3 [4].

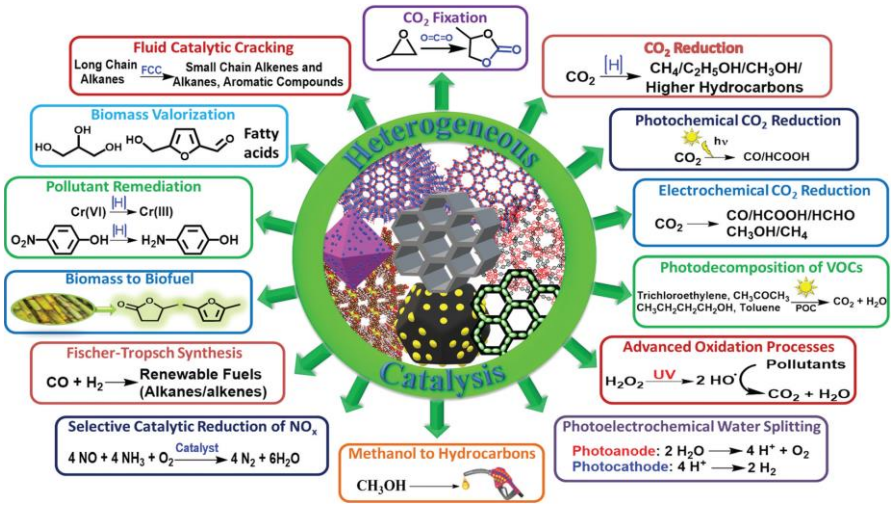

Fig. i.3 - Scheme of various environmental applications of heterogeneous catalysts [4].

Continuous research in this field is required to keep up with an increasingly difficult situation in terms of environmental and energy issues derived from our industrialized society. This demanding task requires interdisciplinary collaboration. Currently, “green chemistry” technologies are searched for in every single process, aiming at using raw materials efficiently, avoiding and/or minimizing the generation of waste or undesirable byproducts.

1.2 Air pollution

1.2.1 Primary and secondary pollutants

Global pollution and consequent climate change are among the most pressing matters that humanity faces nowadays. During the last decade, the situation has caught great attention due to the great number of natural disasters taking place all over the world, more often than usual. The long-term strategy of the *Paris Agreement* [5], adopted in 2015, limits global warming below 2 °C by 2030, which according to many scientists it is a goal difficult to meet. Also, the European Union set itself a target of net-zero greenhouse gas emissions for 2050, which would mean a 60% reduction in emissions compared to 1990 levels [6].

The three major types of pollution are air, water and land pollution. Among them, air pollution is the one that makes the greatest environmental impact, directly threatening the health of living beings. Ambient air pollution is estimated to have caused 4.2 million premature deaths worldwide in 2019 [7]. A study made in 2021 reported that a total

of 8.7 million people have died as a result of burning fossil fuels [8]. Moreover, most of the population is living in zones that do not meet the basic air quality standards set by the World Health Organization [9].

Anthropogenic activities are the main contributor to air pollution. The use of oil, coal, and natural gas as a source of energy continuously emits greenhouse gases to the atmosphere, leading to global warming. These sources can be fixed (industries, services, domestic), mobile (transportation) or even natural (wildfires, volcan eruptions).

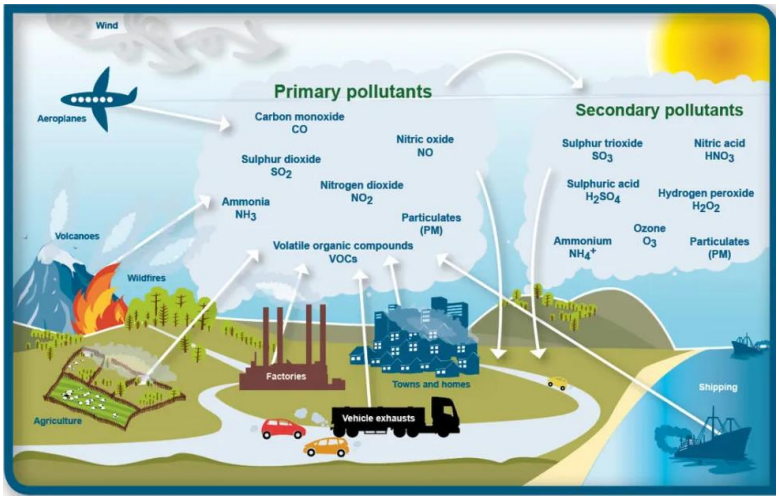

Fig. i.4 - Environmental primary and secondary pollutants [10].

Pollutants can be also divided into primary and secondary pollutants. The formers come directly from the emission source, while the latter are formed when the primary pollutants react, with the aid of solar radiation, with other compounds present in the lower atmosphere (Fig. i.4) [10]. Secondary pollutants are very difficult to control, that is why the emphasis should be put on trying to reduce the emission of primary pollutants in the first place [11].

In this thesis, the abatement of three primary pollutants is studied: particulate matter (PM), volatile organic compounds (VOCs) and carbon monoxide (CO).

1.2.2 Particulate matter

Particulate matter (PM) is a main contributor to the pollution of air and is extremely dangerous upon long-term exposure. It consists of a complex mixture of solid particles and liquid droplets that vary widely in size, shape, and chemical composition (inorganic ions, metallic compounds, organic compounds, elemental carbon, etc.) depending on the source of

emission. Some particles are large or dark enough to be seen with the naked eye (dust or dirt), while others are so small that they can only be detected by an electron microscope [12,13]. PM is commonly divided into two main categories: coarse particles (PM_{10}) and fine particles ($PM_{2.5}$). PM_{10} and $PM_{2.5}$ refer to particles equal or lower in size than 10 µm and 2.5 µm, respectively (Fig. i.5). PM_{10} can stay suspended in air for hours or even days, also can penetrate the lungs and remain there. With respect to $PM_{2.5}$, these particles can pass the lung barrier and even get into the blood stream. Chronic exposure to these particles can lead to serious cardiovascular and respiratory problems as well as premature death [8,14]. Particles bigger than 10 µm in size are referred to as large coarse particles and are not as dangerous as smaller ones since they usually do not enter the lungs, reaching only the nose and throat.

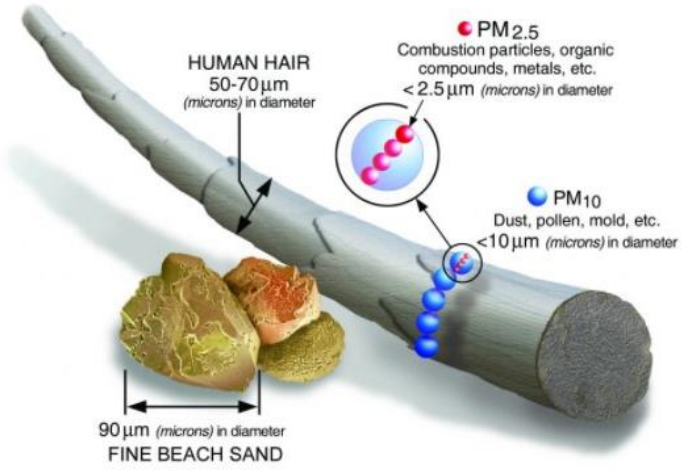

Fig. i.5 - Size comparison of different particulate matter (PM) [12].

PM emission sources are classified in outdoor and indoor, whether they come from open or closed ones, respectively. A common source of outdoor PM are the exhaust gases from vehicles equipped with diesel and gasoline engines, through which they exit mainly in the form of soot [15–18]. Vehicles also release carbonaceous particles containing Si, Zn, and S, as a result of the friction of tires against roads (tire wear particles), in addition to the dust emitted from the friction between brake pads and discs (break wear particles) [19]. PM is also emitted from stationary engines used to generate electricity and to operate compressors and pumps at power and manufacturing plants. Another concerning source of PM emission (indoor PM) comes from coal and wood combustion for heating homes (fireplaces) and cooking, which not only is dangerous for

the residents but also contaminates the atmosphere when coming out of the households [13,20]. The composition of PM is complex and in any particular location will be affected by local gaseous pollutants, meteorology, geography, and seasonal patterns [21].

A schematic representation of PM released by diesel engine exhaust gases is shown in Fig. i.6 [18]. A soluble and an insoluble organic fraction can be differentiated. Solid carbon spheres (soot), approximately 0.01-0.08 µm, are agglomerated with adsorbed and condensed hydrocarbons, and inorganic materials (mostly sulfates), forming bigger agglomerates of about 0.05-10 µm [22]. Other components found in the soluble organic fraction are aldehydes, alkanes, alkenes, aliphatic hydrocarbons, polycyclic aromatic hydrocarbons (PAH's), and even rests of lubricant oil.

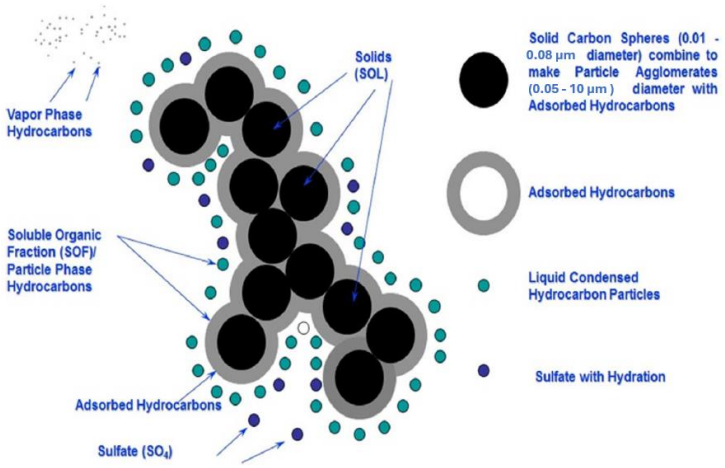

Fig. i.6 - Schematic representation of PM from diesel exhaust gases [18].

Inside the combustion chamber, soot is formed at elevated temperatures in fuel rich regions without sufficient oxygen, near the fuel injector. It is produced from non-burned or partially-burned fuel in the vapor phase, which nucleates constituting a solid phase. The steps leading to the transformation of liquid phase hydrocarbons (fuel) to soot are shown in Fig. i.7 [18].

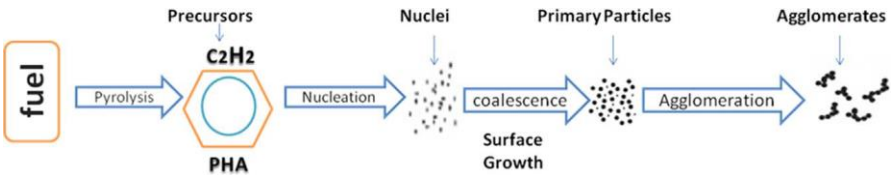

Fig. i.7 - Soot formation process in a diesel engine [18].

The final characteristics of soot highly depend on the type and age of the engine, parameters, type of oil, fuel used, etc. [23]. All this has an effect on the amount of adsorbed hydrocarbons and degree of graphitization (amorphous and graphitic contribution).

Soot consists of agglomerates about 100 μm in size which are composed of clusters of carbonaceous spherules of 10-50 nm, and it presents different proportions of amorphous and graphitic fractions depending on the source (Fig. i.8) [22,23]. Ultrasound baths can be used to disaggregate these agglomerates.

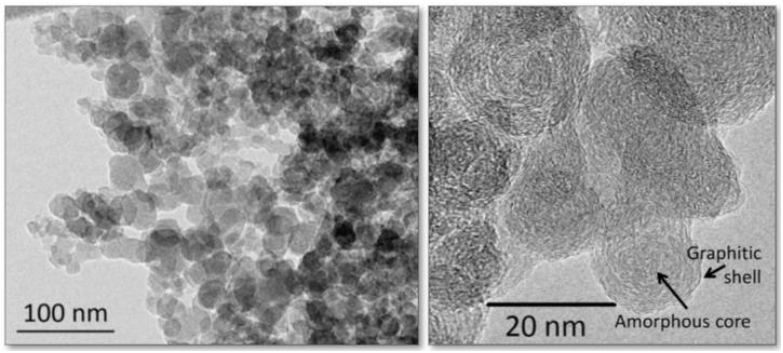

Fig. i.8 - TEM images of real diesel soot [23].

The techniques to control PM released from diesel engines can be separated into pre-combustion and post-combustion. The pre-combustion approach applies fuel modifications such as adding additives or changing fuel composition (adding biodiesel for example), or "in cylinder" modifications like injection timing and injection pressure. The post-combustion control technique involves a diesel particle filter (DPF) to trap the particles. The use of catalysts inside the DPF permits the obtention of catalytic diesel particulate filters (CDPF) that provoke soot burning as it is collected, allowing the passive regeneration of the filter. More insights into DPF systems are presented later (Section 1.2.6).

A wide array of catalysts have been reported for soot combustion, including formulations of noble metals, non-noble metals, metal chlorides, molten salts, alkaline/alkaline earth metals and transition metals that can complete redox cycles (V, Mn, Co, Cu, Fe, etc.) [24,25]. The most used noble metals are Pt, Pd and Rh supported on Al_2O_3, CeO_2-ZrO_2, SiO_2 or TiO_2. However, noble-metal based catalysts have limited availability and high costs and these are the reasons behind the search for alternative catalysts [26]. Other types of catalysts found in the literature are: hydrotalcites, perovskites (ABO_3), spinels (AB_2O_4), mixed

metal oxides, mixtures of metal oxides (composites), three-dimensional ordered macroporous materials (3DOM), etc. [26–29].

1.2.3 Volatile organic compounds

Volatile organic compounds (VOCs) are a large group of carbon-based compounds that evaporate easily at ambient temperature and pressure. These compounds have a high vapor pressure for which they are present in the ambient atmosphere as vapor. Due to their high diffusivity, toxicity, and volatility, VOCs classify as one of the major contributors to environmental pollution. Their impact in the atmosphere depends on their concentration and emission source [30–32].

Most emitted VOCs can lead to the formation of secondary pollutants, such as tropospheric ozone, peroxyacetyl nitrate and secondary organic aerosols. It is well known that these pollutants cause serious environmental problems such as climate change and health effects on living beings.

VOCs come from different sources including petroleum refining, organic raw material production, synthetic resin, textile dyeing and printing, leather manufacturing, transportation, pharmaceutical industry, pesticides manufacturing, coatings, adhesives manufacturing, spraying (aerosols and air fresheners), and the manufacture of electronic equipment (Fig. i.9) [33]. In the case of VOCs emitted from transportation, they are formed due to the incomplete combustion of the fuel in the engine, and include lineal-carbonated chain, aromatic and oxygenated compounds. Similar to PM, these sources are typically divided as “outdoor” and “indoor” sources [34].

Fig. i.9 - Indoor and outdoor sources of volatile organic compounds (VOCs) [33].

VOCs include aldehydes, ketones, esters, acids and alcohols. The heteroatoms which are more frequently present in VOCs are oxygen and sulfur. They are typically classified in different groups: halogenated (polychloromethanes, chlorobenzene, trichlorobenzene), aromatics (benzene, toluene), aliphatic hydrocarbons (saturated alkanes, unsaturated alkanes/alkenes), polycyclic aromatic hydrocarbons (naphthalene, phenanthrene, pyrene), and nitrogen or sulfur containing VOCs (amines, amides, nitro-compounds, methyl mercaptan, dimethyl disulfide) [30,34].

The emission of VOCs can be controlled using methods based on recovery or destruction. The techniques based on recovery include absorption, adsorption, membrane separation, and condensation. On the other hand, destruction methods convert VOCs into carbon dioxide and water. The destruction process can be thermal, catalytic, or biological oxidation [31].

Thermal incineration of VOCs needs temperatures above 800 °C to achieve total oxidation and is generally applied to highly concentrated gaseous streams. In turn, the catalytic oxidation is more convenient for flue streams with low VOC concentration (< 5 % vol) [30]. With this approach, the oxidation can take place at much lower temperatures (250-500 °C) than using non-catalytic thermal methods.

The catalytic oxidation of a generic VOC (hydrocarbon) into CO_2 and water can be expressed by the following equation:

$$C_xH_y + \left(x + \frac{y}{4}\right) O_2 \rightarrow xCO_2 + \frac{y}{2} H_2O \qquad \textit{Equation i.1}$$

The oxidation of VOCs containing chlorine (Cl), sulfur (S), or nitrogen (N) can lead to the formation of complex mixtures of toxic byproducts. These heteroatoms, among others, can bring extra complications by poisoning the catalysts.

Since there is a wide range of VOCs with different properties, and reaction conditions are not always the same, it has been hard to correlate the oxidation of all of them to a single reaction mechanism. Three model mechanisms have been proposed to explain the complete oxidation of VOCs:

i) Mars-van Krevelen (MVK): the adsorbed VOC reacts with surface lattice oxygen rather than with oxygen in the gas phase, reducing the catalyst in this process. The oxygen vacancies so created are replenished in a subsequent step by gas phase oxygen, reoxidizing the catalyst.

ii) Langmuir-Hinshelwood (L-H): this mechanism involves the adsorption of both reactants, VOC and oxygen, on the catalyst surface, which react to produce CO_2 and water that then desorb from the surface.
iii) Eley-Rideal (E-R): in this mechanism only one reactant (VOC) adsorbs on the surface of the catalyst while the other (most of the time oxygen) interacts directly from the gas phase.

In addition to the nature of the VOC, the reaction mechanism followed depends on the catalyst properties as well. Generally, the experimental data will have a good fit using one of the models mentioned.

There are three big categories of catalysts used to abate VOCs [31]:

i) Noble metals: Pt, Pd, or Rh, etc. These metals are very active but come with higher costs and can suffer deactivation by sintering at high temperatures and/or poisoning by sulfur, phosphorus, halogens (chlorine) and others.

ii) Non-noble metals: transition metals and rare earth metal oxides such as CuO, MnO_2, Fe_2O_3, NiO, Cr_xO_y, and Co_3O_4. This category is a cheaper approach, and non-noble metals also show some resistance to poisoning. However, their efficiency is lower in comparison to noble metals.

iii) Mixed oxides: combinations of metal oxides in the search of synergistic effects have been widely reported, such as Mn-Ce, Mn-Cu, Co-Ce, Sn-Ce, Mn-Co, Ce-Cu oxides. These catalysts can act separately (mixtures of single oxides or composites) or as solid solutions.

Generally, all these catalysts are supported on materials with good thermal stability and high specific surface area, such as Al_2O_3, ZrO_2, CeO_2, SiO_2, TiO_2, La_2O_3, MgO, zeolites and carbon-based materials.

Among the target aromatic VOCs commonly found in the literature are benzene, toluene, ethylbenzene and xylene, since they are the most abundant in the environment (over 60% in urban areas) [35]. The former is the one chosen in this work as a representative aromatic target VOC.

Benzene is a compound employed in several industries such as chemical, petrochemical, steel manufacturing, painting and coating manufacturing, among others. It is one of the major indoor air pollutants, related to household products and activities like smoking and cleaning. Benzene is toxic, carcinogenic and can lead to chronic diseases upon long exposure [36–38].

1.2.4 Carbon monoxide

Carbon monoxide (CO) is a colorless and odorless gas that is harmful when inhaled. The main outdoor sources of CO are anthropogenic such as transportation (mobile) or industrial facilities (stationary), along with natural sources as well [39]. Gas heaters, chimneys, furnaces, and stoves also release CO in indoor spaces.

CO is produced as the result of an incomplete oxidation of organic compounds which occurs when there is a shortage of oxygen, and the fuel cannot react completely to produce carbon dioxide and water [40,41]. Exhaust gases from gasoline contain a higher concentration of CO than diesel ones (Section 1.2.6). CO is easily removed from exhaust gases because it is easily adsorbed and oxidized by mobile oxygen species on the catalyst surface [42].

When breathing air with high concentration of CO, a lower amount of oxygen is transported in the blood stream due to the high affinity of hemoglobin towards CO forming carboxy-hemoglobin (COHb). This reduces the amount of hemoglobin available to transport oxygen from the lungs to the rest of the body, thus leading to possible dizziness, confusion, and even death. It is known as the “silent killer” since it gives no clear warning of the risk [43,44]. Considering that CO is a main contributor to air pollution as a primary pollutant, it was selected as the second gaseous contaminant to be studied in this thesis.

1.3 Emission standards for vehicles

Air quality standards are defined worldwide by the World Health Organization (WHO) and regionally, for example, by the European Environment Agency, and by the United States Environmental Protection Agency (EPA) [45–47]. The EPA is required to set National Ambient Air Quality Standards (NAAQS) for six principal pollutants (“criteria” air pollutants) [48]. The EPA also regulates the emissions of VOCs at a national level (40 CFR 59), typically based on the application of products such as: aerosol coatings, architectural coatings, automobile refinish coatings, and consumer products [49]. In Europe, the European Union (EU) regulates VOC emissions in several ways, including the Industrial Emissions Directive and Paints Directive, among others [50].

The most recognized standards are applied or used as reference by other countries or continents through the passing of legislation packages. The EURO 6, US Tier 2 or LEVIII are examples of emission standards set for urban transportation. Each legislation sets its own values for each pollutant and does not necessarily comply with the WHO’s or EPA’s values. It is thought that many European cities still exceed WHO’s

standards. Developing countries, outside Europe, the US and Japan, have adopted emission policies based on European regulations. Argentina started to set limits to vehicle emissions in 1995 taking as reference the US standards, changing in 2002 to European ones [51]. Fig. i.10 shows the emission limits for main pollutants set by the latest standards for diesel and gasoline engines [52].

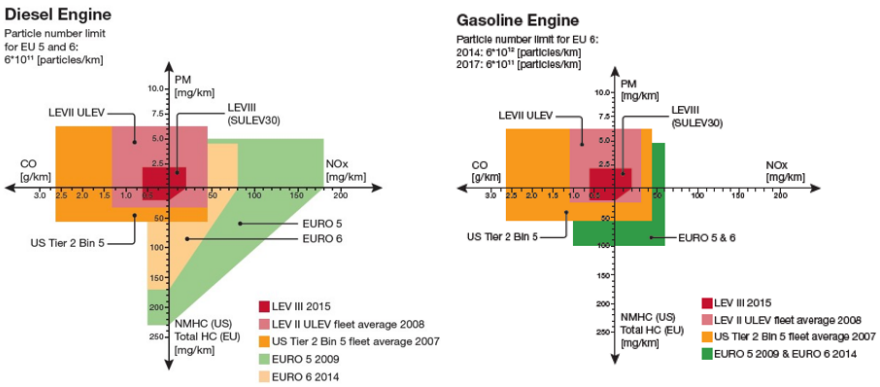

Fig. i.10 - Diesel engine (left) and gasoline engine (right) emission limits evolution in the US and Europe for light-duty vehicles [52].

Diesel and gasoline engines are regulated separately, and a distinction is made for light-duty and heavy-duty vehicles. These vehicles have also different testing procedures.

The Euro 6 for diesel engines has the following maximum values of contaminants for light-duty vehicles: 0.17 g (HC + NO_x)/km, 0.08 g NO_x/km, 0.005 g/km PM and $6x10^{11}$ particles/km. This particle mass limit represents a reduction of 96% from Euro 1 limit. The particle number limit was introduced at the Euro 5 because the particle mass reached a level so low that it became hard to measure. With this additional control, the lower size range of particles is also considered, which are the most dangerous. Different methods can be used to measure size and number of particles emitted such as Scanning Mobility Particle Sizer (SMPS) and Optical Particle Counter (OPC), among others.

As regard to NO_x, the latest limit is 84% lower than the Euro 3 level (where NO_x was first introduced), and 56% lower than Euro 5 [53].

The limits for gasoline vehicles have dropped significantly throughout the years. Even though the Euro 6 NO_x limit is the same as in Euro 5, this value is 60% lower than the one set at Euro 1 level.

In Europe, the next step to further reduce road transport emissions is the Euro 7 norm. Passenger cars and vans will maintain Euro 6 limits, while

for buses and trucks stricter limits will be applied. The novelty that will come with Euro 7 is the control of non-exhaust particle emissions (PM_{10}) from tires and breaks, along with minimum battery durability in electric and hybrid cars. Earlier this year, the Parliament adopted the deal reached with the Council on the Euro 7 regulation and this was the last step in the procedure. The dates of application of the regulation will depend on the kind of vehicle concerned [54]. The Euro 7 will be introduced on 1 July 2025 and will be the strictest standard yet.

1.4 Exhaust after-treatment systems

In the late 1960s, major cities such as Tokyo in Japan and Los Angeles in America, faced serious air quality issues owing to the formation of "photochemical smog" containing ozone. The numerous cars in circulation were seen as the major source of pollution and action had to be taken. In 1970, a Clean Air Amendment Act in America asked for a 90% reduction of CO and HC emissions by 1975, and 90% reduction of NO emissions by 1976. The catalytic converter was thought to be the best solution to tackle this problem [55]. Since then, several exhaust gas after-treatment technologies have been developed by the automotive industry to reduce engine emissions and meet ever increasing regulations set by governments.

These technologies are tailored to the type of engine since the exhaust composition of a diesel engine is not identical to that of the gasoline counter-part (Fig. i.11). There are two major differences between diesel and gasoline engine exhausts: i) the former has higher PM and NO_x content, and ii) it has far less unburned hydrocarbons and carbon monoxide than the latter [25,56]. Due to these differences, the exhaust treatment system is not the same for both types of engines.

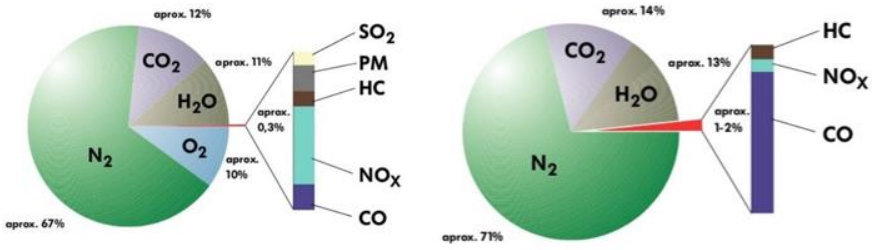

Fig. i.11 - Diesel (left) and gasoline (right) exhaust gas composition.

A typical exhaust treatment system for a diesel car is presented in Fig. i.12. The gases go through four steps: an oxidation catalyst (DOC), a diesel particle filter (DPF), a selective catalytic reduction (SCR) and lastly, an oxidation step called ammonia slip catalyst (ASC) [57].

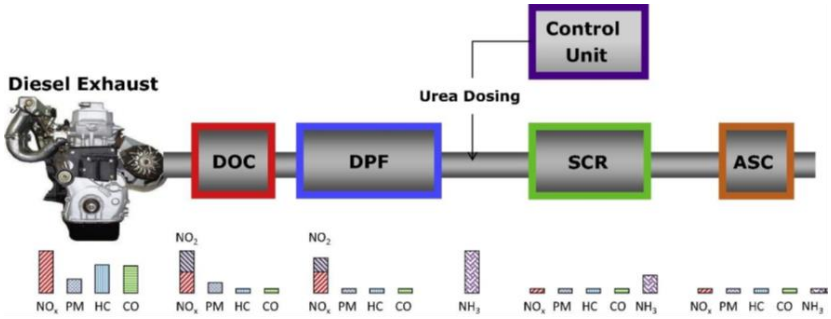

Fig. i.12 - Exhaust treatment system for diesel engines [57].

The first block that the gases face is the DOC, which is commonly a monolith structure (ceramic or metal) washcoated with alumina (Al_2O_3), cerium oxide (CeO_2) and zirconium oxide (ZrO_2), and Pt or Pd (noble metals) as active elements. The main function of this step is to oxidize carbon monoxide (CO) and unburned hydrocarbons (HC) to CO_2 and H_2O. The DOC also oxidizes the volatile organic fraction that covers PM, but the carbon component (soot) continues unconverted downstream. Some NO is also oxidized to NO_2, which is a much more powerful oxidizing molecule than NO and O_2, and whose presence is crucial in the next step [25,58].

Following the DOC, the next block is a diesel particle filter (DPF), whose function is to trap the soot that was produced by incomplete combustion of diesel fuel. The DPF typically consists of a wall-flow ceramic monolith (cordierite or SiC) that traps the PM as the gas flows through its porous walls. The adjacent channels of the filter are alternatively plugged (Fig. i.13) [18].

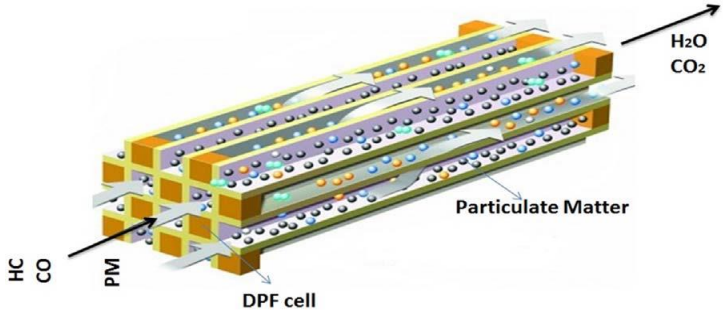

Fig. i.13 - Diesel particule filter (DPF), wall-flow configuration [18].

The removal efficiency of the filter is roughly 99%, but as the particles accumulate inside the porous walls, the pressure soars and the fuel is overspent, affecting the performance of the engine. Due to this reason,

the filter needs to be regenerated periodically. There are two ways in which these filters can be regenerated: active or passive. For active regeneration, external sources (electric heater or flame burner) are used to increase the temperature up to the soot ignition temperature (> 600 °C), in order to burn non-catalytically the trapped soot [25]. On the other hand, the passive control uses catalysts to combust soot at lower temperatures so that the filter does not get plugged and build back pressure. Another passive approach is the use of additives in the fuel (fuel borne catalysts) with the aim of producing soot embedded with catalysts, and therefore, facilitating its oxidation up in the line. However, their use is not recommended as these additives can be eliminated along with exhaust gases thus contributing to the pollution of air [28,59].

The so-called Continuously Regenerating Trap (CRT), pioneered by Johnson Matthey, combines the first blocks together: a DOC is installed upstream of a DPF so that NO_2 is produced ahead and can react with trapped soot after, continuously regenerating the filter (Fig. i.14) [25]. The principle behind the CRT is that NO_2 is a much superior oxidizing agent than oxygen, as previously noted, facilitating the burning process inside the DPF [27].

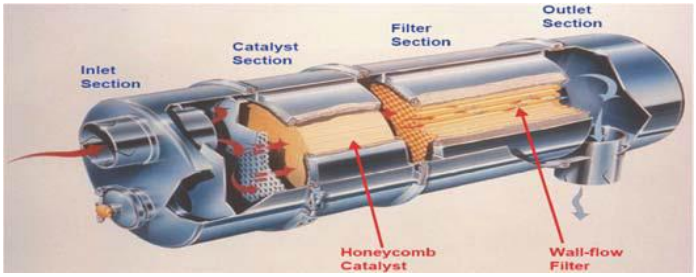

Fig. i.14 - Continuously Regenerating Trap (CRT) system [25].

The next block in the chain is the selective catalytic reduction (SCR). Here, the objective is to reduce the NO_x emissions by reducing them to N_2. Some catalysts employed in this part are vanadium oxide supported silica (V-SiO_2), copper (Cu) and iron (Fe) supported on zeolites. Ammonia is used as a reducing agent and for this a supply of a 30-40% aqueous urea solution (Ad-Blue) is needed. This part adds complexity to the whole treatment system because it means to have a storage unit and pumps for administration. The SCR is generally applied to heavy-duty vehicles (HDV). Other method to deal with NO_x species, more suitable in light-duty vehicles (LDV), is the so called “Lean NO_x Trap” (LNT), which meets the objective by using noble metals. SCR has higher NO conversion, lower cost, and lower sulfur sensibility, in comparison to LNT [28,58].

The last block is the ammonia slip catalyst (ASC). This step is necessary to prevent NH_3 release out to the environment. To comply with NO_x normatives, high dosing of urea is required in the SCR block, and this leads to NH_3 slip. Therefore, any NH_3 left must be oxidized to N_2 and H_2O. The ASC catalyst must have high activity and selectivity toward N_2. Using another DOC step instead of an ASC is also a possibility [11,28].

Several modifications to this system can be found in the market. Car manufacturers create their own technologies and catalysts formulations based on their research, applying unique combinations of the steps presented before, tailored to a specific type of car and engine, with the main objective of reducing costs and space in their vehicles.

Regarding gasoline engines, the Three-Way Conversion catalyst (TWC) has been the conventional method to reduce emissions since 1975, removing simultaneously 90% of the HC, CO and NO_x produced by these engines (Fig. i.15) [60]. TWCs are composed of a substrate coated with combinations of Pt and/or Pd and Rh, alumina and ceria, and also additional promoters. The most common substrates are monolith structures made of metal (stainless steel) or ceramic (cordierite) materials. The addition of ceria provides the capacity to store oxygen under lean conditions and releasing it when the gas goes rich, thus allowing the oxidation of CO and HC when there is not enough oxygen in the gas [55]. This was the original purpose of adding ceria, but nowadays more sophisticated mixed oxide combinations are used, like ceria-zirconia, which improves the oxygen storage capacity (OSC) and thermal stability [61].

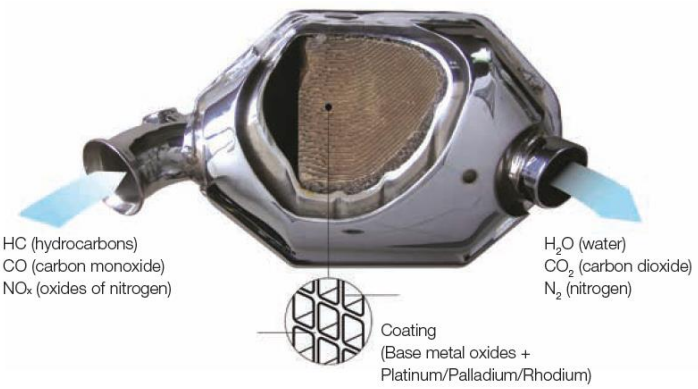

Fig. i.15 - Three-Way Conversion catalyst (TWC) system [60].

Pd and Rh metals not only promote the oxidation of HC but also the reduction of NO. For these catalysts to be efficient, the air/fuel ratio should be stoichiometric (near 14.6). An electronic oxygen sensor, also

called lambda (λ) sensor, is used to control the oxygen pressure and modulate this ratio inside the desired operating window [28,62].

The latest regulations introduced particulate matter (PM) control for gasoline engines as well (Fig. i.10). To face this challenge the TWC was improved into Four-Way Catalysts (FWC) by adding a filter step after or combined in the same substrate with a wall-flow approach (similar to Fig. i.13). With this innovative technology, all four pollutants are removed from the exhaust [63].

***

At this point, it is important to mention both the DPF and TWC systems, for diesel and gasoline engines respectively, represent real scenarios for the application of all catalysts synthesized in this thesis. Also, the prepared catalysts could be used in flue gas streams from industries or even for indoor spaces for PM and VOC abatement.

1.5 Target reactions

1.5.1 Solid-solid-gas phase reaction: soot combustion

In this thesis, soot combustion is the main reaction since it is studied for all synthesized catalysts in all four Chapters of this work.

Combustion is the sequence of exothermic chemical reactions between a fuel and an oxidant accompanied by the production of heat and conversion of chemical species. The fuels used can be in gas, liquid, or solid phase [41].

The soot combustion is a three-phase reaction: solid-solid-gas, and this adds complexity to its evaluation and comparison in a lab-scale. There are several features that play a role in this reaction. Among them, the first one is the type of soot used. The heterogeneity of real soot makes it difficult for catalysts screening because its physicochemical properties depend on the type of fuel, engine, working parameters, etc. Soot can also be obtained in the lab, often called “lab-soot”, but again the type of fuel and methodology used change its final properties [64,65]. As a result of this, commercial carbon black (CB) is often used as model soot for catalytic studies. This is the case in the current work. Also, the soot-to-catalyst ratio used was found to strongly influence the reaction rate as well [24,66,67].

Another factor to consider is the soot-to-catalyst contact, which greatly affects the catalytic result. The most common types of contacts reported are “loose” and “tight”, which are generated by mechanical mixing or milling, respectively. Other less conventional ones can be found too,

such as “wet”, “pressure”, and “super-tight” contact [22,26,68]. A comparison between loose, tight, and wet soot-to-catalyst contacts is reported later in this work for different types of fibrous supports. The precise methodology to reproduce these types of contacts can be found in the Experimental Section (Section 3.1).

The feed composition is also important when evaluating this reaction in the lab-scale. Besides the amount of oxygen, the presence of NO is key. As mentioned before for the CRT system, NO_2 is a more powerful oxidant than oxygen and can boost soot ignition considerably. From this, two mechanisms are commonly reported: i) active oxygen mechanism; ii) NO_2-assisted mechanism. Two graphic representations of these mechanisms are shown in Fig. i.16 and Fig. i.17 for ceria and MnO_x-CeO_2 catalysts, respectively [23,69]. When NO is present, both mechanisms will probably take place at the same time (tandem effect).

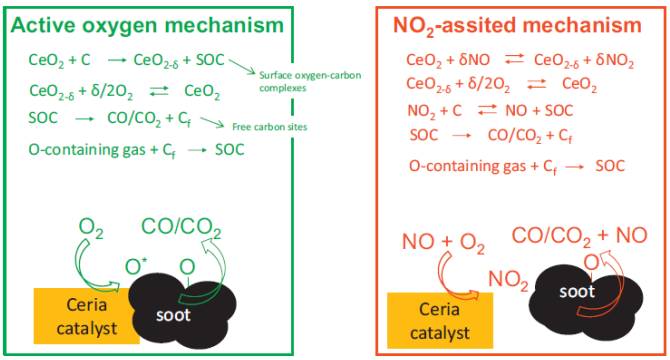

Fig. i.16 - Active oxygen mechanism (left) and NO_2-assisted mechanism in soot combustion [23].

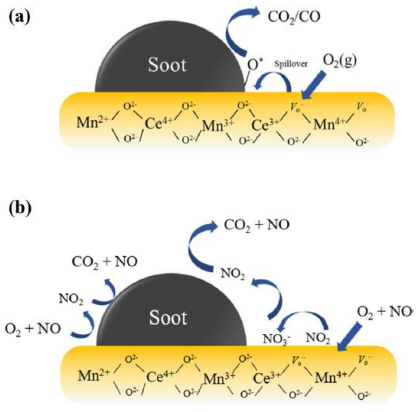

Fig. i.17 - Soot oxidation over MnO_x-CeO_2 in the absence of NO_x (a) and in the presence of NO_x (b) [69].

Fig. i.18 clearly evidences the difference in soot combustion rate when NO_x is present in the feed, in comparison to just having oxygen as an oxidant [28].

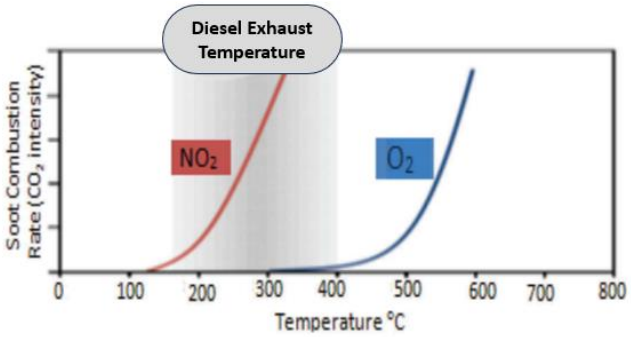

Fig. i.18 - The effect of NO_2 on soot combustion [28].

Lastly, soot properties change with time during the reaction (amount of oxygen, particle size, particle shape, amorphous and graphitic structure, specific surface area, etc.). Therefore, this affects the kinetic parameters such as reaction rates and activation energies, making it difficult to use them for catalytic screening like in other reactions. Thus, kinetic parameters are only valid for specific conditions and are generally not reported. This is the reason why most soot combustion studies consist of heating soot-catalysts mixtures at a fixed rate and finally reporting values like T_{50} (temperature at 50% soot conversion) or T_M (temperature at maximum combustion rate) for catalysts comparison. These values have the same limitations than kinetic parameters but are calculated more easily [23,24].

1.5.2 Solid-gas phase reactions: benzene and CO oxidation

The second type of reactions tested in this thesis involves solid-gas phases. This is a more conventional situation found in heterogenous catalysis in which all particularities that arise from using a solid reactant (like soot) are not involved. The two gas-phase reactants chosen were already introduced in the text: benzene (VOC) and carbon monoxide (Section 1.2.3 and 1.2.4).

The oxidation of benzene is often correlated to the MVK mechanism in the literature [31,32]. In this model, the reaction occurs between surface lattice oxygen on the catalysts and the adsorbed VOC molecules. This results in the formation of oxygen vacancies and the reduced sites are oxidized either by gas-phase oxygen or bulk oxygen (Fig. i.19) [31]. Similarly to benzene oxidation, the oxidation of CO has been related to the MVK mechanism (Fig. i.19) [70,71].

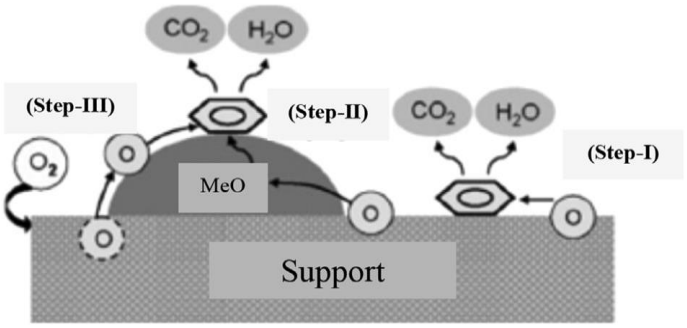

Fig. i.19 - MVK model representation for benzene oxidation over a supported catalyst [31].

***

All three target reactions in this thesis share a similar catalyst background. This is expected since they are all oxidation reactions. Therefore, all types of catalysts listed before for soot combustion (Section 1.2.2) and VOCs (Section 1.2.3) apply as well for CO oxidation.

Among the many active phases found in the literature for these reactions, by far the most common one is ceria (CeO_2), due to its remarkable redox properties, the capacity of storing/releasing oxygen, and good surface oxygen mobility [71,72]. This resulted in an extensive study of ceria-based catalysts throughout the years in many forms: as single oxide, composites, mixed oxides, supported, or even in ternary formulations [62,73]. The most common approach to enhance ceria performance and stability is by creating mixed oxides by doping ceria lattice with foreign elements as Zr, Mn, Co, Cu, and Fe [69,74–77].

Also, Co_3O_4 and MnO_x are often encountered in catalytic oxidation studies since they have very good properties such as multiple oxidation states, excellent reduction ability, high concentration of electrophilic oxygen, and more importantly, they are cheap alternatives [22,31]. Besides, Fe_2O_3 is another transition metal oxide that have been tested in oxidation reactions. Even though not as much active as Co or Mn oxides (when evaluated alone), it is stable, it has low toxicity, low cost and it is environmentally friendly [37,78,79].

In this work, CeO_2, Co_3O_4, MnO_x, and Fe_2O_3 are the metal oxides selected for the catalytic formulations and subsequent evaluations as an alternative instead of scarce and expensive noble metal catalysts. They are applied either as single oxides or deposited on suitable supports with a controlled morphology.

1.6 Fiber-based catalysts

Among the various morphologies commonly used for catalysts design, fiber-based materials have gained much interest

Fibers are elongated elements which typically have cylindrical geometries with a wide range of diameter sizes, from nanometers to millimeters. Fibers come in many forms: chopped, filaments, tow, yarns, knitted, and woven/unwoven fabrics. In addition to that, they can be made from different kinds of materials. This variety of possibilities makes fibers very attractive since they can be specifically produced to fit desired applications.

Fibrous materials are promising in the field of catalysis due to the following characteristics: high length to diameter ratio (aspect ratio), high surface to volume ratio, low pressure drop, high mass transfer and void fraction, safe handling, easy scale-up, and low costs of manufacture [80,81].

Inorganic fibers are commercially produced for a wide range of applications in different fields, providing attractive features such as good mechanical properties, toughness, and thermal resistance, depending on the material they are made of. Inorganic fibers are preferred over organic ones as catalysts since they can resist higher temperatures [82].

Fibrous catalysts are classified as micro-structured catalysts that satisfy the important requirements of catalyst effectiveness and low pressure drop, which is not easily achieved with catalytic pellets in packed beds. The small dimensions of fibers can eliminate diffusion as a rate-controlling factor by providing short diffusion distances. The radial mixing of a fluid is improved by the tortuosity of the fibrous bed which can also provide uniform temperature and concentration profiles. The low resistance to flow of liquids and gases passing through the fibers is one of the main advantages, which is related to their low pressure drop [81,83].

It has been reported in the literature, through simulations, that metallic fiber filters and wire meshes (both in the fibrous category) exhibit lower pressure drop than pellets for similar specific surface area values. Nevertheless, when compared to monoliths, fiber materials present a higher pressure drop. Also, in terms of mass transfer, pellets and wire meshes show similar Sherwood numbers (convective to diffusive mass transfer ratio) for similar Reynolds numbers (laminar or turbulent flow regimens), both being higher than that of monoliths. For the latter, the Sherwood number remains constant for all Reynolds numbers.

Moreover, for lower Reynold numbers, fibers show slightly higher Sherwood numbers [80].

Concerning the materials which catalytic fibers are made of, they are generally divided into: metallic, glass, ceramic, and carbon. Some examples are shown in Fig. i.20.

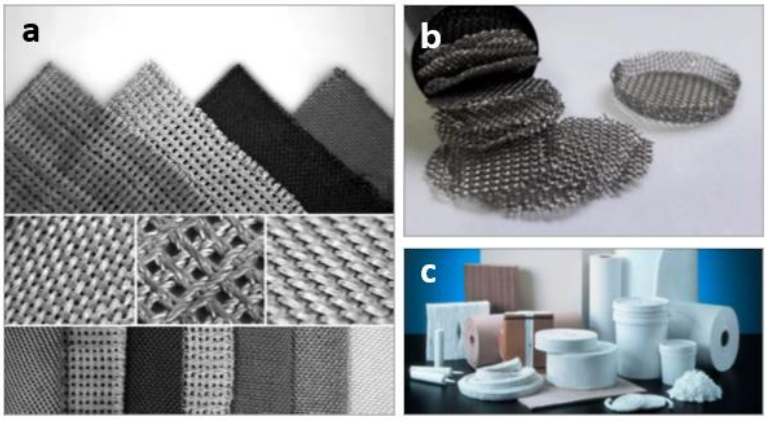

Fig. i.20 - Glass (a), metallic (b) and ceramic (c) structures made from fibers [83,84].

Metallic fibers (thin wires and metallic filaments) can be used as unordered sintered metal fiber sheets for filter application or ordered knitted or woven wire mesh structures. The most common examples of metallic substrates are wire meshes and gauzes. Supported metallic fibers are attractive particularly in terms of great resistance and thermal conductivity. Although, due to their low specific surface area, they must be coated with a layer of a high specific surface area material which is not an easy task [80,81].

Some properties of glass-fiber catalysts are high specific surface area, low cost, good flexibility, inertness, and they do not need to be coated as metallic fibers. Nevertheless, they do need to have the active elements deposited. The coating of these fibers is often done by direct impregnation with a precursor, but also by chemical vapor deposition (CVD). Either high or low specific surface areas can be achieved [80,81,83].

Ceramic fibers are made from combinations of kaolin, alumina, quartz, zirconium oxide and other oxides, that add specific properties such as good thermal stability (better than metallic fibers), mechanical resistance, flexibility, high specific surface area (if there is good porosity), low costs and easiness of coating. They are typically applied as support structures for combustion applications [80,81].

Finally, carbon-based fibers present specific surface areas in the range of 1500-3000 m^2/g, high adsorption capacity, as well as a unique type of surface, being able to have a complex porous structure (microporous, mesoporous, and macroporous). The mechanical properties and pore structure of these fibers are a function of the precursor, preparation method and chemical activation processes [85–87].

* * *

The morphology of a catalyst plays a key role in its catalytic performance. Certain morphologies can expose specific crystalline planes which can give an increase to the catalyst performance [89]. Moreover, one kind of morphology can improve the contact between reactants and active sites, mainly in a reaction that involves a solid reactant as it is the case of soot combustion, where soot-to-catalyst contact is paramount. Several authors have studied the influence of different catalyst morphologies on soot oxidation capacity. Cubes, flowers, spheres, and rods have been compared in many different works, and in most cases, fibers were the best-performing morphology. This is believed to be related to an improved soot-to-catalyst contact, and a higher amount of contact points between soot and active sites, due to the intertwined network generated by fibers [90–93]. A fibrous morphology has been reported to aid as well in the case of a gas-phase reaction, where there is no solid-solid contact needed, e.g. for the oxidation of CO [89,94].

1.6.1 Isolated catalytic fibers

The most common ways of synthesizing fibers are: electrospinning, hydrothermal, and biotemplating. They will be briefly mentioned hereafter.

Electrospinning is a simple technique for generating continuous and thin fibers using a wide range of material precursors. The fiber diameter can be adjusted from micrometers to nanometers. Electrospun fibers have found application in fields such as biomedicine, electric nanodevices, nano sensors, photovoltaics, etc. In heterogeneous catalysis, polymer and inorganic precursors are electrosprayed together and after a calcination step, oxide fibers are created [95–98].

The hydrothermal synthesis is a chemical process that occurs in an aqueous solution of mixed precursors above the boiling temperature of water and at a pressure higher than atmospheric, in a closed vessel like an autoclave [99–101]. Under certain conditions of synthesis, a fibrous morphology can be achieved [90,97].

A very simple yet innovative method of synthesizing fibers is by means of a biotemplate. Biotemplating provides an easy and quick transformation

from organic to inorganic structures (mainly done through thermal treatment), maintaining very complex morphologies only found in nature. This technique is applied in a wide array of fields, such as nanomaterials, sensors, adsorbents, and catalysis (Fig. i.21) [102,103].

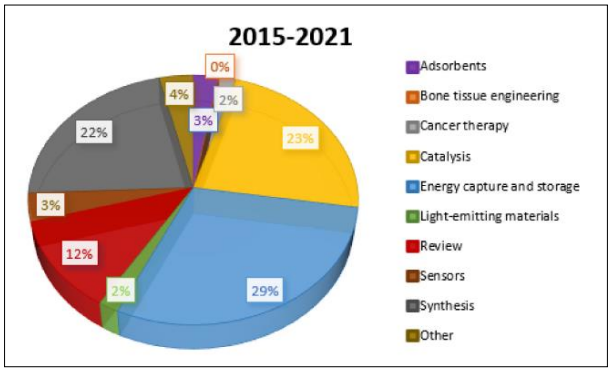

Fig. i.21 - Fields of application for the biotemplating technique [103].

Some authors have synthesized fibrous catalysts in this way utilizing different organic materials such as lens cleaning paper [104], cotton [105–107], egg-shell membranes [108] or scallion root [109] (Fig. i.22).

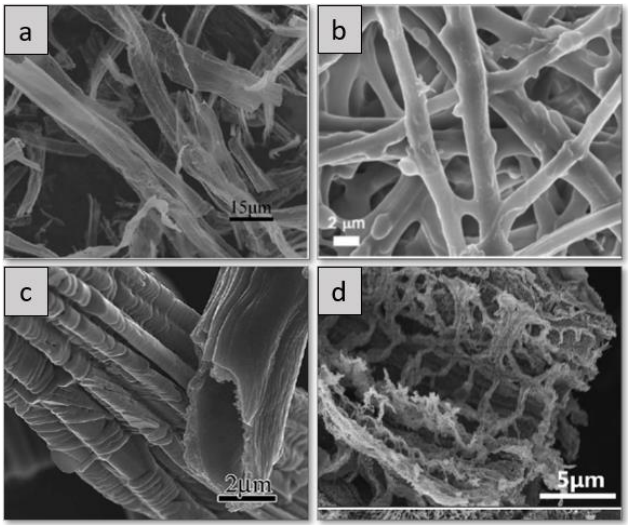

Fig. i.22 - SEM images of ceria fibers from lens cleaning paper (a) [104], ZnO fibrous network from egg-shell membranes (b) [108], Al_2O_3 fibers from cotton (c) [105–107], and ZnO fibers from scallion root (d) [109].

In this work, commercial cotton was chosen as the biotemplate for the obtention of ceramic fibers to be supported by foreign active elements

afterward. The complete synthesis procedure can be found in the Experimental Section (Section 1.1).

1.6.2 Structured fibrous catalysts

Structured catalysts are composed of substrates with a specific design, contrary to particles randomly oriented when pellets are placed into a reactor. A better control of the phenomena occurring in a reactor bed such as reaction, diffusion, heat and mass transfer, and pressure drop, can be achieved with specific designs of substrate geometries. By tailoring the size and shape of the void/space available to a gaseous stream and the surface exposed to this current (containing active sites), great improvements can be attained in the overall process.

Substrates can be either rigid or flexible with diverse geometries. The most widely known example of the former is the monolith which presents parallel inner channels (honeycomb). They come in different materials and arrangements (number of channels, wall thickness, wall-flow channels). As shown in Section 1.4, these substrates are widely used for exhaust after-treatments in transportation, for which they are washcoated with a layer of a porous materials and active elements. These structured catalysts present lower pressure drops in comparison to packed beds, due to the high porosity coating and its regular parallel channels. However, some monoliths like ceramic ones, which have high thermal resistance, present drawbacks like poor radial heat transfer due to the lack of radial mixing.

Other common examples of rigid substrates are ceramic and metallic foams. These materials favor radial mixing, thus improving mass and heat transfers. Additionally, they provide better heat transfer by conduction due to their continuous solid phase, particularly metallic ones. The disadvantage to using these types of substrates is that they are costly to manufacture.

On the other hand, flexible substrates can be considered, which can be manipulated and adapted to fit a specific geometry, for example a tubular reactor. This category includes ceramic papers made from ceramic fibers.

Fig. i.23 shows two examples of structured supports produced with different types of fibers. In the left image, a ceramic paper disk of 16 cm diameter is presented, which is obtained by a paper-making technique that utilizes a mix of ceramic and cellulosic fibers [84,88]. This fibrous substrate is flexible and easy to handle. The intertwined fibrous matrix inside these disks provide a high void fraction and therefore the high porosity leads to low pressure drop, in addition to good radial mixing and

better mass and heat transfers. The fibrous mat can also act as a filter which is promising for particulate matter abatement, for example in a DPF inside a car converter. The synthesis of these ceramic papers will be described later in the Experimental Section (Section 1.2). This synthesis is very versatile since it can be tailored in many different ways such as modifying the types and amounts of fibers used, the type of binder used, the addition of active phases prior or after the mat formation (thermal process), and the deposition method, among others. Evidently, the possibilities are endless. This synthesis method is also very easy and cheap. The right image in Fig. i.23 shows an example of a rigid structure substrate, consisting of wire mesh monoliths (1.6 cm diameter, 3 cm long) created by piling wire mesh disks alongside a metal casing [84]. Both examples shown are easily scaled-up.

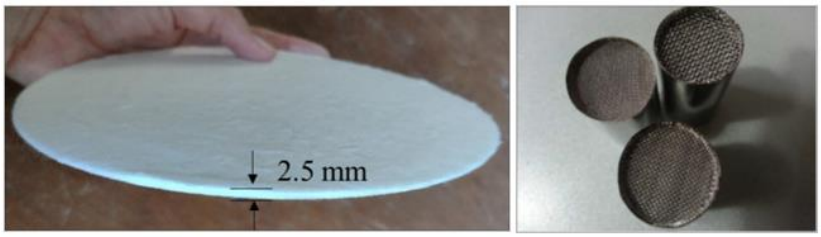

Fig. i.23 - Images of a ceramic paper disk (left) and wire mesh monoliths (right) [84,88].

* * *

It can be concluded from this section that fibers are promising and versatile materials to be used for preparing supported catalysts. The properties of fibers mentioned here are the main reason behind why all the work in this thesis involves fibers, whether isolated or structured, bare or supported by foreign metal oxides.

1.7 Methods for active phase deposition

1.7.1 Conventional deposition techniques

Some of the most conventional methods utilized to deposit catalytic elements over supports are wet impregnation (WI), incipient wetness impregnation (IWI), humid spray, spray drying, chemical vapor deposition (CVP), electrochemical deposition, physical vapor deposition (PVD), and sol-gel.

Impregnation deposition is the simplest and most widespread approach for the preparation of catalysts. The wet impregnation (WI) uses a precursor solution in excess with respect to the pore volume of the support, this makes stirring easy and ensures a homogeneous distribution of the metal precursor. However, due to the lack of chemical interaction between the support and the metal precursor, as the drying process occurs, the precursor can agglomerate on the external surface by migration, producing particles with low dispersion. This is because the pH of the solution is buffered to around the point of zero charge (PZC) of the support [110,111]. The PZC is the pH at which the net surface charge of the particle is equal to zero (sum of positive and negative charges is balanced). The relation between the solution pH and PZC of the support is something that could be studied and optimized to improve the outcome achieved by this impregnation, for example to have a better distribution of the supported phase. The wet impregnation is the first technique applied in this thesis for the addition of active elements on the biomorphic supports.

1.7.2 Glidarc plasma

With the aim of enhancing the anchoring of metal precursor on the support a novel technique is explored: the gliding arc plasma method (GP). In this technique the precipitation and/or deposition of metal oxides is induced by the generation of very active species by plasma. In contrast to WI, these reactive species could generate a better chemical interaction between the support and the precursor, favoring the dispersion of the catalytic phases. In the following, the fundamentals of plasma are introduced.

Plasma was first discovered in 1879 by Sir William Crookes, an English scientist, who called it “radiant matter” because of its luminous quality. In 1897, Sir J. J. Thomson, a British physicist, identified the nature of the matter. It was not until 1928 that the term “plasma” was coined by Irving Langmuir, an American chemist and physicist, because the strongly ionized gas reminded him of blood plasma [112].

Plasma is known as the fourth state of matter and is the most abundant form of ordinary matter in the visible universe. It is created through a process called ionization that adds energy to a gas so that some of the electrons leave their atoms. An ionized gas has unique properties that permit significant improvement of traditional chemical processes, increase their efficiency, and in some cases, stimulate chemical reactions which are impossible to convey by conventional methods [113].

Plasma can be found in natural phenomena: sun, stars, comet tails, lightning (Fig. i.24), aurora borealis and fire, as well as in daily-life products such as plasma TVs, neon signs, and fluorescent tubes. Man-made plasmas bring about numerous possible applications, including thermonuclear synthesis, electronics, lasers, fluorescent lamps, and many others [114].

Fig. i.24 - Benjamin Franklin's first experiments with lightning [114].

Plasmas, as multi-component systems, can exhibit multiple temperatures, for example between electrons and heavy particles. This leads to the classification of plasma as thermal and non-thermal plasma, in terms of thermodynamics. When a quasi-equilibrium is achieved, it is called thermal plasma, a good example in nature is solar plasma. On the other hand, a non-equilibrium results in a non-thermal plasma, and an example in nature is the aurora borealis. Non-thermal plasmas are usually generated at low pressures or at lower power levels. The application areas of these two types of plasma are quite different. Applications of plasma technologies involve many industries: etching and chemical vapor deposition in micro-electronics, thermal spray coatings, production of ozone, stabilization of flames, treatment of synthetic fabrics and polymers, plasma TVs, sterilization of water and air

streams, treatment of exhaust gases, and its use has been extended even to health treatments (ulcers, skin diseases) [114–116].

Since the second half of 20th century, the creation of plasma at lab-scale has been of great interest to transform gases into more reactive species. Typically, in the laboratory, a small amount of gas is heated and ionized by driving an electric current through it, or by shining radio waves into it [113].

Electric discharges applied to gases are the source of electrochemical processes, and depend on various factors:

- Nature of electrodes
- Nature and composition of the medium
- Properties of target molecules
- Electric energy applied

These electric discharges can produce active species which can then react with the target molecules. The targets are generally liquids but can also be solid substances. Liquid targets are generally for waste treatments or pollutant abatement of wastewater. Solid targets can be used to create protective layers on them, modify surface properties, modify adhesion properties or treat solid catalysts. Among the different techniques available, those that operate at atmospheric pressure are the most attractive for ease of use and simplicity [117].

There are different types of plasma discharges such as microwaves, corona, gliding arc, and dielectric barriers. Gliding discharge is a “quenched” plasma since it presents properties of a thermal plasma and those of a non-thermal plasma.

There are various types of plasma-chemical reactions that can occur when generating active species, such as: excitation, recombination, de-excitation, charge transfer, ionization, and dissociation. These reactions produce “primary species” that can react with other primary species, surrounding gas molecules or even with the target. They then form “secondary species” which may be able to react with the target molecules. The major effect of plasma comes from this latter interaction [117].

The gliding arc discharge or “glidarc” was proposed by Lesueur et al. (Lesueur 1988) and developed by Czernichowsky et al. [118]. This technique has been applied in various fields: gases valorization, treatment of residual waters, treatment of solid surfaces, decomposition

of VOCs, improvement of seed germination, elimination of H_2S or N_2O, and partial oxidation of light hydrocarbons.

An example of a glidarc plasma setup is shown in Fig. i.25, which is similar to the one used in this thesis [119]. The specifications of the setup and the parameters applied when using it are explained in detail in the Experimental Section (Section 1.1.3). In this batch reactor, compressed humid air is fed from the top through a nozzle and ionized by applying a high voltage to the electrodes. This creates an arc at the narrowest gap between them which is pushed and broken when the gas flow is increased. As the length of the arc increases (thermal plasma), the temperature of the ionized gas decreases, so that it becomes a non-thermal plasma when breaking into a "plume". The plasma plume contains several species (electrons, cations, radicals) which can react with the target (either liquids or solids) placed at the bottom of the reactor.

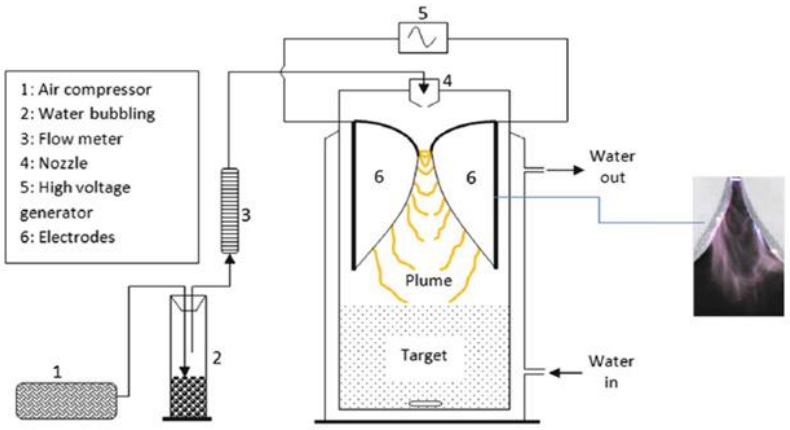

Fig. i.25 - Glidarc plasma batch configuration reactor [119].

The species present in the feeding gas are called "parent species". In the case of humid air as feed, these species are O_2, N_2 and H_2O. These species are partially transformed into primary species when they face the plasma arc because of the energy absorption from the applied voltage. The feeding molecules can suffer cleavage of their bonds by electron impacts and consequently form HO and NO radicals (Equations i.2-5). These radicals are the most numerous species, and this was demonstrated by emission spectroscopy [120]. N_2 is only dissociated when reacting with an O radical [121].

$$H_2O + e^- \rightarrow H^\bullet + HO^\bullet + e^- \qquad \textit{Equation i.2}$$

$$N_2 + O^\bullet \rightarrow NO^\bullet + N^\bullet \qquad \textit{Equation i.3}$$

$$O_2 + e^- \rightarrow 2O^\bullet + e^- \qquad \textit{Equation i.4}$$

$$H^\bullet + NO^\bullet \rightarrow N^\bullet + HO^\bullet \qquad \textit{Equation i.5}$$

Energy is a key parameter since it is the source of the gaseous species activation. The time of exposure to the target is also something to consider in order to achieve a specific objective. It is affected by the geometry of the reactor, energy delivered and gas flow rate. Other geometrical parameters such as electrode gap, distance electrode-target, and electrode thickness, may have an influence in the outcome. Also, temporal post discharge reaction (known as TPDR) will take place if the plasma discharge is switched off, and the target solution is removed from the reactor and kept under controlled conditions. Nevertheless, this last case is not studied in this thesis.

When glidarc plasma is applied to metallic aqueous solutions as targets, the precipitation of these metals precursors as metal oxides/hydroxides can be induced. This is provoked by plasma-generated species which can have oxidizing or reducing character.

The oxidizing effect of plasma glidarc is key for pollutant abatement and environmental applications. It is mainly attributed to the presence of OH radicals, but there is also contribution coming from secondary species such as H_2O_2, as well as N-containing species. An example of this case is the oxidation of Fe(II) to Fe(III) when exposing a solution of Mohr's salt to the plasma [122].

What is more, glidarc discharge in humid air can also cause a reduction of species with high oxidation states. This has been proven by reducing Mn(VII) to Mn(IV) upon exposure [121].

The oxidative and reductive abilities of plasma glidarc in humid air makes it a very attractive technique for the synthesis of metal oxides for heterogeneous catalysis. The last two aforementioned cases were the foundation of the activities presented here, where both liquid and solid targets together are exposed to glidarc plasma, attempting to precipitate metal oxides/hydroxides on solid supports.

2 Objectives

The **main objective** of this work is to develop micro-structured catalysts based on biomorphic fibers for air pollution control in order to abate dangerous types of atmospheric pollutants through oxidation reactions.

The following points establish the **specific objectives** pursued along with the hypotheses considered:

- Develop an easy and feasible method for the synthesis of inorganic fibers from a biological template to be used as catalytic supports, thus taking advantage of the fibrous morphology.
- Obtain supported fibrous catalysts that are able to abate atmospheric pollutants such as soot, benzene and carbon monoxide, through oxidation reactions. It is considered that the deposition of catalytic phases will enhance the activity of the bare biomorphic fibers. To this end, the search for and application of suitable methods to incorporate different catalytic elements will be pursued.
- Assess the physicochemical properties of the catalytic fibers in order to correlate these properties with catalytic activity. To this end, all supported catalysts will be fully characterized. Focus will be placed on understanding how preparation conditions impact on the final characteristics of the solids.

The following scientific questions derived from the specific objectives previously stated will be addressed throughout the course of this thesis.

- Study the physicochemical characteristics of biomorphic fibers obtained after the biological template is removed. Analyze the effect of different metal precursors in the final morphological and textural properties of the inorganic fibers prepared.
- Determine the influence of different deposition methods used to anchor active oxide phases on the morphology of the fibrous supports used.
- Analyze which deposition technique does provide the best distribution of the added elements on the supports. Also, identify which catalytic phases are formed by these techniques and if they change for different types of biomorphic supports.
- Evaluate changes in bulk and surface properties and their impact on activity of the catalysts when adding different amounts of active phase.
- Find out if the same tendency in activity of a catalyst is followed for the different target reactions, which comprise either solid (soot) or gaseous (benzene, CO) reactants.
- Gain insight into the kinetic behaviors and active sites as relevant features for the reactions and catalysts under study.
- Find general trends that correlate good performance with catalytic properties.

3 Strategy

In order to meet the objectives aforementioned and all questions derived from them, the following strategy was pursued.

Fibrous supports were synthesized via a biotemplating route. Different biotemplates are commonly used to produce fibers, as previously mentioned, from which commercial cotton was chosen since it is inexpensive and easily available. Cerium, cobalt, and zirconium precursors were employed in order to produce inorganic fibers. The selection of these species was based on considering that the first two can act as active supports, while the latter as a less active alternative. Additionally, fibrous supports structured as ceramic papers made from commercial SiO_2-Al_2O_3 fibers were used, where cellulosic fibers helped to develop the mat support.

The strategy followed to add active components to fibrous supports involved both the traditional wet impregnation (WI) technique and a novel one, the plasma glidarc (GP). The latter was thought aiming at obtaining a better distribution of the catalyst and to explore catalytic properties resulted from the precipitation by plasma-generated species.

The target reactions selected involved air pollutant removal which are of environmental concern. Soot was chosen as particulate matter, while benzene and carbon monoxide as gaseous reactants. Catalytic oxidations of these pollutants thus involved heterogeneous solid-solid-gas and solid-gas reactions. As active components for these oxidation reactions, the following elements were selected to be deposited on the biomorphic fibers: Mn, Co, Fe oxides (transition metals), along with Ce oxide (lanthanide). In order to find the best formulations for the different reactions, the activity of both bare and supported catalytic fibers were compared.

4 Thesis structure

The current introduction is immediately followed by an Experimental Section in which the catalysts preparations are explained in detail, as well as all characterization techniques used and the catalytic setups and operating parameters. Subsequently, all results obtained are gradually exposed and discussed. To do this in an organized manner and facilitate its reading, this section of the thesis is divided into two parts, comprising two chapters each.

Table i.1 - Thesis structure.

Part - Chapter	Support	Deposition method	Target reactions
Part I - Chapter I	CeO_2 fibers	Wet impregnation (Mn, Co, Ce)	Soot combustion
Part I - Chapter II	Co_3O_4 fibers		Benzene oxidation
Part II - Chapter III	CeO_2 fibers	Plasma-deposition (Mn, Fe)	Soot combustion CO oxidation
Part II - Chapter IV	ZrO_2 fibers		Soot combustion Benzene oxidation

Fig. i.26 - Part I: Chapters I & II (Table i.1).

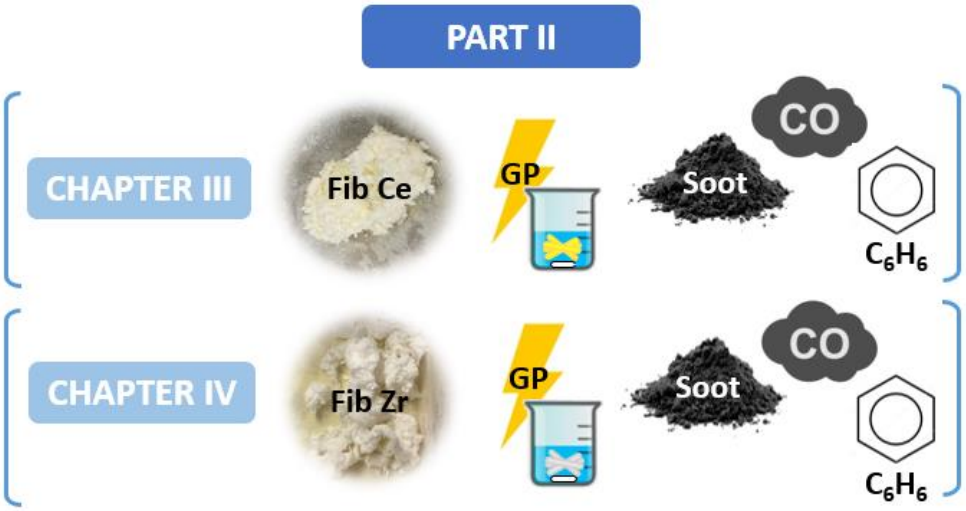

Fig. i.27 - Part II: Chapters III & IV (Table i.1).

5 Graphical abstract

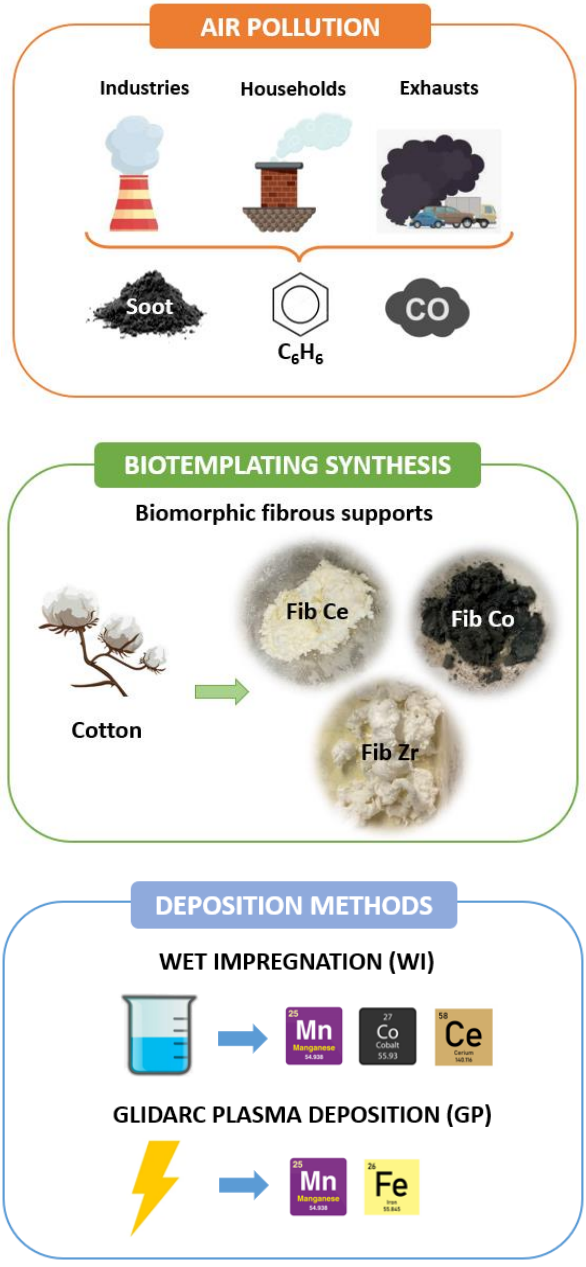

EXPERIMENTAL SECTION

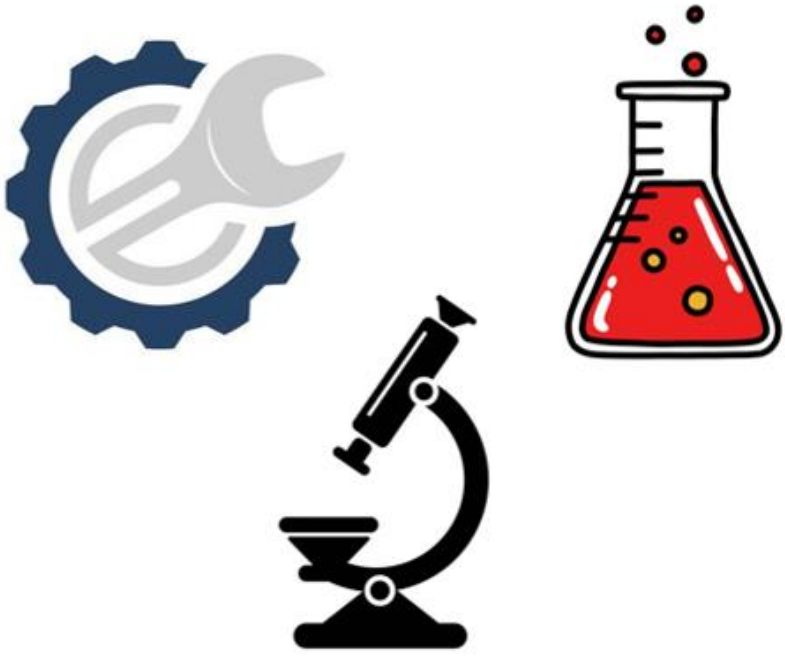

In this work, some activities were carried out in Belgian facilities while others in Argentinean ones. For these activities, both procedures and setups are detailed separately. The labels “BE” and “AR” are used hereafter to note whether the syntheses, characterizations or catalytic tests were done in Belgium or Argentina, respectively.

1 Catalyst preparation

1.1 Synthesis of catalytic fibers (AR, BE)

The synthesis of fibrous catalysts comprises two steps. In the first one, biomorphic fibrous supports are produced (Fig. e.1), followed by a deposition step of active elements. For the second step, two methods are utilized: wet impregnation (WI) and glidarc plasma precipitation-deposition (GP). Also, commercial fibers are used for which only the second part of the synthesis is needed.

1.1.1 Biomorphic fibers as supports

A biotemplating route was employed to obtain bare biomorphic fibers [123]. This first step involves an incipient wetness impregnation (IWI) of the biological template (commercial cotton) to obtain a fibrous support. Three different supports were prepared throughout the thesis: CeO_2 fibers (Fib Ce), Co_3O_4 fibers (Fib Co), and ZrO_2 fibers (Fib Zr(B)). The “B” in the latter was added to differentiate it from commercial ones (Fib Zr(C)). No “B” was added to Fib Ce and Fib Co notation since there are no commercial counterparts in this thesis. The main differences in the morphological and textural properties of these fibers will be shown in Chapters I-IV.

In order to obtain the mentioned supports (Fib Ce, Fib Co, and Fib Zr(B)), 2.5 g of cotton were put in contact with a solution of $Ce(NO_3)_3$, $Co(NO_3)_2$ or $ZrO(NO_3)_2$, respectively, in a flask. Nitrate precursors were used because they are completely dissolved in water (solvent) and easily eliminated during thermal treatment making that they do not remain in the substrate. They also help to remove the biotemplate in the calcination step since nitrates form NO_2 and O_2, the former being a powerful oxidant that can transform the organic matrix into CO_2. The quantity of solution used ensures the total absorption of the whole liquid by the cotton (30 mL of liquid for 2.5 g of commercial cotton). Then, the impregnated cotton was dried at 100 °C for 1.5 h and calcined at 600 °C (10 °C/min) in air for 5 h to guarantee the total elimination of the template. Besides, this temperature (600 °C) was used for all calcination

steps for all catalysts in this thesis as it is the maximum temperature value reached in catalytic tests.

The concentration of the nitrate solutions was adjusted in order to obtain 1 g of fibers after calcination. Fig. e.1 shows the transformation of impregnated cotton into Fib Ce and Fib Co after calcination.

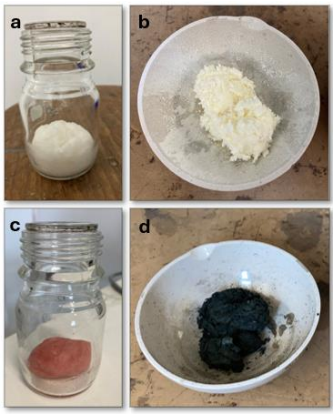

Fig. e.1 - Synthesis of biomorphic fibers: a) Dried cotton after impregnation with $Ce(NO_3)_3$ solution; b) Fib Ce after calcination; c) Dried cotton after impregnation with $Co(NO_3)_2$ solution; and d) Fib Co after calcination.

1.1.2 Wet impregnation

After synthesizing Fib Ce and Fib Co bare supports, a deposition step of Mn, Co or Ce species was carried out by wet impregnation (WI). The setup used is shown in Fig. e.2.

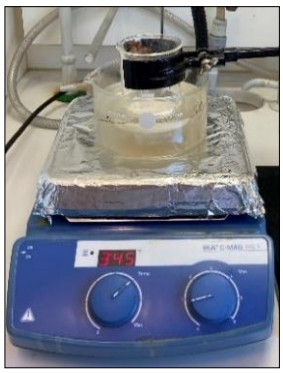

Fig. e.2 - Wet impregnation (WI) setup for supported catalysts preparation.

To this end, 250 mg of Fib Ce or Fib Co were put inside a beaker containing the precursor solution, under gentle stirring, inside an oil bath at 90 °C, until total evaporation of the solvent. Commercial nitrates,

$Mn(NO_3)_2$ or $Co(NO_3)_2$, were employed to deposit Mn or Co oxides on top of Fib Ce. As for Fib Co, $Mn(NO_3)_2$ or $Ce(NO_3)_3$ were used to deposit Mn and Ce oxides. A specific sample using $Fe(NO_3)_3$ was prepared in order to compare activity of Fe-supported on Fib Ce either by wet impregnation and plasma glidarc.

Two different nominal amounts were considered: 5 and 12 wt.%, which are in the range used in the Argentinean group for supported catalysts. Also, the higher value more than doubles the lower so as to compare catalysts with low and high catalytic loadings. From this, four combinations of catalysts resulted for each support. These systems were designated as Fib S-nM, where S = Ce or Co, n = wt.% M, and M = Mn, Co or Ce. Metallic weight percentages (wt.% M) were expressed as follows:

$$wt.\,\%\,M = \frac{wt.\ M}{(wt.\ M + wt.\ Fib\ Ce\ or\ Fib\ Co)} \times 100 \qquad \textit{Equation e.1}$$

Following the impregnation, the fibers are dried for 24 h at 110 °C and calcined for 2 h at 600 °C (5 °C/min) The calcination temperature was chosen in order to avoid any catalysts modification during the soot combustion. The whole synthesis process of catalytic fibers by WI is depicted in Fig. e.3.

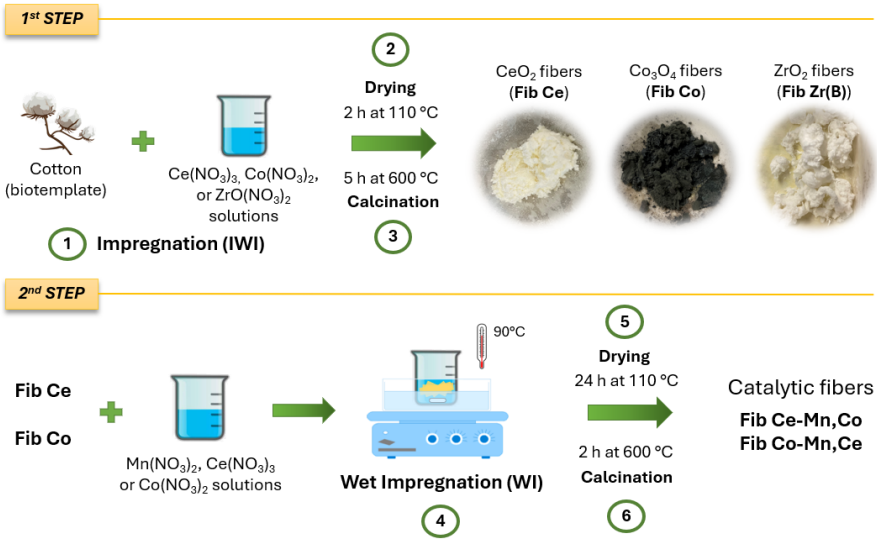

Fig. e.3 - Scheme for the synthesis of catalytic fibers by wet impregnation. Step 1: biotemplating to obtain bare supports (Fib Ce, Fib Co, and Fib Zr). Step 2: wet impregnation of foreign transition metals (Mn, Co or Ce).

All catalyst formulations drawn from this synthesis path are summarized below in Table e.1.

Table e.1 - All formulations for catalysts derived from the wet impregnation synthesis path.

SUPPORT	WET IMPREGNATION					
	Mn		Co		Ce	
	5 wt.%	12 wt.%	5 wt.%	12 wt.%	5 wt.%	12 wt.%
Fib Ce	Fib Ce-5Mn	Fib Ce-12Mn	Fib Ce-5Co	Fib Ce-12Co	-	-
Fib Co	Fib Co-5Mn	Fib Co-12Mn	-	-	Fib Co-5Ce	Fib Co-12Ce

1.1.3 Glidarc plasma

The glidarc plasma technique, in batch configuration, was used for the precipitation-deposition of Mn and Fe species [120,121].

The setup consists of a glass reactor in which two rounded-shaped diverging electrodes are placed in the upper-part and facing each other at a small distance of 2-3 mm. Fig. e.4 shows photographs of the setup to help visualizing its size with the aid of a ruler.

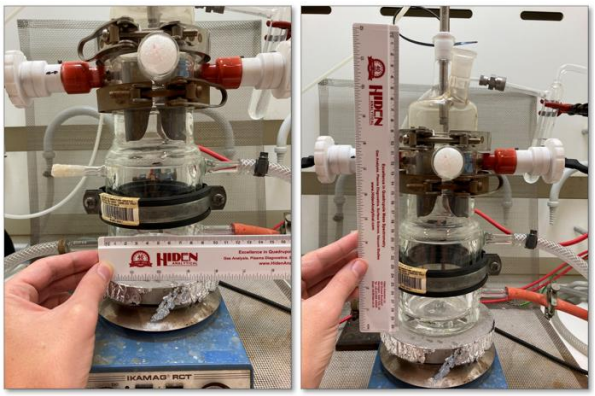

Fig. e.4 - Glidarc plasma (GP) setup in batch configuration, showing the glass reactor diameter (left) and its height (right).

Two diverging aluminum electrodes are connected to a high voltage transformer (220 V/9 kV) which, when turned on, produces an arc where the electrode separation distance is the smallest. The voltage value applied (9 kV) was chosen to achieve a higher concentration of plasma-generated species and therefore to favor the formation of the precipitates. The fed gas is humid air obtained by passing compressed air through a bubbling water flask. When the gas flow rate is rapidly increased from 1 to 5-6 L/min, the arc is pushed along the electrodes and

broken, and a new arc is formed. The collection of arcs forms the "plume". The plasma plume is maintained in this state for the entire experiment.

The targets are placed inside a 250 mL beaker which is deposited at the bottom of the reactor at approximately 2-3 cm from the plume (Fig. e.5).

The first targets exposed were solutions of Mn or Fe precursors alone, $KMnO_4$ 0.75 g/L or $(NH_4)_2Fe(SO_4)_2$ 5 g/L, named KMO and AFS hereafter, respectively. Different volumes were tested first, and from these tests the total volume chosen for both precursors was 100 mL. In the case of KMO, two consecutive batches of 50 mL were used. This is explained in more detail in the first section of Chapter III (Section 3.1). The concentrations mentioned were maintained for all the experiments performed with GP. The precipitates produced from these two solutions are named "KMO ppt" and "AFS ppt".

Next, 250 mg of fibers was added to the precursor solutions. After the exposure of the targets during 30 or 60 min (times experimentally determined to precipitate precursor Mn or Fe salts, respectively), the solid phase separation was done by centrifugation for 60 min at 14000 RPM (RCF = 22830 g) using a HERAEUS Multifuge X1R centrifuge, then dried for 2 h at 110 °C, and finally calcined at 600 °C (5 °C/min) for 2 h.

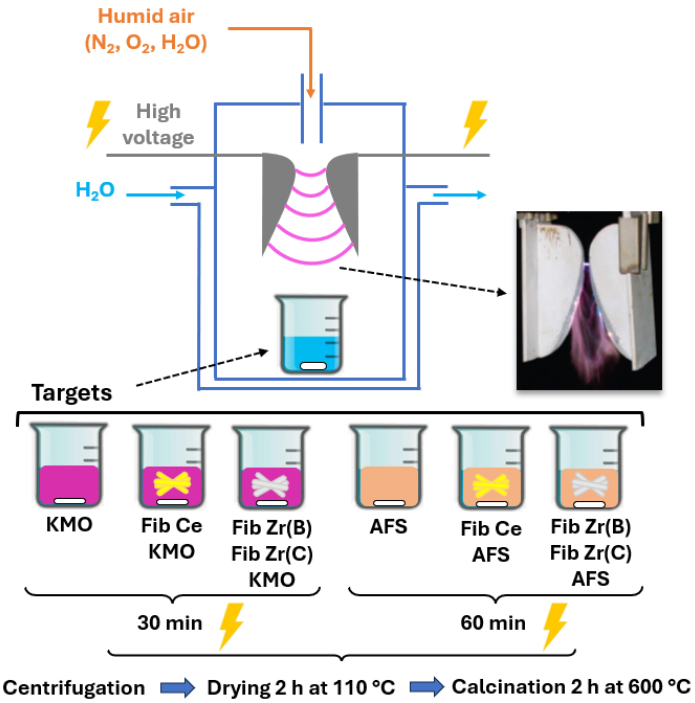

Fig. e.5 - Scheme for all syntheses of catalytic fibers by glidarc plasma.

The supported systems were designated as M-Fib X, where M = Mn or Fe and X = Ce or Zr(B) or Zr(C). Here, the supported element is placed before the support name, whereas for the WI method they are placed after. This is an important nomenclature distinction for the rest of the document. Table e.2 summarizes all assigned names.

Table e.2 - All formulations for catalysts derived from the glidarc plasma synthesis path.

SUPPORT	PRECURSOR SOLUTION	
	KMO	AFS
no support	KMO ppt	AFS ppt
Fib Ce	Mn-Fib Ce	Fe-Fib Ce
Fib Zr(B)	Mn-Fib Zr(B)	Fe-Fib Zr(B)
Fib Zr(C)	Fe-Fib Zr(C)	Fe-Fib Zr(C)

1.2 Development of ceramic papers (AR)

The synthesis of ceramic papers (CP) is done by modifying the standard paper-making technique under the normatives SCAN-C 26:76 and SCAN-M 5:76. Modifications include the partial replacement of cellulosic fibers by ceramic ones, the addition of cationic and anionic polyelectrolytes and a binder [64,124,125]. The full process is depicted in Fig. e.6.

A batch reactor is used for mixing all the materials. For starters, 1 L of NaCl solution 0.01 N is placed inside the reactor, to regulate the ionic strength of the medium. This is followed, in order, by adding: 66 mL of polyvinylamine (PVAm), 10 g of commercial ceramic fibers (SiO_2-Al_2O_3), 5-10 g of binder (colloidal commercial suspension of CeO_2 nanoparticles, 20 wt.% CeO_2, Nyacol®), 1.5 g of cellulosic fibers, and finally 23 mL of anionic polyacrylamide (A-PAM). Every single addition is done after 3 min to ensure homogenization by a shaft stirrer at 80 rpm (IKA RW20).

The addition of cellulosic fibers has the objective of improving the formation of the fibrous matrix, increasing the retention of particles during filtration, since their dimensions are big enough to not go through the mesh (150 mesh = 89 μm). The cationic polyelectrolyte (PVAm) gets adsorbed on the surface of particles and fibers, producing floccules and leaving extra charges in solution (it is added in excess). When the anionic polyelectrolyte is added at the end, the purpose is to neutralize the charges and improve the formation and growing of floccules by a

"crosslinking" mechanism. The exact amount of polyelectrolyte was determined by titration of the mixture at different times of the synthesis [126].

The binder is added in the preparation with the aim of holding all the other components together, providing good mechanical resistance and creating a flexible structure. More importantly, the election of the binder is done to enhance the activity towards the reactions of interest. As mentioned in the introduction, CeO_2 is a very well-known catalyst for oxidation reactions [72,127]. Another possibility to add the binder is to do it after the formation of the matrix by drip impregnation. The latter formulation is named "Pos", while the original one "Pre". All formulations are summarized in Table e.3.

Table e.3 - All ceramic papers formulations.

Binder addition	10 wt.% Ce	20 wt.% Ce
Pre	CP-10Ce-Pre	CP-10Ce-Pos
Pos	-	CP-20Ce-Pos

After all components are added, the solution is poured into the "shaper" column, and it is stirred gently to not break the floccules formed. Then, the solution is filtrated through the mesh (150) and the vessel is emptied by gravity. During this step a small vacuum is generated in the column, which is key for the good formation of the paper disk. Following, to favor water draining, the wet matrix is twice pressed in a hydraulic press at 367 kPa, for 5 min first, and 2 min after. For drying the CP, they are left overnight inside a room with a controlled atmosphere (22 °C and 52 % relative humidity). Finally, a calcination step is carried out at 600 °C for 2 h. In this final stage, the cellulosic fibers along with any amount of polyelectrolyte and water left are eliminated, leaving in the CP disk only ceramic fibers and binder. This brings about a good amount of void inside the fibrous matrix, which is crucial for facilitating the passing of a gaseous stream through the structure.

The synthesis steps are summarized below in Fig. e.6.

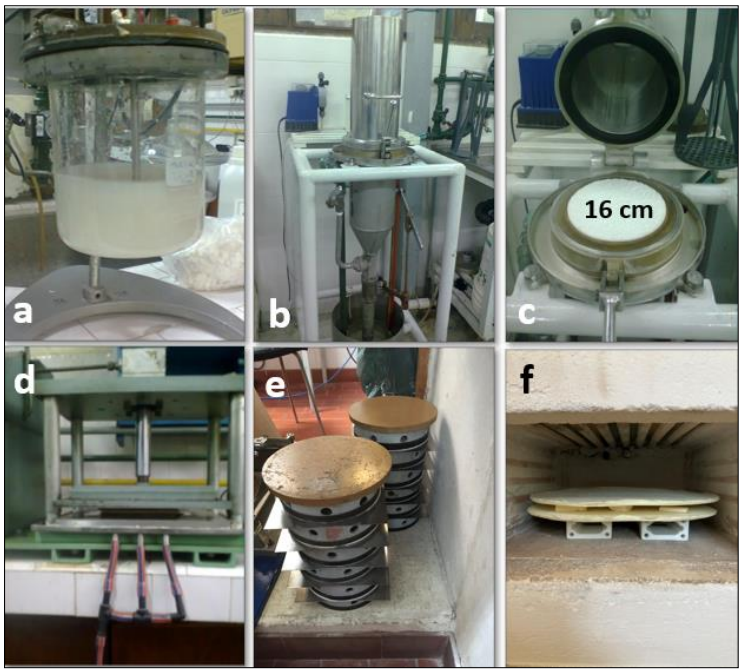

Fig. e.6 - Synthesis of ceramic papers (CP): a) Mixing of components in a batch reactor; b) Filtration through the mesh inside the "shaper" vessel, c) Disk matrix after filtration; d) Pressing; e) Drying; f) Calcination.

Immersion tests of ceramic papers (AR)

The immersion tests were done considering the glidarc plasma exposure of ceramic papers to guarantee that these materials would not be affected by being immersed in an aqueous solution and under acidic conditions as well. To carry out this test, ceramic papers were treated with water at different pH values. Three CP formulations were used: one with 10 wt.% of binder (CeO_2) added prior to the matrix formation (CP-10Ce-Pre) and other two with either 10 wt.% or 20 wt.% CeO_2 added onto the previously formed fibrous mat (CP-10Ce-Pos and CP-20Ce-Pos). The pH value of water was varied with the help of a xxx M HCl solution. This was done purposedly knowing that plasma species induce a decrease in the pH value of the solutions exposed to it due to the formation of acid species such as HONO and HNO_3 [117]. The immersion time also varied between 30 and 60 min. The immersed targets were 1.6 cm diameter CP disks. All disks were dried at 120 °C during 2 h before the final weighing step.

2 Characterization techniques

2.1 X-ray diffraction (BE)

Diffraction occurs when an object in a periodic array scatters radiation coherently, producing constructive interference at specific angles. This happens only when Bragg's law is satisfied. Diffraction from different planes of atoms produces a diffraction pattern, which contains information about the atomic arrangement within the crystal.

X-ray diffraction (XRD) was performed to identify crystalline phases present in the catalysts, either supported or unsupported.

The catalysts were analyzed in a Bruker-D8 advance diffractometer with a Bragg-Brentano geometry, using a LynxEye XE-T detector with Cu Kα radiation (λ = 0.15418 nm) at 40 kV and 30 mA. The samples were scanned in a 2θ range between 5 ° and 80 ° at a scanning rate of 2.2 °/min. Phase identification was done by Panalytical Highscore software.

2.2 Fourier transform infrared spectroscopy - Attenuated total reflectance (BE)

Fourier transform infrared spectroscopy (FTIR) analysis measures the range of wavelengths in the infrared region that are absorbed by a material. Infrared radiation (IR) is sent through the sample and the transmitted beam is detected. The IR spectrum shows the frequencies at which light was absorbed, and these are related to specific vibrations in a molecule. In this way, chemical properties of a sample can be analyzed.

Attenuated total reflectance (ATR-FTIR) is nowadays the dominant FTIR method for solids and liquids analysis because the samples do not require any preparation. In this case, the infrared radiation is passed through an infrared transmitting crystal with a high refractive index, allowing the radiation to eventually reflect within the ATR element several times.

A Bruker FTIR Equinox 55 spectrometer with an ATR module (Bruker Platinum with diamond ATR crystal) was used. A total of 100 scans were taken for the sample and background, in a range of wavenumbers from 4000 to 400 cm^{-1}, in absorbance mode. OPUS 6.5 software was used to collect data and apply an extended ATR correction. This correction fixes the effects of lower peak intensity at longer wavenumbers, and possible shifts when comparing to a conventional transmission spectrum. The

correction parameters were as follows: number of ATR reflections = 1, ATR angle of incidence = 45 °, mean refraction index sample = 1.5.

2.3 Scanning electron microscopy & Energy-dispersive X-ray spectroscopy (AR, BE)

Scanning electron microscopy (SEM) uses a fine beam of high-energy electrons as source of radiation. The images are obtained by the detection and processing of the signals dissipated due to electron-specimen interaction. Secondary and backscattered electrons are mostly used in producing the images.

In energy dispersive spectroscopy (EDS), the characteristic X-rays emitted from the sample are used for elemental and compositional analysis. These X-rays are generated when a vacancy is created in the inner shell of an atom orbital and electrons from the outer shell are transferred to stabilize it (transition from excited state to ground state).

SEM images were obtained to study the morphology of the catalysts prepared. EDS analyses were done to corroborate the presence of supported elements and allowed a semi-quantification.

2.3.1 Argentinean setup (AR)

A SEM Carl Zeiss Sigma equipment coupled with EDS (OXFORD-AZTEX XMAX 80) was used. The samples were coated with an 8 nm layer of gold. The EDS analysis depth was 1 μm. For both SEM and EDS analyses, a voltage of 20 kV was utilized.

2.3.2 Belgian setup (BE)

Images of a soot-impregnated catalyst (wet-contact), along with a fresh and spent catalyst (Fib Ce-12Mn) were taken on a JEOL JSM-7600F Field Emission Scanning Electron Microscope. The samples were not coated. Different images were taken in LM (Low Magnification) and GB-High (Gentle Beam-High Resolution) modes. A combination of secondary and backscattered electrons was chosen to create the images. The acceleration voltage applied ranged from 1 to 5 kV.

2.4 Transmission electron microscopy (AR)

In transmission electron microscopy (TEM), a high energy beam of electrons is transmitted through a very thin specimen (no more than 100 nm) to form an image from the interaction of the electrons with the sample. The magnification of TEM is about 2 million times that of a light microscope and its resolution 1000 times better.

TEM images were obtained for samples prepared in Part II of the thesis, to study the morphology of both the particles that constitute the fibrous support and those from the deposited phases. Their particle size and distribution was also studied. Quantification was done as well by EDS analysis.

TEM images were acquired with a JEOL JEM-2100Plus microscope at an accelerating voltage of 200 kV. A small amount of the fibrous samples was milled using an agate mortar, dispersed in isopropyl alcohol and then sonicated. Finally, some drops from the supernatant liquid (portion of the liquid with the smaller particles) were added onto carbon-coated copper grids (300 mesh). Inevitably, the treatment necessary to obtain TEM images, partially destroys the fibrous structure. The Gatan software (Version 3.5.1 Build 3719) was used to measure the particle size distribution from TEM images.

2.5 N_2 physisorption (BE)

Gas adsorption is a well-known tool for the characterization of the texture of porous solids and fine powders. The IUPAC isotherm and hysteresis classification has been widely adopted and helps to classify the materials and gain information about their porous structure [128].

The equipment used was a Micromeritics Tristar 3000. A degassing step was performed under vacuum (6.6 Pa) at 170 °C for 3-4 h before the analysis. The measurements were done at -196 °C at a relative pressure (p/p_0) range of 0.01-0.99, with N_2 gas as adsorbate. The specific surface area (S_{BET}) was calculated using the Brunauer-Emmet-Teller (BET) method.

2.6 Laser Raman spectroscopy (BE, AR)

Laser Raman spectroscopy (LRS) is a useful technique for material identification. It relies on “Raman scattering”, which occurs when a beam interchanges energy with a system (inelastic process). The frequency shift between the incident beam and scattered beam is called Raman shift. In a Raman spectrum, the detected photons versus Raman shift are plotted. Different materials have different vibrational modes, and for that reason, characteristic Raman spectra. LRS can provide fundamental information about M-O vibrations in a lattice. It can bring information about oxygen vacancies formation, and it is sensitive to the crystalline symmetry and lattice distortion by dopants.

2.6.1 Belgian setup (BE)

The analyses were performed on a Thermo Fisher XRD Raman spectrometer coupled to an Olympus Continuum microscope. The laser used was 532 nm and its power 10 mW. Acquisition time: 5 sec, number of acquisitions per sample: 5 or 10, resolution of 4 cm^{-1}.

2.6.2 Argentinean setup (AR)

The spectra of the samples were obtained using a Horiba JOBIN YVON LabRAM HR spectrometer equipped with a CCD detector cooled to -70 °C using the Peltier effect and coupled to an Olympus confocal microscope with 100X objective lens. The laser power measured above the sample cell was 5 mW, with a collection time of 10 sec and 10 accumulations (resolution = 4 cm^{-1}). The excitation wavelength was 532 nm (diode-pumped solid-state laser).

2.7 Inductively coupled plasma - atomic emission spectroscopy (BE, AR)

Inductively coupled plasma – atomic emission spectroscopy (ICP-AES) is a method of emission spectroscopy that is used to quantify the mass percentage of an element in a sample. It is based on exciting the atoms of the element using a plasma and then analyzing the emission wavelength of the radiation, which is matched to the respective element. Mn, Co, Ce, and Fe wt. % on supported samples were obtained by means of this technique.

2.7.1 Belgian setup (BE)

The analyses were done on a Thermo Scientific iCAP 6500 Duo equipment with Argon plasma and a CID (Charge Injection Device) detector was used. The preparation of the samples was achieved by fusing them using sodium peroxide (Na_2O_2) and sodium hydroxide (NaOH). The spectral range chosen was between 167-785 nm.

2.7.2 Argentinean setup (AR)

Elemental analysis was performed by Inductively Coupled Plasma Emission Spectrometry (ICP), Perkin Elmer Optima 2100 equipment (sequential). The sample pretreatment consisted of complete wet dissolution of the sample by acid digestion (HNO_3-$HClO_4$ mixture 1-5 ratio). The quantitative determination of both elements (Fe and Mn) was carried out using calibration curves from certified standard solutions. The emission lines selected were λ = 238.20 nm for Fe and λ = 259.37 nm

for Mn. From the curve (instrumental response vs concentration), the concentrations of the analytes in each sample were estimated.

2.8 X-ray photoelectron spectroscopy (BE, AR)

X-ray photoelectron spectroscopy (XPS) is based on the photoelectric effect and provides a qualitative and quantitative analysis of a surface. It is a surface-sensitive analytical technique that involves bombarding the surface of a material with low energy and monochromatic X-rays (1.5 keV) and measuring the kinetic energy of the released electrons. The detected electrons come from a depth of 1-10 nm (1-30 atomic layers). XPS spectra are obtained by plotting the energy of the ejected electrons (kinetic energy) and the relative numbers of electrons produced. XPS requires the use of ultra-high vacuum (UHV) to allow the transmission of the ejected electrons from the sample to the analyzer and reduces surface contamination as well. The binding energy of an electron is the property of a material, and it is not affected by the X-ray source used.

The XPS technique was used in this work for surface quantification and chemical state analysis of all synthesized catalysts.

2.8.1 Belgian setup (BE)

The measurements were taken on a SXX 100/206 Photoelectrons Spectrometer (Surface Science Instruments). The monochromatic Al X-ray source was powered at 20 mA and 10 kV. Prior to the analysis, the samples were degassed at 10^{-5} Pa for 12 h in order to eliminate impurities on the surface.

The sample powders pressed in small stainless-steel troughs of 4 mm diameter were placed on an aluminum conductive carousel. The pressure in the analysis chamber was around 10^{-6} Pa. The angle between the surface normal and the axis of the analyzer lens was 55 °. The analyzed area was approximately 1.4 mm^2 and the pass energy was set at 150 eV. In these conditions, the full width measured at half maximum (FWHM) of the Au $4f_{7/2}$ peak for a clean gold standard sample was about 1.6 eV. A flood gun set at 8 eV and a Ni grid placed 3 mm above the sample surface were used for charge stabilization. The following sequence of spectra was recorded: survey spectrum, C 1s, O 1s, Ce 3d, Mn 3s, Mn 2p, Co 2p, and C 1s again to check the stability of charge compensation with time. The C-(C, H) component of the C1s peak of carbon has been fixed to 284.6 eV to set the binding energy scale. Data treatment was performed with the CasaXPS program (Version

2.3.23.PR1.0), and the spectra were decomposed with the least squares fitting routine provided by the software with a Gaussian/Lorentzian (GL30) line shape and Shirley baseline, except from Ce 3d regions in which a linear baseline was chosen. Surface atomic ratios were calculated using peak areas normalized on the basis of acquisition parameters and sensitivity factors provided by the manufacturer.

2.8.2 Argentinean setup (AR)

The analysis was done in a multi-technique Specs equipped with a dual monochromatic X-ray source Ag/Al model XR50 and a hemispheric analyzer PHOIBOS 150 in fixed analyzer transmission mode (FAT). The pass energy used was 30 eV and along with an Al monochromatic anode operating at 300 W. The pressure during the measurement was lower than 10^{-9} mbar. Samples were pressed and vacuumed at 10^{-3} mbar for 10 min at 200 °C, then at ultra-high vacuum for 2 h. Conductive sample holders Specs SH 2/12 were used. A flood gun with 1 eV energy and 0.2 mA current was used to diminish surface charge effects. C 1s signal (carbon contamination) at 284.6 eV was used as reference. All spectra were processed using a Gaussian-Lorentzian (GL30) line shape and Shirley baseline, except from Ce 3d regions in which a linear baseline was applied. CasaXPS software version 2.3.23PR1.0 was used to process the spectral data.

3 Target reactions

3.1 Soot combustion: temperature programmed oxidation tests (BE, AR)

The activity of all fibrous catalysts was studied by means of Temperature Programmed Oxidation (TPO) studies using carbon black from Printex U as model soot, applying a fixed catalyst-soot mass ratio (20-1). The latter appears to be a high catalyst-reactant ratio if thinking about a conventional catalytic reaction. However, it should be considered that in the case of a solid-solid-gas reaction, the validity of the catalytic tests needs the proximity of the catalyst and the solid reactant. Moreover, under real conditions, during the functioning of a DPF, the catalyst-to-soot ratio is high since increasing amounts of trapped soot can cause a high drop and the need of the filter to be regenerated.

Commercial carbon black is preferred for catalysts screening because real soot is heterogeneous, and its properties depend on many parameters such as type and age of engine, running conditions, among others [23]. Instead the composition of commercial carbon black is more uniform, having a lower concentration of adsorbed and condensed hydrocarbons, in addition to a lower amorphous fraction. All of this also makes it more difficult to oxidize than real soot [88]. The primary particle size of Printex U is around 25 nm (0.025 μm), which typically form larger agglomerates of about hundreds of nanometers. Taking this into account, the best performing catalysts in this thesis are expected to perform better in a real case scenario.

Three different types of soot-to-catalyst contact were studied in this thesis. The procedure to obtain these contacts are listed below [68,69].

- Loose contact: catalyst and soot were mixed mechanically, using a spatula, and gently shaking the mixture in a glass container.
- Tight contact: catalysts and soot were ground together for 10 min with the help of an agate mortar.
- Wet contact: catalysts were put in contact with a soot-hexane suspension under gentle stirring, inside an oil bath at 60 °C until evaporation of the solvent and finally dried at 80 °C for 2 h (Fig. e.7) [129,130].

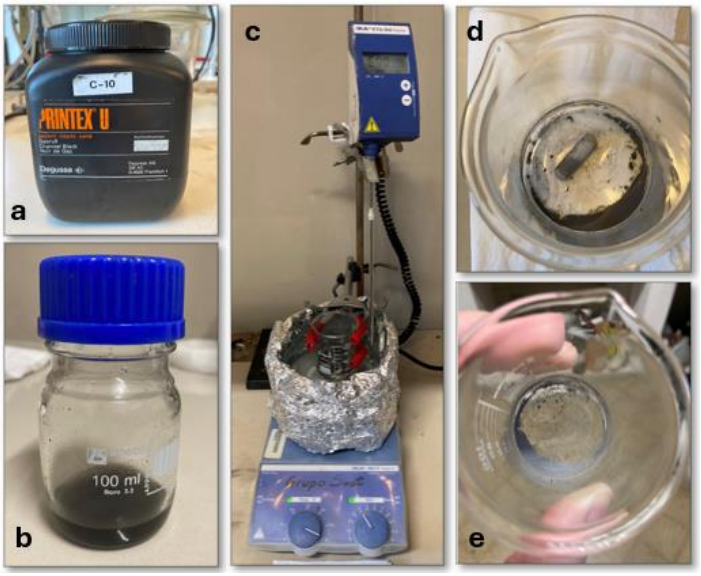

Fig. e.7 - Soot-to-catalyst wet contact technique: a) commercial Printex U; b) soot-hexane suspension; c) oil bath at 60 °C; d) catalyst and soot mixture after hexane evaporation; e) catalyst and soot mixture after drying step (ready for TPO test).

This reaction was performed in two different setups throughout the thesis, and they are described next. From repeated runs done in both facilities, the error to be considered in the evaluation of results is about ± 7.5 °C.

3.1.1 Belgian setup (BE)

A CATLAB Microreactor module from HIDEN ISOCHEMA (Warrington, England) was used (Fig. e.8). The module is coupled with a mass spectrometer (MS) for identification and quantification of gaseous reactants/products. A quartz reactor was used in which a mixture of catalyst-soot was placed, sandwiched with quartz wool. The temperature was raised from room temperature up to 80 °C, then maintained at this value for 1 h, and finally ramped up to 600-750 °C at a rate of 10 °C/min. The total feed flow was 30 mL/min, with a composition of: 10 mL/min Ar and 20 mL/min of 5% O_2 in He (1 mL/min O_2 + 19 mL/min He). The loading of catalysts and soot mixtures (20-25 mg) was done in order to have a 1 cm-high catalytic bed.

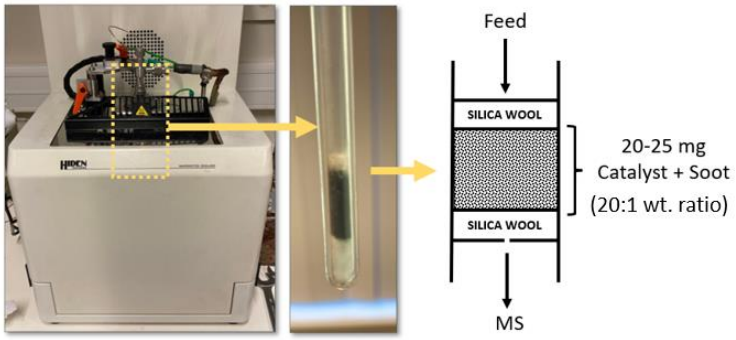

Fig. e.8 - Belgian setup for TPO tests. Details of the reactor loaded with the catalysts mixed with soot in between two silica wool beds.

From MS signals and the gas flow used (30 mL/min), CO_2 molar flows (f_{CO_2}) were calculated. From CO_2 flow profiles against temperature, the value of temperature corresponding to the maximum combustion rate (T_M) was obtained for each catalyst, which corresponds to the temperature at which f_{CO_2} is maximum. Values of T_{10}, T_{50} and T_{90}, which correspond to the temperatures at which 10, 50 and 90% soot conversion is achieved, were obtained from conversion profiles calculated using integrated areas with respect to time (t). These indicators are regularly reported in this document when presenting catalytic results.

Carbon conversion percentage ($x_{C(t)}$) is defined in Equation e.2, where the initial time ("0") was considered as the time at which CO_2 detected comes from soot burning, which depends on each sample. The final time (t_f) corresponds to the time at which CO_2 signal is negligible, $n_{C(t)}$ indicates the molar amount of carbon burned at time t, and n_C^T the total molar amount of carbon burned during the whole TPO experiment.

$$x_{C(t)} = \frac{n_{C(t)}}{n_C^T}.100 = \frac{\int_0^t f_{CO_2}.dt}{\int_0^{tf} f_{CO_2}.dt}.100 \qquad \textit{Equation e.2}$$

Equation e.3 expresses the reaction rate (r) at each time where $n'_{C(t)}$ is the molar amount of carbon burned at a certain time t ($n_{C(t)}$), divided by the weight of catalyst used. Assuming that all carbon is completely transformed into CO_2, $n'_{C(t)}$ equals to $n'_{CO_2(t)}$, the latter being the molar amount of CO_2 formed at a time t, divided by the weight of catalyst. The maximum reaction rate is evidently achieved at the time when T_M is reached. This equation indicates that the reaction rate is equal to the molar flow of CO_2 divided by the weight of catalyst used (f'_{CO_2}).

$$r\left[\frac{mol}{mg\ cat.\ s}\right] = \frac{-dn'_{C(t)}}{dt} = \frac{dn'_{CO_2(t)}}{dt} = f'_{CO_2} \qquad \textit{Equation e.3}$$

3.1.2 Argentinean setup (AR)

The measurements were done using a quartz reactor coupled with a gas chromatograph (GC) from Shimadzu, model GC 2014 (Fig. e.9).

GC parameters: current = 100 mA, column temperature = 31 °C, injector temperature = 50 °C, TCD temperature = 50 °C, column type = packed, column material = stainless steel, column filling = Porapak Q, carrier gas = helium (40 mL/min). The temperature ramp applied by the furnace to the reactor was 5 °C/min from room temperature to a final temperature of 600 °C.

The total feed flow was 20 mL/min, with a composition of 0.1% NO, 18% O_2 and He (balance). These concentrations are close to those typical in exhaust gases of a Diesel engine (300-1650 ppm NO, 5-18% O_2) [23]. However, they differ from those used in the Belgian setup where NO was not available, and the chosen concentration of O_2 was lower (close to 5% O_2). For which, the conditions used in Argentina were more favorable for the evaluation of the catalysts. The amount of catalyst loaded was 50 mg, sandwiched between quartz wool.

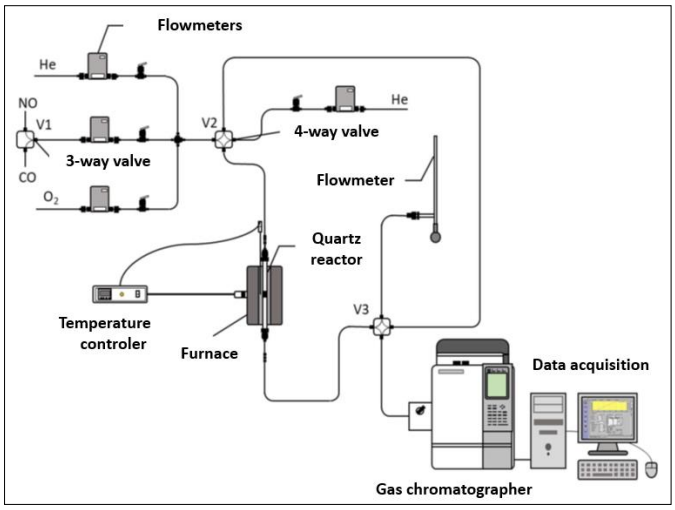

Fig. e.9 - Argentinean setup for TPO tests, showing the main feeding lines, the reactor and the detection system (GC).

The GC measurements (pulses) were done in 20 °C intervals from 80 °C until 600 °C. The CO_2 peaks acquired were integrated for each temperature interval and then these values were plotted as CO_2 profiles from which T_M values are obtained (Fig. e.10).

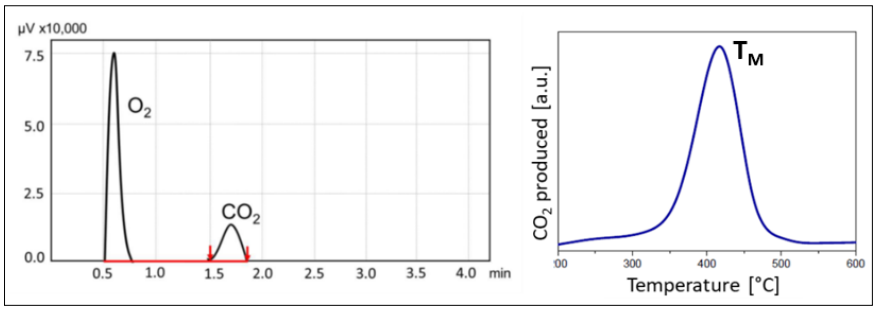

Fig. e.10 - Typical chromatogram obtained running TPO tests, showing O_2 and CO_2 peaks (left) and CO_2 profiles obtained after processing the chromatograms collected at different temperatures (right).

As explained before, the soot conversion $x_{C(t)}$ can be obtained from these profiles using Equation e.2.

3.2 Carbon monoxide oxidation (AR)

The same setup used for soot combustion tests in the Argentinean side, was utilized for CO oxidation. The total feed was 30 mL/min composed of: 1% CO; 2% O_2 and He (balance). The conversion profiles were obtained using the CO_2 areas ($CO_2\ (t)$) from the GC. The final steady value of CO_2 area ($CO_2\ (t_f)$) corresponds to the total CO fed in the reactor (1% CO). CO conversion percentage ($x_{CO(t)}$) is calculated by dividing the CO_2 area value at a specific temperature during the experiment ($CO_2\ (t)$) by $CO_2\ (t_f)$, as expressed by Equation e.4.

$$x_{CO(t)} = \frac{CO_2\ (t)}{CO_2\ (t_f)} . 100 \qquad \textit{Equation e.4}$$

3.3 Benzene total oxidation (BE)

A tubular stainless-steel reactor coupled with a gas chromatograph with a flame ionization detector (FID) was utilized for the benzene total oxidation tests (Fig. e.11).

The feed total flow was 100 mL/min, and its composition was as follows: 200 ppm benzene (brought from a commercial cylinder of benzene diluted in helium at a certified concentration of 2000 ppm), 10 mL O_2/min and He balance. 100 mg of catalyst diluted with 400 mg of quartz (200-315 µm) was loaded inside the reactor in between two small layers of silica wool (Fig. e.11). This gives a space velocity (S_V) of 60000 mL/h.g cat.

The temperature was increased from 50 °C up to 400 °C, with a 50 °C step and at each temperature, so that nine samples were acquired. Average

benzene peak areas were thus obtained (A_{bz}), from which benzene conversion percentages at each temperature were calculated by applying Equation e.5, where A°_{bz} corresponds to the zero-conversion point (initial benzene peak area).

$$x_{bz} = \frac{A^{o}_{bz} - A_{bz}}{A^{o}_{bz}} \cdot 100 \qquad \textit{Equation e.5}$$

Reaction rates were calculated by Equation e.6 both at 250 °C, where conversion values were lower than 20% (assuming differential conditions), being C^{o}_{Bz} the initial concentration of benzene (mol Bz/mol total), X_{Bz} the benzene conversion (at 250 °C), f_{tot} the total molar flow rate (mol tot/s), and *m* the amount of catalyst used (g) [32].

$$r\left[\frac{mol\ Bz}{g\ cat\ .\ s}\right] = \frac{C^{o}_{Bz} \cdot X_{Bz} \cdot f_{tot}}{m} \qquad \textit{Equation e.6}$$

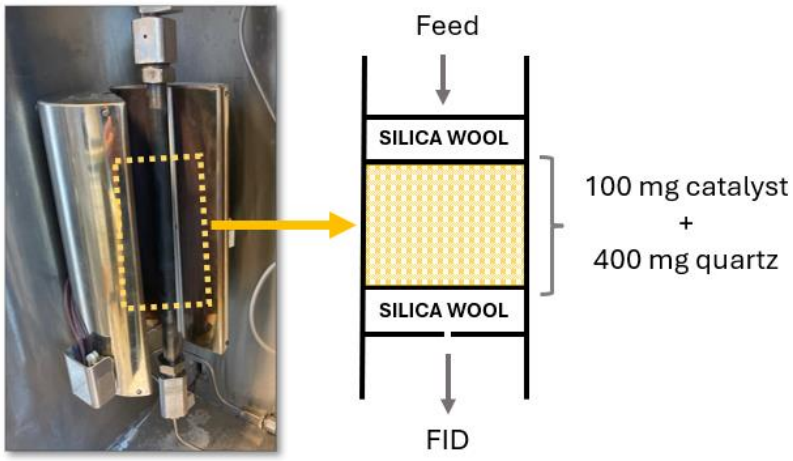

Fig. e.11 - Benzene oxidation setup. Details of the reactor loaded with the catalysts in between two silica wool beds.

PART I - CHAPTER I

Mn and Co decorated biomorphic CeO_2 fibers for soot and benzene oxidation

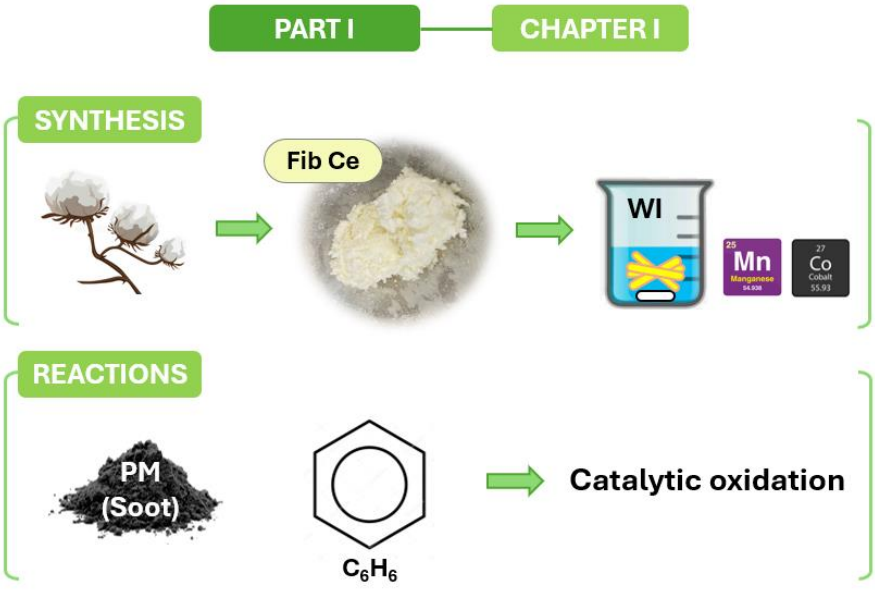

1 Introduction: Mn and Co decorated biomorphic CeO_2 fibers for soot and benzene oxidation

In this chapter, biomorphic ceria fibers are prepared utilizing cotton as a biotemplate. Then, they are supported with Mn and Co phases through a wet impregnation deposition. This synthesis was explained in detail in the Experimental Section (Section 1.1.2).

Cerium oxide (CeO_2) is a pale-yellow powder that crystallizes in the fluorite (CaF_2) structure, with a face-centered cubic (fcc) unit cell within the space group *Fm-3m* (Fig. 1.1 - A) [94]. CeO_2 is the most significant of the oxides of rare earth elements in terms of industrial application, and the academic publications regarding ceria have soared since 1980.

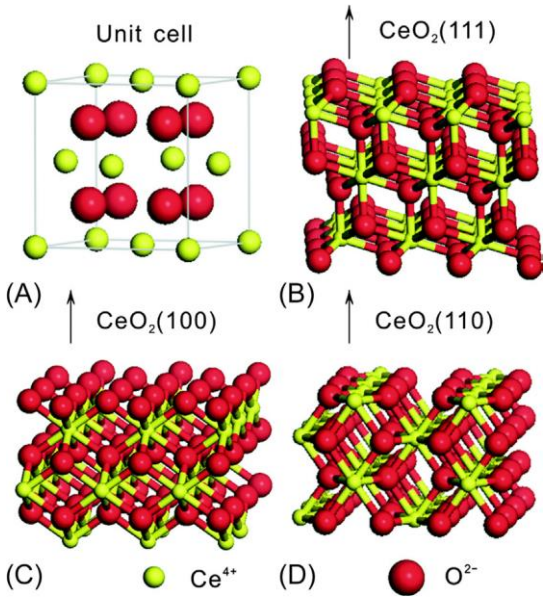

Fig. 1.1 - Structural models of CeO_2 unit cell (A), (111) (B), (100) (C), and (110) (D) crystalline planes [94].

Ceria is used in a large number of technological fields which range from energy and environmental processes to biology and medicine. Its major application is as a support, promoter or catalyst in combination with noble or transition metals for the removal of harmful compounds released from internal combustion engines, for example as a component of three-way catalysts (TWCs). Other applications of CeO_2 are in steam and dry methane reforming to generate syngas, water-gas shift reaction (WGSR), hydrocarbons oxidation and preferential oxidation of CO [62,131,132].

CeO_2 can have a synergistic effect when used with transition and noble metals, whether forming solid solutions or being involved in a composite mixture of oxides. Apart from having a role as a promoter, CeO_2 also finds applications as a stand-alone [72]. The main characteristic of CeO_2 is the ability to balance oxygen oscillations in the gas phase, thus acting as an oxygen buffer. This is possible due to its ability to store and release oxygen, depending on the gas composition - in particular the O_2 partial pressure, by means of shifting its redox couple Ce^{4+}/Ce^{3+}. This cycle is expressed by the reversible Equation 1.1, where R is a reductant and V_o is an oxygen vacancy [72]. Ce and O atoms can maintain the fcc fluorite arrangement for values of $x < 0.25$.

$$CeO_2 + x\,R \leftrightarrow CeO_{2-x} + x\,RO + x\,V_o \qquad \textit{Equation 1.1}$$

This property is commonly called oxygen storage capacity (OSC) and makes CeO_2 attractive as a catalyst for heterogenous catalytic reactions and suitable for TWCs application [42].

The properties of ceria are affected by its morphology, aging conditions, presence of dopants, particle size and specific surface area of the material [131].

The main drawback of CeO_2 is its thermal stability and this is the reason why there is not much interest in using it alone. CeO_2 maintains the fluorite structure when calcined up to 900°C but at high temperatures the sintering of particles takes place and the size of crystallite increases considerably, along with a decrease in specific surface area [125,133]. CeO_2 becomes almost inactive in soot combustion when calcined at 1000°C [23]. Using ceria alone would also incur higher costs than using conventional supports such as Al_2O_3 and SiO_2. To solve this issue, other elements have been added to ceria lattice to form mixed oxides and/or solid solutions. The most common case being the incorporation of Zr which leads to Ce-Zr mixed oxides with higher specific surface area, smaller crystallite size, higher oxygen mobility and exchangeability, and consequently better redox properties and better activity in some reactions [22,42]. Other common doping elements found in the literature are Mn, Fe, Cu, Co, among others [76,77,134].

The main objective here is to utilize a very simple and cost-effective synthesis method to bring about an increase in the activity of the bare fibrous support, which is an active or non-inert support. The addition of foreign transition metals is done hoping to produce a synergistic effect or positive interaction in the composites formed, like the one seen by creating mixed oxides by more complex types of syntheses. In this case,

the chosen metals are Mn and Co, which are low-cost alternatives to noble metals and more environmentally friendly [24,31]. Mn and Co oxides have been extensively studied in oxidation reactions, showing great results based on the coexistence of mixed valence states, their good redox properties and high oxygen mobility [135–137]. While trying to succeed in this task, the change in properties and catalytic performance in two different reactions of unsupported and supported ceria fibers will be studied and discussed. As mentioned in the General Introduction (Section 1.4), a fibrous morphology is promising for improving the contact between reactants, thus favoring catalytic performance.

2 Abstract

Mn or Co supported CeO_2 fiber catalysts were synthesized following a biotemplating route and evaluated in soot combustion and benzene total oxidation. The catalysts were characterized by SEM, EDS, ICP-AES, N_2 physisorption, FTIR-ATR, XRD, RAMAN and XPS. SEM results confirmed that the "twisted ribbon" morphology of the biotemplate was mostly maintained. XRD and Raman showed that Mn and Co cations partially insert into ceria lattice and also segregate at the surface of the fibers. XPS allowed to determine that both set of catalysts exhibit Ce^{3+} and Ce^{4+} surface species, in addition to adsorbed and lattice oxygen. Also, the bulk average oxidation state (AOS) of Mn could be calculated. Following, a study of different types of soot-to-catalyst contact was performed. Compared to bare CeO_2 fibers, the performances for both reactions were improved for the supported catalysts, except for the catalyst with lowest Mn content for soot combustion. The catalytic activity was discussed in terms of the physicochemical features of the supported catalysts.

The results presented in this chapter were published in:

M. Rodriguez, F. Hanon, F. Devred, E.M. Gaigneaux, E.E. Miró and V.G. Milt, "Mn and Co decorated biomorphic ceria fibers catalysts for soot and benzene total oxidation", Chemosphere 359 (2024) 142247.

https://doi.org/10.1016/j.chemosphere.2024.142247

3 Results and discussion

3.1 Morphological analysis by SEM and EDS (AR)

Fig. 1.2 shows some SEM images of commercial cotton. These cellulosic fibers consist of very long (> 1mm) open "twisted ribbons" with a section of approximately 30 µm.

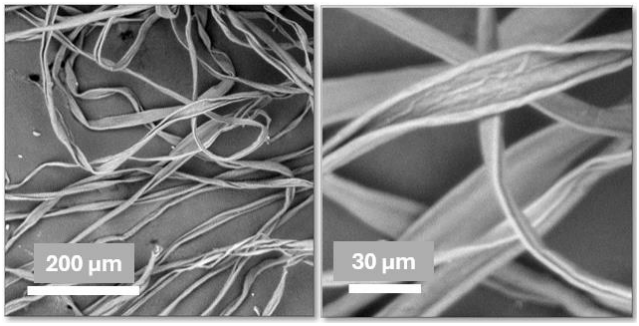

Fig. 1.2 - SEM images of commercial cotton fibers.

After the first step of the synthesis, a fibrous morphology (Fig. 1.3) is evidently attained. Not only helicoidal fibers can be seen, which are morphologically identical to cotton, but also cylindrical ones are created, some of them having closed ends (Fig. 1.3 - c) and others open ends and inner channels (hollow fibers, Fig. 1.3 - e), all with a porous texture. The dimensions of bare ceria fibers are diverse, having lengths from 25 to 300 µm, and sections from 5 to 25 µm (Figs. 1.3).

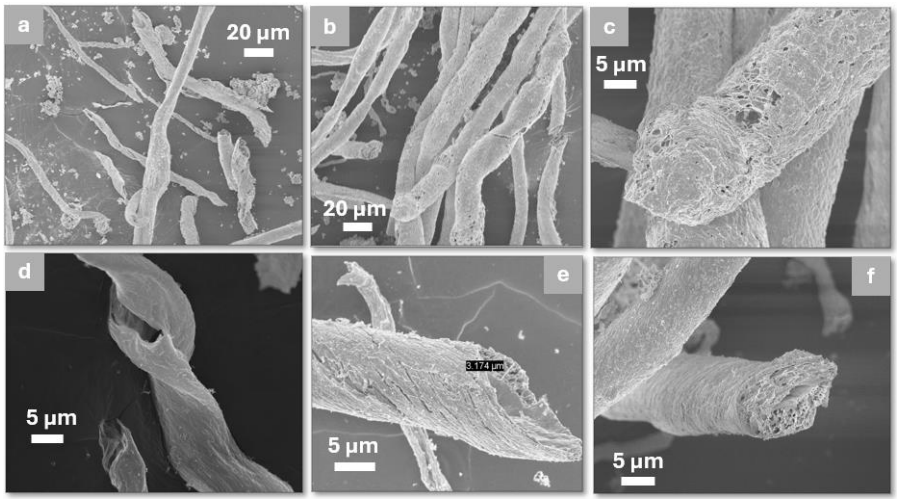

Fig. 1.3 - SEM images of biomorphic CeO_2 fibers (Fib Ce).

Following the deposition of Mn and Co on Fib Ce, the fiber lengths show a slight decrease, likely due to the stirring during the impregnation process and their manipulation. They also are wider and present a different texture (not observed before impregnation) which is attributed to the new species impregnated (Fig. 1.4 and 1.5).

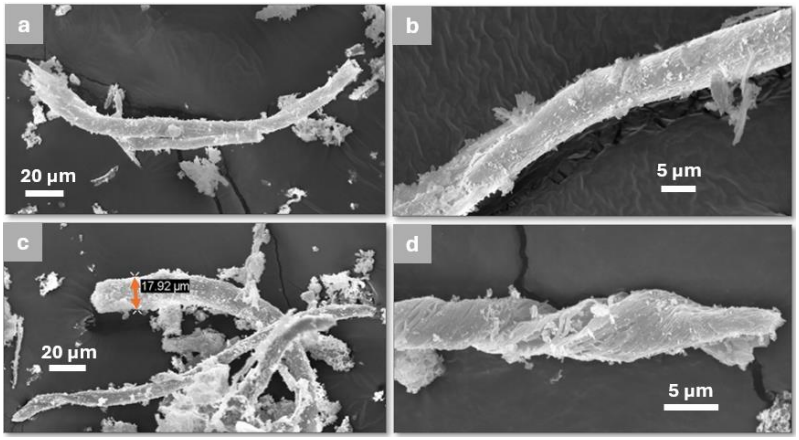

Fig. 1.4 - SEM images of Mn-supported Fib Ce by WI: a,b) Fib Ce-5Mn, c,d) Fib Ce-12Mn.

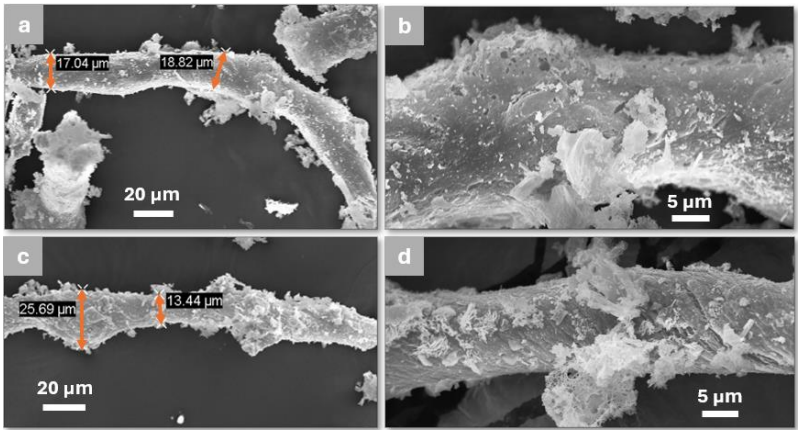

Fig. 1.5 - SEM images of Co-supported Fib Ce by WI: a,b) Fib Ce-5Co, c,d) Fib Ce-12Co.

On the other hand, EDS analysis was performed to study the distribution of the elements deposited. Although this is a semi-quantitative method, it provides a reasonable approach to determine metal contents. To this end, different areas were analyzed for quantification in order to check the distribution of the elements. On the one hand, spot analyses were performed on three different isolated fibers (per sample), and on three

zones per fiber (Zones 1-3, Figs. 1.6 and 1.7 - left). On the other hand, a mapping analysis was carried out covering the fiber area on which the spot analyses were done (Figs. 1.6 and 1.7 - right). Additionally, for each sample, bigger areas containing several bundles of fibers were mapped aiming at obtaining more representative bulk quantification values (Fig. 1.8).

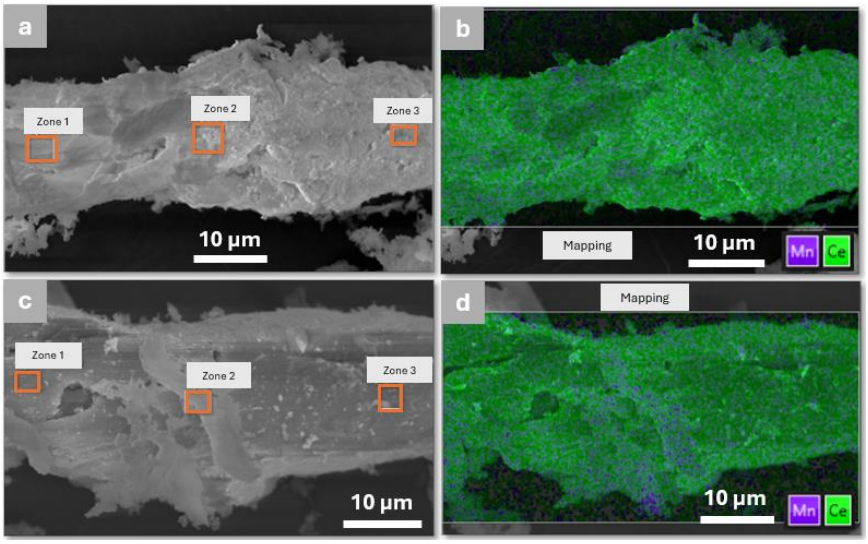

Fig. 1.6 - Spot (left) and mapping (right) EDS analyses of Mn-supported Fib Ce by WI: a, b) Fib Ce-5Mn; c, d) Fib Ce-12Mn.

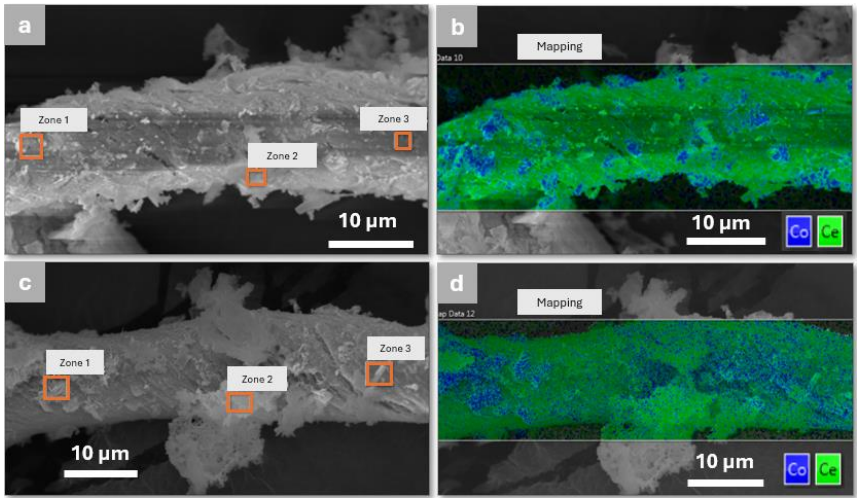

Fig. 1.7 - Spot (left) and mapping (right) EDS analyses of Co-supported Fib Ce by WI: a, b) Fib Ce-5Co; c, d) Fib Ce-12Co.

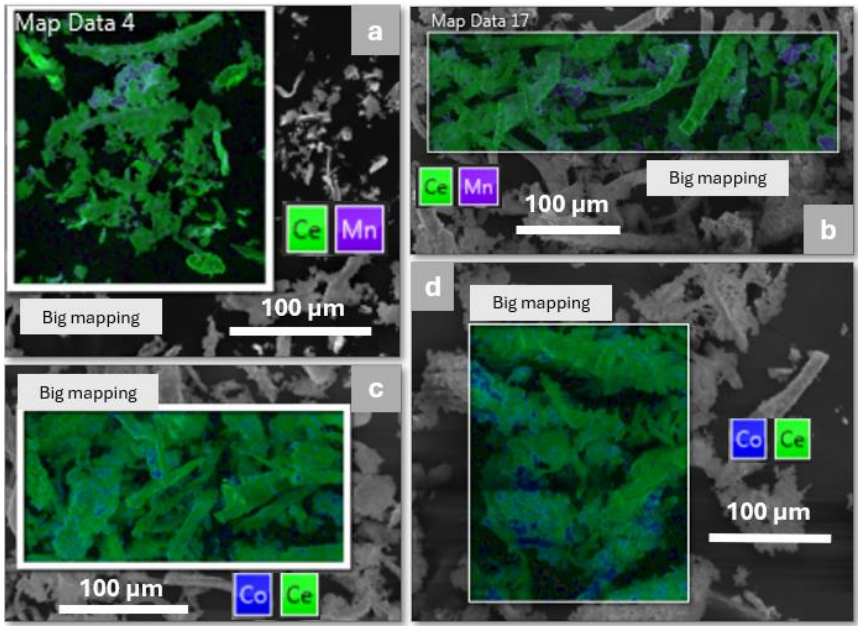

Fig. 1.8 - EDX big mappings of Mn or Co-supported Fib Ce by WI: a) Fib Ce-5Mn, b) Fib Ce-12Mn, c) Fib Ce-5Co, d) Fib Ce-12Co.

All values obtained are reported in Table 1.1 as atomic ratios of metal deposited divided by cerium (M/Ce). As previously mentioned, averages were calculated from spot analyses, per fiber (three zones) and for each sample (nine zones). It can be clearly noticed the presence of Mn and Co deposited on the Fib Ce, despite not being uniformly distributed. However, it has to be considered that the studied zones were separated by not more than 20 µm, for which big area mappings show more representative atomic ratios, closer to the corresponding nominal values. Additionally, ICP results included in Table 1 reveal metallic contents similar to nominal ones, except for Fib Ce-12Mn, which is still considerable higher in content than Fib Ce-5Mn.

Table 1.1 - Spot and mapping EDS analyses from Figs. 1.6, 1.7, and 1.8.

Sample	M*/Ce atomic ratios								
	Fiber N° (**)	Zone 1 (Spot)	Zone 2 (Spot)	Zone 3 (Spot)	Average per fiber (Zones 1, 2 and 3)	Spot average	Mapping per fiber	Big area mapping (wt.% - ICP)	Nominal (wt.%)
Fib Ce-5Mn	1	0.43	0.14	0.17	0.25	0.14	0.22	0.16 (4.7)	0.16 (5.0)
	2	0.07	0.07	0.05	0.06		0.06		
	3	0.10	0.15	0.11	0.12		0.12		
Fib Ce-12Mn	1	0.05	0.16	0.05	0.09	0.16	0.08	0.26 (7.3)	0.43 (12.0)
	2	0.69	0.09	0.09	0.29		0.15		
	3	0.09	0.11	0.10	0.10		0.12		
Fib Ce-5Co	1	0.03	0.05	0.03	0.03	0.10	0.06	0.10 (4.6)	0.15 (5.0)
	2	0.05	0.08	0.03	0.05		0.05		
	3	0.3	0.24	0.07	0.20		0.18		
Fib Ce-12Co	1	1.44	0.24	0.67	0.78	0.39	0.55	0.27 (10.6)	0.40 (12.0)
	2	0.56	0.16	0.08	0.26		0.16		
	3	0.11	0.11	0.13	0.12		0.10		

** M = Mn or Co*

*** Three fibers per sample were analyzed*

3.2 XRD and textural analyses (BE)

The XRD diffractograms depicted in Fig. 1.9 confirm for all samples the formation of ceria with a face-centered cubic fluorite structure (JCPDS 34-0394). After Mn deposition, no peaks coming from Mn species can be observed for any Mn loading. This could mean that manganese is forming amorphous species or is dispersed as small crystallites. Also, the formation of a solid solution should be considered.

On the other hand, for Co-containing samples, a small peak is already present for Fib Ce-5Co at 2θ = 36.9 °, and more peaks appear for Fib Ce-12Co at 2θ = 18.9 °, 31.3 ° and 65.3 °. All of them match with the cubic spinel structure of Co_3O_4 (JCPDS 42-1467). This makes evident the presence of Co on Fib Ce, and the segregation effect observed specially for the higher loading.

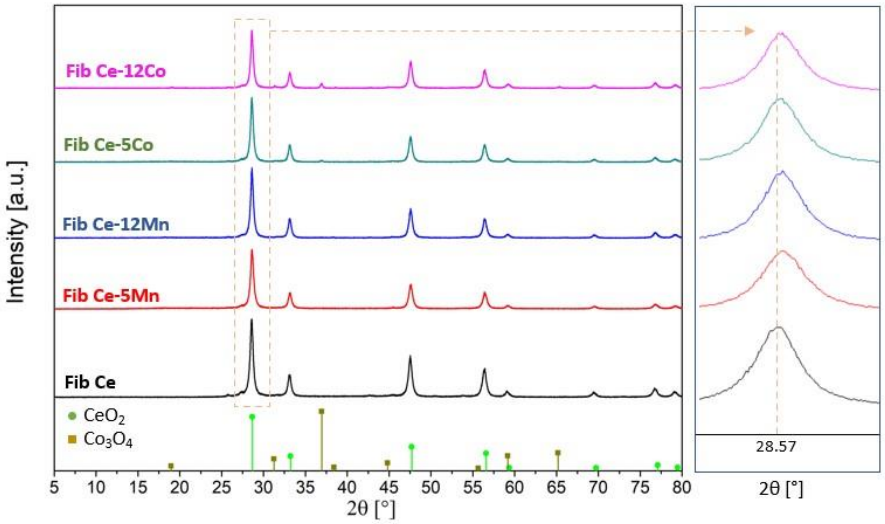

Fig. 1.9 - Diffractograms of Fib Ce-Mn,Co catalysts showing the main peak of CeO_2 magnified (right).

Both for Co or Mn supported fibers, when focusing on the most prominent peak of CeO_2 (1 1 1) placed at 28.57 °, a small shift to higher 2θ values occurs. The value of this shift is approximately 0.045 °, which equals to three times the step of the XRD method used (0.015 °) and thus is significant. The reason behind this could be that some Mn and Co cations have replaced some Ce^{+4} cations in the lattice of ceria. Ionic radius of Mn, Co and Ce cations are as follows: $r(Ce^{4+})$ = 0.94 Å, $r(Mn^{2+})$ = 0.83 Å, $r(Mn^{3+})$ = 0.65 Å, $r(Co^{2+})$ = 0.90 Å, $r(Co^{3+})$ = 0.61 Å [138]. The radii of the supported elements are smaller than that of Ce^{4+}, and this slightly

decreases the lattice parameter (LP) of the cubic unit cell (Table 1.2) and correspondingly increases 2θ angle at which the diffraction occurs. It has been reported that MnO_x signals are only appreciable for molar ratios Mn/Ce > 3, and below this limit a solid solution is expected [75,138]. Mn/Ce ratios for both Mn supported fibers are far below this value (0.16 for 5 wt.% and 0.43 for 12 wt.%). In the case of Co, it has been reported that it can be introduced into the ceria lattice up to an atomic ratio Co/Ce = 0.05 [125]. In the present case, both Co-supported samples have Co/Ce atomic ratios above this value (0.15 for 5 wt.% and 0.40 for 12 wt.%). This means that probably a solid solution is forming at lower atomic ratio values, but once this limit is surpassed, segregation occurs, and this is noticeable in the diffractograms. The segregated Co_3O_4 is forming crystallites of 38 nm in size for Fib Ce-12 Co and 29 nm for Fib Ce-5Co (size measured from XRD and Scherrer equation using diffraction peak at 36.9°), although the latter value has some uncertainty due to the low signal intensity.

The shift in the main CeO_2 diffraction signal does not increase for either Mn or Co samples containing different metal loadings (see magnified image on Fig. 1.9 - right). In the literature, this shift generally changes depending on the type of synthesis (sol-gel, co-precipitation, solution combustion, hydrothermal, etc.), the dopant (typically Mn, Fe, and Co) and their amounts [75,139–141]. In the synthesis mentioned, the nucleation of Ce and Mn or Co species takes place simultaneously, whereas in the current case, CeO_2 is produced first (support), and then Mn or Co species are formed onto this support through the thermal process of calcination, thus not favoring, at first, the formation of the solid solution. However, in this work, this shift is observed, all the more suggesting the formation of solid solutions.

***

The textural analysis of the catalysts by N_2 physisorption showed isotherms of type IV, with a hysteresis loop type H3, based on IUPAC classification (Fig. 1.10), indicating the presence of some mesoporosity. Loops of this type are given by tortuous (about cylindrical) pores opened at both ends and spaces between fibers, with a wide distribution of sizes, showing a broad range of adsorption and desorption pressures. In addition, all hysteresis loops appear at relatively high pressures, which implies the presence of relatively big pores. Besides, it can be observed that the hysteresis loop is less pronounced for impregnated samples which could indicate that the Fib-Ce mesopores are partially filled with catalyst particles. Moreover, after impregnation, the shapes of fibers become more irregular, leaving bigger pores between them (interparticle

porosity), thus making the desorption branch shift to higher pressures. On the other hand, none of the samples present micropores since their isotherms are flat at the beginning of the adsorption process (low relative pressure values).

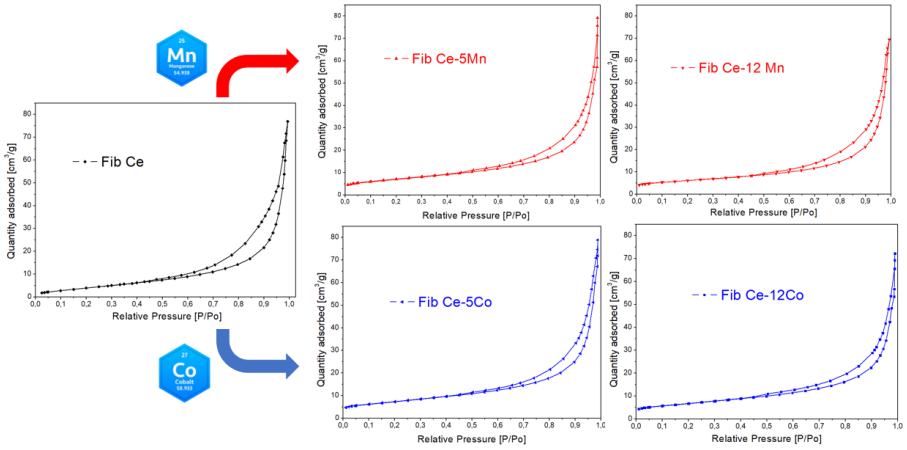

Fig. 1.10 - N_2 physisorption isotherms of Fib Ce-Mn,Co catalysts.

For BET results, all supported samples presented a slight increase in their specific surface area (SSA) in comparison to bare fibers (Table 1.2). One explanation for this behavior could be that the second calcination step after precursor addition helped removing carbon-cellulose remains from the biotemplate. Despite the possible partial blocking of mesopores after addition of phases, the latter could also contribute to the increment of SSA through their own mesoporosity.

Table 1.2 - XRD and textural analyses.

Sample	CeO_2 lattice parameter (LP) [Å]	Crystallite size of support (CeO_2) [nm] *	Crystallite size of supported phase [nm] *	BET Specific surface area (SSA) [m^2/g]	Pore volume (V_p) [cm^3/g] **
Fib Ce	5.41	21	-	17	0.09
Fib Ce-5Mn	5.40	20	-	25	0.09
Fib Ce-12Mn	5.40	22	-	21	0.09
Fib Ce-5Co	5.40	22	29	26	0.10
Fib Ce-12Co	5.40	23	38	24	0.08

**** Calculated by Scherrer equation using peaks at 2θ = 28.6 ° and 36.9 ° for CeO_2 and Co_3O_4, respectively.***

***** Pore volume taken at P/P_o = 0.98.***

3.3 FTIR-ATR analyses (BE)

The FTIR-ATR spectra obtained are pictured in Figs. 1.11 and 1.12. The signals and their assignments are summarized in Table 1.3. All catalysts have several signals in common, a broad band at 3400 cm^{-1} characteristic of -OH stretching and a signal at 1640 cm^{-1} corresponding to H-O-H bending vibrations, both from physisorbed water. Also, signals at 1532, 1325 and 1065 cm^{-1} associated to strongly adsorbed mono-dentate carbonates, which may originate from chemisorption of CO_2, are seen, being the latter formed during the decomposition of the biotemplate or by contact with ambient air [142,143]. Surface carbonate signals are less intense for supported catalysts in comparison to Fib Ce, which could be related to the second calcination step that helps removing remaining carbonates from the surface.

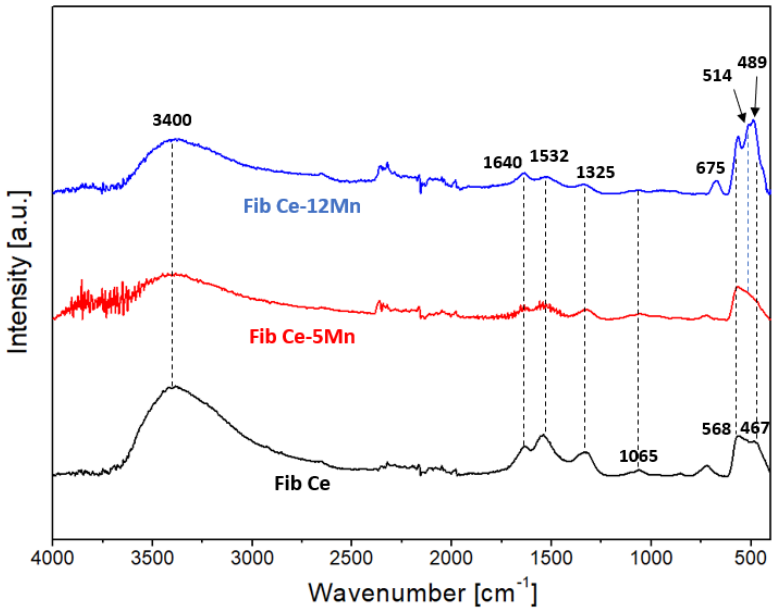

Fig. 1.11 - FTIR-ATR spectra of Fib Ce-Mn catalysts.

Additionally, for bare Fib Ce, a broad peak is observed between 600-400 cm^{-1} with two maxima at 568 cm^{-1} and 467 cm^{-1}, assigned to Ce-O vibrations [144]. These signals are also seen for supported samples. In Mn-supported sample spectra (Fig. 1.11), for 5 wt.%, no significant changes are observed when comparing to the spectrum of the bare support, whereas for 12 wt.%, new bands are present: a peak at 675 cm^{-1}, assigned to the symmetrical vibration of Mn-O-Mn bonds, a band at 514 cm^{-1}, characteristic of Mn-O vibration in octahedral environments [145], and a peak at 489 cm^{-1} originating from Mn-O bending vibrations from Mn^{3+} species [146]. For Co-supported samples (Fig. 1.12), two prominent peaks appear at 663 cm^{-1} and 559 cm^{-1} which are characteristic of Co-O stretching from Co in tetrahedral coordination (Co^{2+}), and octahedral coordination (Co^{3+}), respectively [65].

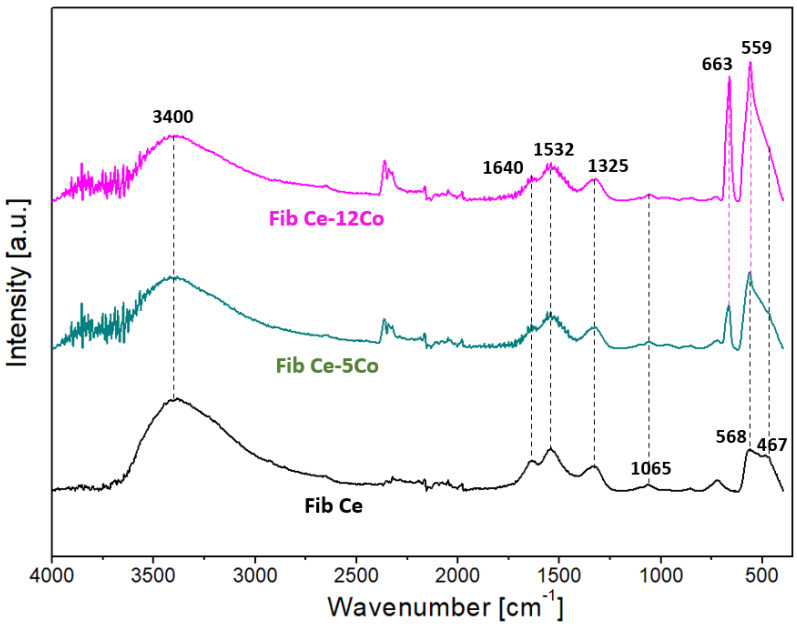

Fig. 1.12 - FTIR-ATR spectra of Fib Ce-Co catalysts.

Table 1.3 - FTIR-ATR signals for Fib Ce-Mn,Co catalysts.

Band position [cm^{-1}]	Assignment
3400, 1640	-OH, H-O-H (physisorbed water)
1532, 1325, 1065	Adsorbed mono-dentate carbonates
675	Symmetrical stretching Mn-O-Mn
514	Mn-O in octahedral environments
489	Mn-O bending
663, 559	Co-O (tetrahedral, octahedral)
568, 467	Ce-O

3.4 LRS analyses (BE)

The spectra obtained for our catalytic fibers are depicted in Fig. 1.13 - a. All catalysts present a prominent peak around 460 cm^{-1} which is due to a first order scattering F_{2g} active mode of the fluorite structure of ceria [38,147]. This peak, after deposition of Mn and Co, shifts from 463 cm^{-1} (Fib Ce) to lower frequencies (red shift), being this shift higher for higher metal contents. Moreover, following the same tendency, this signal broadens and decreases in intensity. These facts could be associated with the formation of a solid solution, as has been mentioned previously when discussing XRD results. As reported, the insertion of Mn and Co cations into ceria lattice can provoke a modification in the Ce-O bonding symmetry of the fluorite structure, thus producing the shift in Raman spectra [76,77]. The presence of defects also broadens the F_{2g} band and contributes to the red-shift.

When looking closer at Fib Ce spectra alone (Fig. 1.13 - b), in addition to the main signal, a small broad band at 550-600 cm^{-1} is observed and can be due to oxygen vacancies in the lattice [148]. A similar situation occurs for Fib Ce-5Mn (Fig. 1.13 - c). This band, attributed to oxygen vacancies, is called “D-band”, and its intensity increases with the doping of ceria with elements of valence state lower than 4 [149].

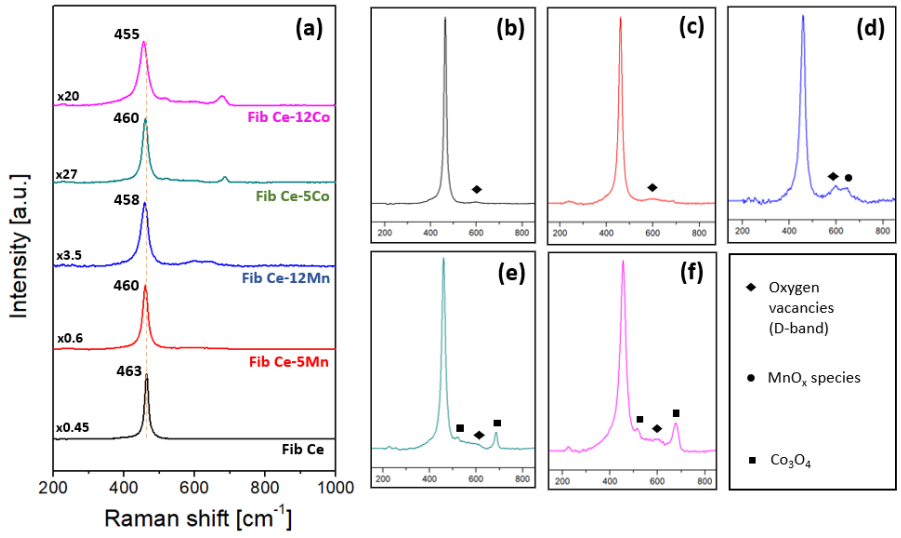

Fig. 1.13 - a) Raman spectra of Fib Ce-Mn,Co catalysts; b) Fib Ce; c) Fib Ce-5Mn; d) Fib Ce-12Mn; e) Fib Ce-5Co; f) Fib Ce-12Co.

For the sample with 12 wt.% Mn (Fig. 1.13 - d), the D-peak has increased considerably, and this could be due to a higher concentration of oxygen vacancies as a result of more Mn insertion and creation of defects in the

lattice. This band is often used as evidence for the formation of Mn-Ce solid solution [138]. Moreover, a new signal is present at 647 cm^{-1}, which could be attributed to a Mn-O symmetric vibration, signaling the presence of MnO_x species like Mn_2O_3 and Mn_3O_4 [150,151]. Although some authors have assigned this signal also to oxygen vacancies [139], in our case the assignment to MnO_x species could be supported by FTIR-ATR spectrum (Fig. 1.11).

For the catalysts containing Co (Fig 1.13 - e, f), apart from the D-peak of ceria, two new signals can be seen at 521 and 685 cm^{-1}, both related to Co_3O_4 spinel F_{2g} and A_{1g} vibration modes [123]. These two bands increase in intensity for the sample with higher Co content. It is worth noting that for Co-supported samples, the decrease in intensity of the main band of ceria is more pronounced than that of Mn-supported samples, which could indicate that Co cations cause more interference in ceria symmetry and its structure vibrations than Mn ones.

3.5 Surface analysis by XPS (BE)

XPS analysis was performed to gain information about the surface of the catalysts. The regions C 1s, O 1s, Ce 3d, Mn 3s, Mn 2p, and Co 2p were analyzed.

Apart from the typical C 1s (C-(C,H)) peak used at 284.6 eV as reference (contamination carbon), another small peak is present for all samples at higher binding energy (288.6 eV) (Fig. 1.14 - left) ascribed to carbonate species [152,153]. This agrees with the small amount of surface carbonates observed by ATR-FTIR.

The O1s spectra were fitted with three peaks (Fig. 1.14 - right). The most prominent one at around 528.8 eV (O_{latt}) corresponds to lattice oxygen; the second one near 531.2 eV (O_{ads}) is due to surface chemisorbed oxygen which contemplates the following species: O_2^-, O_2^{2-}, O^-, CO_3^{2-} (the latter in accordance with C 1s region); and the last one close to 533.5 eV (O_w) is assigned to oxygen from water molecules [79,154,155]. The surface atomic ratios of O_{latt} and O_{ads} reported in Table 1.4 were calculated considering these three oxygen species. Extra fitting data for Fib-Ce are listed in Table 1.5. Fib Ce-5Mn exhibited an increase in the amount of O_{ads} whereas Fib Ce-12Mn showed a decrease, in comparison to Fib Ce. This is also evident looking at the O_{ads}/O_{latt} ratios reported (Table 1.4). For Co-supported catalysts, both samples showed a similar decrease in O_{ads}, having the same O_{ads}/O_{latt} ratio. Furthermore, if only comparing O_{ads} to Ce, the only catalyst that has a significant difference is Fib Ce-5Mn, nearly doubling the value of all others.

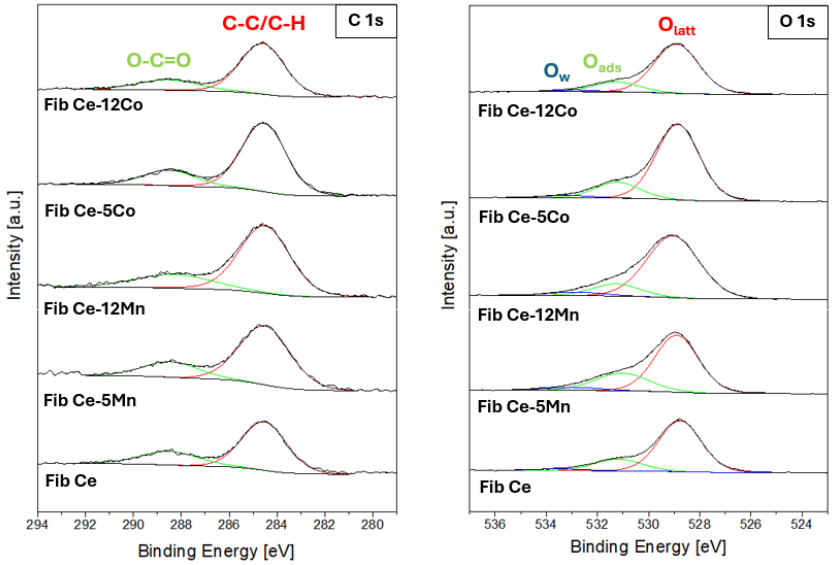

Fig. 1.14 - Surface analysis of Fib Ce-Mn,Co catalysts (XPS): C 1s (left) and O 1s (right) regions and deconvolutions.

Concerning Ce 3d region, all samples were fitted with ten peaks (Fig. 1.15) [156]. The peaks u''', u'', u, v''', v'', and v are related to the Ce^{4+}, whereas the peaks u', u^0, v', v^0 are linked to Ce^{3+} species. Table 1.6 shows both Ce^{3+} percentages and Ce^{3+}/Ce^{4+} ratios. More information about Fib Ce fitting is provided in Table 1.7. All samples were fitted similarly.

After the addition of Mn or Co oxides, an increase in Ce^{3+} concentration was observed for most samples, being highest for Fib Ce-12Mn. The only sample for which Ce^{3+} concentration remained the same was Fib Ce-5Mn, whose Mn/Ce ratio more than doubles its bulk nominal ratio. All other samples, which have M/Ce ratio values lower than the nominal ones, increased the Ce^{3+} amount. This is in line with LRS results (Fig. 1.13, D-band), as a higher amount of surface Ce^{3+} content correlates with a higher amount of oxygen vacancies.

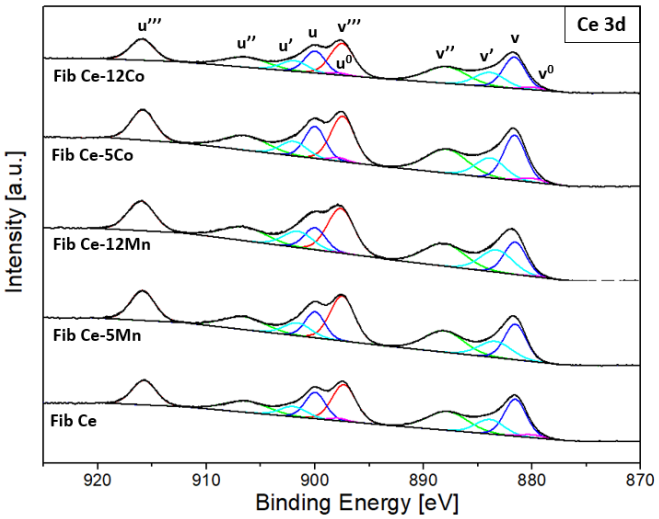

Fig. 1.15 - Surface analysis of Fib Ce-Mn,Co catalysts (XPS): Ce 3d region and deconvolutions.

Regarding Mn, the region of Mn 3s can provide information about the oxidation state of Mn species, which at this point was impossible to determine by other techniques. Multiple splitting occurs in transition metals when they present unpaired electrons in the outer shell that can interact with core electron vacancies generated by photoionization. As a result, two peaks are generally found in Mn 3s region, as can be seen in Fig 1.16.

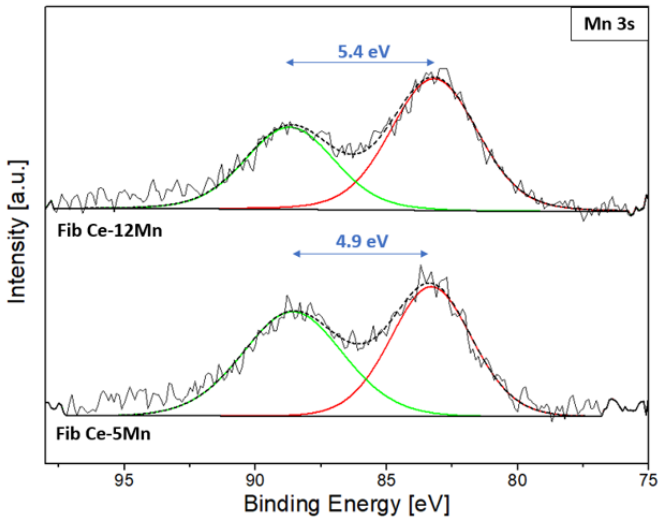

Fig. 1.16 - Surface analysis of Fib Ce-Mn catalysts (XPS): Mn 3s region and deconvolution.

The difference in binding energy between these two peaks, can be used for the calculation of an average oxidation state (AOS) of bulk Mn, according to Equation 1.2 [64,157].

$$AOS = 9.67 - 1.27.\Delta BE \qquad \textit{Equation 1.2}$$

The AOS obtained for Mn was 3.5 and 2.7 for Fib Ce-5Mn and Fib Ce-12Mn, respectively. The higher the Mn content, the lower its oxidation state. For Fib Ce-5Mn, now it could be inferred that Mn should be present mostly in valence Mn^{3+}. Not only a small contribution of Mn^{4+} should be present in order to raise the AOS value above 3, but also some Mn^{2+} seems to be contributing when looking at Mn 2p region (Fig. 1.17). Adding to this, the presence of a satellite in Mn 2p region has been correlated to the presence of Mn^{2+}. For Fib Ce-12Mn, the AOS is lower than 3, signaling a higher contribution of Mn^{2+} in this case. Taking all this into account, Mn 2p regions for both catalysts were deconvoluted accordingly (Fig. 1.17). The binding energies ranges used for Mn $2p_{3/2}$ species were as follows: 640.8-640 eV for Mn^{2+}, 642-641 eV for Mn^{3+}, 643.8-642.5 eV for Mn^{4+}, and 647-645 eV for the satellite, which is in accordance with the literature [135,139,141]. For both Mn-supported samples, the difference between Mn $2p_{3/2}$-$2p_{1/2}$ is 11.6 eV.

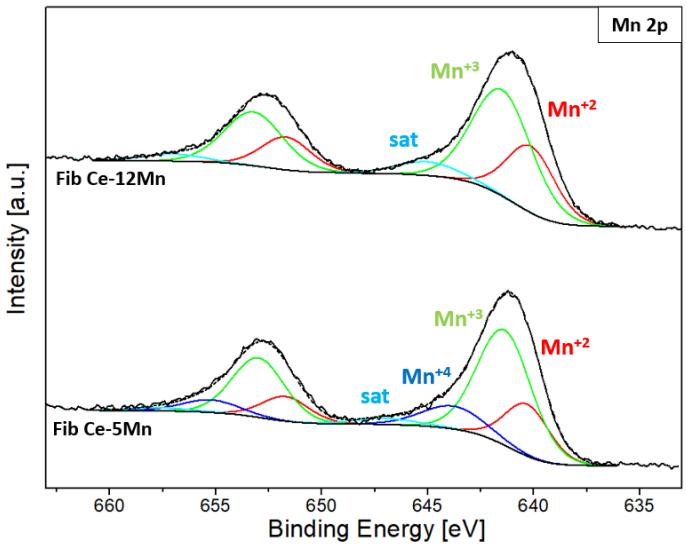

Fig. 1.17 - Surface analysis of Fib Ce-Mn catalysts (XPS): Mn 2p region and deconvolutions.

With respect to Co-supported samples, as Table 1.6 shows, the surface content of Co is lower than the nominal one (bulk), especially in the case

of Fib Ce-12Co. Co 2p region presents a $2p_{3/2}$-$2p_{1/2}$ spin-orbit splitting of about 15.3 eV, and a satellite feature at a distance of 6.7 eV from the main peak, all of which is typical of Co_3O_4 [158–160]. This is shown in Fig. 1.18. The $2p_{3/2}$ region was deconvoluted with Co^{2+} and Co^{3+} species, along with the shake-up satellite peak. The $Co^{2+}/(Co^{2+}+Co^{3+})$ ratios obtained for Fib Ce-5Co and Fib Ce-12Co were 0.54 and 0.57, respectively. The satellite contribution was attributed to Co^{2+} species.

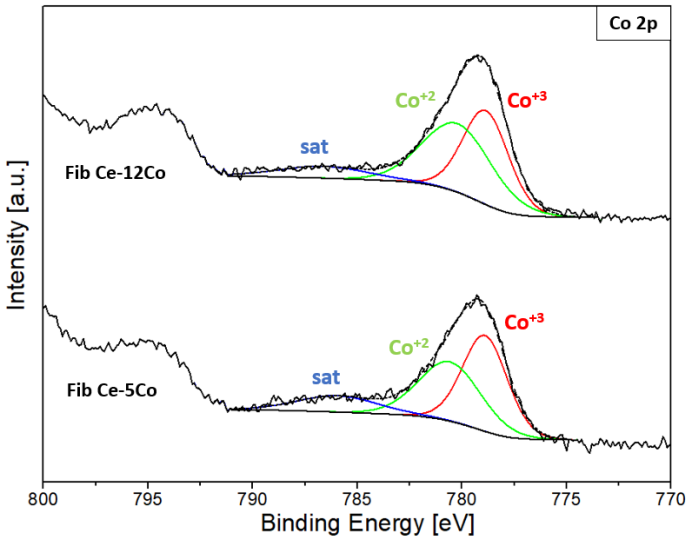

Fig. 1.18 - Surface analysis of Fib Ce-Co catalysts (XPS): Co 2p region and deconvolutions.

Table 1.4 - XPS O 1s region peak positions, O_{ads}/O_{latt} and O_{ads}/Ce atomic ratios.

Sample	Binding energy (eV)			$O_{ads}/(O_{ads}+O_{latt}+O_w)$ (%)	O_{ads}/O_{latt}	O_{ads}/Ce
	O_{latt}	O_{ads}	O_w			
Fib Ce	528.8	531.2	533.5	20.0	0.26	0.50
Fib Ce-5Mn	528.9	531.0	532.8	25.3	0.36	1.03
Fib Ce-12Mn	529.0	531.3	532.9	14.4	0.18	0.47
Fib Ce-5Co	528.9	531.2	533.1	17.3	0.22	0.48
Fib Ce-12Co	528.9	531.3	532.9	16.8	0.21	0.51

Table 1.5 - XPS O 1s region fitting for Fib Ce.

Peak assignment	Species	RSF	Peak decomposition		
			BE (eV)	FWHM	Raw area
O_{latt}	O^{2-}	2.93	528.8	2.0	20316.3
O_{ads}	O_2^-, O_2^{2-}, O^-, CO_3^{2-}		531.2	2.2	5279.0
O_w	O^{2-}		533.5	2.3	835.4

Table 1.6 - XPS Surface characteristics of Fib Ce-Mn,Co catalysts.

Sample	Binding energy (eV)										$Ce^{3+}/(Ce^{3+}+Ce^{4+})$ (%)	Ce^{3+}/Ce^{4+}	M*/Ce (Nominal)	ΔBE Mn 3s (eV) (AOS**)
	Ce $3d_{5/2}$					Ce $3d_{3/2}$								
	v_o	v	v'	v''	v'''	u_0	u	u'	u''	u'''				
Fib Ce	880.0	881.5	883.9	887.8	897.3	897.8	900.0	902.0	906.3	915.8	16.0	0.19	-	-
Fib Ce-5Mn	880.0	881.5	883.4	888.1	897.5	897.0	900.0	901.6	906.5	915.9	16.1	0.19	0.35 (0.16)	4.9 (3.5)
Fib Ce-12Mn	879.4	881.6	883.3	888.1	897.6	897.7	900.0	901.6	906.5	916.0	19.3	0.24	0.35 (0.43)	5.4 (2.7)
Fib Ce-5Co	880.0	881.6	883.8	887.9	897.4	897.8	900.0	902.0	906.4	915.9	17.9	0.22	0.10 (0.15)	-
Fib Ce-12Co	879.9	881.6	883.9	887.9	897.5	897.8	900.0	901.9	906.4	915.9	18.2	0.22	0.16 (0.40)	-

** M = Mn or Co*

*** AOS = Average oxidation state of Mn (Equation 1.2)*

Table 1.7 - XPS Ce 3d region fitting for Fib Ce.

Peak assignment	Species	RSF (Spin-orbit)	Peak decomposition		
			BE (eV)	FWHM	Raw area
u'''	Ce^{4+}	21.12 ($3d_{3/2}$)	915.8	2.6	15811.8
u''	Ce^{4+}		906.3	4.8	13506.9
u'	Ce^{3+}		902.0	2.9	7277.5
u	Ce^{4+}		900.0	2.2	14521.0
u_0	Ce^{3+}		897.8	1.8	1169.3
v'''	Ce^{4+}	30.5 ($3d_{5/2}$)	897.3	2.6	23717.7
v''	Ce^{4+}		887.8	4.4	20465.0
v'	Ce^{3+}		883.9	3.0	11026.6
v	Ce^{4+}		881.5	2.4	22001.6
v_o	Ce^{3+}		880.0	2.5	1771.6

3.6 Catalytic evaluations - Soot combustion (BE)

3.6.1 Comparison of different soot-to-catalyst contacts

Prior to study the catalysts for the oxidation of soot, a comparison between different types of soot-to-catalyst contact was carried out. The results obtained using the bare support (Fib Ce) are shown in Fig. 1.19. Loose contact gave a catalytic performance really close to the non-catalytic reaction (blank). With this contact, soot agglomerates are not broken and are merely dispersed on the catalyst, thus not providing a good contact. On the other hand, when using tight contact, the best activity was achieved, which is expected since this approach increases the number of contact points between soot and the catalyst. Milling can also decrease the particle size of the catalyst, thus increasing its surface area, and boosting its performance. This is a regular situation found in the literature where outstanding catalytic results are always the ones run with tight contact. However, it is common belief that tight contact does not represent a realistic scenario when picturing a DPF functioning. Finally, when wet contact is applied, the outcome is in the middle of the last two mentioned situations, being closer to the latter. Therefore, wet contact is a very promising approach to achieve good contact without compromising the catalyst morphology (Fig. 20). It has been reported that wet contact provides better homogeneity and reproducibility than conventional contact types [68]. Based on this, wet contact was used for all catalytic tests reported in the rest of this section.

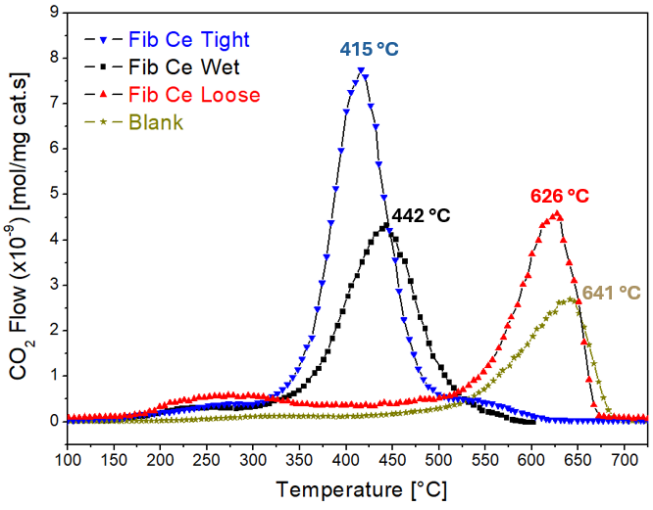

Fig. 1.19 - Comparison of soot-to-catalyst contact for Fib Ce in soot combustion: tight, wet and loose contacts.

3.6.2 SEM images of soot-Fib Ce in wet contact

In order to better appreciate the soot-to-catalyst contact chosen, some SEM images were taken prior and after soot incorporation on Fib Ce by wet impregnation (Fig. 1.20). It can be clearly seen that soot particles appear very well dispersed at the surface of Fib Ce (Fig. 1.20 - c,d), which can be compared to commonly reported contacts [129,130]. Indeed, the contact achieved between soot particles and ceria fibers resembles a tight interaction without affecting the catalyst morphology.

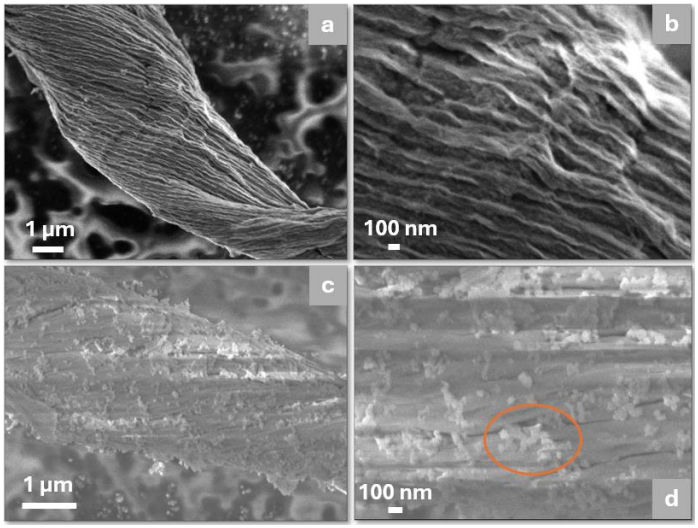

Fig. 1.20 - SEM images of Fib Ce (a,b) and soot-Fib Ce mixture in wet contact (c,d). The colored circle in "d" stands out and agglomerate of soot particles.

3.6.3 Soot combustion tests

The T_M values obtained for the different catalytic fibers are presented in Fig. 1.21 as a function of the metal contents deposited. Additionally, T_{10}, T_{50} and T_{90} are reported in Table 1.8. The CO_2 profiles along with soot conversion sigmoidal curves are depicted in Fig. 1.22. In these profiles, some samples exhibit a small CO_2 peak at temperatures below 300 °C which is attributed to the solvent leftovers (hexane) used for soot impregnation that were not completely eliminated by drying.

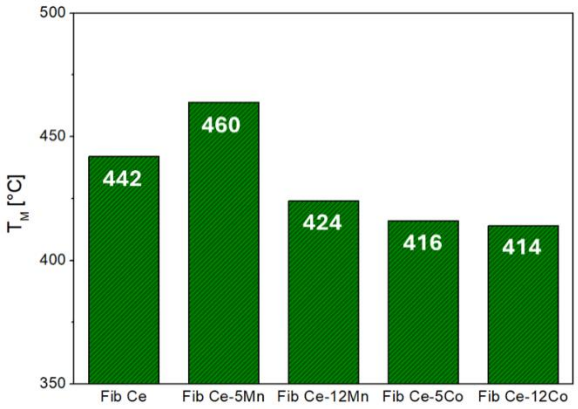

Fig. 1.21 - Maximum soot combustion rate temperature (T_M) for Fib Ce-Mn,Co catalysts.

Based on typical temperatures found in diesel exhaust gases, which are between 200 and 450 °C, T_M values around 400 °C are considered good enough in terms of a DPF regeneration, even more for feeds lacking NO_x (as the current case).

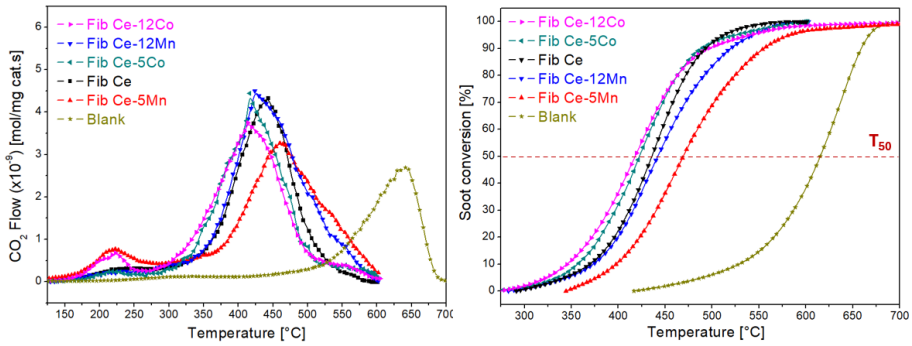

Fig. 1.22 - Catalytic activity of Fib Ce-Mn,Co catalysts for soot oxidation: CO_2 flow (left) and soot conversion profiles (right).

All supported samples managed to decrease T_M of Fib Ce, enhancing the activity, except for Fib Ce-5Mn. The best performing catalysts for the reaction were the Co-supported ones, being the activity for both loadings used very similar.

As previously shown in Table 1.2, the addition of Mn and Co to Fib Ce slightly increased its specific surface area. Several papers have attributed a good activity to a bigger specific surface area, but if indeed this mostly applies in gas or liquid phase reactions, in a system with a solid reactant, a big specific surface area does not always correlate directly with more numerous contact points, as in the case of catalytic

soot combustion. In this vein, if a catalyst has a huge specific surface area but small pores (e.g., micropores), a lot of this area will not be able to interact with soot particles. Soot agglomerates are around 100 μm in size (General introduction - Section 1.2.2) and can be easily disaggregated by applying an ultrasound bath, forming smaller particles between 10-50 nm [88]. In the case of our mesoporous biomorphic fibers and considering that ultrasound was performed in this work to disperse soot particles, it could be inferred that soot particles would get inside mesopores. Considering this, textural features of our catalytic fibers would favor soot-to-catalyst contact. However, Fib Ce-5Mn does not follow this trend as its catalytic activity was lower than that of bare Fib Ce. In order to clarify this behavior, other properties of the developed fibrous catalysts should be considered.

Fib Ce-5Mn exhibits the highest surface O_{ads}/Ce ratio (more than twice than the other samples) and has a Mn AOS of 3.5. This implies the presence of Mn^{4+}, Mn^{3+}, and Mn^{2+} on the catalyst surface. In addition, the surface concentration of Mn is much higher than the nominal one. Moreover, it is probable that the oxidation activity of Mn^{4+} species is lower than that of Ce^{4+}, thus, in part, the partial covering of the ceria surface by Mn^{4+} could decrease catalytic activity. Accordingly, the absence of bulk segregated phases would make soot-to-catalyst contact difficult. On the other hand, in the case of Fib Ce-12Mn, the surface concentration of Mn is closer to that of the bulk. The latter also presents the lowest AOS of Mn (2.7), and the presence of the redox couple Mn^{2+}/Mn^{3+} species. Moreover, this sample has the highest Ce^{3+} and O_{latt} contents among all catalysts. These facts could be related to the T_M order observed: Fib Ce-12Mn < Fib Ce < Fib Ce-5Mn (Fig. 1.21).

In the case of Co-containing samples, both samples containing 5 or 12 wt.% significantly enhance the activity of Fib Ce. Co_3O_4 has been widely reported as a very active phase in oxidation reactions due to mobile oxygen inside its spinel structure, good reducibility, and the presence of electrophilic oxide species, among others [31]. However, no differences are observed in the corresponding T_M values for both amounts of Co. In contrast to that observed for Mn-samples, segregated oxidic bulk species (Co_3O_4 spinel) were observed by XRD and Raman. Also, being the oxidation of soot a solid-solid-gas reaction, the homogeneous segregation of Co_3O_4 on the fibrous support improves the contact between the catalyst and the solid reactant and consequently enhances catalytic activity. This increase in activity could also be related to the surface composition, as the Ce^{3+}/Ce^{4+} ratio slightly increased while

O_{ads}/O_{latt} ratio decreased if compared to those of the bare support (Table 1.4).

For both catalytic systems, when Ce^{3+} and O_{latt} surface concentrations increase, an improvement in activity is evidenced. This could be explained if considering that lattice oxygen preferentially oxidizes soot particles and the vacancies generated adsorb oxygen coming from the gas phase, which restores the lattice oxygen depleted [161].

Comparing catalytic activities here reported with literature data [23], it can be observed that good catalysts have T_{50} values around 450 °C, tested including NO in the feed, being these values close to those of catalytic CeO_2 fibers, these last tested without feeding NO. This outstands the performance of the micro-structured catalysts here prepared.

As expected, when supporting transition metal oxides (MnO_x or CoO_x) onto biomorphic fibers (Fib Ce) by means of a simple wet impregnation technique, there is a dependence on the type of metal added and its amount on the activity, since they have intrinsic properties on their own, and this results in different outcomes for different formulations.

Table 1.8 - Catalytic activity of Fib Ce-Mn,Co catalysts in soot combustion.

Catalyst	T_{10} [°C]	T_{50} [°C]	T_{90} [°C]	T_M [°C]
Blank	528	615	659	641
Fib Ce	373	440	523	442
Fib Ce-5Mn	397	469	555	460
Fib Ce-12Mn	373	442	520	424
Fib Ce-5Co	356	422	488	416
Fib Ce-12Co	346	418	496	414

3.7 Catalytic evaluations - Benzene oxidation (BE)

The benzene conversion results obtained for all catalysts are depicted in Fig. 1.23. The temperatures corresponding to 10 (T_{10}), 50 (T_{50}), and 90 (T_{90}) % benzene conversion are listed in Table 1.9. Also, reaction rates (r) at 200 °C are shown. The values obtained are in the range with those reported by Y. Guo et al. for different types of metal oxides [32].

Bare Fib Ce (CeO_2 fibers) performed poorly (T_{50} = 379 °C) and this activity is similar to that of other CeO_2 catalysts prepared by different methods [34,73]. This is the opposite to the behavior observed for bare Fib Ce in soot combustion. However, all supported catalysts tested increased considerably the activity of the bare support (Fib Ce) for benzene oxidation. The incorporation of either Mn or Co on Fib Ce led to the formation of solid solutions, as seen by XRD and Raman, which increase the mobility of lattice oxygen. As observed by catalytic tests, this feature positively impacts on benzene oxidation [36].

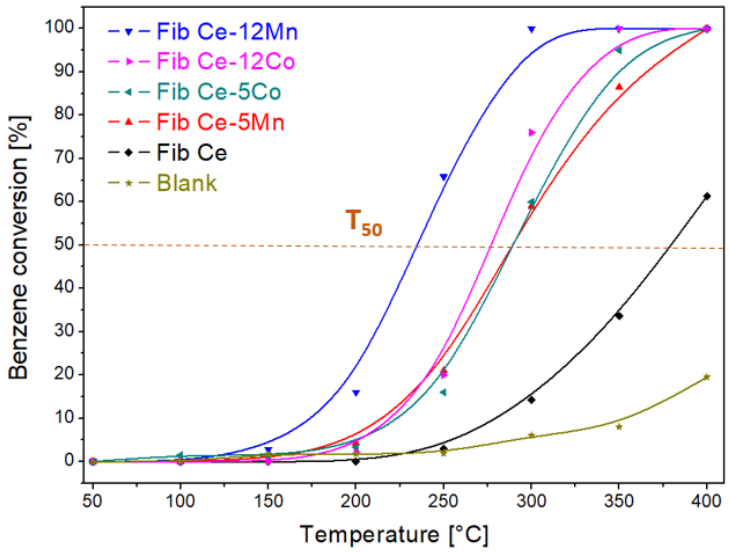

Fig. 1.23 - Catalytic activity of Fib Ce-Mn,Co catalysts for benzene oxidation: benzene conversion profiles.

Both Co-supported catalysts, and Fib Ce-5 Mn, showed a similar catalytic performance, being their T_{50} around 280 °C. In the case of Co containing samples, no significant differences are observed in their physical-chemical properties, as both of them showed the presence of a solid solution and Co_3O_4 segregation, along with similar surface composition. The catalyst containing 5 wt.% Mn showed an improvement in benzene oxidation activity, which was not the case for soot oxidation.

This is not surprising since benzene oxidation is a heterogeneous solid-gas reaction, which does not require solid-solid contact.

The best performing catalyst was Fib Ce-12Mn, having the lowest T_{50} value, which can be interpreted considering that this catalyst shows the highest Ce^{3+}/Ce^{4+} surface ratio and O_{latt} concentration (XPS, Tables 1.4 and 1.6), along with the presence of oxygen vacancies (LRS, Fig. 1.13). The latter could facilitate benzene adsorption and oxidation. Also, the AOS of bulk Mn on this sample was 2.7 (Table 1.6), lower than that of the sample containing 5 wt.% Mn, which could help in the redox cycle of ceria under reaction conditions.

There are many factors that can influence the mechanism followed by reactants in VOCs oxidation such as the catalyst properties (active metal and support), nature of VOCs, concentration, and setup parameters for catalytic tests. The most mentioned mechanisms are the Mars-Van Krevelen (MVK), Langmuir-Hinshelwood (L-H), and Eley-Rideal (E-R) models [31,32,34]. Benzene oxidation is believed to follow a MVK mechanism, starting by the adsorption of benzene on the catalyst surface, then reacting with lattice oxygen, and finally the reduced metal being re-oxidized by oxygen from the gas phase [36].

Taking this into account and knowing that O_{latt} is playing an important role in the performance of these catalysts, it could be inferred that the MVK mechanism is mainly taking place, in which benzene is adsorbed either on the support or on metal oxides added (General Introduction - Fig. i.19).

Table 1.9 - Catalytic activity of Fib Ce-Mn,Co catalysts for benzene oxidation.

Catalyst	T_{10} [°C]	T_{50} [°C]	T_{90} [°C]	r_{250}* [µmol Bz/g cat. s]
Blank	354	> 400	> 400	2.4E-4
Fib Ce	280	379	> 400	5.4E-3
Fib Ce-5Mn	214	289	366	3.2E-2
Fib Ce-12Mn	173	235	288	8.6E-2
Fib Ce-5Co	224	289	349	2.8E-2
Fib Ce-12Co	220	277	332	3.5E-2

**** Reaction rate at T = 250 °C.***

The reaction rate of the best catalyst (Fib Ce-12Mn) at 250 °C is 0.08 µmol Bz/g cat. s., which is comparable to values reported by Y. Guo et al. for Ag and Co, Mn - catalysts [32]. In order to check the catalytic stability of this sample, successive runs were carried out (Fig. 1.24). Although an

initial deactivation is observed, the catalyst maintained the catalytic activity after the three consecutive cycles. This deactivation effect could be related to CO_2 and H_2O adsorption during storage of this sample, as the different stability runs were carried out several months after the original sample was tested.

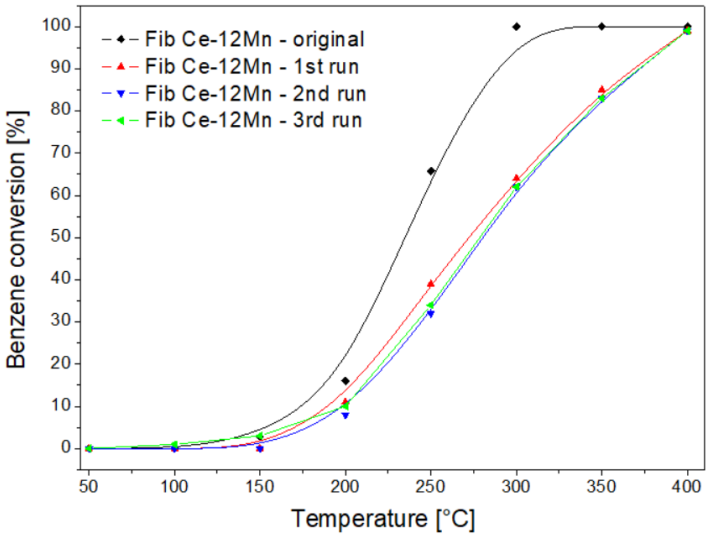

Fig. 1.24 - Stability test in benzene oxidation for Fib Ce-12Mn.

4 Main findings

Catalytic supported fibers were obtained following a facile synthesis method which only requires two consecutive impregnations, it is inexpensive and waste-free. Moreover, this method could be extended to using other biotemplates from organic wastes. These catalysts retained the morphology of the original biotemplate to a great extent, but also open helicoidal fibers from cotton transformed into cylindrical fibers with and without inner channels, presenting a porous texture. The addition of Mn or Co on ceria fibers (Fib Ce) caused a shift in the main signals of CeO_2 phase (XRD and LRS profiles), which was attributed to the insertion of some Mn and Co cations into ceria lattice. The segregation of Co_3O_4 phase was evidenced by these techniques. Furthermore, the deposition of the catalysts also affected surface Ce^{3+}/Ce^{4+} and O_{ads}/O_{latt} atomic ratios differently for both transition metals and both amounts used.

In soot combustion tests, the only sample that showed a lower activity than Fib Ce was Fib Ce-5Mn, which is expected to be related to a bad contact of Mn species with soot particles. Moreover, the surface of this catalyst had the highest O_{ads}/Ce ratio and a Mn/Ce ratio doubling the nominal, both properties that could also affect its contact and performance. On the other hand, the good-performing catalysts, which lowered the T_M value obtained for the bare support, presented higher Ce^{3+} and O_{latt} surface contents. This could be related to an improved and faster reoxidation of the reduced metal after its reaction with soot. In addition, the segregation of the deposited metal oxides and lower surface composition seemed to increase the soot-to-catalyst contact and clearly enhanced the catalytic performance.

For benzene oxidation, all catalysts improved the activity of the bare support. Opposite to soot combustion, Fib Ce-5Mn decreased considerably the T_{50} value of Fib Ce, despite the properties mentioned above. All supported catalysts proved that a key characteristic to boost benzene oxidation is to have solid solutions at least partially with a part of the Ce cations replaced in the lattice. The best performing catalyst here (Fib Ce-12Mn) considerably lowered the T_{50} value. The highest Ce^{+3}/Ce^{+4} ratio, highest O_{latt} concentration, presence of oxygen vacancies, and lower surface AOS, were the main qualities correlated to its outstanding activity. The MVK mechanism is believed to occur based on O_{latt} influence towards benzene oxidation.

From the catalytic evaluations in two different oxidation reactions, using the same series of catalysts, it is evidenced that each reaction has its own particularities. Different properties of the catalysts will have a

different impact on each reaction, both reactions being intrinsically non-identical. It was found that, while Fib Ce-12Co is the most active for soot combustion, in the case of benzene oxidation, Fib Ce-12Mn is the best one.

PART I - CHAPTER II

Co_3O_4 biofibers as an alternative active support for soot and benzene oxidation

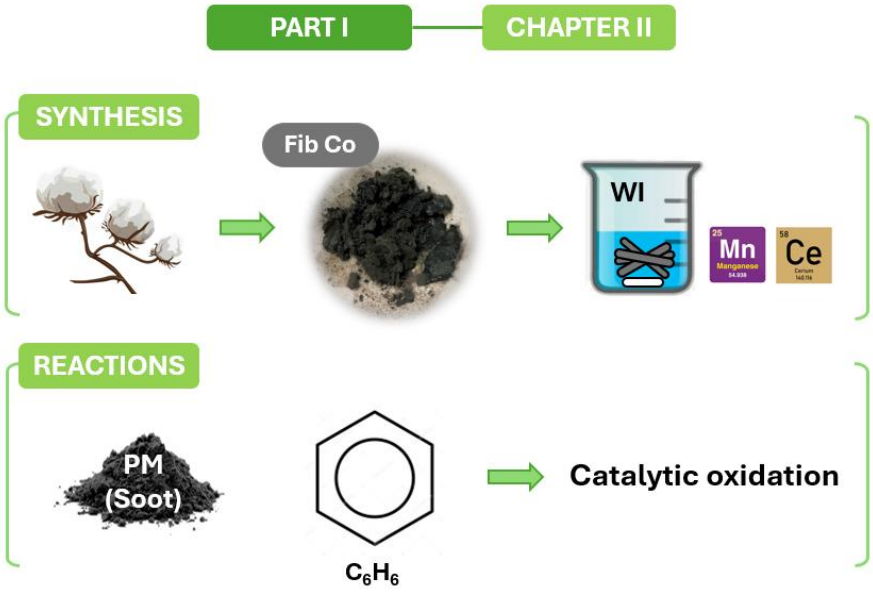

1 Introduction: Co_3O_4 biofibers as an alternative active support for soot and benzene oxidation

This Chapter is connected to Chapter I, in which CeO_2 fibers were "decorated" with Mn and Co phases and evaluated in the reactions of soot combustion and benzene oxidation. It follows the same type of synthesis and shares the same sequence of characterizations and tested reactions. Now, in turn, a different type of active support is studied towards the aforementioned oxidation reactions, expanding the scope, and not restricting the possibilities to ceria as the only building block available for this type of synthesis.

Oxide spinels are mixed oxides with general formula AB_2O_4, in which A and B are cations located in tetrahedral and octahedral position, respectively. They are used in numerous applications, such as magnetic materials, gas sensors, photocatalysis, adsorbents, as well as for catalytic applications like combustion, water gas-shift reaction, CO oxidation, methanol reforming, etc. [22]. In this case, the chosen active support is the cobalt oxide spinel (Co_3O_4), a mixed-valence metal oxide, which is known as one of the most active metal oxide catalysts for the total oxidation of VOCs. In this spinel structure, Co^{2+} occupies a tetrahedral site, while Co^{3+} an octahedral one (Fig. 2.1) [136,159,162]. The good activity of Co_3O_4 is related to its excellent reduction ability, presence of oxygen vacancies, and high concentration of surface electrophilic oxygen species [22,31,34,160].

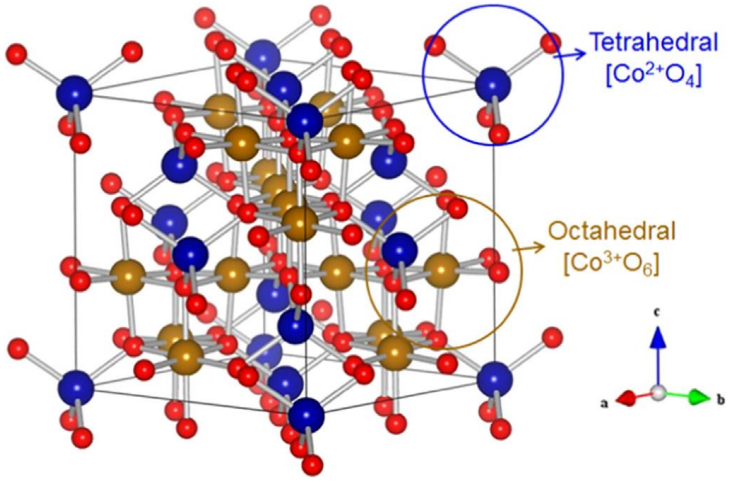

Fig. 2.1 - Co_3O_4 spinel crystalline structure [162].

PART I – CHAPTER II

The main objective in Chapter II is to verify the feasibility (as it was achieved in Chapter I) of improving the activity of an active support with some of the formulations proposed here (addition of different amounts of Mn or Ce oxides). The influence and interactions between the deposited phases and the support will be studied, and how they affect the properties of the catalysts. Finally, the performance of these catalysts will be measured in the oxidation of soot and benzene. Throughout this Chapter, a contrast with Chapter I is made to highlight the main differences and similarities encountered. Whether the objective is fulfilled or not, insight can be gained from studying these systems.

2 Abstract

Mn and Ce supported on Co_3O_4 biofibers were prepared by means of a biotemplate and subsequent wet impregnation. The catalysts were evaluated in soot combustion and benzene oxidation.

Several characterizations were applied on these catalysts such as: SEM, EDS, ICP-AES, N_2 physisorption, FTIR-ATR, XRD, RAMAN and XPS. The fibrous morphology was evident in SEM images and EDS analysis confirmed the presence of the supported metals on the fibers. By XRD, FTIR-ATR, and Raman, the metal oxides formed in the synthesis were identified. XPS analysis showed a variation in the concentration of oxygen species and Co^{3+}/Co^{2+} ratios after the deposition step, being lower after the addition of Mn (more Co^{2+}) and higher after Ce addition (more Co^{3+}). Also, Mn average oxidation state (AOS) was calculated using the binding energy separation between the peaks in Mn 3s region.

For soot combustion, a comparison of three different soot-to-catalyst contacts was made with bare Co_3O_4 fibers prior to the main tests, similarly to what was done in Chapter I for CeO_2 fibers. Then, only Ce-supported samples managed to bring an improvement in activity. Lastly, for benzene oxidation, none of the supported formulations could enhance considerably the performance of the bare Co_3O_4 support.

3 Results and discussion

3.1 Morphological analyses by SEM and EDS (AR)

SEM images of cotton and bare Co_3O_4 fibers (Fib Co) are shown in Fig. 2.2. It is evident that a fibrous morphology was attained from the elimination of the template. Similar to Fib Ce in Chapter I, the new fibers exhibit a wide range of sizes, with lengths ranging from 25 to 200 µm and sections from 3 to 15 µm. Fib Co (Fig. 2.2 - b) are more cylindrical, shorter, and thicker than ribbon-shaped cotton's cellulosic fibers (Fig. 2.2 - a). Open helicoidal fibers are hardly seen, and many of them present inner channels (hollow fibers).

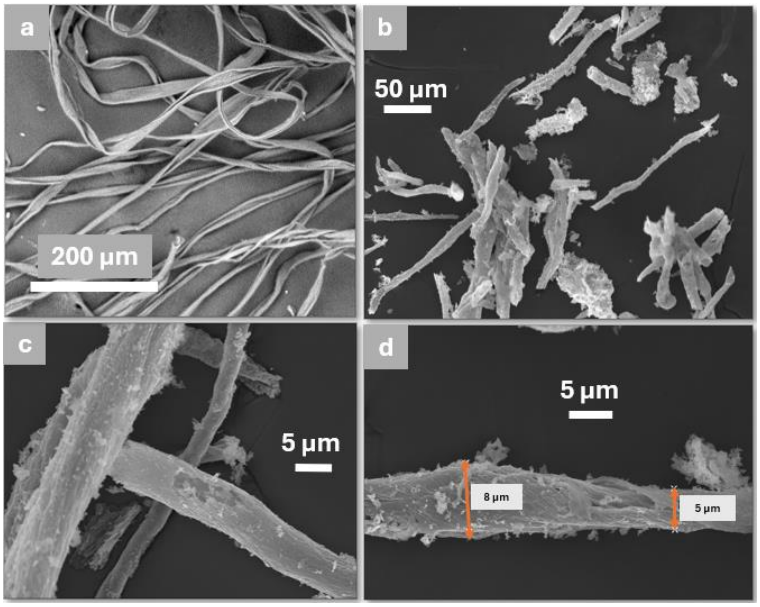

Fig. 2.2 - SEM images of cotton (a) and Fib Co (b, c, d).

The same situation is observed for Mn and Ce supported fibers (Fib Co-Mn,Ce) in Figs. 2.3 and 2.4. The supported fibers are shorter due to the stirring applied during the impregnation step and sample manipulation which inevitably can break some of them. The texture also changes: bare Fib Co exhibit a tree-crust morphology, whereas after the addition of either Mn or Ce, part of supported fibers preserve this morphology, and others show a higher degree of rugosity (Fig. 2.3 - b, Fig. 2.4 - d).

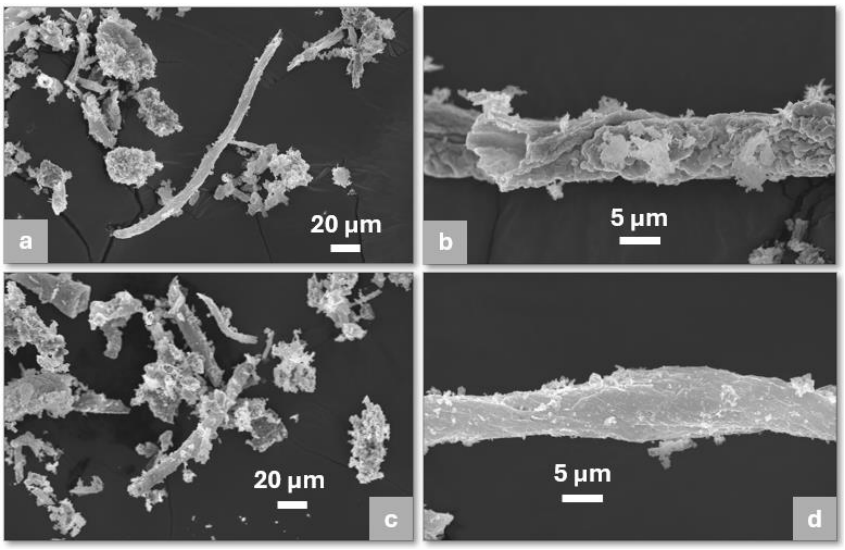

Fig. 2.3 - SEM images of Mn-supported Fib Co by WI: of Fib Co-5Mn (a,b) and Fib Co-12Mn (c,d).

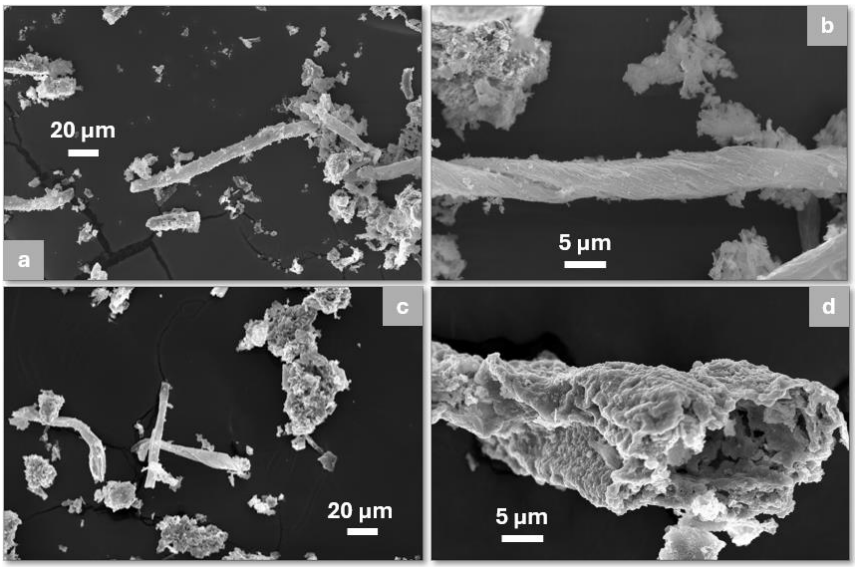

Fig. 2.4 - SEM images of Ce-supported Fib Co by WI: Fib Co-5Ce (a,b) and Fib Co-12Ce (c,d).

The images obtained by EDS analysis are shown in Figs. 2.5 and 2.6, and the quantification values obtained for the supported catalysts are listed in Table 2.1, as metal ratios (M/Co). The approach followed was identical to the one described in Chapter I. Images of spot analyses are depicted in Fig. 2.5 - a,c and Fig. 2.6 - a,c; mappings in Fig. 2.5 - b,d and Fig. 2.6 - b,d; and finally big area mappings in Fig. 2.7.

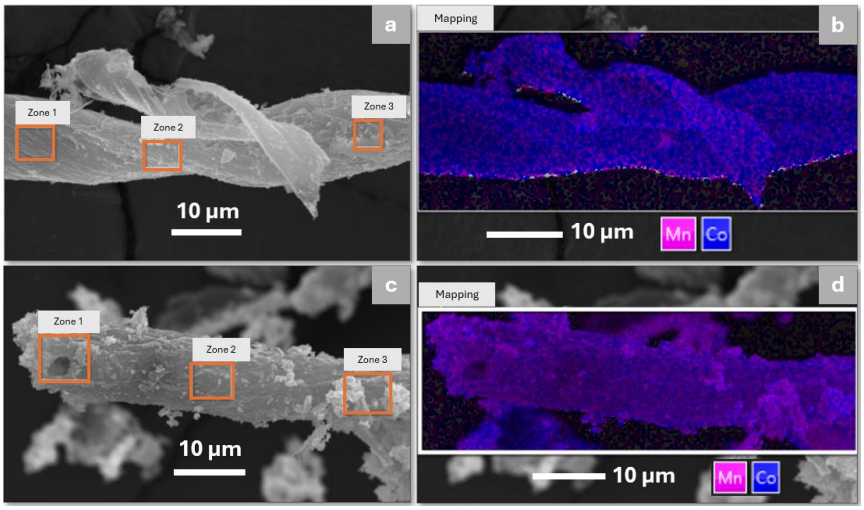

Fig. 2.5 - Spot (left) and mapping (right) EDS analyses of Mn-supported Fib Co by WI: Fib Co-5Mn (a,b) and Fib Co-12Mn (c,d).

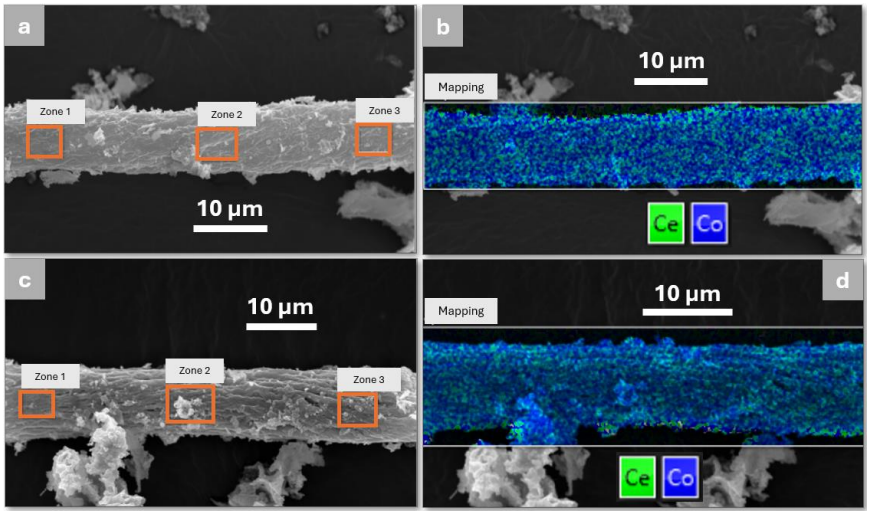

Fig. 2.6 - Spot (left) and mapping (right) EDS analyses of Ce-supported Fib Co by WI: Fib Co-5Ce (a,b) and Fib Co-12Ce (c,d).

The calculated averages (M/Co ratios) for individual fibers per sample (Fibers 1, 2, and 3) for spot analysis (Zones 1, 2, and 3), along with mapping analysis per sample (Fibers 1, 2, and 3), exhibit a heterogeneous distribution of the deposited metals, as the atomic metal ratios obtained are different for each zone (spot) and fiber (mapping) (Table 2.1). This situation was as well observed in Chapter I when preparing supported ceria fibers using the wet impregnation technique. Most catalysts gave averages of Mn/Co ratios close to the nominal ones. Finally, big area mappings for all samples showed Mn/Co ratios very close to the nominal ones, confirming once again that all the intentioned amounts of Mn and Ce were successfully deposited.

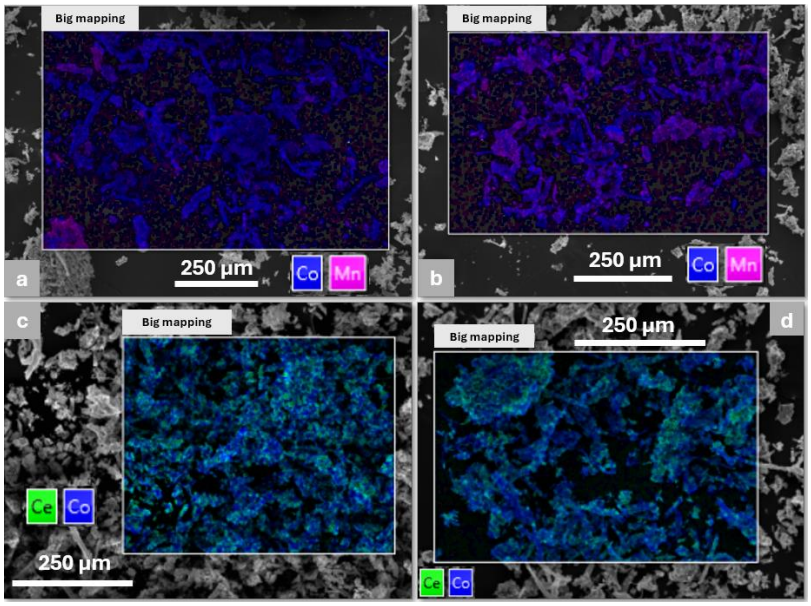

Fig. 2.7 - EDS big mappings of Mn or Ce-supported Fib Co by WI: a) Fib Co-5Mn, b) Fib Co-12Mn, c) Fib Co-5Ce, d) Fib Co-12Ce.

Table 2.1 - Spot and mapping EDS analyses from Figs. 2.5, 2.6 and 2.7.

Sample	M*/Co atomic ratios								
	Fiber N° (**)	Zone 1 (Spot)	Zone 2 (Spot)	Zone 3 (Spot)	Average per fiber (Zones 1, 2 and 3)	Spot average	Mapping per fiber	Big mapping (wt.% - ICP)	Nominal (wt.%)
Fib Co-5Mn	1	0.01	0.01	0.02	0.01	0.02	0.02	0.09 (5.5)	0.08 (5)
	2	0.01	0.04	0.01	0.02		0.03		
	3	0.01	0.02	0.02	0.02		0.03		
Fib Co-12Mn	1	0.08	0.06	0.05	0.06	0.18	0.06	0.25 (13.7)	0.20 (12)
	2	0.20	0.38	0.18	0.30		0.25		
	3	0.27	0.18	0.21	0.22		0.22		
Fib Co-5Ce	1	0.03	0.03	0.03	0.03	0.03	0.03	0.04 (7)	0.03 (5)
	2	0.03	0.03	0.04	0.03		0.05		
	3	0.03	0.04	0.03	0.04		0.03		
Fib Co-12Ce	1	0.18	0.17	0.19	0.18	0.08	0.17	0.07 (11)	0.08 (12)
	2	0.03	0.02	0.03	0.02		0.03		
	3	0.05	0.04	0.04	0.05		0.05		

** M = Mn or Ce*

*** Three fibers per sample were analyzed*

3.2 XRD and textural analyses (BE)

The diffractograms obtained by XRD analysis are depicted in Figs. 2.8 and 2.9, for Fib Co-Mn and Fib Co-Ce, respectively. References were added at the bottom of each graph showing only the main signals from the metal oxides phases concerned.

For the bare support, that is Fib Co, all the characteristic peaks from the cubic spinel structure of Co_3O_4 (JCPDS 42-1467) are clearly seen [160,163,164]. The diffraction peaks are placed at 2θ = 19.0, 31.3, 36.8, 38.5, 44.8, 55.6, 59.3, 65.2 and 77.3 °, with their corresponding crystal planes being (1 1 1), (2 2 0), (3 1 1), (2 2 2), (4 0 0), (4 2 2), (5 1 1), (4 4 0), and (5 3 3).

After 5 wt.% Mn deposition, no significant changes are evident. However, for the 12 wt.% Mn sample, several new peaks appear (Fig. 2.8). The broad peak at 2θ = 33 ° along with two smaller ones around 24.6 ° and 55 °, are assigned to the bixbyite Mn_2O_3 phase (JCPDS 73-1826) [165,166]. The main peak of Co_3O_4 has a clear shoulder on the left, at 2θ = 36.4°. This signal was ascribed to hausmannite Mn_3O_4 spinel phase (JCDPS 24-0734) [166,167]. In contrast to Mn-supported Fib Ce (Chapter I), MnO_x supported phases are clearly seen here for 12 wt.% sample, highlighting a different behavior of the supports when impregnated using the same method and Mn precursor solution.

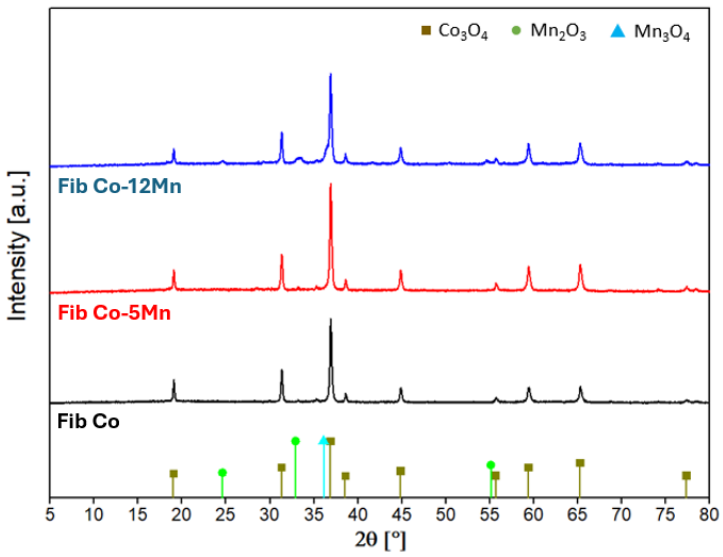

Fig. 2.8 - X-Ray diffractograms of Mn-supported Fib Co.

For Ce-supported Fib Co (Fig. 2.9), the main characteristic diffraction peaks from ceria with a face-centered cubic fluorite structure (JCPDS 34-0394) are present at 2θ = 28.5, 33, 47.5 and 56.3 °; all of which increase in intensity when going from 5 to 12 wt.% Ce [123,168].

After depositing 5 or 12 wt.% Ce on Fib Co, a small shift downward in the 2θ value of the signal (2 2 0) from Co_3O_4 occurs (0.03 and 0.04 °, respectively), which corresponds to a small increase (0.01 Å) of the Co_3O_4 lattice parameter (LP). In the case of Mn-supported Fib Co, this shift was even lower (0.004 and 0.012 ° for 5 and 12 wt.% Mn on Fib Co, respectively), being not significant considering the precision of the XRD machine (step = 0.015 °). This could be explained by the replacement of some Co^{3+} cations in the spinel structure by bigger Mn^{3+} and Ce^{4+} cations, being their ionic radius: r(Co^{3+}) = 0.61 Å, r(Mn^{3+}) = 0.65 Å , r(Ce^{4+}) = 0.94 Å [169]. Nevertheless, the FWHM values do not change appreciably, which is reflected in the crystallite size of Co_3O_4 remaining practically constant (Table 2.2). This is not surprising for the case of supported oxides (wet impregnation).

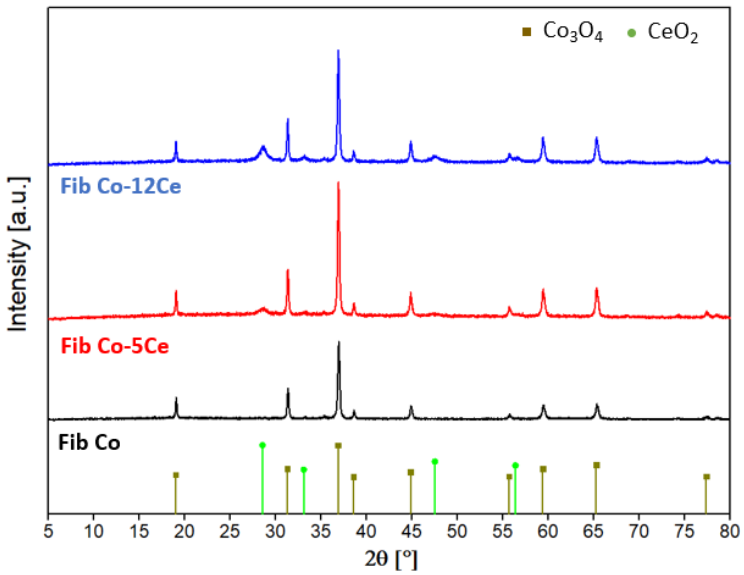

Fig. 2.9 - X-Ray diffractograms of Ce-supported Fib Co.

Concerning the textural analysis when performing N_2 physisorption, all catalysts follow essentially a type II isotherm, typical of nonporous or macroporous adsorbents (Fig. 2.10). The desorption branch appears practically identical to the adsorption one, forming a very small hysteresis loop placed at high relative pressure, evidencing the absence of mesopores [128]. This could indicate a slightly different

decondensation/evaporation mechanism from irregular voids formed between big particles (interparticle porosity). A small increase in the specific surface area (SSA) of the bare support occurred after impregnation of Mn or Ce (Table 2.2). Also, based on the negligible adsorption values at low relative pressures, all samples lack microporosity.

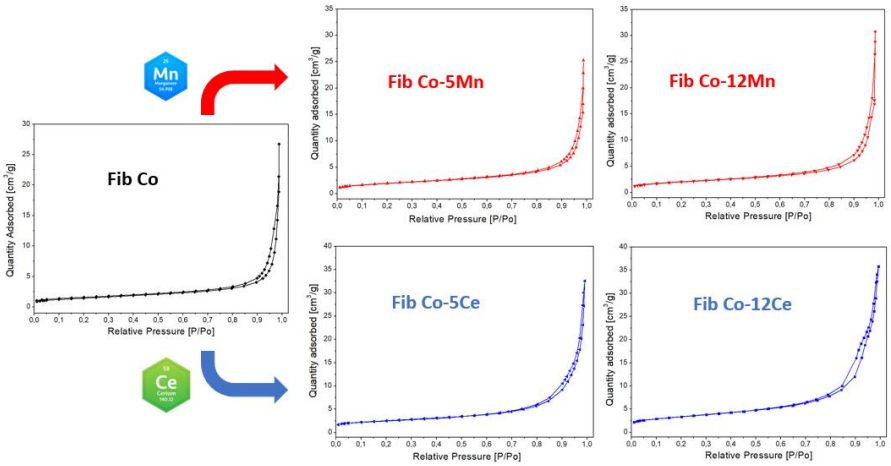

Fig. 2.10 - N_2 physisorption isotherms for Fib Co-Mn,Ce catalysts.

Table 2.2 - XRD and textural analyses.

Sample	Co_3O_4 lattice parameter (LP) [Å]	Crystallite size of support (Co_3O_4) [nm] *	Crystallite size of supported phase [nm] *	BET Specific surface area (SSA) [m^2/g]	Pore volume (V_p) [cm^3/g] **
Fib Co	8.07	48	-	5	0.022
Fib Co-5Mn	8.07	46	-	7	0.023
Fib Co-12Mn	8.07	47	11	7	0.025
Fib Co-5Ce	8.08	49	8	9	0.036
Fib Co-12Ce	8.08	50	10	12	0.044

**** Calculated by Scherrer equation. For Co_3O_4 the peak at $2\theta = 31.3°$ was used, for Mn_2O_3 the peak at $2\theta = 33°$ and for CeO_2 the peak at $2\theta = 28.5°$.***

***** Pore volume taken at $P/P_o = 0.98$.***

3.3 FTIR-ATR analyses (BE)

The spectra obtained for all catalysts are shown in Figs. 2.11 and 2.12, for Mn-supported and Ce-supported Fib Co, respectively. All band positions and assignments are summarized in Table 2.3.

For the bare support (Fib Co), a broad weak band is present at 3400 cm^{-1} from -OH stretching vibrations and another one at 1640 cm^{-1} corresponding to bending vibration of H-O-H, both probably due to physisorbed water [144,170]. This sample also shows weak peaks at approximately 1520, 1330 and 1045 cm^{-1} which are assigned to adsorbed mono-dentate carbonates groups probably coming from the biotemplate decomposition [142,143]. All the signals mentioned practically disappear after the impregnation process (zoomed areas). Finally, at lower wavenumbers, there are two sharp and well-defined peaks at 658 and 555 cm^{-1} corresponding to Co-O stretching from Co in tetrahedral (Co^{2+}) and octahedral coordination (Co^{3+}), respectively (Fig. 2.11) [65,163]. For Mn-deposited catalysts (Fig. 2.11), just for 12 wt.% Mn a new signal can be distinguished at 487 cm^{-1} which matches to Mn-O bending vibration from Mn^{3+} species [145,146,167]. The signal at 514 cm-1due to Mn-O in octahedral environment, as seen in Chapter I, could probably be overlapped by more intense Co-O signals.

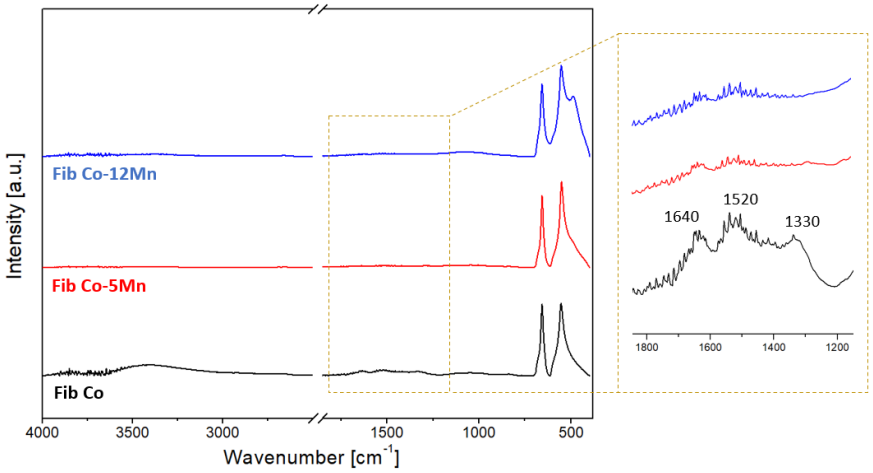

Fig. 2.11 - FTIR-ATR spectra of Mn-supported Fib Co (left) and magnified region (right).

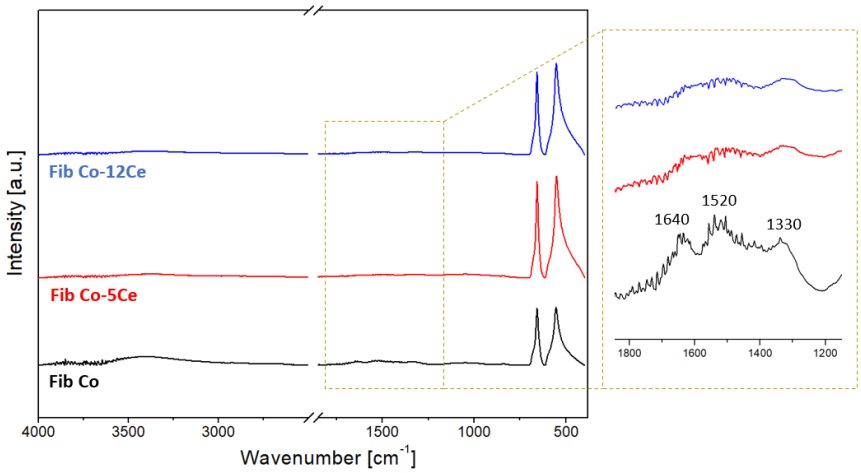

Fig. 2.12 - FTIR-ATR spectra of Ce-supported Fib Co (left) and magnified region (right).

As regards Ce-supported samples (Fig. 2.12), no signal can be seen from Ce-O vibration in the metal-oxygen region (expected at 565 cm^{-1} and 470 cm^{-1}, as seen in Chapter I - Fig. 1.11), probably because of the overlapping by the two very intense Co-O bands.

Table 2.3 - FTIR-ATR signals assignment for Fib Co-Mn,Ce catalysts.

Band position [cm^{-1}]	Assignment
3400, 1640	-OH, H-O-H (physisorbed water)
1520, 1330, 1065	Adsorbed mono-dentate carbonates
487	Mn-O
658, 555	Co-O (tetrahedral, octahedral)

3.4 LRS analyses (BE)

The spectra obtained by Raman spectroscopy analyses are shown in Figs. 2.13 and 2.14. For all samples, three typical signals from Co_3O_4 spinel are observed: two medium-intense bands located at 470 and 514 cm^{-1} from E_g and F_{2g} symmetry modes, followed by the main and most intense peak at 678 cm^{-1} corresponding to the A_{1g} mode [137,169]. The latter is attributed to Co^{3+}-O^{2-} bond vibration in the CoO_6 octahedron [171]. Also, the band at 606 cm^{-1} (F_{2g}) can be barely observed.

For Mn-supported samples (Fig. 2.13), as Mn content increases, the F_{2g} band from Co_3O_4 around 606 cm^{-1} becomes more intense. Moreover, for 5 and 12 wt.% catalysts, the main peak of Co_3O_4 presents a shoulder around 656 cm^{-1}, which could be evidence of Mn_2O_3 phase and/or Mn_3O_4 [172,173], being in accordance with XRD results shown in Fig. 2.8 [150,167].

Regarding Ce-supported Fib Co (Fig. 2.14), no clear signs of CeO_2 are evident. The main scattering band from CeO_2 phase is expected around 460 cm^{-1}, but the more intense Co_3O_4 peak at a similar frequency is probably hiding it [38,147]. For these samples, there is no increment of the F_{2g} band at 606 cm^{-1} from Co_3O_4 with increasing Ce content.

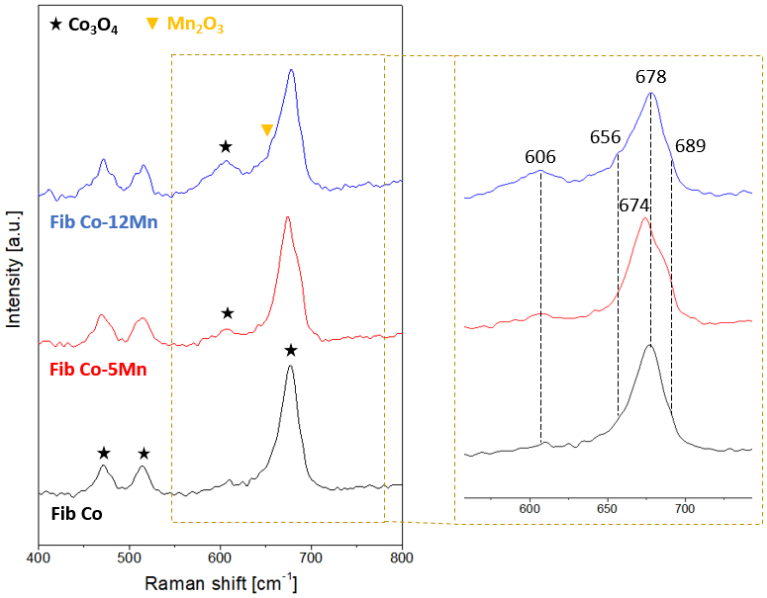

Fig. 2.13 - Raman spectra of Mn-supported Fib Co (left) and magnified region (right).

For both series of supported fibers, the samples with 5 wt.% presented a red shift of the main signal of Co_3O_4 at 678 cm^{-1} (A_{1g} band), which could be attributed to the Co_3O_4 lattice distortion originated by the introduction of either Mn or Ce [171]. As the metal content increases, no shift can be seen for this signal. Moreover, for all supported samples, the A_{1g} signal exhibits a shoulder around 690 cm^{-1}, which is more pronounced for 5 wt.% samples, highlighting the added metal-Co_3O_4 effect interaction.

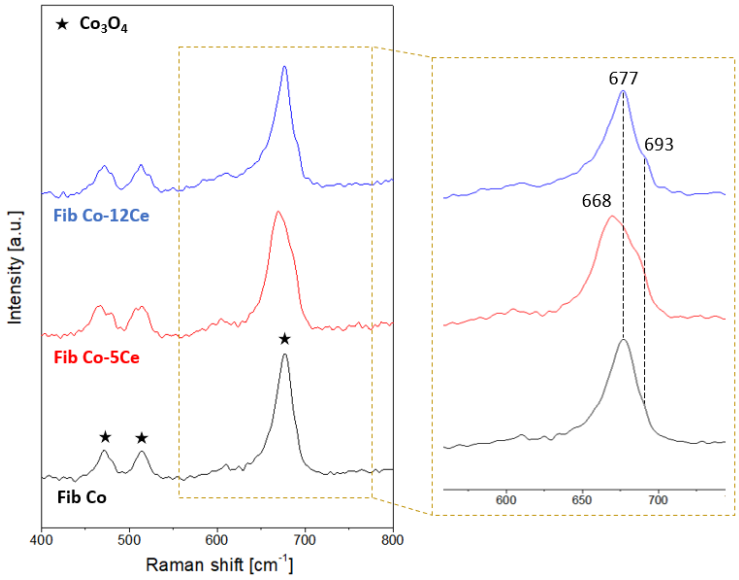

Fig. 2.14 - Raman spectra of Ce-supported Fib Co (left) and magnified region (right).

3.5 Surface analyses by XPS (BE)

The surface of the catalysts was analyzed by XPS measuring the following regions: C 1s, O 1s, Co 2p, Mn 3s, Mn 2p, and Ce 3d.

Starting from C 1s region, for all samples, a main peak is present at 284.6 eV which was used as reference (C-(C-H) contamination carbon). Also, another smaller peak at higher binding energies was observed and assigned to surface carbonate species in agreement with FTIR-ATR spectra (Figs. 2.11 and 2.12) [152,153]. The stacked C 1s spectra for all samples is presented in Fig. 2.15 - left.

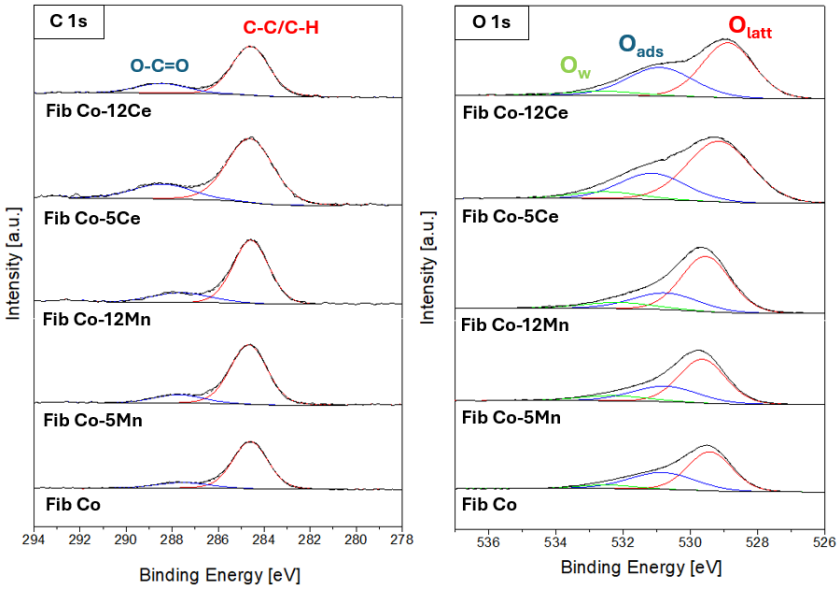

Fig. 2.15 - Surface analysis of Fib Co-Mn,Ce catalysts (XPS): C 1s (left) and O 1s (right) regions and deconvolutions.

The O 1s spectra and their deconvolutions for all catalysts are depicted in Fig. 2.15 - right. Three types of oxygen species were differentiated: the main peak between 528.9 and 529.6 eV is assigned to lattice oxygen (O_{latt}); secondly, a less intense peak between 530.7 and 531.1 eV that can be attributed to surface defects or surface-adsorbed oxygen species on oxygen vacancies (O_{ads}); and lastly, a broad weak peak between 532.1 and 532.6 eV ascribed to oxygen from hydroxyl groups and water species (O_w) [93,166,174]. The position of these peaks, along with some additional important ratios, are listed in Table 2.4. From this table, it can be noticed that after Mn deposition, the concentration of O_{ads} decreased considerably. This could be explained by the occupation of surface oxygen Co_3O_4 vacancy sites by MnO_x species and/or the interaction of the

latter with electrophilic species on the surface (O_2^-, O_2^{2-}, and O^-). On the other hand, for Ce-supported samples, no pattern is seen: for 5 wt.% Ce the amount of O_{ads} species decreases, while for 12 wt.% Ce it remains similar. Interestingly, all supported samples showed an increase of O_{ads} when related to Co content (O_{ads}/Co), being more pronounced for the Ce ones.

Fig. 2.16 shows the spectrum obtained for the bare support (Fib Co) in Co 2p region. The graph presents the characteristic doublet from split-orbit coupling for 2p orbitals (Co $2p_{1/2}$-$2p_{3/2}$) along with their corresponding satellite peaks. The binding energy difference between the main peaks is around of 15.3 eV, which is commonly reported for Co_3O_4 phase [159,169]. Co $2p_{3/2}$ signal was used for processing and quantification. All supported samples were fitted and the corresponding deconvoluted stacked spectra are shown in Fig. 2.17. The main Co $2p_{3/2}$ peak was fitted with two peaks assigned to Co^{3+} and Co^{2+} species, at 779.3 and 780.9 eV, respectively. Both peaks were matched to weaker satellites peaks at higher binding energies [160,175]. Moreover, Co^{3+}/Co^{2+} ratio was altered after the impregnation step: it slightly decreased after the addition of Mn, whereas after Ce deposition it increased to a higher degree (Table 2.5).

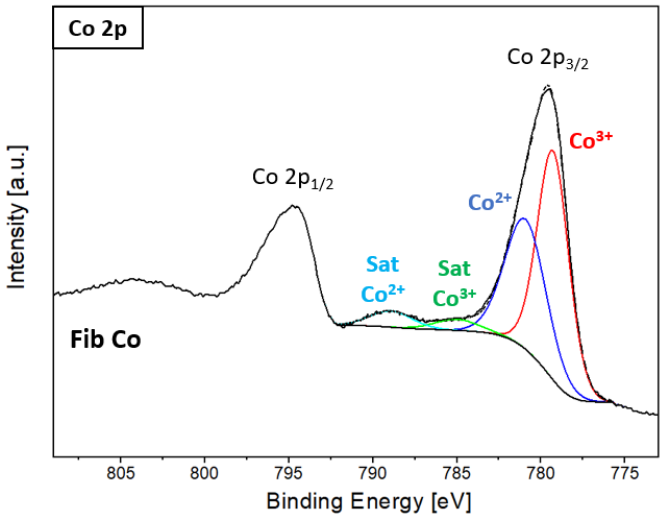

Fig. 2.16 - Surface analysis of Fib Co catalyst (XPS): Co 2p core level and deconvolution.

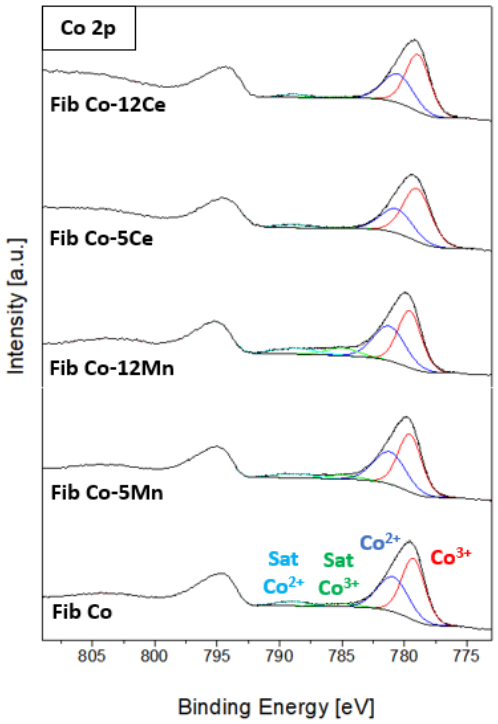

Fig. 2.17 - Surface analysis of Fib Co-Mn,Ce catalysts (XPS): Co 2p region and deconvolutions.

For Mn-supported samples, both Mn 3s and Mn 2p core levels were studied. For the former, the gap between the two peaks (ΔBE) due to multiple splitting was used to determine the average oxidation state (AOS) of Mn (Fig. 2.18). The separation of these signals was similar for both samples, giving AOS values of 3.3 and 3.2 for Fib Co-5Mn and Fib Co-12Mn, respectively (Table 2.5). As previously done in Chapter I (Section 3.5), these values were calculated using the following reported equation [157,176]:

$$AOS = 9.67 - 1.27.\Delta BE \qquad \textit{Equation 2.1}$$

This equation correlates oxidation states of different bulk mixed-valent manganites and binary Mn oxides with surface features taken from XPS measurements.

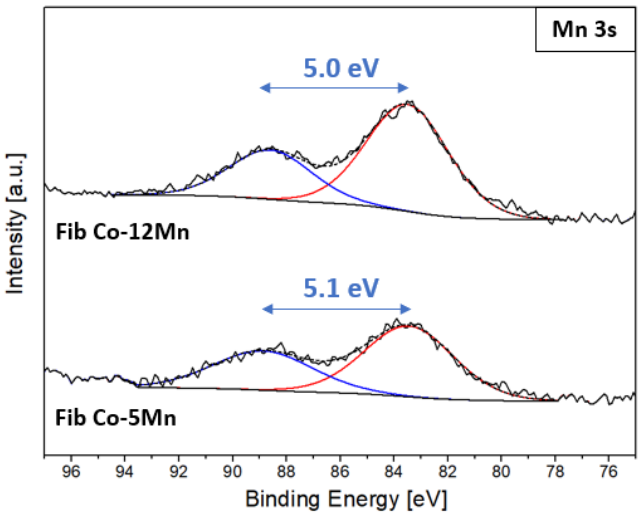

Fig. 2.18 - Surface analysis of Fib Co-Mn catalysts (XPS): Mn 3s region and deconvolutions.

Regarding Mn 2p spectra, the two major peaks corresponding to Mn $2p_{3/2}$-$2p_{1/2}$, separated 11.6 eV, can be seen in Fig. 2.19 (same as observed for Fib Ce-Mn samples in Chapter I - Section 3.5). The Mn $2p_{3/2}$ peak was decomposed with three components at 640.9, 642.2 and 645 eV, assigned to Mn^{2+}, Mn^{3+}, and Mn^{4+} species [135,139,141]. The Mn^{3+}/Mn^{2+} ratio obtained was 1.4 for both samples which indicates an important contribution of Mn^{3+} species on the surface. Additionally, considering the AOS values obtained, the presence of Mn^{4+} species on the surface is evident. This agrees with XRD bulk results, where Mn_2O_3 and Mn_3O_4 were observed. However, the presence of bulk MnO_2 cannot be discarded as AOS values are slightly higher than 3. On the other hand, the binding energies of Co^{3+} and Co^{2+} shift to higher values for Fib Co-5Mn and Fib Co-12Mn, whereas they shift to lower values for Fib Co-5Ce and Fib Co-12Ce. These shifts are very small and could be caused by a change in the chemical environment of Co species. Also, the same tendency can be observed for O 1s binding energies (Table 2.4).

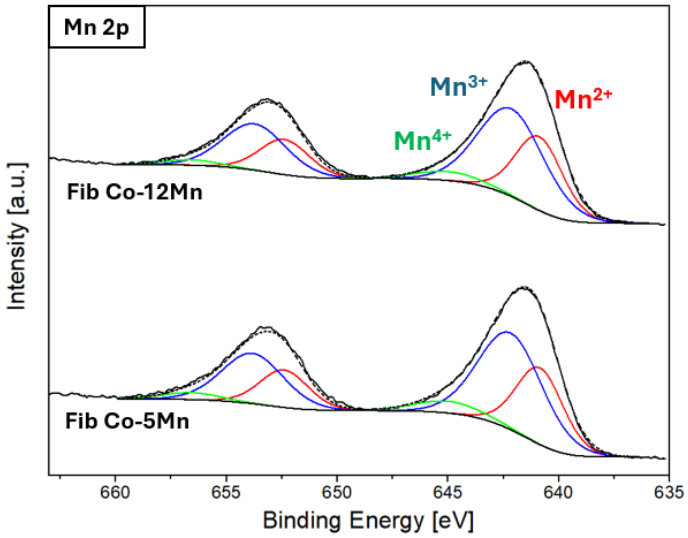

Fig. 2.19 - Surface analysis of Fib Co-Mn catalysts (XPS): Mn 2p region and deconvolutions.

For Ce-supported samples, Ce 3d spectra were collected. The deconvolution was done using ten peaks (Fig. 2.20) as usually reported and as was done in Chapter I [64,156,177]. The peaks labelled u''', u'', u, v''', v'', and v, are assigned to Ce^{4+} species, whereas peaks u', u^0, v', v^0, correspond to Ce^{3+} species. Areas obtained from orbital $3d_{5/2}$ were used for quantification purposes. The band positions of all signals, along with Ce^{3+} content and Ce^{3+}/Ce^{4+} ratio values, are listed in Table 2.6. After increasing Ce content, there is a small decrease in Ce^{3+} concentration and therefore on Ce^{3+}/Ce^{4+} ratio. Moreover, it can be noted from Table 2.5 that the metal ratio (Ce/Co) on the surface increases considerably in comparison to the nominal one, with multiplying factors of 23 and 12.5 for 5 and 12 wt.% Ce, respectively. For Mn-supported samples, Mn/Co ratios increased to a lesser extent by a factor between 4-5, for both metal contents.

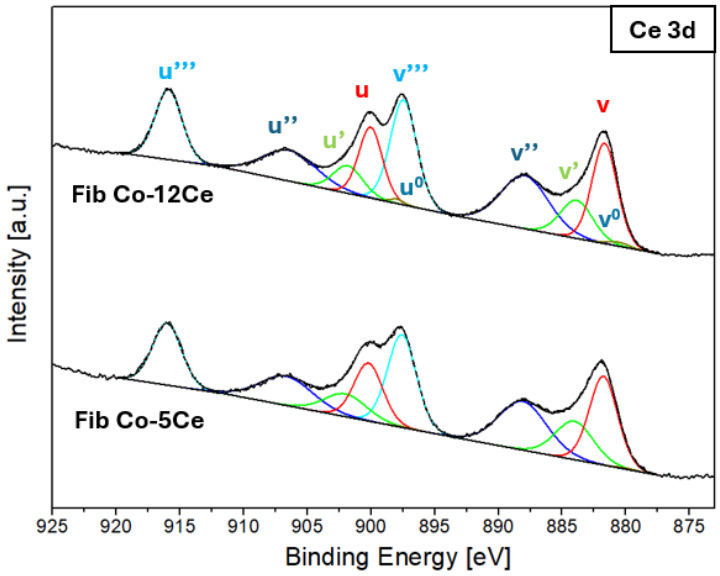

Fig. 2.20 - Surface analysis of Fib Co-Ce catalysts (XPS): Ce 3d region and deconvolutions.

The surface M/Co ratios are drastically higher (in comparison to nominal values) than those obtained in Chapter I for Mn and Co supported on Fib Ce following the same synthesis path. In that case, the increment did not surpass a 2.5 multiplying factor. This could indicate that the use of Co_3O_4 fibers as support (this Chapter) lead to a notorious surface enrichment of the supported metal oxides.

Table 2.4 - XPS O 1s core level peak positions, O_{ads} %, O_{ads}/O_{latt} and O_{ads}/Co atomic ratios.

Sample	Binding energy (eV)			O_{ads} / (O_{ads}+ O_{latt}+ O_w) (%)	O_{ads}/O_{latt}	O_{ads}/Co
	O_{latt}	O_{ads}	O_w			
Fib Co	529.4	530.8	532.5	36.1	0.63	0.9
Fib Co-5Mn	529.6	530.7	532.3	29.8	0.50	1.0
Fib Co-12Mn	529.5	530.8	532.1	25.8	0.40	1.1
Fib Co-5Ce	529.1	531.1	532.5	28.4	0.44	1.5
Fib Co-12Ce	528.9	530.9	532.6	37.3	0.66	2.6

Table 2.5 - XPS Co 2p core level peak positions, Co^{3+}/Co^{2+} and M/Co atomic ratios, and Mn AOS.

Sample	Binding energy (eV)			Co^{3+}/Co^{2+}	M*/Co (Nominal)	Mn^{3+}/Mn^{2+}	ΔBE Mn 3s (eV) (AOS**)
	Co^{3+}	Co^{2+}	Co^{3+} sat, Co^{2+} sat				
Fib Co	779.3	780.9	785.0 , 788.9	1.3	-	-	
Fib Co-5Mn	779.6	781.2	785.0 , 788.8	1.2	0.4 (0.08)	1.4	5.0 (3.3)
Fib Co-12Mn	779.6	781.2	785.0 , 788.7	1.2	0.8 (0.20)	1.4	5.1 (3.2)
Fib Co-5Ce	779.0	780.6	785.0 , 788.0	1.7	0.7 (0.03)	-	-
Fib Co-12Ce	778.9	780.5	785.0 , 788.8	1.5	1.0 (0.08)	-	-

** M = Mn or Ce*

*** Average oxidation state of bulk MnO_x*

Table 2.6 - XPS Ce 3d core level peak positions, Ce^{3+} % and Ce^{3+}/Ce^{4+} atomic ratios.

Sample	Binding energy (eV)										$Ce^{3+}/(Ce^{3+}+Ce^{4+})$ (%)	Ce^{3+}/Ce^{4+}
	Ce $3d_{5/2}$					Ce $3d_{3/2}$						
	v_o	v	v'	v''	v'''	u_0	u	u'	u''	u'''		
Fib Co-5Ce	880.0	881.7	883.5	888.1	897.6	897.6	900.2	901.6	906.7	916.0	16.4	0.20
Fib Co-12Ce	880.6	881.7	883.9	887.9	897.4	898.0	900.0	901.8	906.4	915.9	14.3	0.17

** M = Mn or Ce*

3.6 Catalytic evaluations - Soot combustion (BE)

3.6.1 Comparison of different soot-to-catalyst contacts

As was done in Chapter I (Fig. 1.19), the bare support was first tested and compared using different types of soot-to-catalyst contact, in the combustion of soot. The procedure for obtaining these contacts was explained in the Experimental Section (Section 3.1). The results obtained for each contact are shown in Fig. 2.21 as CO_2 profiles as a function of the temperature. A very similar situation to Fib Ce is observed for Fib Co as active support. Loose contact mixture presents an activity close to that of the blank, meaning that the contact is poor, and the catalyst cannot act properly. When considering the wet contact mixture, the performance improves greatly, and finally for tight contact the best T_M value is achieved, being around 400 °C. As was previously discussed in Chapter I, the latter contact increases the contact points between the catalyst surface and soot particles, which in turn boosts the catalytic activity. The drawback of tight contact is the loss of the catalyst morphology (fibers in this case) which does not occur for wet contact. All catalytic tests in the next section (Section 3.6.2) were carried out using wet contact.

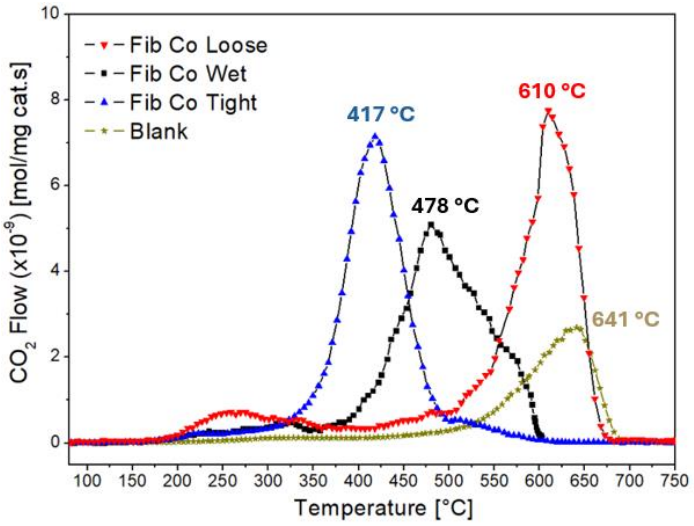

Fig. 2.21 - Comparison of soot-to-catalyst contact for Fib Co in soot combustion: tight, wet and loose contacts.

In the final Chapter of this thesis (Chapter IV), it will be proved that the differences between these types of contact is directly related to the intrinsic activity of the support used.

3.6.2 Soot combustion tests

The catalytic results obtained using wet catalyst-to-soot contact are shown in Fig. 2.22 where T_M values as a function of the metal content deposited are shown. CO_2 flow profiles normalized by the amount of catalyst used (per run), along with their corresponding soot conversion curves, are reported in Fig. 2.23. Also, T_{10}, T_{50}, T_{90}, and T_M values are summarized in Table 2.7.

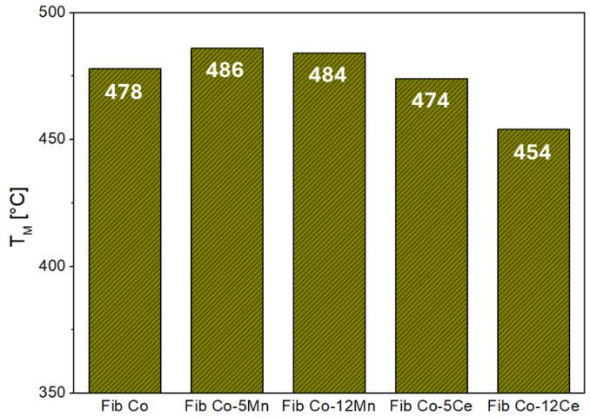

Fig. 2.22 - Maximum soot combustion rate temperatures (T_M) for Fib Co-Mn,Ce catalysts.

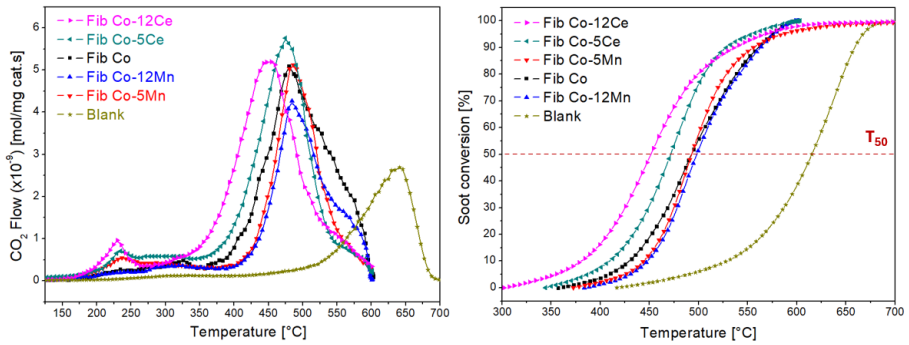

Fig. 2.23 - Catalytic activity of Fib Co-Mn,Ce catalysts for soot oxidation: CO_2 flow (left) and soot conversion profiles (right).

The T_M value obtained for the bare support was 478 °C. This value is 36 °C higher than the T_M value obtained for Fib Ce in Chapter I. Evidently, CeO_2 is intrinsically a more active phase than Co_3O_4 for the combustion of

soot, despite all the good properties of the spinel mentioned in the Introduction of this Chapter.

Both Mn-supported catalysts performed slightly worse than the support alone. This was not expected since MnO_x phases are commonly very active in this reaction [135,178]. Moreover, when increasing the amount from 5 to 12 wt.% Mn, the activity of this catalyst remained similar. From XRD results (Section 3.2), MnO_x phases were evident in Fib Co-12Mn, and it was mentioned that probably no solid solution was formed after the deposition of Mn. This can also be supported with Raman results. This scenario is opposite to what was seen in Chapter I (Mn was supported on Fib Ce), where MnO_x phases were absent in XRD diffractograms and there was evidence of solid solution formation. Probably, this is one reason why Fib Co-Mn catalysts did not perform well: a bad distribution (or segregation) of bulk MnO_x and no insertion of Mn inside the spinel structure. In terms of surface properties, both the Co^{3+}/Co^{2+} ratio and O_{ads} concentration decreased if compared to bare Fib Co, which could also negatively affect the performance of these catalysts.

Contrary to Mn-supported samples, the addition of CeO_2 to Fib Co enhanced the activity of the bare support. For 5 wt.% Ce, a slight improvement was seen, whereas for 12 wt.% Ce the increase in activity was notorious.

Both, for 5 wt.% and 12 wt.% Ce content, the segregation of CeO_2 was observed by XRD, although it was not possible to corroborate by Raman (signal overlapping).

For this series of catalysts, in comparison to Fib Co, three distinctive points from XPS results (Section 3.5) are worth recalling: i) Co^{3+}/Co^{2+} ratio suffered an increase, being higher for the lower Ce content; ii) the concentration of total Ce on the surface was considerably high, showing a great accumulation of this rare earth element, reaching an atomic ratio Ce/Co = 1 for Fib Co-12Ce; and iii) O_{ads}/Co ratio increased in great manner for both Ce amounts. All these factors might play a role under reaction conditions.

From the first point mentioned (i), a higher concentration of Co^{3+} could be correlated with a better reducibility of the support. This could help in the replenishment of oxygen vacancies by lattice oxygen from the support, and not only from gaseous oxygen (O_2 (g)). Also, the more amount of Co^{3+}, the more soot can be oxidized by this species (in addition to Ce^{4+} sites).

Following with the second point (ii), as stated in the Introduction of Chapter I, CeO_2 capacity of storing and releasing oxygen by its redox couple is a main advantage in the reaction of soot combustion, thus the

preferential accumulation of CeO_2 on the surface would expectedly help in reaction.

Lastly, the third point (iii) is connected to O_{ads} species which comprise very reactive oxygen species that can oxidize soot very efficiently. It has been mentioned that these species are the main responsible of conducting this reaction. However, in Chapter I this was not the case since the supported catalyst Fib Ce-5Mn increased the concentration of O_{ads} and the O_{ads}/Ce ratio but performed worse than the support alone. Thus, just increasing the O_{ads} species amount is not a guarantee for a better performance. The outcome of the reaction depends on several properties of the catalyst.

Table 2.7 - Catalytic activity of Fib Co-Mn,Ce catalysts in soot combustion.

Catalyst	T_{10} [°C]	T_{50} [°C]	T_{90} [°C]	T_M [°C]
Blank	528	615	659	641
Fib Co	429	492	560	478
Fib Co-5Mn	444	492	556	486
Fib Co-12Mn	448	498	564	484
Fib Co-5Ce	409	471	523	474
Fib Co-12Ce	380	451	537	454

3.7 Catalytic evaluations - Benzene oxidation (BE)

The results obtained in benzene oxidation tests, for all catalysts, are shown in Fig. 2.24 as conversion profiles. T_{10}, T_{50}, and T_{90} values are summarized in Table 2.8. Also, reaction rates (r) at 250 °C were calculated and added to Table 2.8.

The first thing worth noticing is that Fib Co performed appreciably better for benzene oxidation than Fib Ce (tested in Chapter I), showing a T_{50} value 75 °C lower (Fig. 2.25). This is proof that, if just bare active supports were to be compared, Fib Co would be a better candidate. Co_3O_4 spinel properties (such as good reducibility, and presence of oxygen vacancies and hydrophilic oxygen species) are preferable than those of CeO_2 fluorite in this reaction, differently to what happened for soot combustion. For CeO_2, the replenishment of oxygen vacancies by lattice oxygen is less probable due to its lower reducibility, which could negatively impact on benzene oxidation [179,180].

Unfortunately, Mn-supported samples experienced a similar situation as in soot combustion tests. The activity was notably worse as the Mn

content increased. Despite MnO_x phases being reported as very active for benzene oxidation, the bad performance of Fib Co-Mn samples was unexpected [35,73]. There is no contact influence in this case (gas phase reaction), thus the attribution to a worse performance depends just on the interaction of both phases (deposited metal oxides and support).

Regarding Ce-supported Fib Co, only a small increase in activity was attained in comparison to the support. T_{50} and T_{90} values were pretty similar for both Ce contents used, making the increase in Ce content redundant. The properties of these catalysts that were beneficial for soot combustion previously discussed, did not have a considerable effect on the oxidation of benzene. Again, this highlights the intrinsic difference between a three-phase and a two-phase reaction.

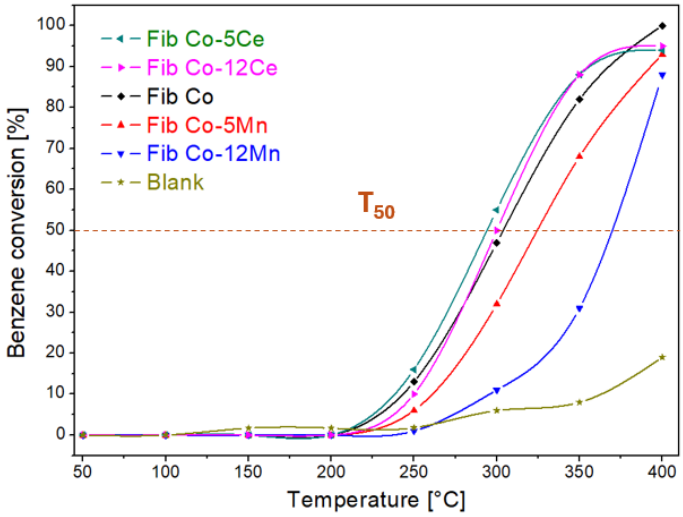

Fig. 2.24 - Benzene conversion profiles for Fib Co-Mn,Ce catalysts.

The tendency seen in Chapter I for supported Fib Ce in benzene oxidation tests in terms of oxygen species, was not followed by these catalysts: an increase in O_{latt} surface concentration favored the activity of Fib Ce-Mn and Fib Ce-Co, whereas it was detrimental for Fib Co-5Mn and Fib Co-12Mn catalysts. It could be possible that the MVK mechanism is not the preferred path of reaction followed by these specific catalysts and/or other properties affect to a greater extent the catalytic activity.

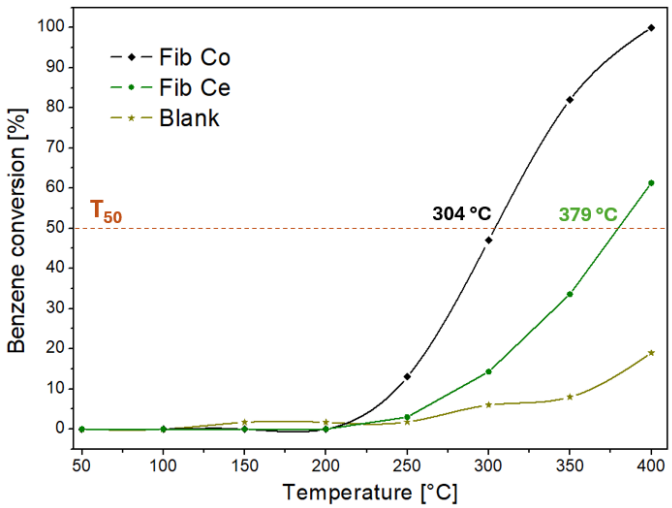

Fig. 2.25 - Benzene conversion profiles: comparison between Fib Ce and Fib Co.

Even though Fib Co performed better than Fib Ce as an active support (Fig. 2.25), when supported either with Mn or Ce (Fig. 2.24), it was not possible to boost its activity considerably, as was achieved for Fib Ce (Chapter I). Moreover, Mn-supported samples performed worse.

The formation of solid solutions between the Co_3O_4 support and the supported phases could play an important role in this reaction, and Fib Co did not show this property as clearly as Fib Ce did.

Table 2.8 - Catalytic activity of Fib Co-Mn,Ce catalysts in benzene oxidation.

Catalyst	T_{10} [°C]	T_{50} [°C]	T_{90} [°C]	r_{250}* [µmol Bz/g cat. s]
Blank	354	> 400	> 400	2.4E-4
Fib Co	237	304	368	1.8E-2
Fib Co-5Mn	257	325	394	8.2E-3
Fib Co-12Mn	294	367	> 400	1.4E-3
Fib Co-5Ce	230	293	357	2.2E-2
Fib Co-12Ce	250	300	357	1.4E-2

**** Reaction rate at T = 250 °C.***

4 Main findings

In this Chapter, pure Co_3O_4 biofibers (Fib Co) were prepared using cotton as biotemplate and then supported with Mn and Ce contents (5 or 12 wt.%) by wet impregnation.

The fibrous morphology was corroborated by SEM images and EDX analyses proved the presence of Mn and Ce on the support, showing a heterogeneous distribution of the elements on the fibers. This result is similar to that observed in Chapter I for supported CeO_2 fibers with Mn or Co.

The deposited phases were identified by XRD, where two Mn oxides (Mn_2O_3 and Mn_3O_4) were observed for Fib Co-12Mn, and the CeO_2 fluorite phase was clearly present for both Ce-supported samples (Fib Co-5Ce and Fib Co-12Ce). Contrary to what was observed in Chapter I when Mn was deposited on Fib Ce, MnO_x formed after impregnation on Fib Co could be detected by XRD. LRS and FTIR techniques complemented the identification of the support and supported phases and functional groups, respectively.

The surface enrichment of Mn or Ce on Fib Co was evident in XPS spectra, from which metal-to-cobalt ratios (M/Co) derived from this analysis were markedly higher than the nominal values, especially for Fib Co-Ce samples. This is another interesting difference with Chapter I, where the surface metal ratios were closer to the nominal ones.

Mn-supported samples performed worse in soot combustion than the bare support. This was correlated to a bad distribution MnO_x species on Fib Co, supported by XRD, which could result in a poor overall contact with soot particles. A decrease in Co^{3+}/Co^{2+} ratio on the surface, along with O_{ads} concentration, were also mentioned as possible factors to explain the bad activity. On the other hand, Ce-containing samples managed to decrease the T_M value of Fib Co, more notably for 12 wt.% (Fib Co-12Ce). These samples, in turn, showed a higher content of Co^{3+} and Ce/Co ratio, providing more active sites that can carry out the oxidation of soot particles.

Regarding benzene oxidation, Fib Co-Mn samples performed worse than Fib Co, drastically shifting the T_{50} to higher temperatures, specially for Fib Co-12Mn. In addition to the reasons mentioned before for soot combustion to explain the bad performance, it is interesting to note that Mn-supported samples showed a higher content of O_{latt}. Recalling Chapter I results, the well-performing catalysts exhibited increasing amounts of O_{latt}, and this was correlated to the MVK mechanism probably taking place. Thus, it could be deduced that this mechanism might not

be the preferred path of reaction followed by Fib Co-Mn studied in this Chapter. However, it is not possible to determine the reaction mechanism followed with the results presented here. On the other hand, the addition of Ce to Fib Co, slightly enhanced the activity of the bare support. This is not surprising in view of the results from Chapter I, where bare Fib Ce showed a poor activity.

When comparing benzene conversion curves of Chapters I and II (Figs. 1.23 and 2.24, respectively), it could be concluded that the intrinsic activity of bare Fib Co is markedly better than Fib Ce. However, the addition of either Mn or Co improved notably the activity of Fib Ce. Just by adding 5 wt.% of the active phase to Fib Ce (i.e. Fib Ce-5Mn or Fib Ce-5Co) is enough to match the activity of the best performing sample for supported Fib Co catalysts. Furthermore, when adding 12 wt.% of the active phase to Fib Ce (Fib Ce-12Mn or Fib Ce-12Co), conversion profiles shifted to even lower temperatures. This stands out the bad performance of Fib Co being used as support, both for this method of impregnation (WI) and for this reaction (benzene oxidation).

The different catalytic results observed here in both tested reactions, even though they are both oxidation reactions, exhibited the distinct behavior from catalysts towards three-phase (solid-solid-gas) and two-phase (solid-gas) reactions.

PART II - CHAPTER III

Plasma-assisted deposition of Mn and Fe phases on CeO_2 biofibers for soot and CO oxidation

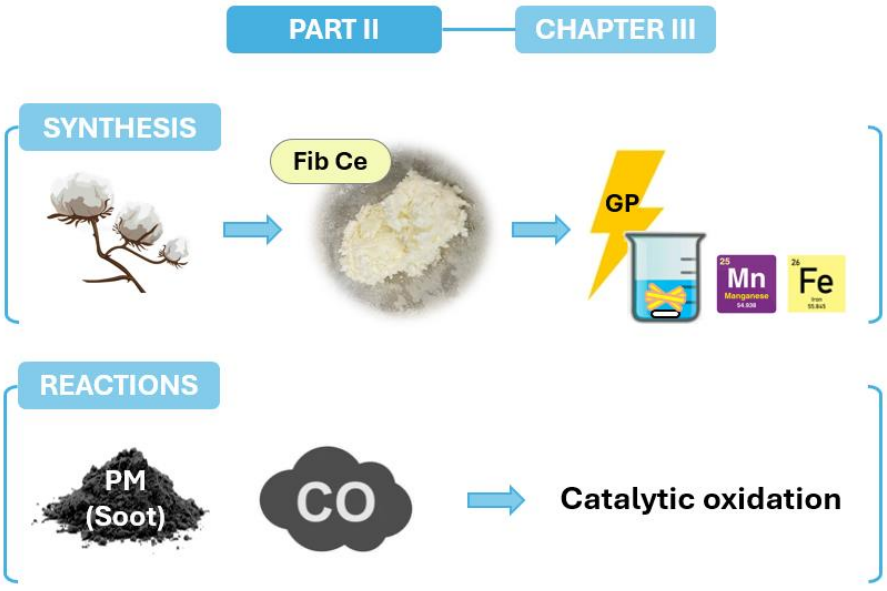

1 Introduction: Plasma-assisted deposition of Mn and Fe phases on CeO_2 biofibers for soot and CO oxidation

In this Chapter, a different deposition technique is explored - the glidarc plasma technique (GP) - which is a novel precipitation-deposition method and explored for the first time using fibrous supports as targets. This was possible thanks to previous studies carried out in the Belgian institute. The fundamentals of the technique were mentioned in the General Introduction (Section 1.5.2), and the reader is referred to this section to recap the concepts. In the Experimental Section (Section 1.1.3) the setup configuration and parameters used for all GP synthesis were detailed. The GP setup is very simple and runs under mild conditions, providing a facile way to obtain oxide precipitates from a solution.

The results presented in the starting section of this Chapter come from GP exposure of Mn or Fe precursor solutions alone. Next, the first attempts at exposing structured targets to GP were made. The materials used were ceramic papers (CP), a macro-structured material whose synthesis was already explained (Experimental Section - Section 1.2) and from which the Argentinean group posses experience. This was the original idea when this method was first considered. It had been reported the successful precipitation of metal oxides from precursors exposed to plasma [119,121,122,157]. Based on this, it was proposed that it could be worth exposing to GP a structured material with a high void fraction. In this hypothetical scenario, the nucleation of the precipitates could occur inside the CP (aside from the external surface) and, after drying and calcination steps, a structured catalyst with good distribution of the active phase, generated by plasma species, could be obtained. Unfortunately, these attempts were not successful, and this will be briefly shown in this Chapter.

After these unexpected results, a change from the original plan was needed. At this point, the decision to switch to isolated fibers (micro-structured supports) was taken. If these systems could be studied and optimized, then these same materials could be structured, for example, via the synthesis of CP presented before, altering the recipes by replacing ceramic or cellulosic fibers with the catalytic fibers obtained after exposure to GP. Other methods to structure the plasma-supported fibers are not discarded either.

PART II – CHAPTER III

Biomorphic ceria fibers (Fib Ce), synthesized in Chapter I, were chosen as the alternative, as these fibers acted as a good support for deposited phases and showed good catalytic performance, contrary to Fib Co in Chapter II. Fib Ce were immersed in two different precursor solutions (Mn or Fe) and exposed to GP. The resulting fibrous catalysts were characterized and tested in two oxidation reactions: soot and CO oxidation.

2 Abstract

Mn and Fe oxides were plasma-precipitated on a fibrous ceria support and evaluated in two reactions of environmental interest, (1) soot combustion and (2) CO oxidation. Pure CeO_2 fibers (Fib Ce) were obtained via the biotemplate route with the idea of starting from a support already active in oxidation reactions, and then further improving its activity by supporting on its surface Fe or Mn oxides. The precipitates were identified by XRD, FTIR and LRS, and their loadings and distributions were assessed by ICP and EDS respectively. α-Fe_2O_3 and Mn_3O_4 phases were detected. XPS confirmed the presence of Mn or Fe on the surface of Fib Ce and revealed that the deposition of Fe (Fe-Fib Ce) gave a superficial Fe/Ce ratio much higher than the bulk one, while it provoked an increase in Ce^{3+}/Ce^{4+} and O_{ads}/Ce ratios. On the contrary, Mn-supported sample (Mn-Fib Ce) did not affect considerably the Ce^{3+}/Ce^{4+} and O_{ads}/Ce surface ratios and presented a Mn/Ce ratio closer to that of the bulk. For reaction (1), the deposition of Fe by plasma drastically degraded the performance of the bare support, whereas Mn deposition greatly increased the activity of Fib Ce. The same activity order was observed for reaction (2): Mn-Fib Ce > Fib Ce > Fe-Fib Ce.

Most of the results presented in this Chapter were published in:

M. Rodriguez, S.A. Leonardi, F. Hanon, E.E. Miró, V.G. Milt, E.M. Gaigneaux, "Plasma-assisted deposition of Mn and Fe phases on CeO_2 biomorphic fibers for soot combustion and CO oxidation", Catalysis Today 431 (2024).

https://doi.org/10.1016/j.cattod.2023.114457.

3 Setting up the GP technique

3.1 Precipitation of Mn and Fe oxides

In order to start studying the GP system, the first step needed was to expose precursors alone, either $KMnO_4$ (KMO) or Mohr's salt (AFS). Even though some authors have reported the use of this technique, it was important to corroborate whether the precipitates would be formed or not with the current setup conditions, using parameters reported elsewhere [157,181].

In addition to this, the necessity of creating a new methodology in which a lower amount of liquid is used was crucial. Bearing in mind that either small pieces of CP or low amounts of fibers were going to be exposed (i.e. no more than 250 mg), the use of the reactor at its maximum capacity (300 mL) was impractical for sample manipulation and recovery. The chosen approach was to place inside the glass reactor either a Petri dish for CP disks, or a beaker (250 mL) for fibers. Fig. 3.1 illustrates the formation of KMO precipitate (KMO ppt) using the full reactor (Fig. 3.1 - a,b) or a beaker with a lower amount of solution (Fig. 3.1 - c,d) prior and after exposition to GP.

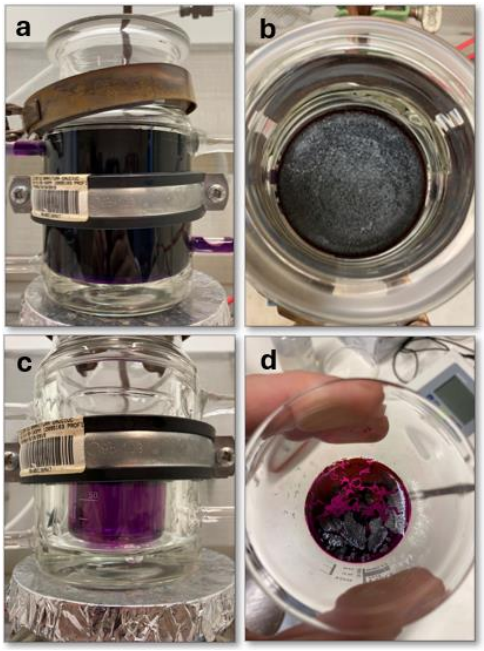

Fig. 3.1 - $KMnO_4$ solution (KMO) as target exposed to glidarc plasma (GP) using different volumes: 300 mL with KMO prior (a) and after (b) GP exposure, and beaker with KMO prior (c) and after (d) GP exposure.

The first evaluations were done using four different precursor volumes: 25, 50, 100, and 300 mL (full reactor). In Fig. 3.2, the amounts of KMO ppt (manganese oxides) obtained after its separation from the liquid, drying and calcination (as explained in the Experimental Section - Section 1.1.3), are reported. Although no linear relation is seen, the amount of KMO ppt increased as the volume of precursor solution did, which could be ascribed to the proximity of the plasma plume to the liquid surface. Interestingly, there is not much difference between exposing 50 mL and 100 mL, as would be expected.

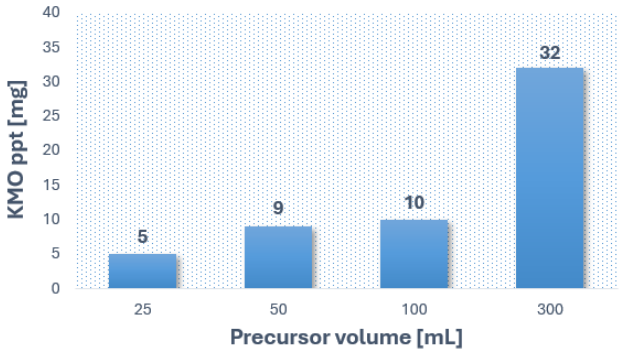

Fig. 3.2 - Amount of precipitate obtained (KMO ppt) as a function of the volume of precursor solution (KMO) used.

As regards the second precursor (AFS), the changes before and after GP exposure for two different volumes are depicted in Fig. 3.3. The change in color to a dark orange denotes the formation of AFS ppt.

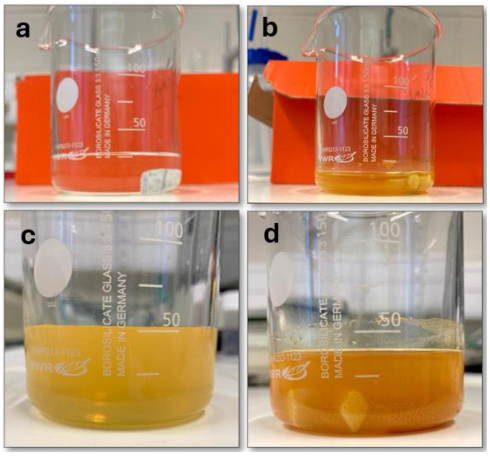

Fig. 3.3 - Mohr's salt solution (AFS) as target exposed to glidarc plasma (GP) using different volumes: 25 mL of AFS prior (a) and after (b) GP exposure, and 50 mL of AFS prior (c) and after (d) GP exposure.

As was done for the previous precursor, four different solution volumes were exposed and their corresponding amounts of AFS ppt obtained are presented in Fig. 3.4. In this case, bigger amounts of precipitates were obtained for the same volumes.

The physical appearance of both calcined precipitates can be seen in Fig. 3.5.

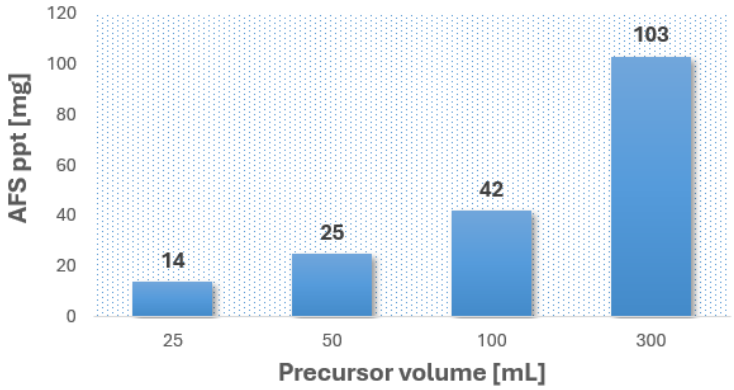

Fig. 3.4 - Amount of precipitate obtained (AFS ppt) as a function of the volume of precursor solution (AFS) used.

Fig. 3.5 - Images of calcined precipitates obtained by GP exposing Mn or Fe precursor solutions: KMO ppt (left) and AFS ppt (right).

At this point, the conditions to produce KMO ppt and AFS ppt via GP are guaranteed. Also, the expected quantities of precipitates to be formed for different volumes exposed can be estimated. From this information, an amount of Mn and Fe precipitates that will form can be approximated for the volumes of precursor solutions chosen for the synthesis. These amounts will be referred as “nominal” contents throughout the rest of the document and are calculated after phase identification by XRD (Chapter III - Section 4.1).

3.2 Deposition of Mn oxide on ceramic papers

The ceramic papers (CP) were never treated under wet conditions for long periods of time (they were only humidified during wet impregnation processes for the incorporation of catalytic precursors). Therefore, before immersing these structures in aqueous solutions and subjecting them to the gliding arc plasma, it was essential to test the resistance of the CP in wet conditions. The procedure followed for the immersion tests was explained in the Experimental Section - Section 1.2.

The histogram in Fig. 3.6 shows the mass retention percentages (Y axis) for three different samples, for both pH values and times applied. The "Pos" formulations had the greatest mass retention, being higher for 20% Ce sample. The posterior addition of binder helps at maintaining better the CP structure. The "Pre" sample showed a mass retention higher than 96% which is still a great outcome. No big differences in mass loss are observed for the different pH values and times used. This simple test indicated that these materials can be immersed in other solutions without suffering any considerable mass loss.

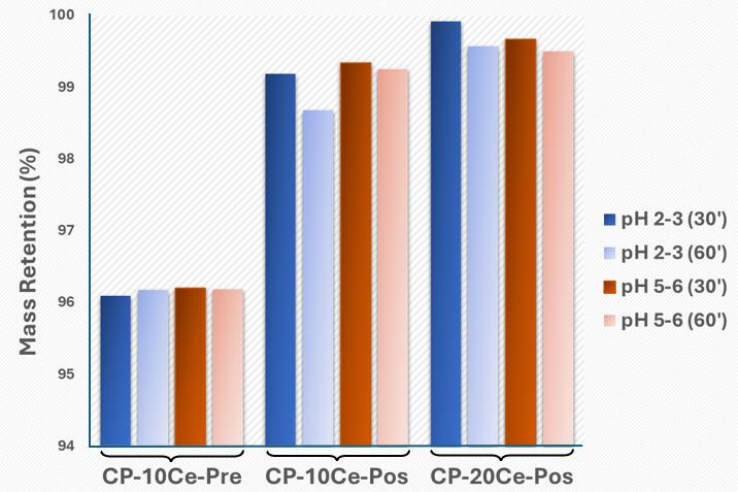

Fig. 3.6 - Immersion tests of ceramic papers (CP): mass retention varying immersion time and pH values.

Even though CP-Pre had a lower mass retention, these formulations showed a better distribution of Ce inside the structure in comparison to CP-Pos as their images show (Fig. 3.7). Fig. 3.7 - c exposes the cracks on the top layer of a CP-Pos disk. The red arrow in Fig. 3.7 - d, evidences the lack of binder along the entire thickness of the CP structure. Based on this, the Pre formulation would be preferred since it presents a better distribution of the binder.

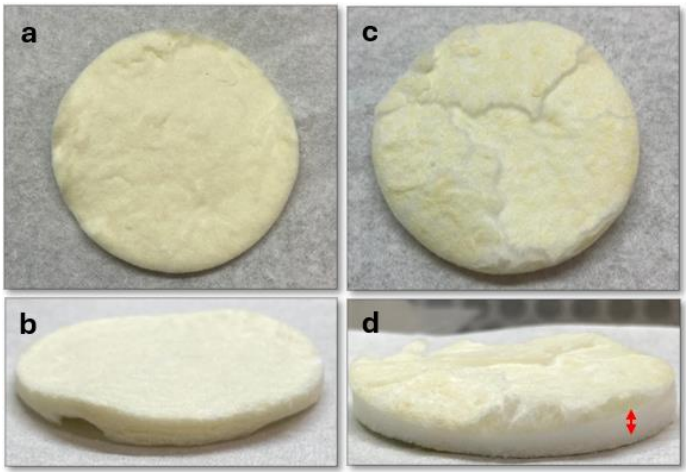

Fig. 3.7 - Top and lateral views of CP impregnated with CeO_2 binder either during the CP preparation or after: CP-Pre (a,b) and CP-Pos (c,d). The red arrow indicates the thickness of the CP disk.

Next, the CP were tried as support for catalysts by the GP technique. To this end, a few small CP disks were placed in a Petri dish, then covered by KMO solution, and exposed to GP. The concentration of KMO solution was the same as that used for the precursor alone.

After the GP exposure, the surplus solution was carefully removed with a Pasteur pipette, and the disks were dried at 2 h 110 °C and calcined 2 h 600 °C. The whole sequence is illustrated in Fig. 3.8. KMO ppt is mostly present on the surface of the CP, and only on the top layer. No precipitate was seen on the bottom face of these disks nor inside them when cutting them open (Fig. 3.8 - c,d). The first issue could be solved by flipping the disks over and repeating the experience, but the main problem is that the precipitate does not nucleate inside the structure, as it was expected to happen. The nucleation process through which the precipitate is formed could be mostly taking place in the liquid surface close to the plasma plume.

Stirring is believed to aid greatly the performance of GP by helping to distribute the active species that reach the liquid surface (close to the plume). In this scenario, the precipitation could occur in the totality of the liquid and not just on the very surface. However, a big constraint for these experiments is the fact that no magnetic stirring can be used during GP tests since this would probably damage the CP structure.

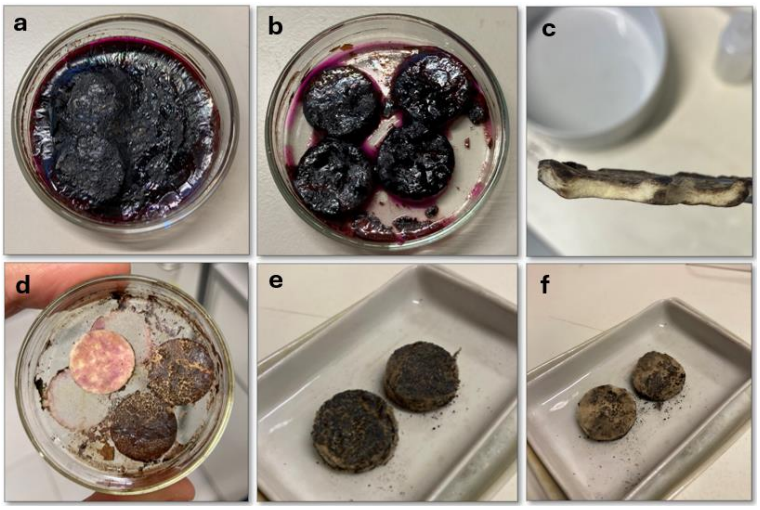

Fig. 3.8 - KMO precipitation on CP by GP: a) immersed CP disks after GP exposure; b) KMO surplus removed; c) cross-section view of a dried-cut exposed CP; d) bottom side of dried disks; e) calcined disks; f) drip wet-impregnated calcined disks.

As an alternative, to favor the precipitation throughout the CP structure, some disks were drip-impregnated with KMO solution until saturation and then exposed to GP. In this way, the absence of free liquid phase could guarantee the precipitation on the CP alone. However, as Fig. 3.8 - f shows, a heterogeneous distribution of KMO ppt, loosely attached, is clearly observed on the calcined CP disks.

Another variable that had been modified was the distance of the Petri dish from the plume, but it was found that the closer it was, the worse the stability of the plume. This made it impossible to keep the GP on for the time needed.

All these drawbacks, added to the challenging manipulation of these materials in wet conditions, made the plasma-deposition of CP not promising or achievable.

Specific modifications to the GP setup should be made in order to make possible the stirring of the solution while maintaining the structure of the CP. For example, to place a small basket where the CP is placed and separated from the stirrer or bubbling gaseous nitrogen inside the reactor. These lines of research remain open for future work.

Having reached this point, another course of action was taken. In the following section, the deposition of oxides by GP on isolated micro-fibers will be described.

3.3 Deposition of Mn or Fe oxides on biomorphic fibers

After the unsuccessful attempts with CP, isolated fibers were tried next. All parameters and procedure followed for the plasma-deposition of Mn and Fe species on Fib Ce are detailed in the Experimental Section (Section 1.1.3).

For Mn precipitation-deposition, two batches of 50 mL KMO and 125 mg Fib Ce were exposed to GP consecutively. This equals to one batch with 100 mL KMO and 250 mg Fib Ce, as mentioned in the synthesis procedure. This decision was taken based on the results shown above in Section 3.1. After centrifugation, both batches were placed together in a crucible prior to drying and calcination. This was done in order to achieve more Mn content on the final catalyst. For AFS exposure, only one batch of 100 mL AFS and 250 mg Fib Ce was used.

The whole contents of the beakers exposed to GP (targets), recovered from the reactor, and after centrifugation, are shown in Fig. 3.9 - a,c. The physical appearance of Mn or Fe oxides supported on Fib Ce (after calcination) can be seen in Fig. 3.9 - b,d.

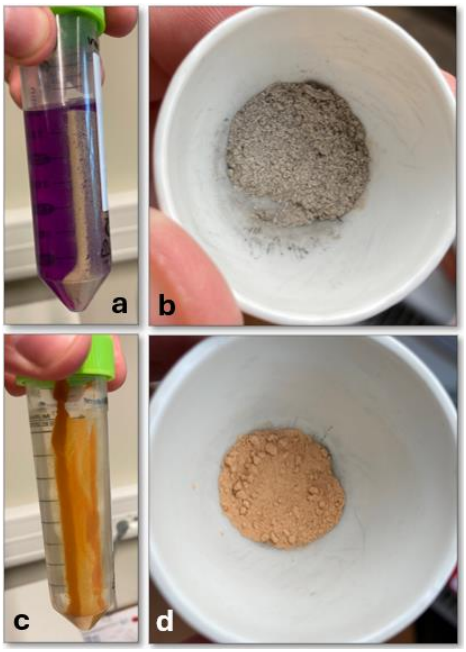

Fig. 3.9 - Deposition of KMO ppt (a,b) and AFS ppt (c,d) on Fib Ce by GP. Centrifugated solid-liquid mixtures after GP exposure (a,c). Calcined samples (b,d).

In these systems, the possibility of stirring the liquid along with the fibers makes it more efficient than with CP (as previously discussed). It homogenizes the distribution of plasma-generated species reaching the liquid surface and the precipitates throughout all the fibers. As Fig. 3.9 shows, the plasma-deposition of Mn or Fe phases on a fibrous support (Fib Ce) appears to be successful.

Starting from next section, several techniques are used to characterize the precipitates, the support, and supported samples obtained.

4 Results and discussion

4.1 XRD analyses (BE)

The diffractograms of the isolated precipitates and plasma-supported Fib Ce are shown in Figs. 3.10 and 3.11. The pattern of the precipitate obtained from KMO (KMO ppt) matched with the pure tetragonal hausmannite phase Mn_3O_4 (JCPDS 24-0734) [145,167], whereas the precipitate from AFS (AFS ppt) matched with the rhombohedral hematite phase α-Fe_2O_3 (JCPDS 33-0664) (Fig. 3.10) [182,183]. As a result of phase identifications and considering that the amount of precipitates with or without the presence of fibers in the beaker is the same, now it is possible to calculate nominal atomic or mass ratios (M/Ce), where M = Mn or Fe (Table 3.1).

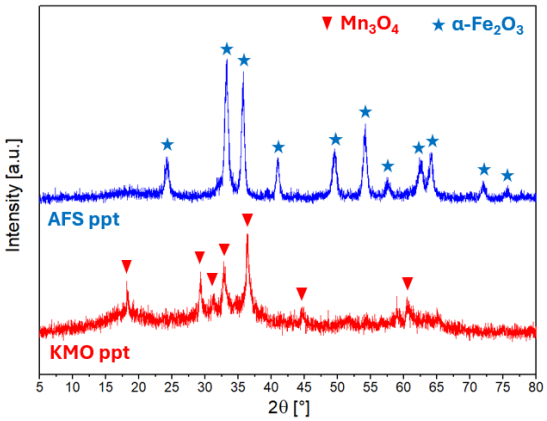

Fig. 3.10 - Diffractograms of precipitates obtained from KMO or AFS precursors salts.

Bare Fib Ce (Fig. 3.11) present the characteristic peaks associated to the cubic fluorite structure (JCPDS 34-0394) [148,168]. These are clearly maintained after the fibers were exposed to the plasma. After Mn deposition, no signals can be seen from MnO_x species, which could be explained by a good distribution of this phase or being the amount or the size of the deposited crystallites below the detection limit of the technique (< 4 nm). An amorphous precipitate is ruled out based on the crystallinity seen on KMO ppt as the same precipitate is expected to be formed (Fig. 3.10). Another important fact that has been reported about Mn-Ce systems is that MnO_x signals are only appreciable for molar ratios Mn/Ce > 3, being only 0.16 (nominal ratio) for Mn-Fib Ce (Table 3.1) [75,138]. For Fe-Fib Ce, two small broad peaks can be seen at 2θ = 35.6

and 54 ° coming from α-Fe_2O_3 phase, being its most intense signal at 33.2 ° probably overlapped by the CeO_2 peak.

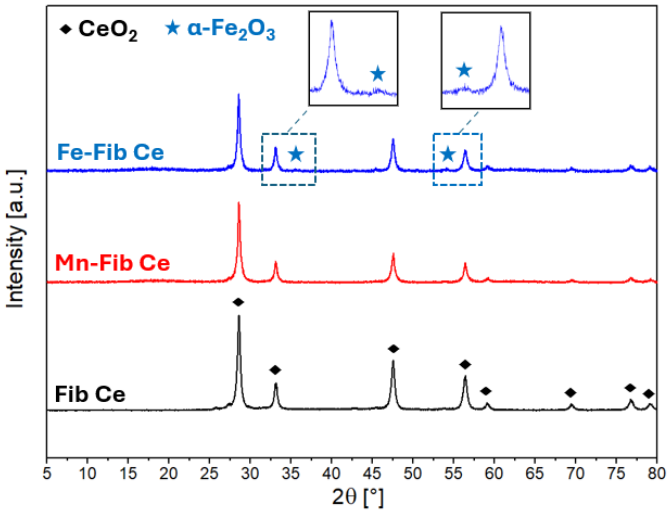

Fig. 3.11 - Diffractograms of plasma-supported fibers.

4.2 SEM and EDS analyses (AR)

Scanning electron microscopy (SEM) was performed to study the morphology of the synthesized catalysts. All images shown in this section correspond to fresh catalysts.

Fig. 3.12 brings back two images from Chapter I, where the change from commercial cotton to Fib Ce is evidenced. To avoid repetition, the reader is referred back to Chapter I - Section 3.1, for more images and a detailed description of Fib Ce.

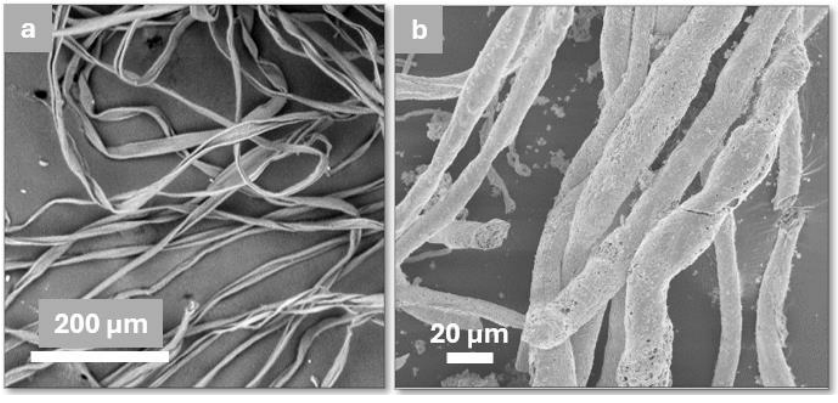

Fig. 3.12 - SEM images of commercial cotton (a) and Fib Ce (b) (Chapter I).

After Mn and Fe deposition on Fib Ce by GP (Fig. 3.13 - a, Fig. 3.14 - a), the fibers are shortened (comparing to Fib Ce) probably due to the stirring applied in the beaker during plasma exposure, the effect of plasma itself, and/or sample manipulation. Their lengths now range from 20 to 100 μm and diameters from 5 to 20 μm (average values determined by measuring at least 50 fibers).

Energy-dispersive X-ray (EDS) analysis helped to corroborate the presence of the supported species on the fibrous support. As performed in previous chapters (Chapters I and II), spot (Fig. 3.13 - c, Fig. 3.14 - c), mapping (Fig. 3.13 - d, Fig. 3.14 - d), and big area mappings (Fig. 3.13 - b, Fig. 3.14 - b) analyses were carried out. All values obtained are summarized as atomic ratios (Fe/Ce or Mn/Ce) in Table 3.1. The nominal weight percentages of precipitates deposited on Fib Ce were close to those reported by ICP analyses (Table 3.1). Mn and Fe can evidently be seen on the corresponding metal-Fib Ce (Fig. 3.13 - d, Fig. 3.14 - d), however the values given by EDS showed a heterogeneous distribution of these elements. Zonal analysis averages are three and four times lower than the bulk ones (obtained by ICP), for Mn-Fib Ce and Fe-Fib Ce, respectively. Mappings followed the same trend. This means that not all the precipitate was formed on (and/or attached to) the fibrous support during the deposition, and that the rest probably remained isolated or trapped between fibers.

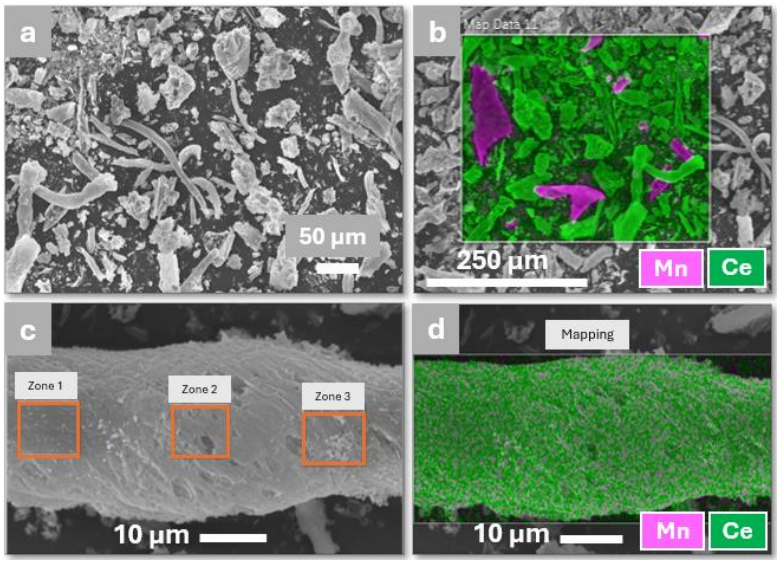

Fig. 3.13 - SEM images and zonal and mapping EDS analyses for Mn-Fib Ce; a) SEM image, b) big mapping; c) zonal; d) mapping.

This is corroborated by the quantification of the big areas (Fig. 3.13 - b, Fig. 3.14 - b), where the contents of Mn and Fe were really close to the bulk ones. Interestingly, no signals due to MnO_x phases were seen in the diffractogram of Mn-Fib Ce (for repeated tests as well), which would be expected when looking at Fig. 3.13 - b, despite the possible reasons mentioned before. It is worth considering that the depth of EDS analysis is around 1 μm and does not involve the entire fiber volume.

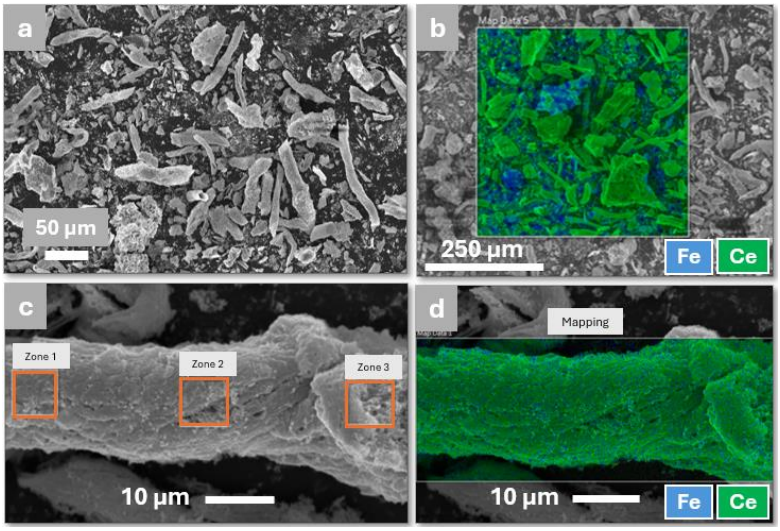

Fig. 3.14 - SEM images and zonal and mapping EDS analyses for Fe-Fib Ce; a) SEM image, b) big mapping; c) zonal; d) mapping.

In view of the above results, it can be inferred that the precipitation of metal oxides when using the glidarc technique can occur in both the homogeneous liquid phase and also on the biomorphic support. Since the latter presents intrinsic irregularities and defects owing to the preparation method, it is expected that the nucleation might take place in preferential sites throughout the fibrous structure. This inevitably provokes a heterogeneous distribution of the plasma-assisted precipitates. Indeed, as reported, from the competition between homogeneous and heterogeneous nucleation, the second one is favored due to its lower activation energy [184].

Table 3.1 - Mn/Ce and Fe/Ce atomic ratios for zonal and mapping EDS analyses.

Sample	M*/Ce atomic ratios								
	Fiber N° (**)	Zone 1 (Spot)	Zone 2 (Spot)	Zone 3 (Spot)	Average per fiber (Zones 1, 2 and 3)	Spot average	Mapping per fiber	Big area Mapping, Fig. 12 and 13 - b (wt. % - ICP)	Nominal (wt. %)
Mn-Fib Ce	1	0.01	0.02	0.02	0.02	0.04	0.02	0.14 (3.3)	0.16 (4.8)
	2	0.06	0.09	0.04	0.06		0.08		
	3	0.03	0.03	0.03	0.03		0.04		
Fe-Fib Ce	1	0.05	0.06	0.06	0.06	0.08	0.07	0.31 (9.4)	0.35 (9.9)
	2	0.07	0.08	0.08	0.08		0.11		
	3	0.09	0.09	0.11	0.10		0.14		

** M = Mn or Fe*

*** Three fibers per sample were analyzed*

4.3 TEM analyses (AR)

Fig. 3.15 shows both TEM images of the fibrous catalysts synthesized and the histograms that display particle-size distributions. In the case of the bare fibers (Fib Ce) elongated hexagonal prism-shaped particles around 51 nm average size were observed (Fig. 3.15 - a,b,c), whereas the sample containing Mn (Mn-Fib Ce) presents smaller rounded-edged particles 8 nm size (Fig. 3.15 - d,e,f). For the catalyst containing Fe (Fe-Fib Ce), besides ceria particles, more spherical particles 29 nm average size are observed (Fig. 3.15 - g, h,i).

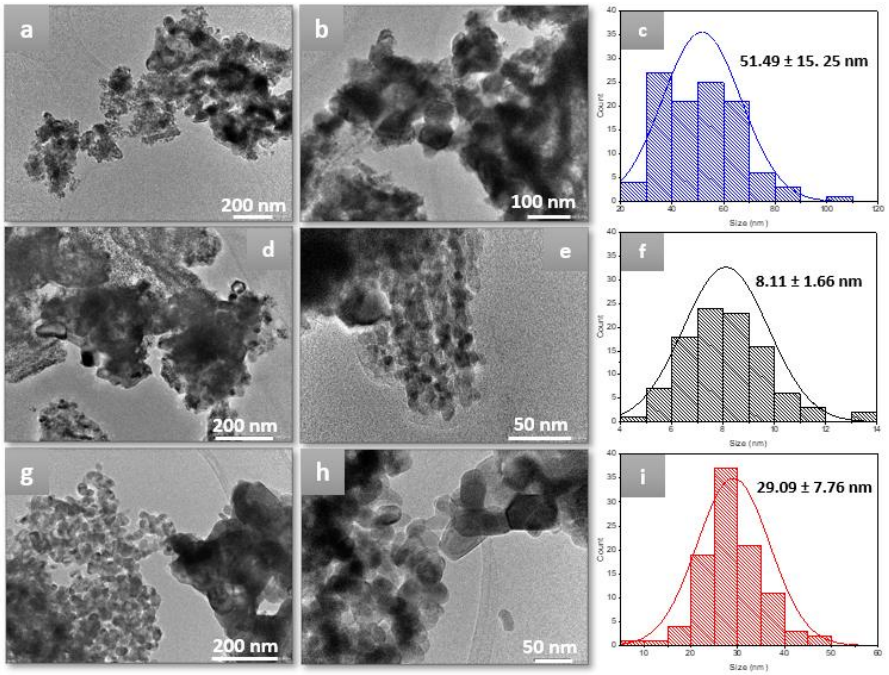

Fig. 3.15 - TEM images of CeO_2 in Fib Ce (a, b), Mn_3O_4 in Mn-Fib Ce (d, e) and Fe_2O_3 in Fe-Fib Ce (g, h), and the corresponding particle size distributions (c, f, i).

As TEM-EDS mappings show (Fig. 3.16), both Mn (Fig. 3.16 - c) and Fe (Fig. 3.16 - f) appear well distributed on ceria particles. The higher intensity of Fe signals (Fig. 3.16 - f), if compared to Mn ones (Fig. 3.16 - c), comes from the higher content of Fe (Table 3.1).

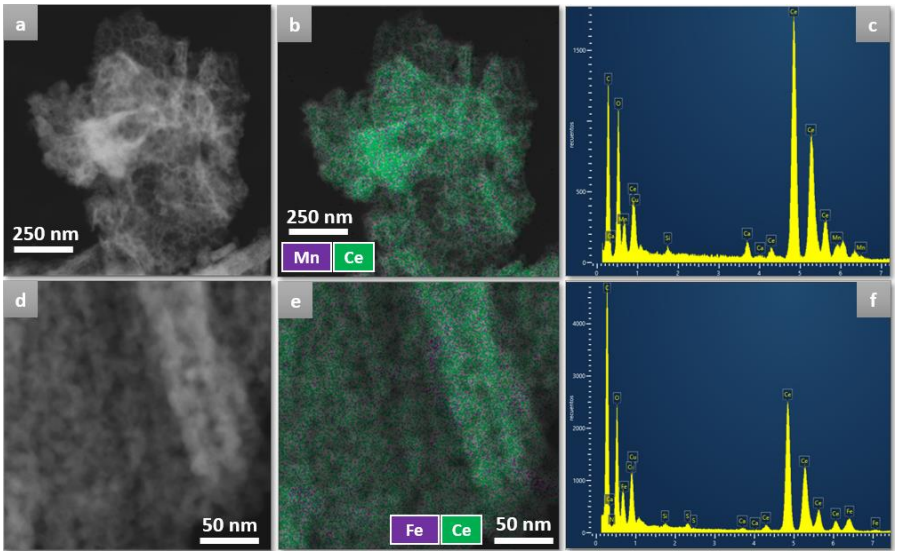

Fig. 3.16 - TEM-EDS mapping images of Mn-Fib Ce (a, b) and Fe-Fib Ce (d, e), and their corresponding EDS spectra (c, f).

4.4 FTIR-ATR analyses (BE)

FTIR-ATR spectroscopy was carried out to further characterize the surface of the prepared catalysts. The analysis was done both on the bulk precipitates (KMO ppt and AFS ppt) and the supported fibers (Figs. 3.17 and 3.18, respectively). All samples had two signals in common: a broad band around 3400 cm^{-1} due to -OH stretching and a low intensity peak at 1640 cm^{-1} from H-O-H bending vibrations, both from physisorbed water.

The spectrum corresponding to KMO ppt (Fig. 3.17) shows, in the metal-oxygen region, two signals at 611 and 490 cm^{-1} corresponding to the vibration of Mn species in tetrahedral (Mn^{2+}) and octahedral (Mn^{3+}) sites in the Mn_3O_4 spinel, respectively [145,167,185]. In addition, this sample has weak broad bands at around 1530 and 1400 cm^{-1}, associated to adsorbed monodentate and bridged carbonates [143]. On the contrary, AFS ppt does not show the presence of carbonate bands, but a broad band around 1140 cm^{-1} attributed to sulphate species [186], which are probably remaining amounts of Mohr's salt precursor. The absence of carbonates could be explained by a displacement of this species by the sulphates (the same occurring for plasma-supported samples, Fig. 3.18) [187]. Furthermore, two prominent peaks are present at lower wavenumbers, at 521 and 436 cm^{-1}, which correspond to Fe-O stretching vibrations from α-Fe_2O_3 phase, along with a clear shoulder around 580 cm^{-1} from Fe_3O_4 phase [182,188]. Band positions and their assignment are listed in Table 3.2.

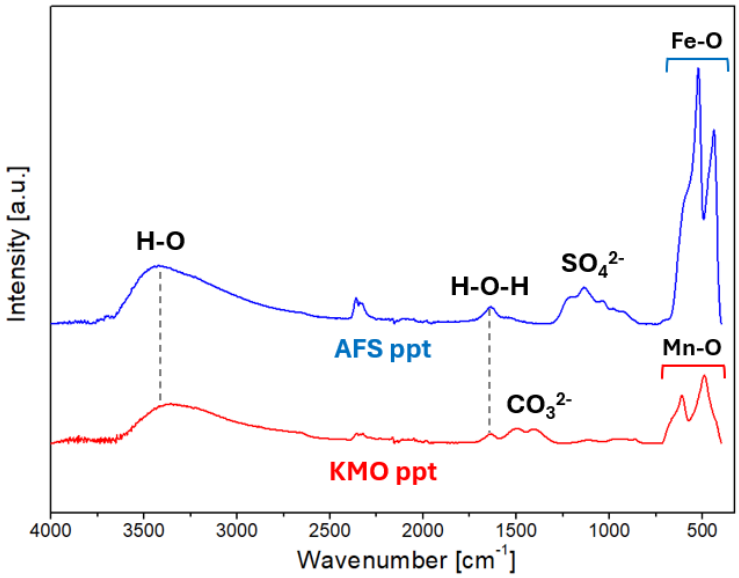

Fig. 3.17 - FTIR-ATR spectra of KMO ppt and AFS ppt.

Regarding the fibrous catalysts (Fig. 3.18), for the bare support (Fib Ce) it is evident that there is a greater contribution from surface carbonates (monodentate) at 1532, 1325 and 1065 cm^{-1}, which comes from the template decomposition. Also, two maxima in the metal-oxygen region are present at 568 and 467 cm^{-1}, which are assigned to Ce-O vibrations [144,189]. The contribution of these signals can be seen on the supported samples as well. For Mn-Fib Ce, the peak from KMO ppt around 490 cm^{-1} appears slightly, but a new signal around 430 cm^{-1} is now clear. The latter is another characteristic band from Mn^{3+} species in an octahedral site in Mn_3O_4, which is barely seen as a shoulder for KMO ppt [145,167,185]. On the other hand, the spectrum of Fe-Fib Ce clearly shows the signals corresponding to Fe-O bonds (idem Fig. 3.17).

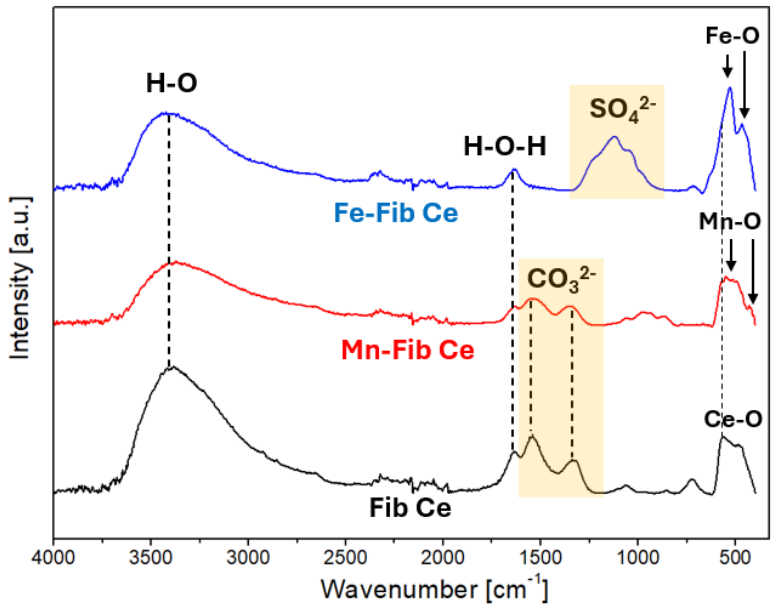

Fig. 3.18 - FTIR-ATR spectra of plasma-supported fibers.

Table 3.2 - Summary of all assigned FTIR-ATR signals.

Band position [cm^{-1}]	Assignment
3400, 1640	-OH, H-O-H (physisorbed water)
1530, 1400, 1325, 1065	Adsorbed carbonates (monodentate or bridged)
1140	Sulphate (SO_4^{2-})
611, 490, 430	Mn-O
580, 521, 436	Fe-O
568, 467	Ce-O

4.5 LRS analyses (AR)

Laser Raman spectroscopy was used to study the interaction between the support and the supported metal oxides and also helps in the phase assignment of the latter. The spectra obtained for all catalysts are depicted in Fig. 3.19.

The bare support (Fib Ce) shows a very intense peak at 463 cm^{-1} assigned to a first order scattering F_{2g} active mode of the fluorite phase [147,168]. Both supported samples exhibit this signal, but its intensity decreases considerably, which highlights the influence of Mn and Fe species on Ce-O scattering.

In Mn-Fib Ce sample, a broad peak can be noticed at about 640 cm^{-1} (inset) which is characteristic of the A_{1g} mode from Mn-O breathing vibration of Mn^{2+} species in tetrahedral coordination inside Mn_3O_4 spinel [150,167].

In the case of the Fe-containing sample, the signal at 228 cm^{-1} is assigned to the A_{1g} mode, while the peaks 228, 295 and 414 cm^{-1} to the E_{1g} mode, all of them due to α-Fe_2O_3 phase [182,188].

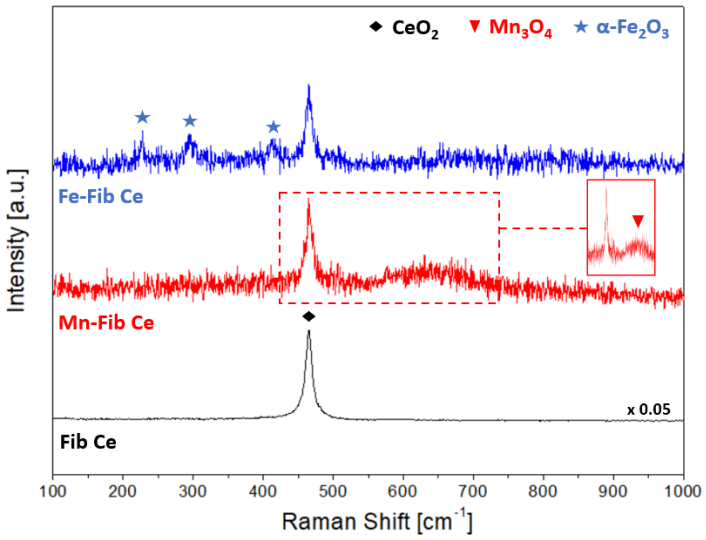

Fig. 3.19 - LRS spectra of plasma-supported samples.

These results further confirm that the precipitates generated in the presence of the Ce-fibrous support are the same as those produced without it (precipitate powders, ppt).

4.6 Surface analyses by XPS (AR)

To obtain more information about the surface of the catalysts, XPS measurements were carried out. Core levels C 1s, O 1s, Ce 3d, Mn 3s, Mn 2p, and Fe 2p, were studied, correspondingly.

Apart from the main signal of C 1s (C-(C,H)) at 284.6 eV (reference), another peak is present at higher binding energies around 288.6 eV which is related to carbonate species. These signals are common for all supported samples and precipitates (Fig. 3.20 - a,b). For KMO ppt, two extra peaks appear in the range of 291-298 eV which show the presence of K on the surface of the precipitate (Fig. 3.20 - left). Therefore, the presence of K-MnO_x species should not be discarded (not clearly evident by XRD). This is not the case for Mn-Fib Ce sample, probably due to K being in very low quantity (Fig. 3.20 - right).

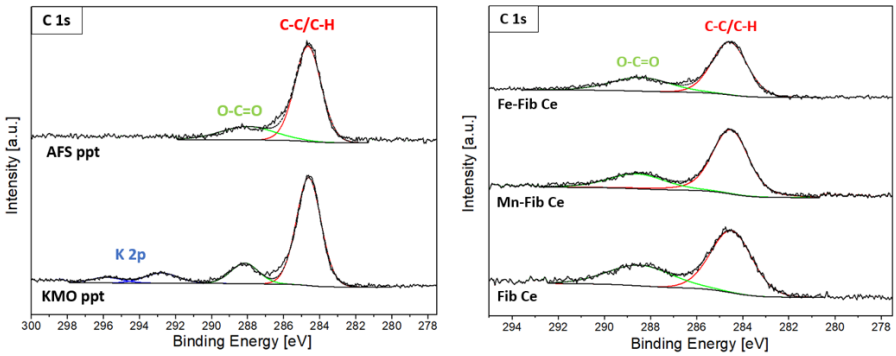

Fig. 3.20 - Surface analysis (XPS) of bare precipitates (left) and plasma-supported samples (right): C 1s region and deconvolutions.

Concerning Ce 3d region, all catalysts were fitted using ten peaks (Fig. 3.21) [64,156,177]. Peaks u’’’, u’’, u, v’’’, v’’, and v, match to Ce^{4+} species; while peaks u’, u^0, v’, v^0, correspond to Ce^{3+} species. Table 3.3 shows the values of binding energies corresponding to the different signals, along with Ce^{3+}/Ce^{4+}, Mn/Ce, and Fe/Ce atomic ratios, for all three catalysts. Table 3.4 provides details concerning the peak deconvolution for Fib Ce and plasma-supported fibers were done following the same approach. The addition of Mn to Fib Ce decreased the Ce^{3+}/Ce^{4+} ratio, whereas the Mn/Ce ratio is about 1.7 times higher than that obtained by ICP (bulk). On the other hand, when Fe was supported, the contribution of Ce^{3+} on the surface is higher than that of Fib Ce, and therefore Ce^{3+}/Ce^{4+} ratio as well. The percentage of Ce^{3+} is often related to the presence of defects and oxygen vacancies on the surface, which could promote the chemisorption of oxygen [69]. Also, the surface Fe/Ce ratio is 1.5 times

higher than that of the bulk (ICP) which confirms the preferential presence of Fe on the surface (Table 3.3).

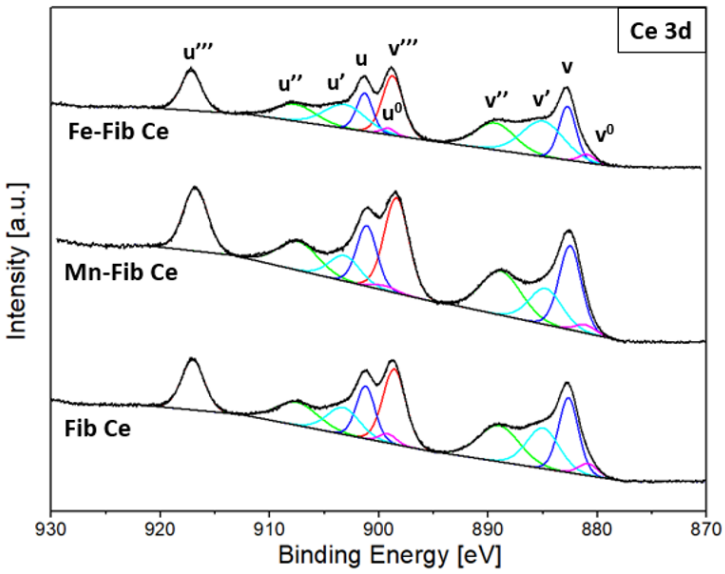

Fig. 3.21 - Surface analysis of plasma-supported samples (XPS): Ce 3d core level regions and deconvolutions.

As regard to O 1s core level, the spectra were deconvoluted in three peaks (Fig. 3.22). The most intense peak around 529 eV (O_{latt}) is assigned to lattice oxygen; the following peak near 531.5 eV (O_{ads}) is due to chemisorbed oxygen species (O_2^-, O_2^{2-}, O^-, CO_3^{2-}); and the last broad peak around 533 eV (O_w) corresponds to oxygen from water molecules [79,93]. All exact values are listed in Table 3.5. It is worth noticing that the signals corresponding to Fe-Fib Ce experienced a small shift to higher binding energies, showing the interaction between α-Fe_2O_3 and CeO_2. Moreover, after Fe deposition, the amount of O_{ads} increased by two in comparison to Fib Ce, whereas O_{ads}/Ce atomic ratio increased by three. This could be explained considering that the presence of Fe can enhance the reduction from Ce^{4+} to Ce^{3+}, thus increasing the concentration of adsorbed oxygen species. Contrariwise, Mn-Fib Ce did not have its amount of O_{ads} considerably affected and has a slightly increased O_{ads}/Ce ratio.

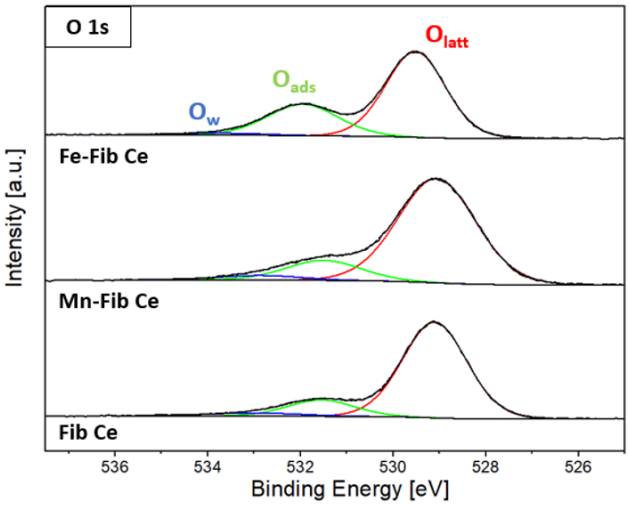

Fig. 3.22 - Surface analysis of plasma-supported samples (XPS): O 1s core level regions and deconvolutions.

For KMO ppt and Mn-Fib Ce, Mn 3s and Mn 2p core levels were analyzed. The region of Mn 3s exhibits two peaks due to multiple splitting effects (Fig. 3.23). As previously done, the separation of these peaks (ΔBE) was used to determine the average oxidation state (AOS) of bulk Mn, by means of Equation 3.1, as reported elsewhere [157,176].

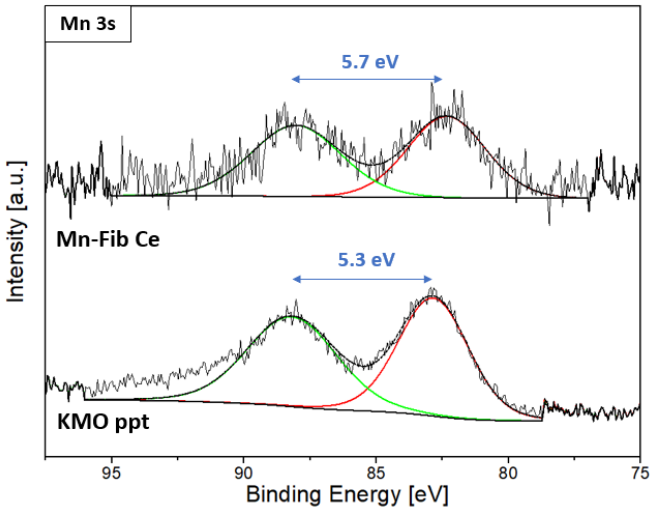

Fig. 3.23 - Surface analysis of plasma-supported samples (XPS): Mn 3s core level regions and deconvolutions.

The ΔBE value is around 5.3 and 5.7 eV for KMO ppt and Mn-Fib Ce, respectively (Fig. 3.23). These peak separation values are in accordance with Mn_3O_4 spinel phase [190].

$$AOS = 9.67 - 1.27.\Delta BE \qquad \textit{Equation 3.1}$$

Applying this equation, an AOS of 2.9 and 2.45 are obtained for KMO ppt and Mn-Fib Ce, respectively. The theoretical AOS of Mn in Mn_3O_4 is 2.67 based on the ratio 2:1 between Mn^{3+} and Mn^{2+}. These results imply the presence of both Mn^{2+} and Mn^{3+} at the surface. Based on this, Mn 2p regions for KMO ppt and Mn-Fib Ce were fitted as follows: the peaks at 640.2 and 652.3 eV are assigned to Mn $2p_{3/2}$-$2p_{1/2}$ from Mn^{2+}; peaks located at 641.6 and 653.6 eV correspond to Mn $2p_{3/2}$ -$2p_{1/2}$ from Mn^{3+}, and finally the peaks at 645 and 657 eV due to a satellite which has been related to Mn^{2+} species (Fig. 3.24). The separation between the main peaks due to spin-orbit splitting are 11.5 and 11.8 eV for KMO ppt and Mn-Fib Ce, respectively. These values are typical of Mn phases in mixed valence state. All mentioned signals are in line with several works found in the literature [135,139,141].

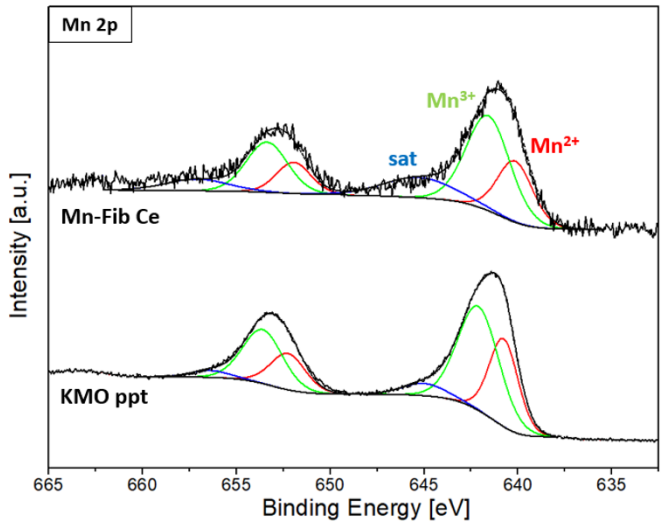

Fig. 3.24 - Surface analysis of plasma-supported samples (XPS): Mn 2p core level regions and deconvolutions.

Fe 2p regions for AFS ppt and Fe-Fib Ce are shown in Fig. 3.25. For the former, two main peaks can be clearly seen, characteristic of the spin-orbit splitting, having a separation of 13.4 eV, a typical value encountered for α-Fe_2O_3 phase [191,192]. Also, a clear satellite is present at around 719 eV, also commonly assigned for this phase. Since the most intense

peak is centered at 710-711 eV, it is ruled out the presence of Fe^{2+}. The main peak around 710 eV (assigned to Fe^{3+}) was deconvoluted in three peaks at 710.4, 712, and 713.8 eV. This approach can be explained by multiple splitting occurring for Fe^{3+} in XPS analysis, resulting in several final states and therefore different peaks at slightly higher binding energies [193,194]. Regarding the Fe-supported sample (Fe-Fib Ce), the situation is more complicated due to the interference of Auger peaks from Ce (MNN) at 716.3 and 732.5 eV. To process the spectrum of this sample, a ratio between Ce 3d and Ce Auger total areas was calculated for Fib Ce (bare support). Then, this ratio was maintained for Fe-Fib Ce after the corresponding calculation of its Ce 3d area. For the quantification of Fe, Ce Auger signals in Fe 2p region were not considered. The non-deconvoluted spectra of Fe 2p regions are shown in Fig. 3.26, in which the analysis is simplified, and the values of the main signals are detailed along with their separations.

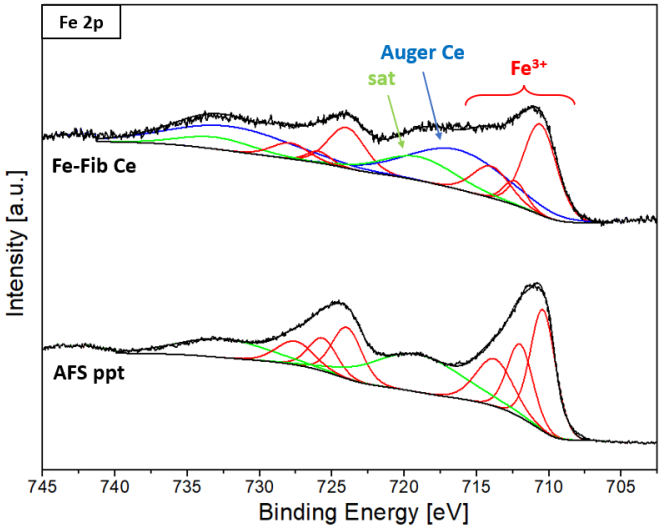

Fig. 3.25 - Surface analysis of plasma-supported samples (XPS): Fe 2p core level regions and deconvolutions.

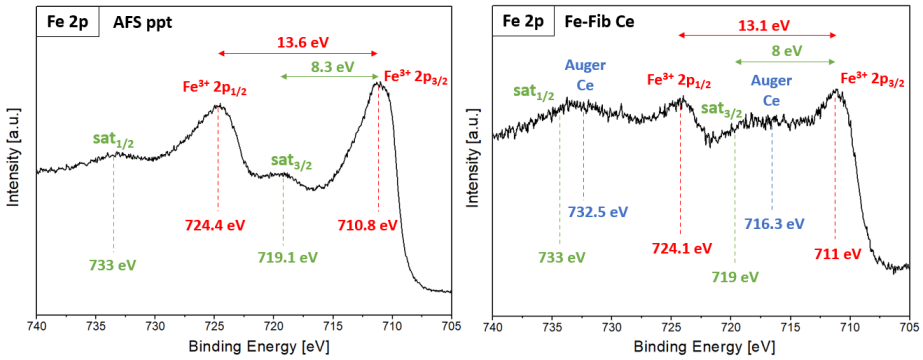

Fig. 3.26 - Non-deconvoluted XPS spectra of Fe 2p regions for AFS ppt (left) and Fe-Fib Ce (right).

Table 3.3 - XPS Ce 3d region peak positions, Ce^{3+}/Ce^{4+}, Mn/Ce and Fe/Ce atomic ratios.

Sample	Binding energy (eV)										$Ce^{3+}/(Ce^{3+}+Ce^{4+})$ (%)	Ce^{3+}/Ce^{4+}	Surface M*/Ce (Bulk ICP)
	Ce $3d_{5/2}$						Ce $3d_{3/2}$						
	v_o	v	v'	v''	v'''	u_0	u	u'	u''	u'''			
Fib Ce	880.8	882.6	885.0	889.0	898.6	899.2	901.2	903.3	907.5	917.0	25	0.33	-
Mn-Fib Ce	881.1	882.5	884.7	888.8	898.4	899.5	901.1	903.1	907.4	916.8	18	0.23	0.19 (0.11)
Fe-Fib Ce	880.9	882.7	885.0	889.4	898.7	899.1	901.3	903.1	907.7	917.2	33	0.50	0.50 (0.34)

** M = Mn or Fe*

Table 3.4 - XPS Ce 3d region fitting for Fib Ce.

Peak assignment	Species	RSF (Spin-orbit)	Peak decomposition		
			Peak	FWHM	Raw area
u'''	Ce^{4+}	21.12 ($3d_{3/2}$)	917.0	2.5	22227.7
u''	Ce^{4+}		907.5	4.6	18991.9
u'	Ce^{3+}		903.3	2	16889.3
u	Ce^{4+}		901.2	3.5	19050.5
u_0	Ce^{3+}		899.2	1.8	2972.1
v'''	Ce^{4+}	30.5 ($3d_{5/2}$)	898.6	2.5	33341.6
v''	Ce^{4+}		889.0	4.4	28776.5
v'	Ce^{3+}		885.0.	2	25589.8
v	Ce^{4+}		882.6	3.5	28864.4
v_o	Ce^{3+}		880.8	2.1	4503.2

Table 3.5 - XPS O 1s region peak positions, O_{ads}/O_{latt} and O_{ads}/Ce atomic ratios.

Sample	Binding energy (eV)			O_{ads} / (O_{ads} + O_{latt} + O_w) (%)	O_{ads}/O_{latt}	O_{ads}/Ce
	O_{latt}	O_{ads}	O_w			
Fib Ce	529.1	531.6	533.0	14.5	0.18	0.37
Mn-Fib Ce	529.1	531.5	532.9	15.0	0.18	0.46
Fe-Fib Ce	529.5	532.0	533.8	29.5	0.43	1.14

4.7 Catalytic evaluations - Soot combustion (AR-BE)

4.7.1 Soot combustion tests

The results obtained after soot combustion evaluations (wet contact) are shown in Figs. 3.27 and 3.28. Also, the corresponding T_{10}, T_{50}, T_{90} and T_M values extracted from the graphs are summarized in Table 3.6.

All catalysts presented a considerable catalytic effect in comparison to the blank, significantly diminishing T_M and T_{50} values. Evidently, the lower these values, the easier the soot is burnt.

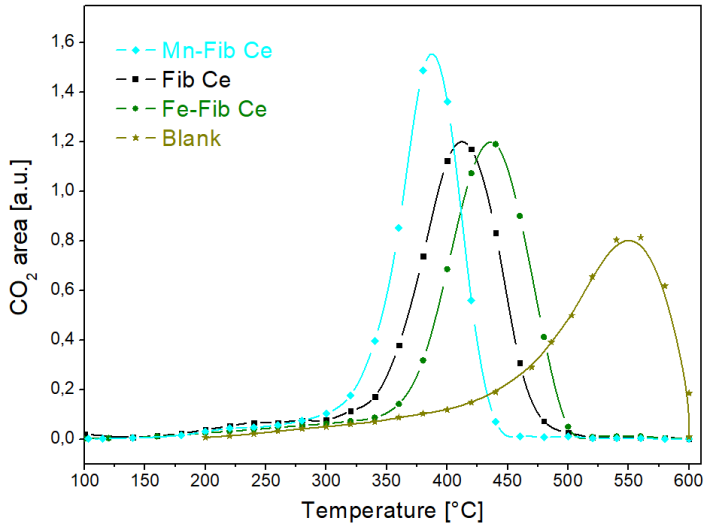

Fig. 3.27 - Soot combustion of plasma-supported Fib Ce: TPO profiles.

The active support used here, Fib Ce, presented a good activity with a T_M of 412 °C. This is a good value already as the temperature window regularly found in diesel exhaust gases is between 200-450 °C, allowing a passive regeneration inside a DPF. This result is not surprising based on the intrinsic characteristic of CeO_2 which makes it a well-known and widely used catalyst for this reaction [22,72,131].

After Fe deposition on the support, the activity decreased, shifting T_M and T_{50} to higher values, therefore the expectation of obtaining a better catalyst than bare Fib Ce was not attained. Indeed, as reported, the catalytic performance of bulk α-Fe_2O_3 was not as promising with T_M values around 460 °C and T_{50} values higher than 450 °C [78,79,195]. Taken this into account, it could be deduced that α-Fe_2O_3 is in general a less active phase than CeO_2. Thus, the blocking of sites of the more active CeO_2 by Fe species, supported by high Fe/Ce bulk and surface atomic ratios, is the first obvious reason that could explain the

detrimental effect brought by Fe. As seen by XPS, Fe deposition affected the amount of O_{ads}, with a marked increment in comparison to Fib Ce (Table 3.5), hinting that this could be another reason to explain the bad activity of this catalyst.

On the other hand, when Mn was supported on Fib Ce, an increase in activity was seen, lowering T_M and T_{50} values. In this case, the activity of the support was not affected by the presence of plasma-deposited MnO_x species. On the contrary, and as expected, the addition of Mn enhanced the performance of Fib Ce. As MnO_x species were not evident in the diffractogram of Mn-Fib Ce (Fig. 3.11), this phase is probably very well distributed on the support after the synthesis, and this could be a key factor. Based on previously shown characterizations, it was concluded that Mn is probably as Mn_3O_4, as divalent Mn^{2+} and Mn^{3+}, which is of great help in terms of reducibility of the catalyst.

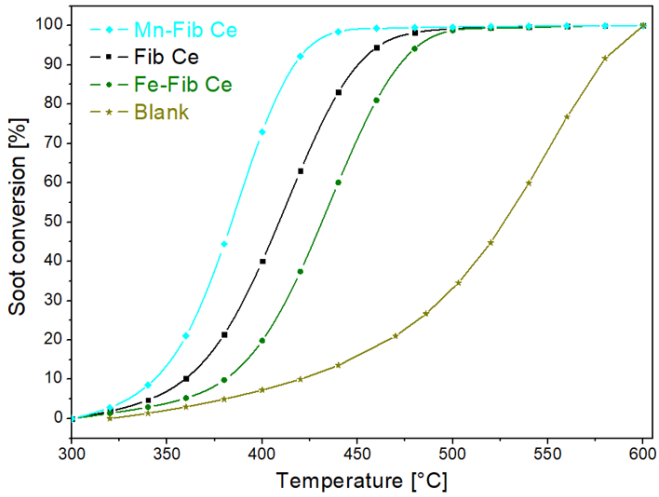

Fig. 3.28 - Soot conversion profiles of plasma-supported Fib Ce.

Table 3.6 - Catalytic activity of plasma-supported Fib Ce in soot oxidation.

Catalyst	T_{10} [°C]	T_{50} [°C]	T_{90} [°C]	T_M [°C]
Blank	420	527	578	550
Fib Ce	359	409	454	412
Mn-Fib Ce	343	384	418	386
Fe-Fib Ce	380	432	475	435

4.7.2 Mechanical stability of catalytic biofibers

An important property to be tested is the mechanical stability of the biomorphic fibers. To check this, a sample recovered after a catalytic test (which had been previously subjected to two wet impregnation steps during catalyst synthesis and soot impregnation) was analyzed by SEM. The images are shown in Fig. 3.29. As can be observed, the fibrous morphology is greatly preserved.

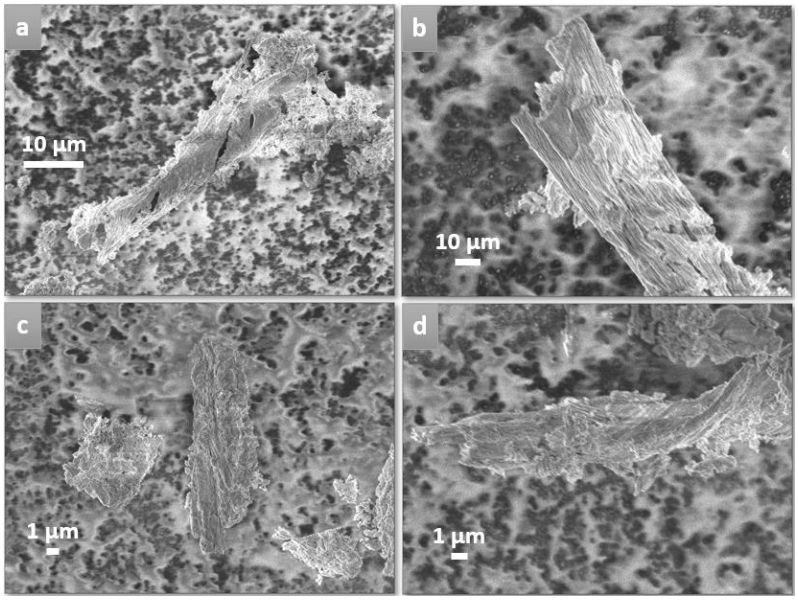

Fig. 3.29 - SEM images of spent Mn-Fib Ce catalyst after soot combustion reaction. Different fibers and magnifications (a-d).

4.7.3 Activity comparison between WI and GP samples in soot combustion

The best performing Mn-supported sample from Chapter I (Fib Ce-12Mn), synthesized by wet impregnation (WI), can be now compared (Fig. 3.30) to the plasma-supported (GP) Mn sample from this Chapter (Mn-Fib Ce). Both samples managed to decrease the T_M value of bare Fib Ce (T_M = 442 °C, O_2-assisted).

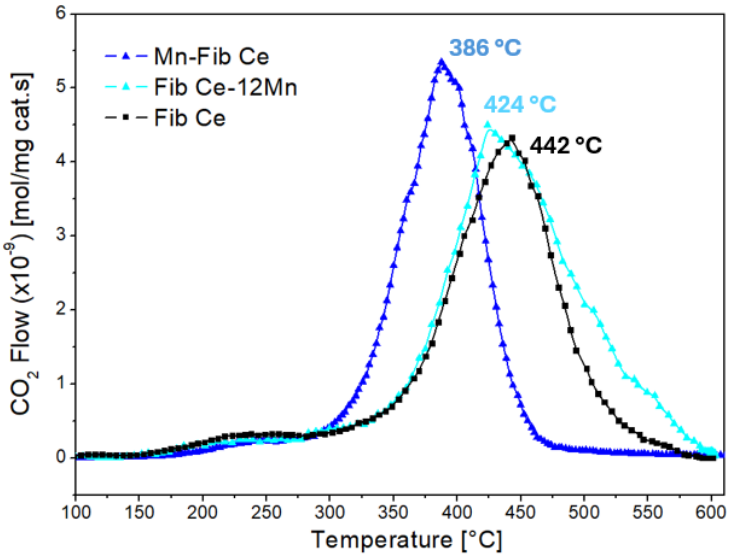

Fig. 3.30 - Comparison of Mn-supported samples activity in soot combustion for WI and GP synthesis methods (BE setup).

Mn-Fib Ce (GP) showed a better performance than Fib Ce-12Mn (WI), lowering the T_M value by 38 °C, despite having just 3.3 wt.% Mn (almost four times less Mn content). The intrinsic properties of Mn_3O_4, along with a small particle size and good distribution of this phase on Fib Ce, could explain the outstanding activity difference.

Regarding Fe deposition, a sample with 10 wt.% Fe prepared by WI (Fib Ce-10Fe) is compared (Fig. 3.31) to the plasma-supported (GP) Fe sample from this Chapter (Fe-Fib Ce).

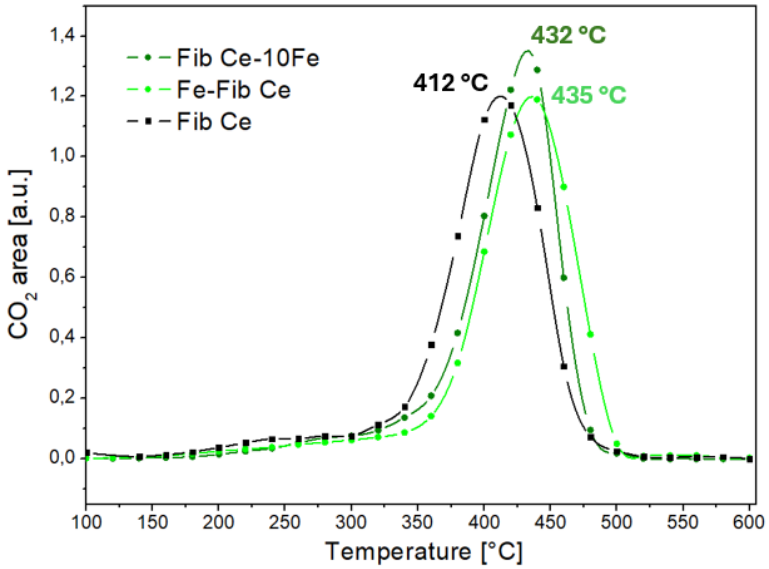

Fig. 3.31 - Comparison of Fe-supported samples activity in soot combustion for WI and GP synthesis methods (AR setup).

In this case, both samples performed worse than the support alone (T_M = 412 °C, NO_2-assisted) and increased the T_M similarly. Different than with Mn, the same Fe phase was identified in these two samples (α-Fe_2O_3), and both samples contain practically the same amount of Fe (around 10 wt.%). Unfortunately, no marked differences were found for both deposition methods.

4.8 Catalytic evaluations - CO oxidation (AR)

CO oxidation reaction results are presented in Fig. 3.32 along with T_{10}, T_{50}, T_{90} values for each catalyst summarized in Table 3.7.

Looking at the conversion profiles, it is evident that the catalysts followed the same activity pattern seen in soot combustion tests. Even though this reaction is intrinsically different from soot combustion (since it does not involve a solid reactant), the same reasons mentioned above can be considered to explain the behavior of plasma-supported fibers. Furthermore, the MVK mechanism has been evoked to describe CO oxidation on oxides [70,71], in which adsorbed CO reacts with lattice oxygen leaving a vacancy which is subsequently filled by either gaseous or lattice oxygen (O_{latt}). Thus, the latter plays a crucial role in replenishing oxygen being used in the reaction, and therefore the decrease of O_{latt} after Fe deposition could further justify the decreased in activity, having a lower capacity of oxygen refilling. On the other hand, the invariable O_{latt} after Mn deposition maintains the intrinsic oxygen mobility of Fib Ce, aiding in reaction and boosting the activity considerably.

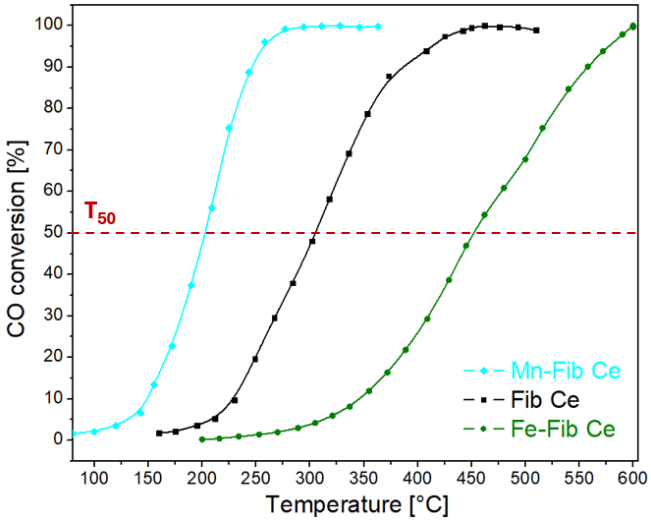

Fig. 3.32 - CO conversion profiles of plasma-supported Fib Ce.

A common approach to enhance the activity in oxidation reactions, in either pure CeO_2 or α-Fe_2O_3, is to create Fe-Ce mixed oxides. This can produce structural defects in the catalysts, increase the amount of oxygen vacancies, improve redox properties and gain thermal stability [77,195,196]. This is typically obtained following hydrothermal, co-

precipitation or sol-gel routes of synthesis. By supporting Fe on CeO_2, as in this study, doping is not expected to occur. Moreover, during the analysis of the characterization results, no evidence was seen of the formation of a solid solution.

In the same vein as with Fe-Ce systems, Mn-Ce mixed oxides are a common approach to create very active catalysts [69,74,139,147]. However, in the current case, it was proven that an improvement of bare CeO_2 activity can also be achieved by depositing Mn on its surface.

Table 3.7 - Catalytic activity of plasma-supported Fib Ce in CO oxidation.

Catalyst	T_{10} [°C]	T_{50} [°C]	T_{90} [°C]
Fib Ce	228	305	386
Mn-Fib Ce	148	202	245
Fe-Fib Ce	345	452	557

4.9 Catalytic evaluations - Benzene oxidation (BE)

The plasma-supported catalysts prepared in this chapter were also tested in the benzene oxidation. The benzene conversion profiles are shown in Fig. 3.33 and T_{10}, T_{50}, T_{90} values are listed for each catalyst in Table 3.8.

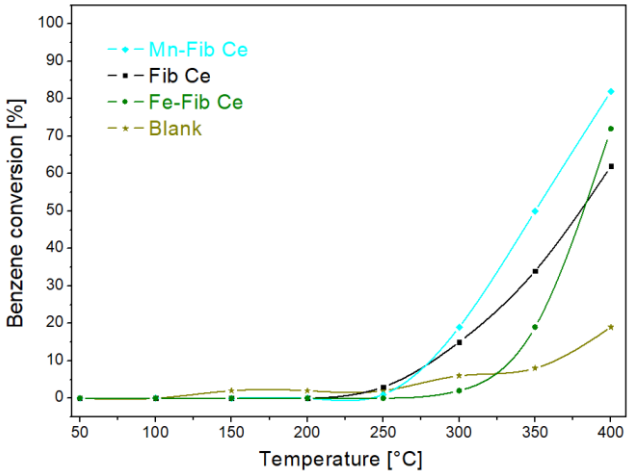

Fig. 3.33 - Benzene conversion profiles for plasma-supported Fib Ce.

The Mn-supported catalyst was the only one that managed to increase the activity of the support above 300 °C but not to a great extent. Again, maintaining the original concentration of O_{latt}, in addition to Mn present in a mixed valence state (Mn_3O_4) and the low particle size of this phase, could be behind this improvement in activity. On the contrary, Fe-Fib Ce performed similarly than Fib Ce, reaching a slightly higher conversion only at 400 °C.

Table 3.8 - Catalytic activity of plasma-supported Fib Ce in benzene oxidation.

Catalyst	T_{10} [°C]	T_{50} [°C]	T_{90} [°C]
Blank	354	> 400	> 400
Fib Ce	280	379	> 400
Mn-Fib Ce	275	350	> 400
Fe-Fib Ce	323	378	> 400

5 Main findings

The deposition of active species on fibrous supports using glidarc plasma has not been reported until now. In this work we report the use of this technique to anchor either Mn or Fe oxides over CeO_2 biomorphic fibers to obtain micro-structured catalysts.

The precipitates produced by exposing Mn and Fe precursor solutions to plasma were identified as Mn_3O_4 and α-Fe_2O_3, respectively. The presence of these phases on the plasma-supported fibers was corroborated by XRD, FTIR-ATR and LRS. This result highlights the benefits of the gliding arc plasma technique (GP) that allows the preparation of both powdered and supported oxides on fibrous structures.

In the case of Mn-Fib Ce, a good distribution of Mn was seen at the nanoscale (TEM-EDS) along wit a low particle size (8 nm), but also in terms of bulk (XRD). Additionally, the Mn/Ce atomic ratios obtained on big mappings (SEM-EDS) were similar to those reported by ICP. A good distribution of Fe was also evident in Fe-Fib Ce at a small scale (TEM-EDS) with particle size of around 29 nm. The atomic ratios (Fe/Ce) were similar for big mappings (SEM-EDS) and ICP, and some segregation of α-Fe_2O_3 occurred since two characteristic signals from α-Fe_2O_3 were spotted in the diffractogram. This could be due to a higher content of this phase (9.4 wt.%) if compared to Mn-supported sample (3.3 wt.%) to which no peaks were assigned.

Regarding the surface properties, Fe-Fib Ce sample provoked a marked increase in the amount of O_{ads} while Mn-Fib Ce did not modify it considerably. In addition to this, Fe-Fib Ce increased the content of Ce^{3+} whereas Mn-Fib Ce decreased it with respect to the bare support. Finally, both samples presented a M/Ce surface atomic ratio higher than their nominal value (bulk), which is expected.

Both for soot and CO oxidations, the same activity order was found: Mn-Fib Ce > Fib Ce > Fe-Fib Ce. The deposition of Fe was detrimental for Fib Ce which could be related to the blocking of sites of the more active CeO_2 sites. The marked increment of O_{ads}/O_{latt} and Ce^{3+}/Ce^{4+} atomic ratios, accompanied by its particle size, could also explain the lower catalytic behavior observed when compared to Fib Ce. On the other hand, Mn deposition enhanced the activity of Fib Ce, which might be connected to the good distribution of Mn_3O_4 (surface and bulk), its lower particle size, higher Ce^{3+} content and Mn being in a mixed-valence state.

The decrease of lattice oxygen (O_{latt}), as observed with Fe-Fib Ce, appeared prejudicial for the activity in both reactions, which might coincide with a slow oxygen replacement. This fact makes even more

sense for CO oxidation since this reaction is believed to follow the MVK mechanism.

So far in this thesis the difference between reactions involving a solid and gaseous reactants have been demonstrated and emphasized. In the current chapter, the same trend in activity was obtained for both types of reactions, which was not the case in previous chapters. This clearly indicates that the nature of the gaseous reactant, whether it is benzene or carbon monoxide, will also play a key role in the performance of the catalysts.

PART II - CHAPTER IV

Plasma-supported ZrO_2 fibers for soot and benzene oxidation

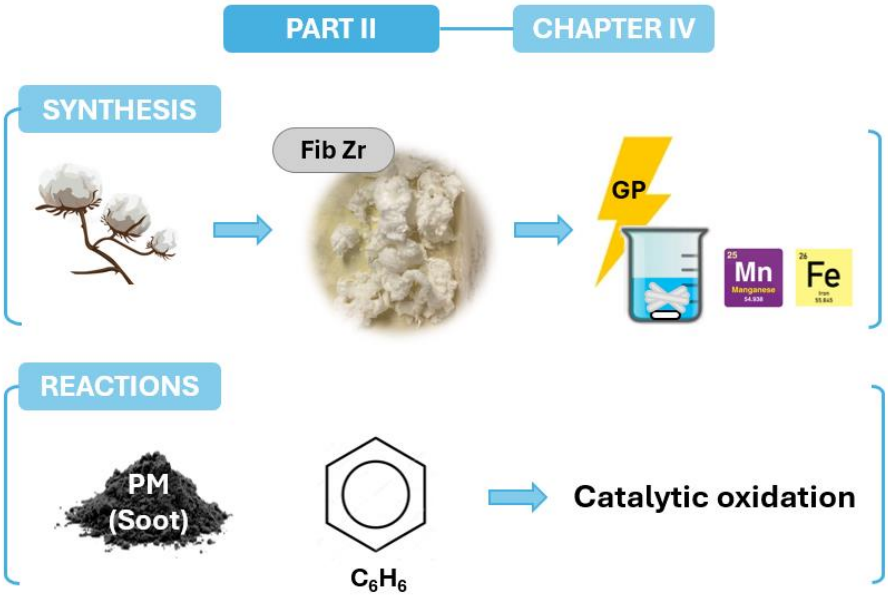

1 Introduction: Plasma-supported ZrO_2 fibers for soot and benzene oxidation

In this last chapter, biomorphic and commercial ZrO_2 fibers are employed as different types of support, on which Mn and Fe oxides are added by glidarc plasma-deposition (GP), following the same deposition procedure applied in the previous chapter (Chapter III) and detailed in the Experimental Section (Section 1.1.3).

So far in this thesis, all syntheses involved the use of active supports as the building block, before the addition of extra active phases either by wet impregnation (WI) or plasma deposition. Therefore, the idea of performing and studying the plasma deposition utilizing a more conventional type of support surged.

The most common kind of supports employed in catalysts are refractory oxides which are metal oxides that have high melting points (1500-2700 °C) and are stable under operating conditions. Some examples are: Al_2O_3, SiO_2, Al_2O_3-SiO_2, zeolites, TiO_2, ZrO_2, MgO and CaO. [197].

ZrO_2 is well known for the following properties: chemical stability, inherent hardness, high melting point (about 2700 °C), excellent thermal stability, high resistance for corrosion, abrasiveness, biocompatibility, etc. [198]. It is stable in both oxidizing and reducing atmospheres and possesses both acid and base properties (amphoteric), which makes it an acid-base bifunctional oxide [199]. Zirconia-based materials have found a variety of uses as implants, coatings, gas sensors, semiconductors, catalysts, fuel cell, optical devices, and others [200].

Concerning its catalytic application, zirconia has been used as an active component in reactions like hydrogenation, cracking and isomerization. Also, as a support, zirconia has been tried in reactions such as low-temperature water-gas-shift and CO oxidation reactions [201]. A remarkable activity for the transesterification reaction in the production of biodiesel has been reported for ZrO_2, mainly ascribed to its tunable surface acid-base properties [202]. In addition, ZrO_2 is a good platform for the synthesis of precious metal-based catalysts, since it behaves similarly to Al_2O_3 in having donor sites for good anchoring and stabilization of atoms of the supported metal [203].

Zirconia might form in different crystal structures (polymorphic nature) such as monoclinic (m-ZrO_2), tetragonal (t-ZrO_2), and cubic (c-ZrO_2). Two different graphic representations of these three arrangements of ZrO_2 are shown in Fig. 4.1 [201,202].

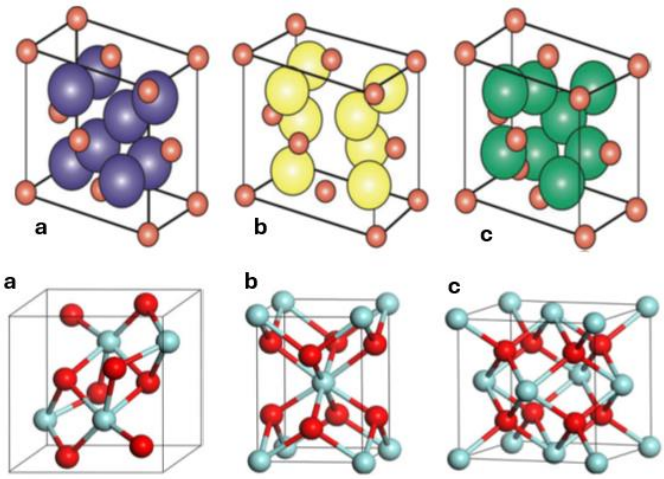

Fig. 4.1 - Crystal structure of m-ZrO_2 (a), t-ZrO_2 (b), and c-ZrO_2 (c) [201,202].

The first objective of this chapter is to synthesize biomorphic zirconia fibers and to determine which kind of phases are obtained following this path. Secondly, the plasma precipitation-deposition is attempted to anchor Mn or Fe species on these fibers. After the synthesis, several characterization techniques are used to further understand the properties of the catalysts, and finally catalytic runs are carried out in order to study the activities of the developed catalysts towards soot and benzene oxidation reactions.

All the studies performed for the biomorphic catalysts were done as well with a series of catalysts derived from commercial zirconia fibers. The results are continuously compared throughout the chapter, in addition to some specific comparisons with results presented in previous chapters.

2 Abstract

Plasma glidarc precipitation-deposition was performed to deposit Mn or Fe oxides on biomorphic zirconia fibers (Fib Zr(B)) produced by means of a cotton biotemplate. The same process was carried out with commercial zirconia fibers (Fib Zr(C)) as well. These catalysts were synthesized to be tested in the reactions of soot and benzene oxidation. SEM shows that Fib Zr(B) retained to a great extent the morphology of cotton. Both series of supported catalysts were first characterized by XRD, ATR-FTIR and LRS. Fib Zr(B) presented the tetragonal phase (t-ZrO_2) while Fib Zr(C) exhibited the monoclinic one (m-ZrO_2). By XRD, the cryptomelane phase ($K_xMn_8O_{16}$) was identified only for Mn-Fib Zr(B). In the case of Fe-supported samples, the α-Fe_2O_3 phase appeared clearly in both in biomorphic and commercial fibers. The presence and loadings of the added metals were confirmed by EDS and compared to bulk ICP quantification values. TEM images showed smaller particle size for Fib Zr(B) than Fib Zr(C). Also, the particles of both supports had different shapes and the same happened for deposited metal oxides, that depending on the support, showed different morphologies as well. TEM-EDS exhibited a good distribution of Mn or Fe on both supports. XPS confirmed that Mn has an average oxidation state between 3+ and 4+ (mainly as Mn^{3+} and Mn^{4+}). The O_{ads}/O_{latt} surface atomic ratio of both supports decreased after Mn deposition and increased with Fe deposition. Also, Fe-supported samples showed a higher accumulation on the surface with Fe/Zr atomic ratios above unity.

A soot-to-catalyst contact study showed no differences in activity for three different types of contact when using Fib Zr(C) as catalyst. For the supported series of catalysts, Mn-containing samples improved the activity considerably in soot combustion. On the other hand, Fe addition only caused a positive effect on commercial fibers, performing similarly as Mn-Fib Zr(C). In benzene oxidation tests, bare supports were almost inactive and Mn-supported catalysts were the only ones that increased the activity, although not significantly.

Most of the results presented in this chapter will be sent for publication to **Applied Catalysis A: General**, special edition titled: **"Catalysis in the Americas"** (Invitation to participate accepted).

3 Results and discussion

3.1 XRD and textural analyses (BE)

In order to study crystalline phases present in Fib Zr(B), three different calcination temperatures were used in the biomorphic synthesis route (Experimental Section - Fig. e.3). Also, the impact of the possible phase changes on the specific surface area (SSA) and catalytic activity in soot combustion was analyzed.

The diffractograms obtained for the three different calcination temperatures are presented in Fig. 4.2. For all samples, the signals at 2θ = 30.3, 35.3, 50.4, 60.2 and 62.9 ° belong to the tetragonal phase of ZrO_2 (t-ZrO_2, JCPDS 17-0923). For the sample calcined at 800 °C (Fib Zr(B)-800), two new signals are evident at 2θ = 28.3 and 31.4 ° which correspond to the monoclinic phase of ZrO_2 (m-ZrO_2, JCPDS 37-1484). The signal at 2θ = 28.3 ° merely appears for Fib Zr(B)-700 [204–207].

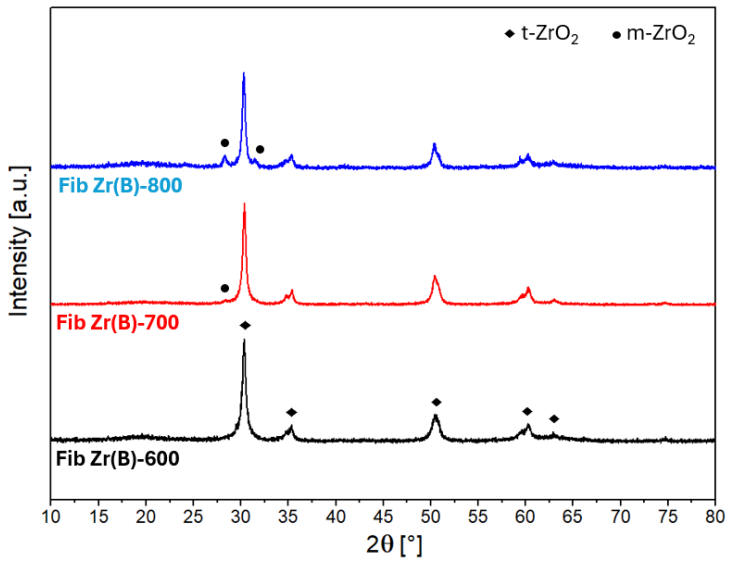

Fig. 4.2 - Diffractograms of biomorphic ZrO_2 fibers (Fib Zr(B)) calcined at different temperatures.

The following equation has been used to calculate the tetragonal phase percentage (% t) by using the intensity of main diffraction peaks from tetragonal (I_t) and monoclinic (I_m) phases [208]:

$$\%\, t = \frac{I_t(101) + I_t(110)}{I_t(101) + I_t(110) + I_m(-111)} \times 100 \qquad \textit{Equation 4.1}$$

The peaks of t-ZrO_2 at 2θ = 30.3 and 35.3 ° correspond to crystallographic planes (101) and (110), respectively, while the peak at 2θ = 28.3 ° is generated by the (-111) plane of m-ZrO_2. The percentage values of the tetragonal phase (% t) calculated were 100, 94, and 88 % for Fib Zr(B)-600, Fib Zr(B)-700, and Fib Zr(B)-800, respectively. This shows numerically how much the amount of t-ZrO_2 diminishes with the increase of calcination temperature.

The specific surface area (SSA) values of these supports (obtained by N_2 physisorption and the BET method) as a function of the calcination temperature are shown in Fig. 4.3. All samples have relatively low specific surface area values (between 8 and 20 m^2/g), with the sample calcined at 600 °C (Fib Zr(B)-600) exhibiting the highest value.

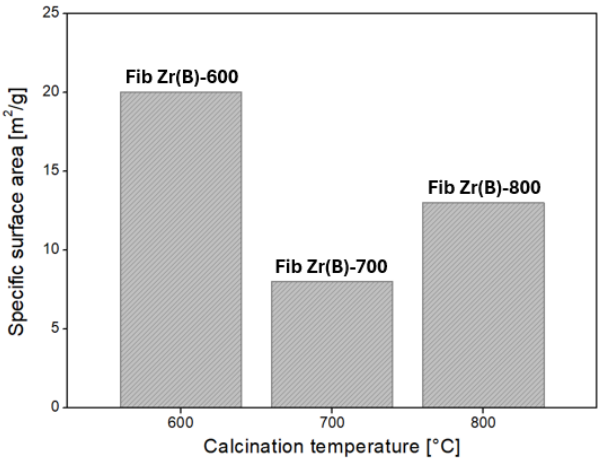

Fig. 4.3 - Specific surface area of Fib Zr(B) for different calcination temperatures.

In order to select the calcination temperature, a quick catalytic screening in soot combustion was done for these three batches of biomorphic zirconia fibers. The sample calcined at 600 °C performed the best, and consequently, Fib Zr(B)-600 was the chosen support for the following deposition process by glidarc plasma (GP) technique. These catalytic results are shown and discussed later in the Chapter (Section 3.7). Hereafter, in all catalyst formulations used, Fib Zr(B)-600 is simply named Fib Zr(B).

The diffractograms of the Mn or Fe supported Fib Zr(B) by GP are presented in Fig. 4.4. The diffraction pattern of Fib Zr(B) was already described before (Fig. 4.2), and it is included in the graph to facilitate the comparison. The Mn-supported sample shows several small peaks at 2θ = 12.8, 18.1, 28.7, and 37.5 °, all of which coincide with the signals found

in the cryptomelane phase $K_xMn_8O_{16}$ (JCPDS 29-1020) [209,210]. Cryptomelane is part of the so-called octahedral molecular sieves (OMS) which present tunnel structures of edge-sharing [MnO_6] octahedra. It is a mixed oxide that combines Mn^{4+} and Mn^{3+} with alkali and/or alkali earth cations that reside inside the tunnels to stabilize the structure (in this case K^+) [210,211]. In contrast to what was observed for Mn-Fib Ce in Chapter III, where no diffraction peaks coming from MnO_x were observed, here it was possible to detect the presence of the cryptomelane phase on Fib Zr(B).

As regards to the Fe-supported sample, many new signals appeared after the deposition of iron oxides by GP at 2θ = 24.2, 33.2, 35.6, 40.9 and 54.1 °, which match with the rhombohedral hematite phase α-Fe_2O_3 (JCPDS 33-0664) [182,183].

When Mn was added to Fib Zr(B), the SSA of this sample remains similar to that of the support alone (20 m^2/g), whereas after Fe deposition, the value decreases to 12 m^2/g (Table 4.1).

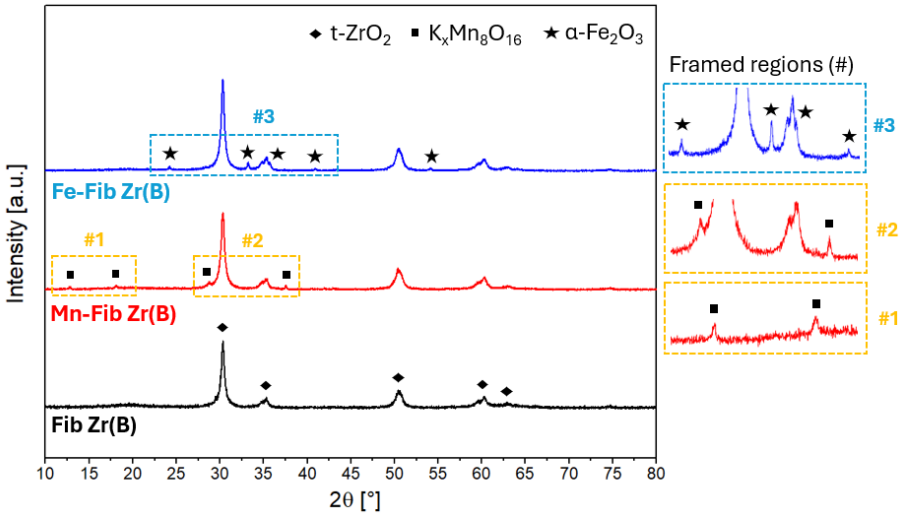

Fig. 4.4 - Diffractograms of plasma-supported Fib Zr(B). Magnified regions (right).

In Fig. 4.5, the adsorption isotherms for these samples are shown. Fib Zr(B) and Mn-Fib Zr(B) exhibit a similar pattern, following a type IV isotherm (which may indicate that these samples have some cylindrical mesopores opened at both ends or bottle-like mesopores), forming a hysteresis loop that ends around P/P_o = 0.4, being more pronounced for the former. The loop covers a wide range of pressures, which indicates that whatever their shape they present a marked diversity of sizes. The

shape resembles a H3 type of loop which is given by non-uniform aggregates plate-like particles but also by a macropore network which are not completely filled with pore condensate [128,212].

The Fe-supported sample, in turn, is matched with a type II isotherm (non-porous or macroporous adsorbents), where the small hysteresis loop occurs at high relative pressures (very similar emptying mechanism closing at P/P_o = 0.75), which may be provoked by interparticle mesoporosity caused by bigger particles.

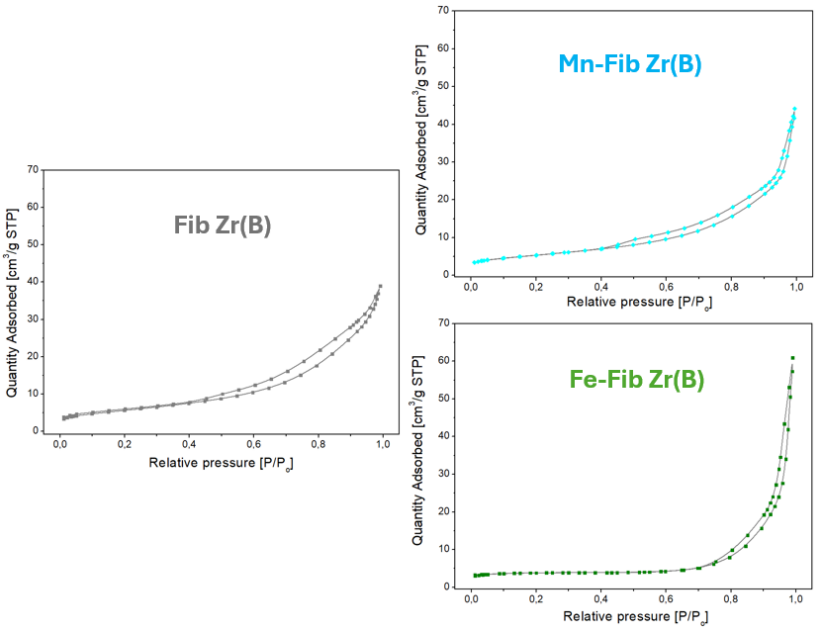

Fig. 4.5 - N_2 physisorption isotherms of plasma-supported Fib Zr(B).

The diffractograms for Mn,Fe-supported Fib Zr(C) are presented in Fig. 4.6. For bare Fib Zr(C), all signals correspond to the monoclinic phase of ZrO_2 (m-ZrO_2, JCPDS 37-1484). Contrary to what happened for Mn-Fib Zr(B), in this case there is an absence of signals coming from MnO_x species which could indicate a good dispersion of the supported phase. Regarding Fe-Fib Zr(C), the two most intense signals of α-Fe_2O_3 (JCPDS 33-0664) appeared at 2θ = 33.2 and 35.6 °.

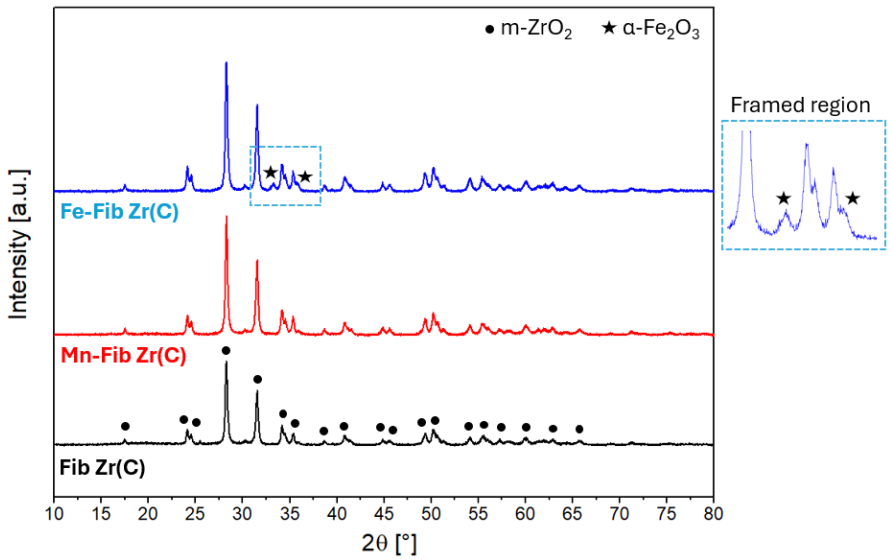

Fig. 4.6 - Diffractograms of plasma-supported Fib Zr(C). Magnified region of Fe-Fib Zr(C) (right).

In terms of specific surface area (SSA), Fib Zr(C) showed a very low value of 3 m^2/g when N_2 physisorption was performed. The supported samples, either with Mn or Fe, slightly increased the SSA to 6-7 m^2/g (Table 4.1). However, such small differences are insignificant when considering the error of the technique (5-10%). The crystallite size of these samples (calculated using the Scherrer equation) is around 32 nm, being bigger than those of the biomorphic formulations (Table 4.1).

The N_2 adsorption isotherms of bare and supported commercial fibers exhibit a type II isotherm, all of them exhibiting a huge type H4 hysteresis loop that ends around $P/P_0 = 0.4$ (Fig. 4.7). This type of loop is associated with solids consisting of aggregates or agglomerates of particles forming slit shaped pores with uniform size and/or shape [212]. This could be expected as commercial fibers are very regular in shape (Section 3.2). Also, the Mn,Fe-supported samples showed a higher quantity adsorbed (around 33 cm^3/g) in comparison to Fib Zr(C) of 17.5 cm^3/g.

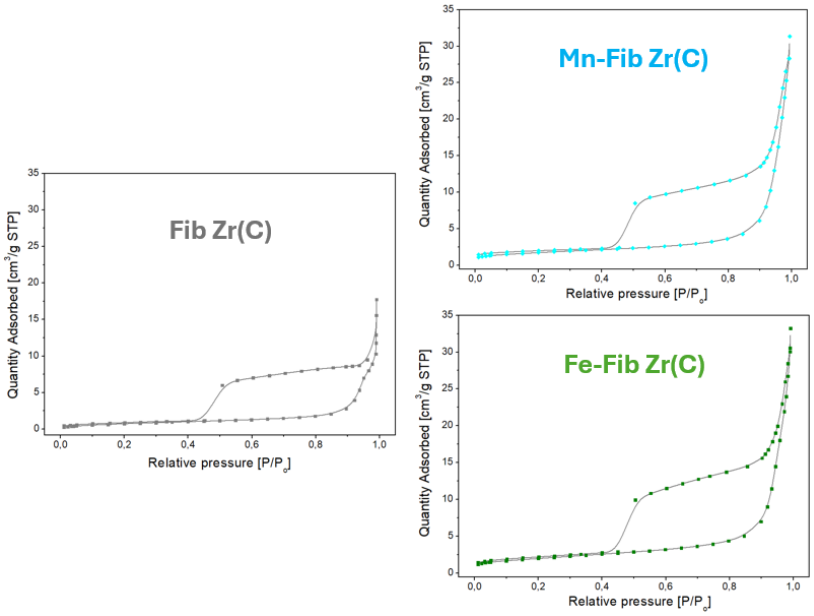

Fig. 4.7 - N_2 physisorption isotherms plasma-supported Fib Zr(C).

Table 4.1 - XRD and textural analyses.

Sample	Crystallite size of support (ZrO_2) [nm] *	Crystallite size of supported phase [nm] *	BET Specific surface area (SSA) [m^2/g]	Pore volume (V_g) [cm^3/g] **
Fib Zr(B)	19	-	20	0.05
Mn-Fib Zr(B)	17	39	19	0.06
Fe-Fib Zr(B)	19	35	12	0.08
Fib Zr(C)	31	-	3	0.03
Mn-Fib Zr(C)	33	-	6	0.04
Fe-Fib Zr(C)	32	21	7	0.04

**** Calculated by Scherrer equation using the following peaks (2θ): 30.3 ° for Fib Zr(B), 28.2 ° for Fib Zr(C), 37.5 ° for MnO_x, and 33.2 ° for α-Fe_2O_3.***

***** Pore volume taken at P/P_o = 0.98.***

For both biomorphic and commercial fibers, it can be inferred that they do not show any microporosity due to the lack of N_2 adsorption at low relative pressures.

3.2 Morphological analysis by SEM and EDX (AR)

SEM images obtained from biomorphic (Fib Zr(B), prepared as described in the Experimental Section and commercial zirconia fibers (Fib Zr(C)) are shown in Fig. 4.8. For the former, the template morphology was highly maintained. Translucid fibers (1 μm thick) are formed (Fig. 4.8 - a,b), resembling the cotton cellulosic fibers. Their lengths reach up to 60 μm and their widths are lower than 5 μm. Most fibers are open-helicoidal and closed ones were almost not seen. This is a clear difference if compared to bare CeO_2 (Fib Ce) and Co_3O_4 (Fib Co) biofibers (from Chapters I, II and III), synthesized via the same route, which presented a majority of bigger cylindrical fibers with inner channels of different diameters, and not many open helicoidal ones. Also, the texture of these fibers (Fib Ce and Fib Co) was different, showing a more robust texture.

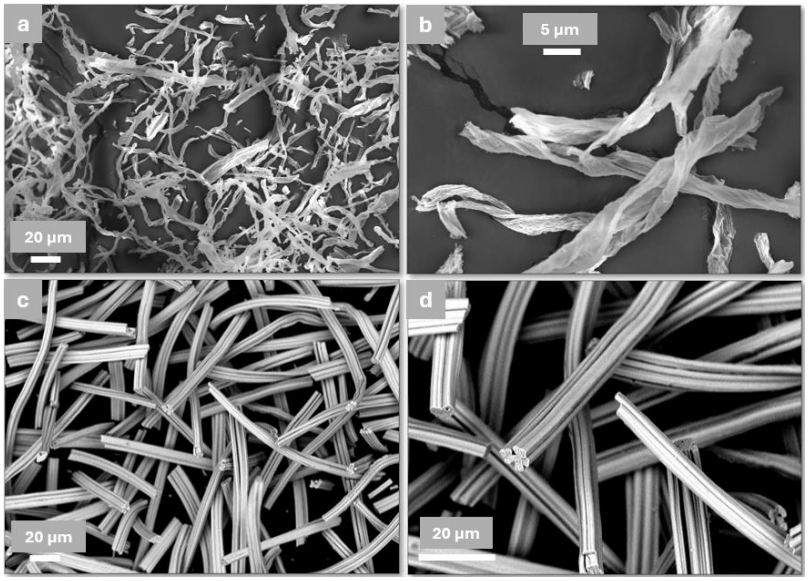

Fig. 4.8 - SEM images of biomorphic and commercial ZrO_2 fibers: Fib Zr(B) (a,b) and Fib Zr(C) (c,d).

On the other hand, Fib Zr(C) are arranged in bundles of several small cylindrical fibers, with uniform lengths of 80-100 μm and widths of 5 μm approximately (Fig. 4.8 - c,d). As can be clearly observed, these fibers are more regular in shape and size than biomorphic ones.

In Fig. 4.9, Mn-supported samples are presented. Shorter fibers compared to bare supports are visible (Fig. 4.9 - a,c), probably broken during the plasma-deposition process, along with some isolated particles which were not anchored to the surface of the support.

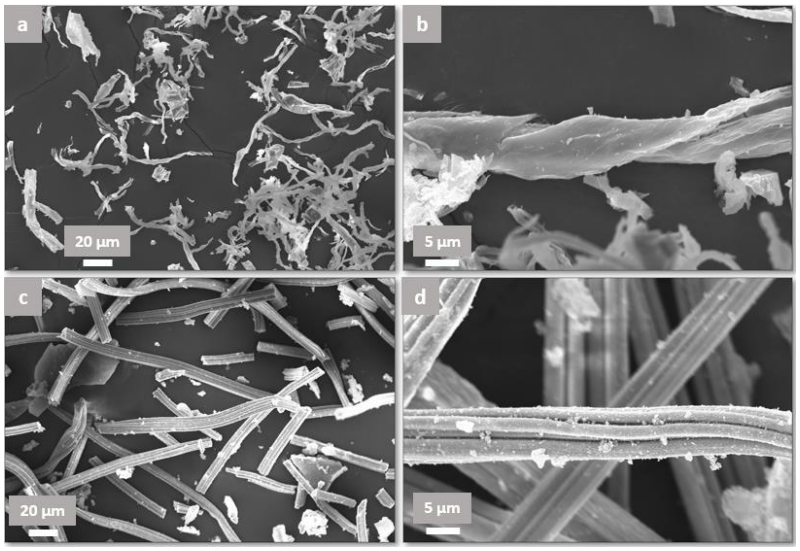

Fig. 4.9 - SEM images of Mn-Fib Zr(B) (a,b) and Mn-Fib Zr(C) (c,d).

The same situation occurs for Fe-supported samples in Fig. 4.10 - a,c. It is worth noting that commercial supported fibers, either with Mn or Fe, seem to be more covered with precipitate than biomorphic ones (Fig. 4.9 - b,d and Fig. 4.10 - b,d).

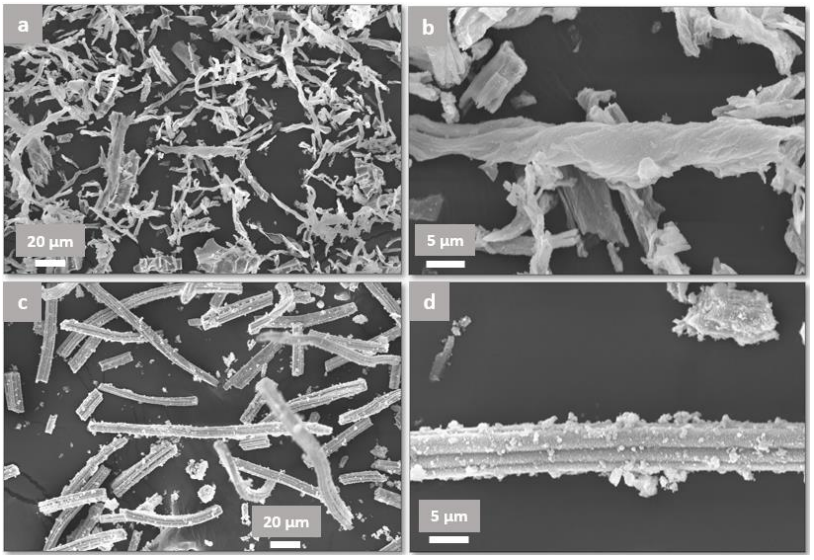

Fig. 4.10 - SEM images of Fe-Fib Zr(B) (a,b) and Fe-Fib Zr(C) (c,d).

The fibers on which EDS analysis was performed are shown in Figs. 4.11 and 4.12. As has been done in all previous chapters, spot (Figs. 4.11 - a,c

and 4.12 - a,c), mapping (Figs. 4.11 - b,d and 4.12 - b,d), and big area mappings (Fig. 4.13) were acquired for all samples. All values obtained from this technique are reported as atomic metal ratios in Tables 4.2 and 4.3, for Fib Zr(B) and Fib Zr(C) series of catalysts, respectively.

Generally, for all samples, the spot values (Zones 1-2-3) are different from each other, highlighting a heterogeneous distribution of Mn or Fe on isolated fibers. Furthermore, for Mn-supported samples, spot averages are lower than big mapping values, which indicates that the precipitate stays aside from (or in between) the fibers as well. This is evident in Fig. 4.13 - a,c and highlights a heterogeneous distribution of the Mn oxides. Contrariwise, Fe-supported samples presented no big differences between spot averages and big mapping values, showing a more uniform distribution of this phase on ZrO_2 fibers (Fig. 4.13 - b,d).

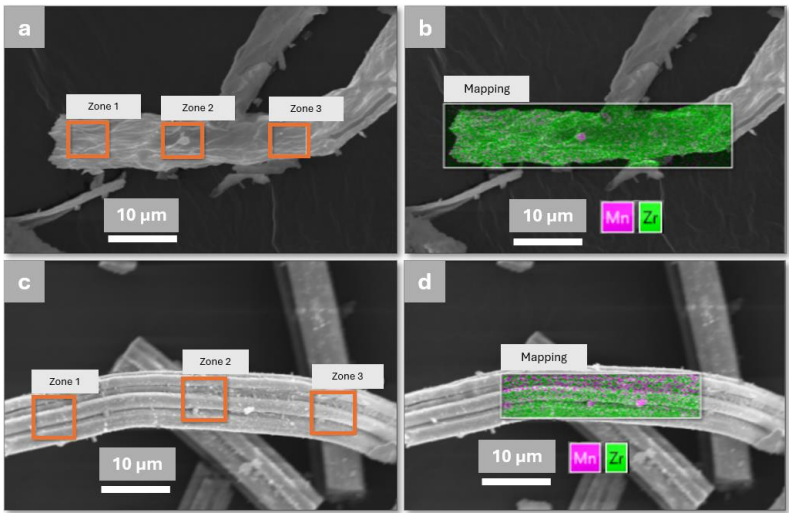

Fig. 4.11 - EDS spot and mapping analyses of Mn-Fib Zr(B) (a,b) and Mn-Fib Zr(C) (c,d).

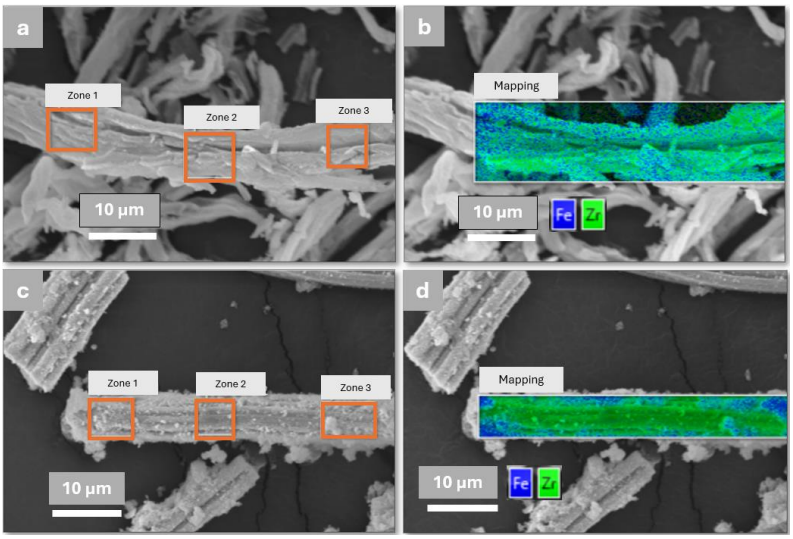

Fig. 4.12 - EDS spot and mapping analyses of Fe-Fib Zr(B) (a,b) and Fe-Fib Zr(C) (c,d).

The big mapping images show more and bigger agglomerates of Mn in Mn-Fib Zr(B) and Mn-Fib Zr(C) (Fig. 4.13 - a,c), whereas the Fe-supported samples seem to have a better distribution of the precipitate avoiding its agglomeration (Fig. 4.13 - b,d). The quantification values of these big areas gave atomic metal ratios considerably higher than the nominal ones for all samples. Recapping from the previous Chapter (Chapter III), the nominal values come from the exposure of precursors alone to GP, in the same volumes used for the catalytic synthesis. This assumes that the same MnO_x and FeO_x phases are obtained when a support is present in the solution. Then, it could be inferred that the precipitates are, in general, in higher quantities than those expected. However, wt.% values obtained by ICP analysis (also included in Tables 4.2 and 4.3), show a different trend. Mn content in Mn-supported samples are close to the nominal value (4.0), while for Fe-supported samples, the corresponding values are nearly half as much as the expected one (9.9). This discrepancy could be due to an accumulation of FeO_x on the first surface layers of the catalysts, for which its quantification by a bulk technique (ICP) gives a lower and more reliable value. If considering the ICP contents of both Mn and Fe-ZrO_2 samples, similar metal oxide contents are obtained (around 4-5 wt.%, Tables 4.2 and 4.3).

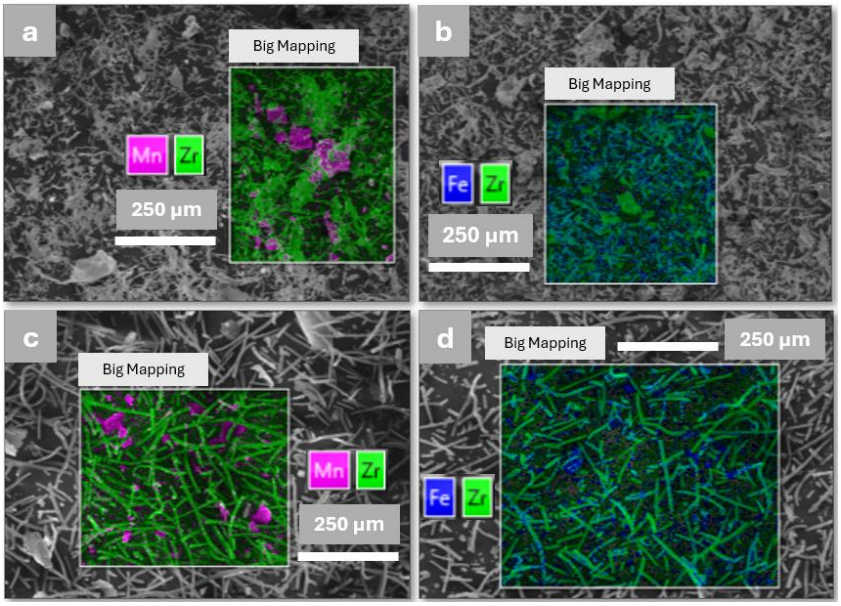

Fig. 4.13 - EDS big mapping analyses of Mn-Fib Zr(B) (a), Fe-Fib Zr(B) (b), Mn-Fib Zr(C) (c), and Fe-Fib Zr(C) (d).

It is important to mention that the Mn/Zr nominal atomic ratios and wt.% reported in Table 4.2 and 4.3 were calculated assuming that KMO precipitate (KMO ppt) would be $K_xMn_8O_{16}$ based on the phase assignation done previously (XRD). These numbers change slightly in comparison to those mentioned in Chapter III where Mn_3O_4 phase was assumed to calculate these values.

Table 4.2 - Mn/Zr and Fe/Zr atomic ratios for zonal and mapping EDS analyses in supported Fib Zr(B).

Sample **	M*/Zr atomic ratios								
	Fiber N°	Zone 1 (Spot)	Zone 2 (Spot)	Zone 3 (Spot)	Average per fiber (Zones 1, 2 and 3)	Spot average	Mapping per fiber	Big area mapping, Fig. 13 (a,b) (wt.% - ICP)	Nominal (wt.%)
Mn-Fib Zr(B)	1	0.03	0.06	0.03	0.04	0.04	0.04	0.18 (4.0)	0.10 (4.0)
	2	0.06	0.05	0.03	0.05		0.05		
	3	0.02	0.02	0.02	0.02		0.05		
Fe-Fib Zr(B)	1	0.70	0.75	0.61	0.68	0.60	0.80	0.65 (5.4)	0.25 (9.9)
	2	0.61	0.70	0.82	0.71		0.80		
	3	0.54	0.43	0.52	0.50		0.60		

** M = Mn or Fe*

*** Three fibers per sample were analyzed*

Table 4.3 - Mn/Zr and Fe/Zr atomic ratios for zonal and mapping EDS analyses in supported Fib Zr(C).

Sample **	M*/Zr atomic ratios									
	Fiber N°	Zone 1 (Spot)	Zone 2 (Spot)	Zone 3 (Spot)	Average per fiber (Zones 1, 2 and 3)	Spot average	Mapping per fiber	Big area mapping, Fig. 13 (c,d) (wt.% - ICP)	Nominal (wt.%)
Mn-Fib Zr(C)	1	0.02	0.01	0.01	0.02	0.07	0.05	0.20 (3.8)	0.10 (4.0)
	2	0.10	0.16	0.12	0.13		0.15		
	3	0.07	0.07	0.08	0.07		0.06		
Fe-Fib Zr(C)	1	0.48	0.27	0.47	0.41	0.30	0.45	0.35 (4.8)	0.25 (9.9)
	2	0.20	0.27	0.27	0.24		0.50		
	3	0.22	0.10	0.42	0.24		0.14		

** M = Mn or Fe*

*** Three fibers per sample were analyzed*

3.3 TEM analysis (AR)

TEM images for all catalysts are shown in Fig. 4.14. Bare Fib Zr(B) (Fig. 4.14 - a) exhibits rounded-edge particles 13.6 ± 3.8 nm size (inset picture), whereas Fib Zr(C) appear as bigger particles 69.8 ± 22.9 nm (inset image) with marked edges (Fig. 4.14 - d). For Mn-Fib Zr(B) the same morphology as that of the support is observed, along with the appearance of bigger rounded particles (Fig. 4.14 - b). On the contrary, for Fe-Fib Zr(B), a different morphology can be appreciated, consisting of short rods of 19.9 ± 3.8 nm width and about 60 nm length (Fig. 4.14 - c).

In the case of supported commercial fibers, Mn-Fib Zr(C) maintains the morphology of the bare fibers, showing also lengthened particles (rods), probably ascribed to manganese oxides (Fig. 4.14 - e). For Fe-Fib Zr(C), it can be noticed that the morphology is similar to that of Fib Zr(C), with the presence of slightly bigger particles with more rounded edges (Fig. 4.14 - f).

It is worth noticing that rods are obtained for both Fe-Fib Zr(B) and Mn-Fib Zr(C), being more rounded in the former and with more marked edges in the latter.

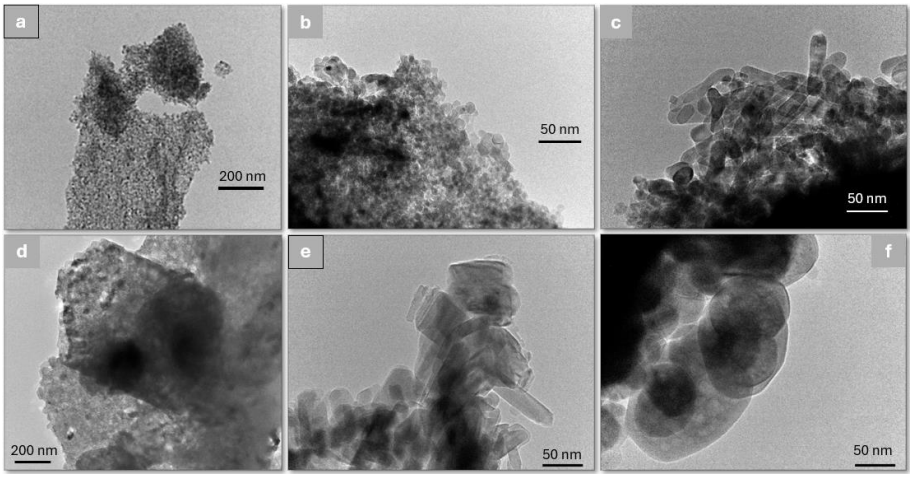

Fig. 4.14 - TEM images of Fib Zr(B) (a), Mn-Fib Zr(B) (b), Fe-Fib Zr(B) (c), Fib Zr(C) (d), Mn-Fib Zr(C) (e), and Fe-Fib Zr(C) (f).

Additionally, EDS analysis was performed on all catalysts to study the distribution of the plasma-deposited elements (Mn or Fe) on the supports (Figs. 4.15 and 4.16), where Fig. 4.15 - a, e and Fig. 4.16 - a, e correspond to bright field images whereas Fig. 4.15 - b, f and Fig. 4.16 - b, f to dark field ones.

As regard to the biomorphic fibers, Mn appears well distributed all along Fib Zr(B) as it is observed in Fig. 4.15 - d, whereas in the case of Fe-Fib Zr(B), Fe appears to be more concentrated on the rod zone (bottom part of Fig. 4.15 - f). For which, the rod morphology could be linked to plasma-precipitated Fe oxides.

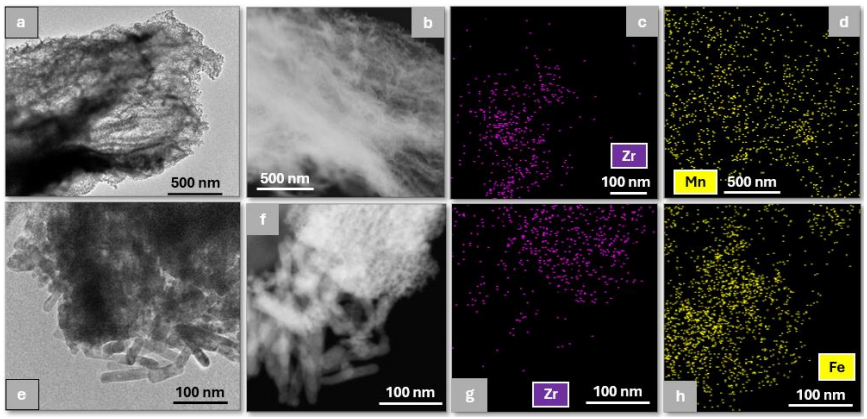

Fig. 4.15 - TEM images and EDS analyses of Mn-Fib Zr(B) (a,b,c,d) and Fe-Fib Zr(B) (e,f,g,h).

Regarding commercial fibers, Fig. 4.16 - d shows that Mn oxides are distributed throughout the sample appearing more concentrated on the rods (Fig. 4.16 - a). This agrees with what was previously observed in Fig. 4.14 - e, for which marked-edge rods could be associated with Mn species. On the other hand, for Fe-Fib Zr(C), Fe is completely covering the zirconia fiber (Fig. 4.16 - e-h).

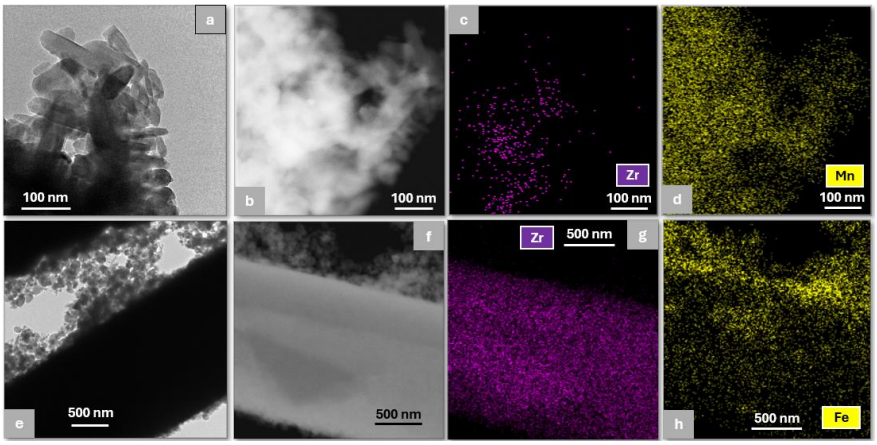

Fig. 4.16 - TEM images and EDS analyses of Mn-Fib Zr(C) (a, b, c, d) and Fe-Fib Zr(C) (e, f, g, h).

3.4 LRS analyses (BE)

LRS can further be used to corroborate the phase assignations done previously by XRD results. The LRS spectra obtained for Fib Zr(B) and Fib Zr(C) are shown in Fig. 4.17.

The Raman bands at 147, 265, 319, 463, and 642 cm^{-1} seen for Fib Zr(B) correspond to t-ZrO_2. The Fib Zr(C) sample shows several peaks centered at 178, 190, 221, 304, 333, 346, 381, 475, 501, 536, 557, 614, and 638 cm^{-1} which correspond to m-ZrO_2 [206,213–215].

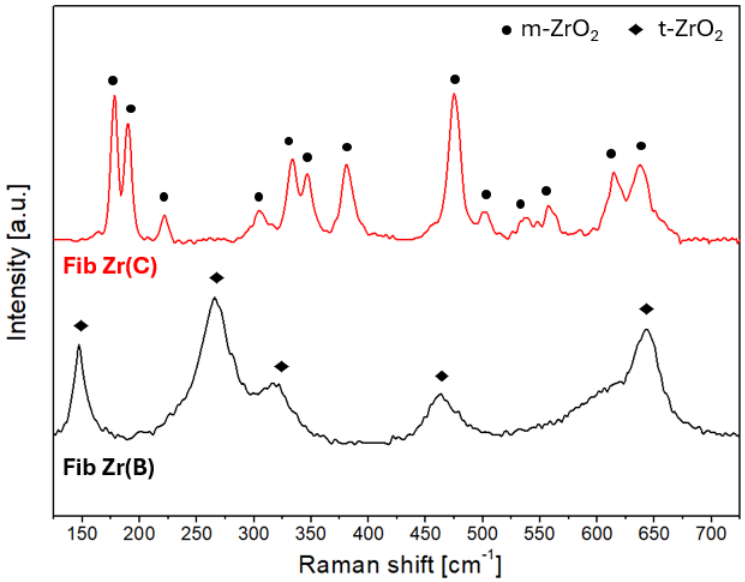

Fig. 4.17 - Raman spectra of Fib Zr(B) and Fib Zr(C).

It can be confirmed that the biomorphic fibers are constituted of tetragonal ZrO_2 (t-ZrO_2), whereas monoclinic ZrO_2 (m-ZrO_2) is the main phase present in commercial fibers. These spectra confirm XRD results. On the other hand, LRS spectra of the supported formulations (for both series of catalysts, not shown), were very similar to those of bare supports.

3.5 FTIR-ATR analyses (BE)

Figs. 4.18 and 4.19 show the FTIR-ATR spectra for Fib Zr(B) and Fib Zr(C) series of catalysis, respectively. All signal assignations made are summarized in Table 4.4.

All samples in Fib Zr(B) series (Fig. 4.18) show characteristic signals coming from physisorbed water on the sample: a broad band at 3400 cm^{-1} due to -OH stretching, and a small signal at 1646 cm^{-1} corresponding to H-O-H vibrations. The bands located at 1542, 1360, and 1100 cm^{-1} are associated to strongly adsorbed carbonates, which could originate from CO_2 chemisorption after the template decomposition or from ambient air contact [142,143,216]. This agrees with what was observed for biomorphic CeO_2 and Co_3O_4 fibers in Chapters I, II, and III. These carbonate bands are less pronounced after Mn deposition and are not present in the Fe-supported sample. In the latter, a broad band with a maximum at 1140 cm^{-1} is observed, which is related to sulphate species coming from the precursor (Mohr's salt) and remaining in the catalyst after calcination. As mentioned in the previous chapter (similar situation), the absence of carbonates could be due to the displacement of these species by the sulphates [187,217].

In the metal-oxygen region, a broad band situated at approximately 690 cm^{-1} is present in Fib Zr(B) and also for both supported samples. As reported and according to XRD and LRS results, this band is assigned to Zr-O vibrations from t-ZrO_2 [218]. Besides, another band at 436 cm^{-1} is observed both for bare and catalytic biomorphic samples, also coming Zr-O vibrations of t-ZrO_2 [219].

For Mn-Fib Zr(B), a clear shoulder appears at 511 cm^{-1} that matches Mn-O vibrations in the cryptomelane structure. Other peaks at 462 and 682 cm^{-1} are expected from stretching modes of MnO_6 octahedral of cryptomelane which are probably overlapped by t-ZrO_2 signals [210].

As regard to Fe-Fib Zr(B) two new bands can be seen at 580 and 530 cm^{-1} which correspond to Fe-O stretching vibrations, the latter is ascribed to α-Fe_2O_3 phase and the former to Fe_3O_4 [182,188]. The other signal expected for α-Fe_2O_3 phase should appear around 435 cm^{-1}, but in this case is probably overlapped with the intense peak of Zr-O. Although the magnetite phase was not detected by XRD, it should be considered that the FTIR-ATR technique is more superficial.

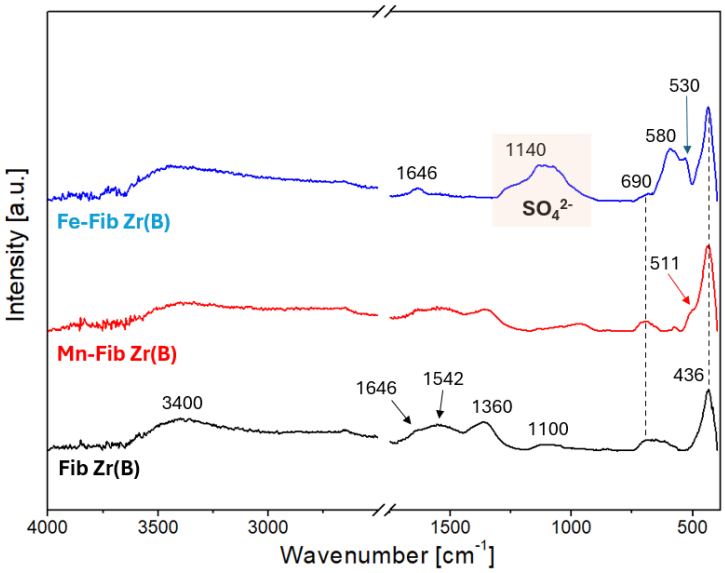

Fig. 4.18 - FTIR-ATR spectra of Mn,Fe-Fib Zr(B).

For the series of commercial fibers (Fig. 4.19), no signal due to physisorbed water is seen nor due to carbonates, probably due to their low SSA (Table 4.1).

Fib Zr(C) presents three strong absorption bands at 727, 577, and 490 cm^{-1}, along with a weak peak at 418 cm^{-1} which are all attributed to Zr-O stretching vibrations in the m-ZrO_2 structure [220].

No signal could be assigned to MnO_x species in Mn-Fib Zr(C) which could be masked by the more intense Zr-O bands.

Regarding Fe-Fib Zr(C), two new signals are evident at 520 and 434 cm^{-1} which are typical of α-Fe_2O_3 phase [183,221]. The peak around 580 cm^{-1} from Fe_3O_4 (if present) seen for Fe-Fib Zr(B) could be masked here by the ZrO_2 peak at 577 cm^{-1}. Also, if comparing Figs. 4.18 and 4.19, it can be noticed that the surface sulphates signals are weaker for Fe-Fib Zr(C), as a consequence its low SSA.

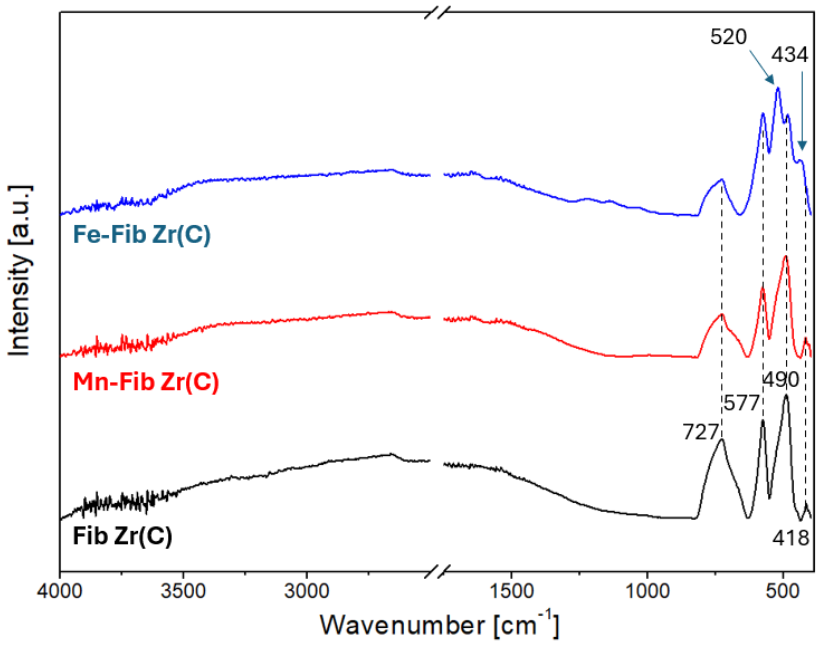

Fig. 4.19 - FTIR-ATR spectra of Mn,Fe-Fib Zr(C).

Table 4.4 - FTIR-ATR signal assignations for all catalysts.

Band position [cm^{-1}]	Assignment
3400, 1646	-OH, H-O-H (physisorbed water)
1542, 1360, 1100	Adsorbed mono-dentate and bridged CO_3^{2-}
1140	Sulphate (SO_4^{2-})
690, 436	Zr-O in t-ZrO_2
727, 577, 490, 418	Zr-O in m-ZrO_2
511	Mn-O in $K_xMn_8O_{16}$
530, 520, 434	Fe-O in α-Fe_2O_3
580	Fe-O in Fe_3O_4

3.6 Surface analysis by XPS (BE)

The following XPS core regions were studied correspondingly: C 1s, O 1s, Zr 3d, Mn 3s, Mn 2p, and Fe 2p. They are discussed in the same order.

Fig. 4.20 shows the C 1s region for all catalysts. The main peak due to carbon in C-(C,H) bonds at 284.6 eV (reference) along with a less intense peak around 288.6 eV (carbonate species), appear in all six samples. For the supported samples containing Mn, Mn-Fib Zr(B) and Mn-Fib Zr(C), two more signals are present at higher binding energies which correspond to K 2p spin-orbit doublet (K $2p_{3/2}$-$2p_{1/2}$) evidencing that some K is left on these samples from the precursor used in the synthesis (KMO). Reminding Chapter III, where Mn was supported on Fib Ce, no peak from K was seen in this region. This is an important distinction and could help to explain that different MnO_x phases are formed when the support used changes via this synthesis method.

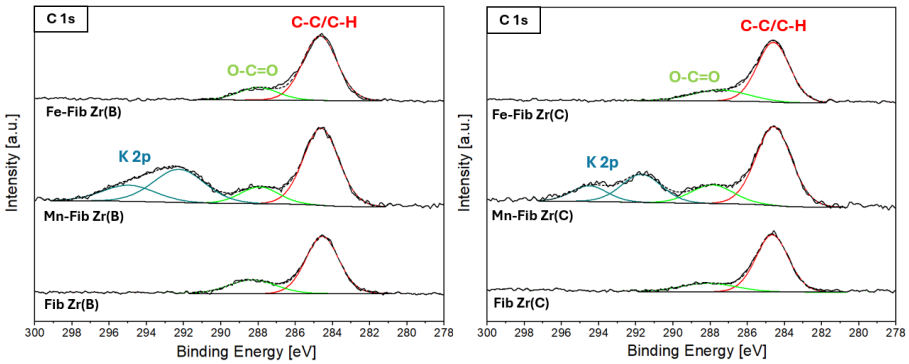

Fig. 4.20 - Surface analysis (XPS) of C1s regions for plasma-supported Fib Zr(B) (left) and Fib Zr(C) (right).

Regarding O 1s core level (Fig. 4.21), in this case all samples were fitted using only two peaks: a main peak between 529.3-529.8 eV (O_{latt}) corresponding to lattice oxygen, and a second peak characteristic of chemisorbed oxygen species (O_2^-, O_2^{2-}, O^-, CO_3^{2-}) [79,93]. There was no need to add another peak due to oxygen from water molecules as done in previous chapters. All atomic ratio values derived from these deconvolutions are listed in Table 4.5.

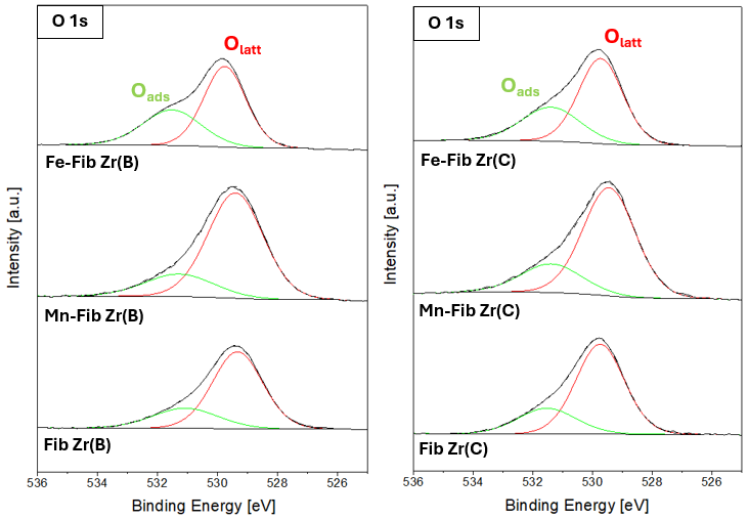

Fig. 4.21 - Surface analysis (XPS) of O1s regions for plasma-supported Fib Zr(B) (left) and Fib Zr(C) (right).

The amount of O_{ads} (and consequently the O_{ads}/O_{latt} ratio), decreased after Mn addition and increased after Fe deposition for both supports, being this effect a bit more pronounced for the biomorphic fibers. The Fe-containing samples showed a marked increase in the O_{ads}/Zr ratio reaching both a similar value. Apparently, the presence of α-Fe_2O_3 on the surface is providing a considerable amount of O_{ads} species. Mn-Fib Zr(B) did not affect much the original O_{ads}/Zr ratio of the support, whereas Mn-Fib Zr(C) suffered a marked increase to a value of 1. When comparing metal ratios (M/Zr), a higher amount of Mn accumulated on the surface of Fib Zr(C) than on Fib Zr(B), and these values are bigger than the nominal one (0.10), as expected. This is in line with EDS results shown in Tables 4.2 and 4.3, where higher amounts of Mn than those expected were found. Concerning Fe-supported samples, both of them showed considerable increments of surface M/Zr ratios with respect to the nominal value (0.25), evidencing that there is more Fe than Zr on the surface of both catalysts. Again, this agrees with the values presented in Tables 4.2 and 4.3.

Table 4.5 - XPS O 1s region peak positions, O_{ads}/O_{latt} and O_{ads}/Zr atomic ratios (XPS).

Sample	Binding energy (eV)		O_{ads} (%)	O_{ads}/O_{latt}	O_{ads}/Zr	M*/Zr (Nominal)
	O_{latt}	O_{ads}				
Fib Zr(B)	529.3	531.1	25.5	0.34	0.60	-
Mn-Fib Zr(B)	529.4	531.3	21.0	0.27	0.64	0.35 (0.10)
Fe-Fib Zr(B)	529.8	531.5	37.7	0.60	2.24	1.50 (0.25)
Fib Zr(C)	529.7	531.5	25.7	0.35	0.66	-
Mn-Fib Zr(C)	529.4	531.4	23.6	0.31	1.00	0.65 (0.10)
Fe-Fib Zr(C)	529.7	531.4	34.6	0.53	2.28	1.92 (0.25)

** M = Mn or Fe*

The Zr 3d core region for all catalysts is shown in Fig. 4.22 and the corresponding binding energies for all peaks are summarized in Table 4.6. The peaks corresponding to Zr $3d_{5/2}$ (Zr^{4+}) centered at 181.7-182.2 eV and their spin-orbit couples Zr $3d_{3/2}$ (Zr^{4+}) at 184.1-184.6 eV exhibit a separation of 2.3-2.4 eV [206,222].

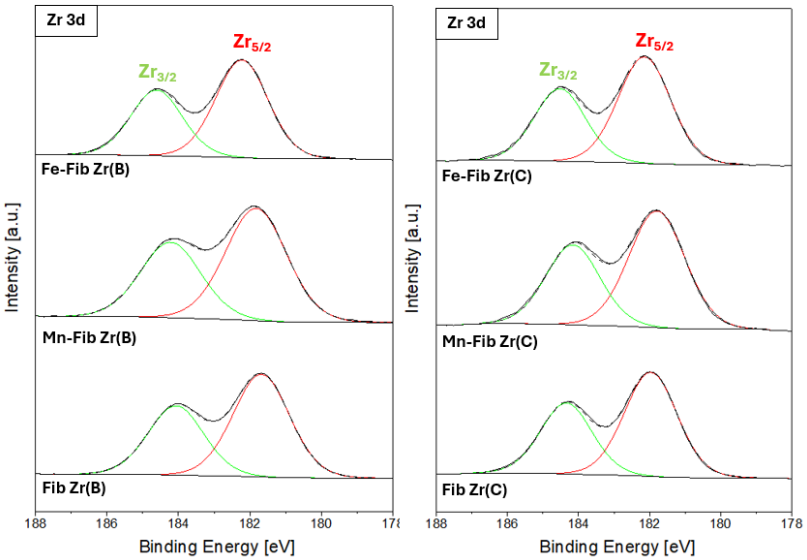

Fig. 4.22 - Surface analysis (XPS) of Zr 3d regions for plasma-supported Fib Zr(B) (left) and Fib Zr(C) (right).

Table 4.6 - XPS Zr 3d binding energies and separation.

Sample	Binding Energy (eV)		ΔBE (eV)
	Zr $3d_{5/2}$	Zr $3d_{3/2}$	
Fib Zr(B)	181.7	184.1	2.4
Mn-Fib Zr(B)	181.8	184.2	2.4
Fe-Fib Zr(B)	182.2	184.6	2.4
Fib Zr(C)	182.0	184.3	2.3
Mn-Fib Zr(C)	181.8	184.2	2.4
Fe-Fib Zr(C)	182.1	184.5	2.4

The ΔBE values for Mn-supported samples are indicated in Fig. 4.23. As in previous chapters, the peak separation (ΔBE) found in Mn 3s region was used applying Equation 4.2 to calculate the average oxidation state (AOS) of Mn [157,176].

$$AOS = 9.67 - 1.27 \times \Delta BE \qquad \textit{Equation 4.2}$$

The AOS obtained were 3.70 and 3.75 for Mn-Fib Zr(B) and Mn-Fib Zr(C), respectively. These results prove the co-existence of Mn^{3+} and Mn^{4+} species in these catalysts.

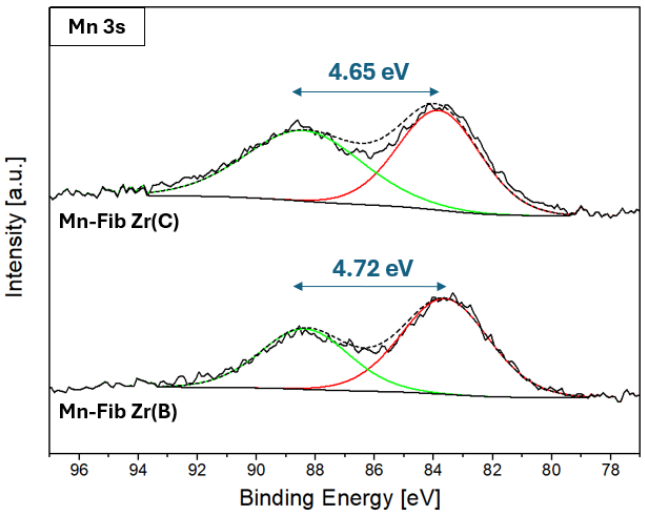

Fig. 4.23 - Surface analysis (XPS) of Mn 3s regions for Mn-Fib Zr(B) and Mn-Fib Zr(C).

The fitting of Mn 2p regions for both Mn-containing samples are shown in Fig. 4.24. The main peaks of the Mn $2p_{3/2}$-$2p_{1/2}$ presented a binding energy gap (ΔE) of about 11.6 eV. After the peak fitting, the resulted binding energies ranges for Mn^{2+}, Mn^{3+} and Mn^{4+} species were as follows: 640.6-640.3 eV, 641.7-641.4 eV, and 643.2-642.9 eV [135,141].

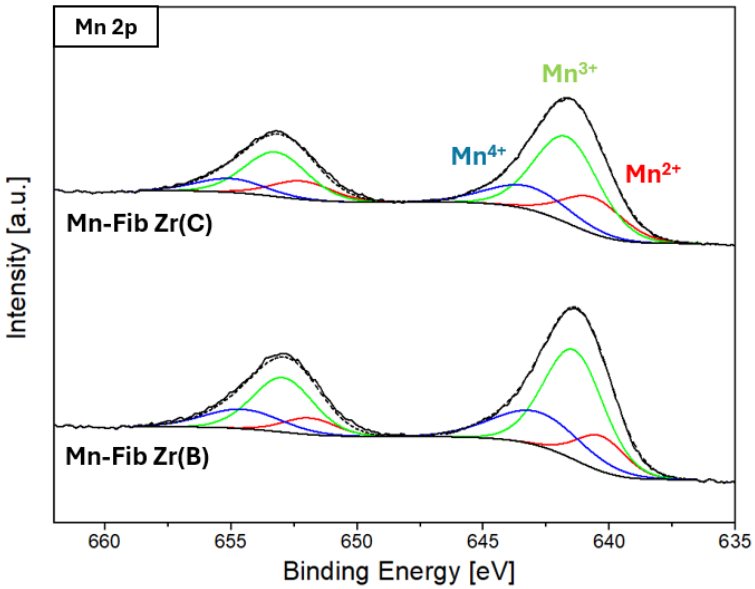

Fig. 4.24 - Surface analysis (XPS) of Mn 2p regions for Mn-Fib Zr(B) and Mn-Fib Zr(C).

The XPS spectra for the Fe-containing samples are depicted in Fig. 4.25. The binding energy separation (ΔE) between the two orbitals was 13.5 eV. A similar approach to the one applied in Chapter III was followed here for processing Fe 2p regions. Thus, several peaks centered at 710, 711.7 and 713.8 eV were assigned to Fe^{3+} species (multiple splitting), along with a satellite at 718.7 eV [192–194].

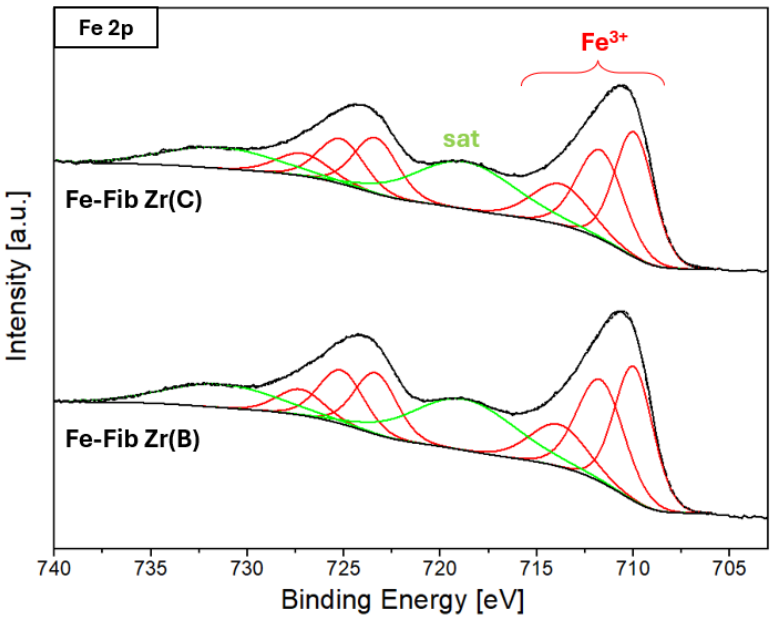

Fig. 4.25 - Surface analysis (XPS) of Fe 2p regions for Fe-Fib Zr(B) and Fe-Fib Zr(C).

3.7 Catalytic evaluations - Soot combustion (BE)

3.7.1 Activity in soot combustion of ZrO_2 biofibers calcined at different temperatures

As mentioned before in Section 3.1, the first catalytic tests were performed with Fib Zr(B)-600, Fib Zr(B)-700, and Fib Zr(B)-800 in the reaction of soot combustion (wet contact conditions). The aim of these tests was to select the most active of them to be used as a support in the plasma-precipitation synthesis and subsequent studies. The CO_2 flow profiles for these three samples are shown in Fig. 4.26.

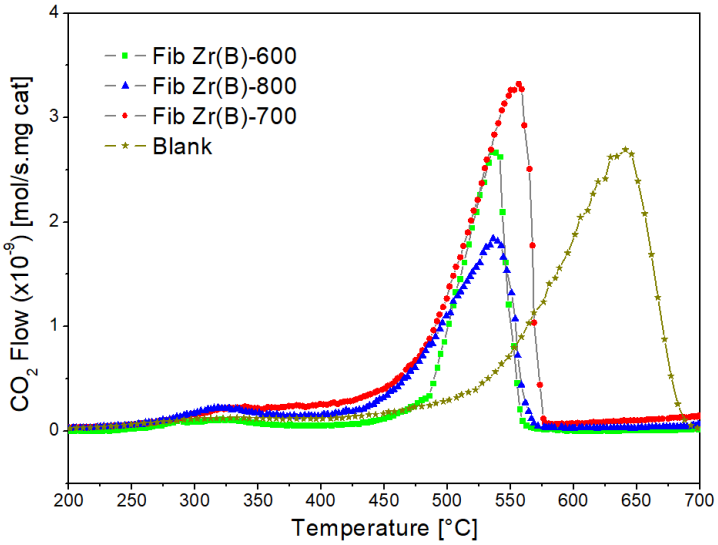

Fig. 4.26 - Soot combustion tests using Fib Zr(B) calcined at different temperatures: Fib Zr(B)-600, Fib Zr(B)-700, and Fib Zr(B)-800.

The biomorphic fibers calcined at different temperatures exhibit similar T_M values between 537 and 556 °C. These results could be correlated to their SSA values presented in Section 3.1 (Fig. 4.3) since they follow the same pattern, although not being significantly different. However, the three fibrous samples enhanced the reaction if compared to the non-catalytic soot combustion temperature (T_M = 640 °C).

Since Fib Zr(B)-600 has the highest SSA and the best T_M value in soot combustion, it was selected as support for all catalytic preparations, as previously described in this chapter.

3.7.2 Comparison of different soot-to-catalyst contacts

As reported in Chapters I and II for active supports (Fib Ce and Fib Co), a comparison of three different types of soot-to-catalyst contact was done here. The results obtained using Fib Zr(C) are presented in Fig. 4.27.

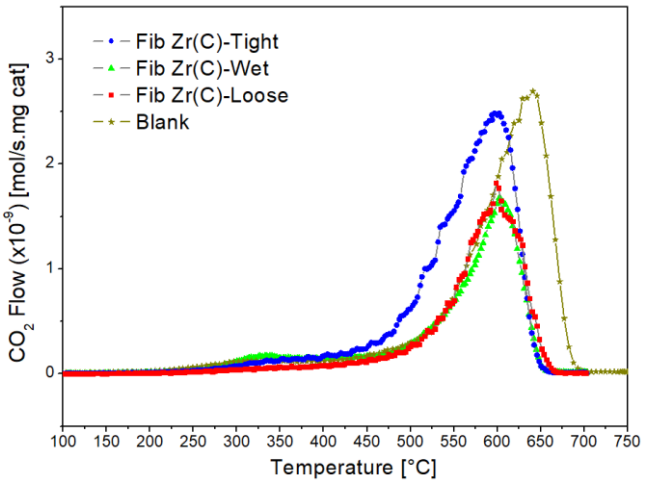

Fig. 4.27 - Soot-to-catalyst contact study comparing commercial zirconia fibers (Fib Zr(C)) in soot combustion.

From what was seen in previous chapters (Chapters I and II) when performing this contact comparison study, the order in activity was always: tight > wet > loose > blank.

In the current case (Chapter IV), all three contacts resulted in similar activities (T_M around 600 °C) and not much different from that of the blank. The contact study was done only with commercial fibers (Fib Zr(C)) although a similar behavior is expected to occur for the biomorphic ones (Fib Zr(B)) where TPO profiles would be shifted to lower temperatures (Fig. 4.26).

When active supports and catalysts are studied under different soot-to-catalyst conditions, the activity profiles are clearly distinguished as seen in Chapter I and II. Nevertheless, for a less active support like the current case (ZrO_2), the contact does not make an impact on the catalytic activity (Fig. 4.27). The conclusion that can be drawn from these tests is that the impact of the different types of soot-to-catalyst contacts strongly depend on the intrinsic activity of the support.

As done in previous chapters, wet contact was the one selected for all catalytic tests that are described afterward, since this approach provides an intermediate contact between tight and loose (for active formulations) while preserving the fibrous morphology.

3.7.3 Soot combustion tests

The CO_2 flow and soot conversion profiles derived from TPO tests for all samples are presented in Fig. 4.28 and Fig. 4.29. The corresponding T_{10}, T_{50}, T_{90} and T_M values extracted from the graphs are summarized in Table 4.7.

Among the series of biomorphic catalysts, the best performing sample was Mn-Fib Zr(B) with a T_M of 493 °C. Fe-Fib Zr(B) and Fib Zr(B) showed a similar T_M value, but the latter gave better T_{10}, T_{50}, and T_{90} values (related to different CO_2 peak shapes). The addition of Fe on this support practically did not have any positive effect on the activity.

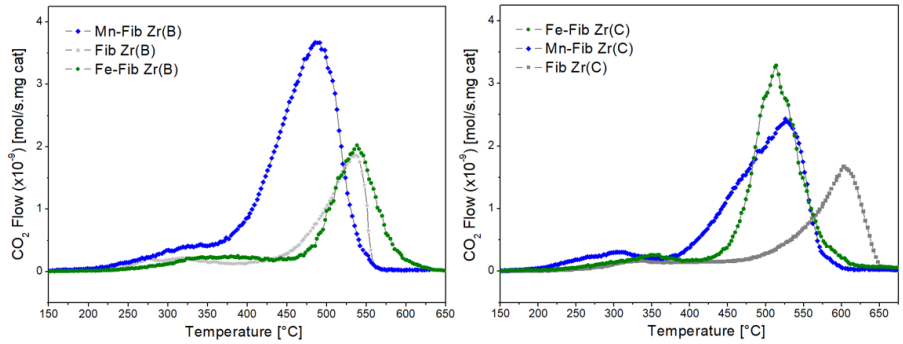

Fig. 4.28 - Soot combustion: CO_2 flow profiles for Mn,Fe-Fib Zr(B) (left) and Mn,Fe-Fib Zr(C) (right) catalysts.

Regarding the series of commercial fibers, both Mn and Fe supported samples lowered considerably the T_M value of the support in a similar manner (around 520 °C). This is the first difference in comparison to biomorphic fibers results, but also the degree of improvement in activity (gap in T_M values) is much higher for commercial fibers ($\Delta T_M \approx$ 80-90 °C) than for biomorphic fibers ($\Delta T_M \approx$ 45 °C) which can be seen in Fig. 4.28 and Table 4.7.

It is worth mentioning that Mn-Fib Zr(C) has a lower amount of catalytic phase (3.8 wt.%) in comparison to Fe-Fib Zr(C) (4.8 wt.%) and managed to have a similar activity.

It is important to consider that Mn-supported fibers contain K, as detected by XPS. As reported, alkali metals can enhance the ability of the catalysts to release active oxygen species and they can also form low-melting point compounds, which can wet the soot surface increasing the soot-to-catalyst contact [223–225].

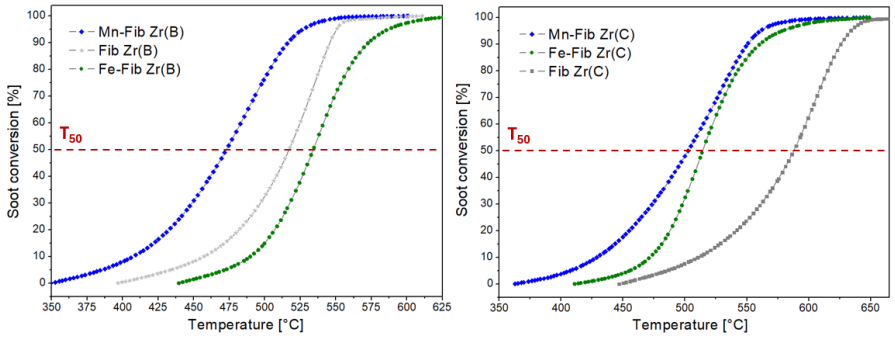

Fig. 4.29 - Soot conversion profiles for Fib Zr(B) (left) and Fib Zr(C) (right) catalysts.

On the other hand, if Fe-containing fibers are compared, Fe-Fib Zr(C) resulted more active towards soot combustion, which could be ascribed to the smaller crystallite size (XRD-Table 4.1). Contrary to what was observed for the biomorphic catalyst, an improvement in T_M was observed because the activity of bare commercial fibers is considerably worse than that of bare biomorphic fibers.

In terms of real application of these catalysts, for example in a DPF, the best T_M values achieved here do not look promising since the temperature of exhaust gases is reported to be in the range of 200-450 °C. Therefore, in order to continuously regenerate the soot trapped inside the filter, a T_M value inside the mentioned temperature window is paramount.

Table 4.7 - Summary of T_{10}, T_{50}, T_{90}, and T_M values for Fib Zr(B) and Fib Zr(C) catalysts.

Catalyst	T_{10} [°C]	T_{50} [°C]	T_{90} [°C]	T_M [°C]
Blank	528	615	659	641
Fib Zr(B)	458	517	546	537
Mn-Fib Zr(B)	407	473	516	493
Fe-Fib Zr(B)	489	534	573	538
Fib Zr(C)	511	588	625	604
Mn-Fib Zr(C)	429	502	550	525
Fe-Fib Zr(C)	472	514	560	513

There is an important distinction to be made with respect to using Fib Zr(B) and Fib Zr(C) as support in soot combustion: considerable amounts

of CO are produced as by-product. This fact was not mentioned before for Fib Ce and Fib Co because the amount of CO detected by the MS was extremely little or null. In Table 4.8, the selectivity values towards CO_2 (S_{CO2}) and CO (S_{CO}) for all catalysts tested here are listed, along with those of the supports from Chapters I and II as reference. These selectivities were calculated at their corresponding T_M values, as the latter are representative indicators of catalytic activity.

Looking at the supported formulations, it is evident that the catalytic phases added greatly improved the selectivity towards CO_2, being higher for MnO_x species.

Table 4.8 - CO_2 and CO selectivities in soot combustion for Fib Ce, Fib Co, Mn,Fe-Fib Zr(B), and Mn,Fe-Fib Zr(C) catalysts.

Chapter	Catalyst	Selectivities at T_M	
		S_{CO2}	S_{CO}
Chapter I	Fib Ce	100	0
Chapter II	Fib Co	93	7
Chapter IV	Fib Zr(B)	74	26
	Mn-Fib Zr(B)	95	5
	Fe-Fib Zr(B)	84	16
	Fib Zr(C)	71	29
	Mn-Fib Zr(C)	92	8
	Fe-Fib Zr(C)	87	13

3.8 Catalytic evaluations - Benzene oxidation (BE)

The results in the reaction of benzene oxidation for all catalysts are shown in Fig. 4.30 and all T_{10}, T_{50}, T_{90} and T_M values extracted from the graphs are listed in Table 4.9.

In general, the activity of all samples was quite poor. The bare supports, Fib Zr(B) and Fib Zr(C), were almost non-active even at 400 °C. This expose that ZrO_2, no matter its crystalline phase (t-ZrO_2 or m-ZrO_2), does not have good properties towards the oxidation of benzene. Moreover, the type of fibrous morphology did not have a significant effect either, as was seen previously for soot combustion where the biomorphic ones performed better than commercial ones.

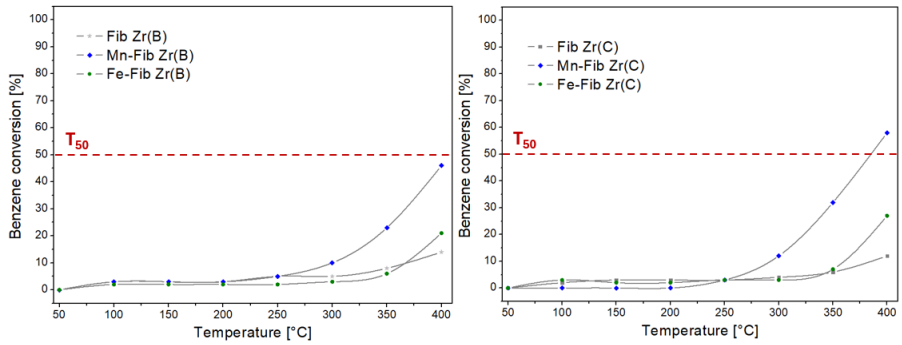

Fig. 4.30 - Benzene conversion profiles for plasma-supported Fib Zr(B) (left) and Fib Zr(C) (right) catalysts.

Fe-supported samples performed very similarly to their corresponding supports, and Mn formulations showed an increase in activity at high temperatures, being more significant for Mn-Fib Zr(C).

Table 4.9 - Catalytic activity of plasma-supported Fib Zr(B) and Fib Zr(C) catalysts in benzene oxidation.

Catalyst	T_{10} [°C]	T_{50} [°C]	T_{90} [°C]
Blank	354	> 400	> 400
Fib Zr(B)	368	> 400	> 400
Mn-Fib Zr(B)	298	> 400	> 400
Fe-Fib Zr(B)	368	> 400	> 400
Fib Zr(C)	386	> 400	> 400
Mn-Fib Zr(C)	292	385	> 400
Fe-Fib Zr(C)	361	> 400	> 400

3.9 Catalytic evaluations - CO oxidation (AR)

Both series of supported zirconia fibers were evaluated in the reaction of CO oxidation as well. The corresponding profiles are shown in Fig. 4.31 and T_{10}, T_{50}, T_{90} values for each catalyst are summarized in Table 4.9.

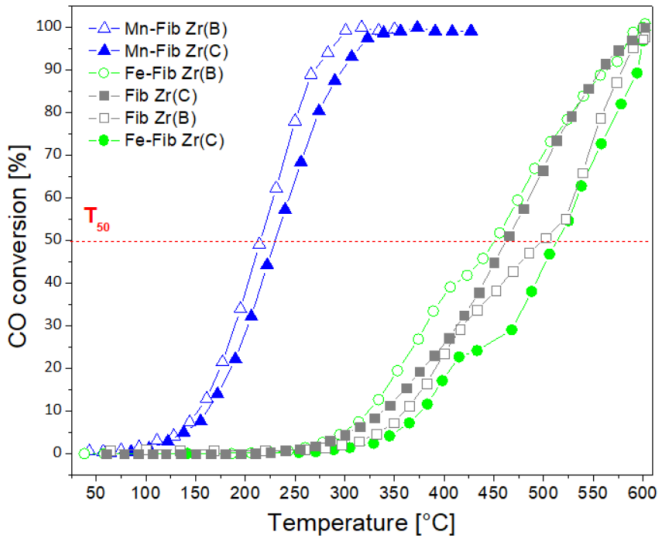

Fig. 4.31 - CO conversion profiles for plasma-supported Fib Zr(B) (left) and Fib Zr(C) (right) catalysts.

Even though both bare supports showed a poor activity in this reaction, the Mn-supported formulations, that is Mn-Fib Zr(B) and Mn-Fib Zr(C), significantly decreased T_{50} values. Their performance is close to that seen for Mn-Fib Ce, indicating that a good activity can be achieved by adding Mn to zirconia fibers, being the latter practically non-active for this reaction.

Table 4.9 - Catalytic activity of plasma-supported Fib Zr(B) and Fib Zr(C) catalysts in CO oxidation.

Catalyst	T_{10} [°C]	T_{50} [°C]	T_{90} [°C]
Fib Zr(B)	361	498	578
Mn-Fib Zr(B)	151	215	269
Fe-Fib Zr(B)	322	450	562
Fib Zr(C)	338	462	557
Mn-Fib Zr(C)	161	229	297
Fe-Fib Zr(C)	376	514	594

3.10 Catalytic comparison of all supports (BE)

3.10.1 Comparison in soot combustion

A comparison of all supports used in this thesis for the combustion of soot is shown in Fig. 4.32 as CO_2 flow profiles. The order in activity is as follows: Fib Ce > Fib Co > Fib Zr(B) > Fib Zr(C). It is noticeable that all prepared biomorphic fibers are more active than the commercial ones.

The big gap in performance between Fib Zr(B) and Fib Zr(C) could be related to the higher SSA and smaller particle sizes (TEM - Fig. 4.14, XRD - Table 4.1) of the former. Also, the fibrous morphology achieved via the biomorphic route is probably providing a better soot-to-catalyst contact (wet contact) than the commercial ones.

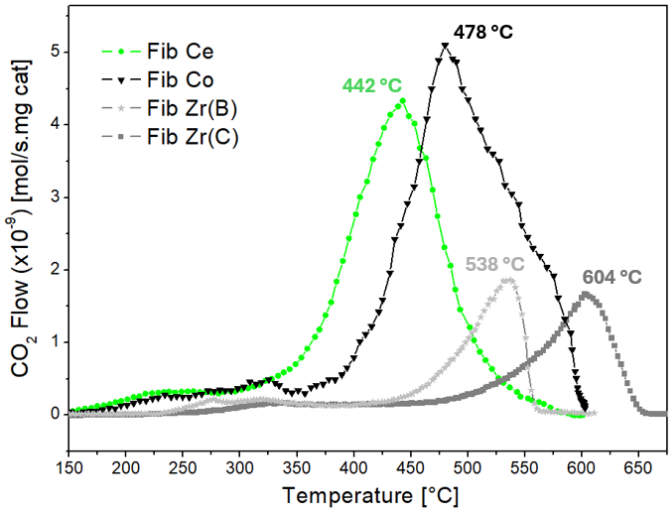

Fig. 4.32 - Comparison of all fibrous supports in soot combustion using wet soot-to-catalyst contact.

Both Fib Ce and Fib Co biomorphic fibers, fully analyzed in Chapters I and II, are evidently more active than bare zirconia fibers. This demonstrates that the supports selected for this chapter are less active in comparison to active ones.

3.10.2 Comparison in benzene oxidation

The performance in the reaction of benzene oxidation for all different supports used so far was also made. The order in activity is as follows: Fib Co > Fib Ce >> Fib Zr(B), Fib Zr(C). This is depicted in Fig. 4.33, where both ZrO_2 fibrous support (from the current chapter) showed no activity at all, followed by Fib Ce and finally Fib Co, the latter being the most active support.

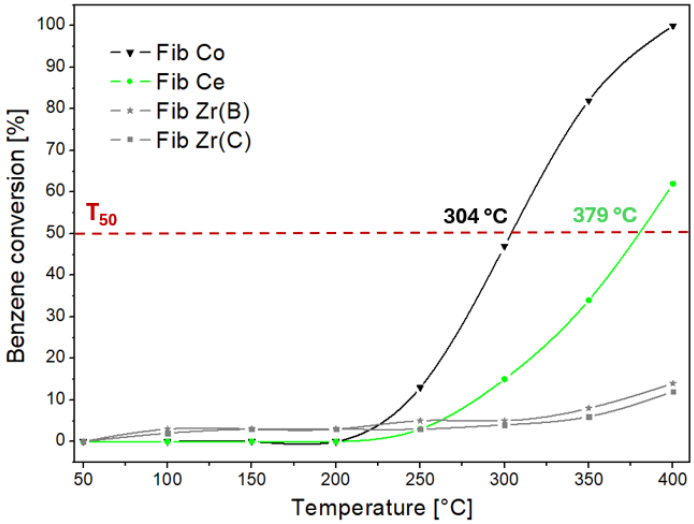

Fig. 4.33 - Comparison of all fibrous supports in benzene oxidation.

4 Main findings

Zirconia biofibers were synthesized utilizing cotton as biotemplate. It was noticed in SEM images that zirconia greatly maintained the morphology of cotton, which is probably a result of the chemical and thermal stability of zirconia.

The tetragonal phase (t-ZrO_2) was identified by XRD first and LRS afterward in Fib Zr(B) sample (calcined at 600 °C). For higher calcination temperatures in the biomorphic synthesis path (700 and 800 °C), the appearance of the monoclinic phase (m-ZrO_2) was evident. Also, bare commercial fibers (Fib Zr(C)) presented only the monoclinic phase.

In terms of textural properties, Fib Zr(B) exhibited a higher specific surface area (SSA) with smaller crystallite size than Fib Zr(C). Also, upon physisorption of N_2, all samples presented isotherms type IV or II, with a clear difference in their hysteresis loop shapes, which clearly evidences the presence of pores with different shapes and sizes.

Regarding the phases from metal oxides deposited via glidarc plasma (GP), the precipitate formed from Mn precursor was clearly identified in Mn-Fib Zr(B) as cryptomelane ($K_xMn_8O_{16}$). Contrarily, for Mn-Fib Zr(C), no peak could be assigned in XRD. On the other hand, for both Fe-containing samples, the hematite phase (α-Fe_2O_3) was evident in the diffractograms. The vibrations of the metal oxides mentioned, along with bands from other functional groups, were corroborated by ATR-FTIR as well.

The quantification of Mn and Fe on the supports by EDS-SEM showed a heterogeneous distribution in both spot and mapping analyses performed on isolated fibers. Big mapping values were generally higher than nominal values for all samples, being most significant for Fe-Fib Zr(B) catalyst. However, bulk quantification by ICP reported values close to nominal ones for Mn-samples and half as much as for Fe-samples.

TEM images, at a more nanometric scale, evidenced smaller particle size for Fib Zr(B) than Fib Zr(C), as well as a different morphology. For supported samples, different morphologies of the supported particles were seen which varied according to the support used. Lastly, EDS quantification at this scale showed a good distribution of the added metals.

In XPS analysis, the presence of potassium on the surface of Mn-supported samples was noticed, which is in line with the phase assignation done previously (cryptomelane structure). Additionally, the average oxidation state (AOS) of Mn was calculated and a similar value was obtained for both Mn-samples (around 3.7), therefore it was

assumed that both samples exhibit the same phase but with a slightly different Mn^{3+}/Mn^{4+} ratio. Furthermore, a significant accumulation of Fe on the surface was seen with Fe/Zr ratios considerably higher than nominal values.

* * *

The soot-to-catalyst contact study shed some light on the importance of the intrinsic activity of a support for the comparison of different types of contact in the reaction of soot combustion. It was found that for a low activity support or catalyst (Fib Zr(C)), the expected difference in activity between loose, tight and wet contacts does not occur, since all of them performed similar (T_M around 600 °C). This specific test was only done with commercial fibers, but the same behavior is expected to happen for biomorphic ones with the only difference that their CO_2 profiles would be shifted to lower temperatures (with a T_M value of 538 °C).

A comparison in the performance of soot combustion between all types of supports used throughout this thesis was done, in which the order found is as follows: Fib Ce > Fib Co > Fib Zr(B) > Fib Zr(C). This clearly highlights CeO_2 properties towards this reaction. It is interesting to note that Fib Zr(B) decreases the T_M by 66 °C in comparison to Fib Zr(C), which is possibly related to a higher SSA and smaller particle size. In addition, the fibrous morphology achieved from the biomorphic synthesis route could provide a better soot-to-catalyst contact (wet contact) than commercial ones.

Regarding supported biofibers, Mn-Fib Zr(B) managed to enhance the bare support activity, decreasing T_M from 537 to 493 °C (44 °C temperature-gap), while Fe-Fib Zr(B) did not affect it whatsoever. On the other hand, both Mn and Fe supported commercial fibers improved the activity of Fib Zr(C) in the same degree ($\Delta T_M \approx$ 80-90 °C). For the latter, even though Mn-Fib Zr(C) has a lower content of catalytic phase, it resulted almost as active as Fe-Fib Zr(C).

In both series of catalysts, the cryptomelane structure ($K_xMn_8O_{16}$) proved to be more active than the hematite phase (α-Fe_2O_3). This could be related to the mixed-valence state of Mn (Mn^{3+}/Mn^{4+}) along with the presence of K on the surface that favors soot-to-catalyst contact and the release of active oxygen species.

CO_2 and CO selectivities (calculated at T_M values) showed considerable amounts of CO released as by-product for Fib Zr(B) and Fib Zr(C). However, this was not the case when testing active supports (Fib Ce and Fib Co), where CO production was negligible. In all cases, after Mn or Fe addition, the selectivity towards CO_2 was greatly improved.

The activity of both bare supports in the oxidation of benzene was poor, almost being inactive at 400 °C. Only Mn-supported samples showed a slight improvement, reaching around 50% conversion of benzene at 400 °C. A comparison of all supports used in this thesis for this reaction clearly showed that Fib Co is the most active among them.

Despite the fact that some of the catalysts studied in this chapter might not have proven to be very successful for the chosen target reactions (especially in the case of benzene oxidation), this does not imply that in other scenarios they could provide good catalytic performances. For example, the prepared ZrO_2 fibers could be tested in reactions where ZrO_2 properties play a key role (hydrogenation, isomerization and transesterification). The same could be applied for Fe-supported fibers: they could be tried in reactions where iron oxides are known to be active (water-gas shift reaction, dehydrogenation and Fenton process).

GENERAL OBSERVATIONS

At this point in the thesis, where all results have been presented and discussed, it is interesting to compile some trends and patterns seen throughout the whole thesis concerning the syntheses procedures, as well as specific catalysts properties linked to good activity. Furthermore, the main properties of the best catalytic formulations found in this work are summarized, followed by a comparison to the performance of catalysts from the literature for all target reactions.

Morphology of supported biomorphic catalysts

As regard to both deposition techniques (WI and GP), a similar trend was seen for the supported fibers, which shortened and widened after the deposition of active phases. This can be clearly seen in the following picture (Fig. go. 1) taking Fib Ce as example.

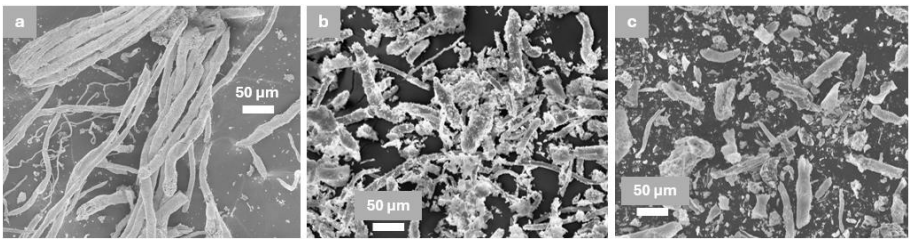

Fig. go. 1 - Morphological changes of biomorphic Fib Ce (a) after WI (b) and GP (c) depositions.

Correlations of good performance and catalytic properties for soot oxidation

From all results obtained for the soot oxidation reaction, some tentative correlations between catalysts properties and their activity can be made. However, it should be noted that synthesizing a catalyst with these properties will not guarantee a good performance, since this depends on a combination of factors.

Fig. go. 2 shows the influence of the Mn average oxidation state (AOS_{Mn}) with respect to T_M values, for all Mn-supported Fib Ce catalysts prepared in this thesis. It can be clearly seen that the lower the AOS_{Mn}, the lower the T_M, i.e., a better activity is attained.

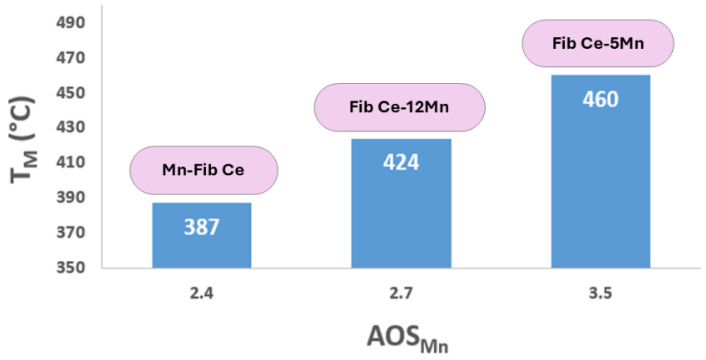

Fig. go. 2 - Mn average oxidation state (AOS_{Mn}) vs Temperature at maximum soot combustion rate (T_M) for all Mn-supported Fib Ce catalysts.

Another pattern was encountered regarding the concentration of Ce^{3+} species in the catalysts surface (Fig. go. 3). This column graph highlights that supported Fib Ce catalysts that showed a higher content of Ce^{3+} on the surface, performed better, therefore lower T_M values.

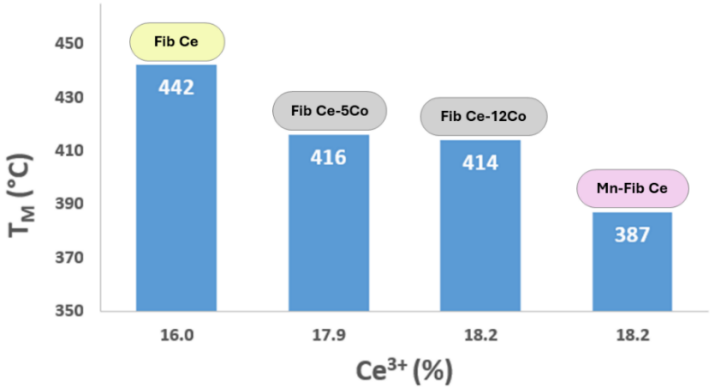

Fig. go. 3 - Surface Ce^{3+} content vs Temperature at maximum soot combustion rate (T_M) for supported Fib Ce catalysts.

Correlations of good performance and catalytic properties for benzene and CO oxidation

Finally, in a similar vein to soot oxidation, tentative correlations between catalysts properties and activity in CO and benzene oxidation reactions are reported next.

Fig. go. 4 shows that supported Fib Ce with a higher concentration of O_{latt} on the surface than the support, managed to decrease the T_{50} value in benzene oxidation. A similar trend is evident in Fig. go. 5 for Mn-

supported Fib Zr which considerably decreased the T_{50} value of their respective bare supports.

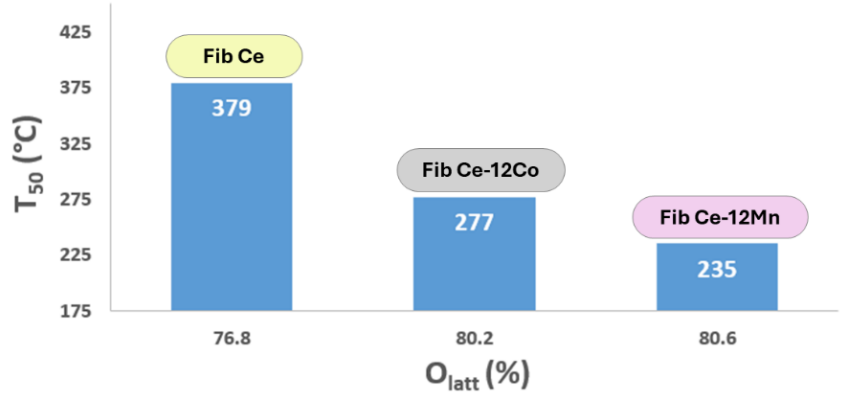

Fig. go. 4 - Surface lattice oxygen concentration (O_{latt}) vs Temperature at 50% benzene conversion (T_{50}) for supported Fib Ce catalysts.

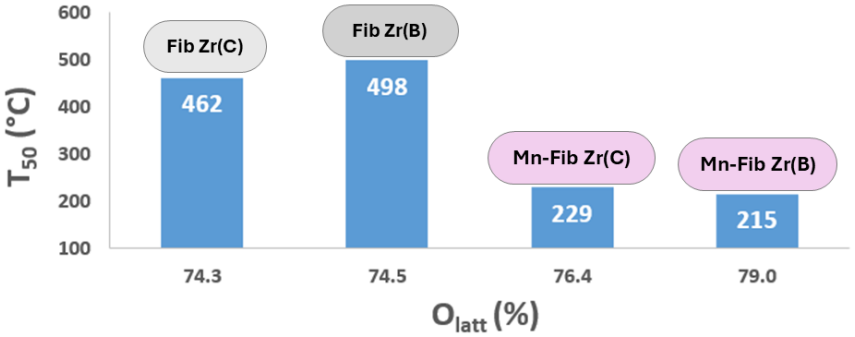

Fig. go. 5 - Surface lattice oxygen concentration (O_{latt}) vs Temperature at 50% CO conversion (T_{50}) for Mn-supported Fib Zr catalysts.

Similarly to what was reported in Fig. go. 6 for soot combustion, among all Mn-supported catalysts tested in CO oxidation, the best performing one was the one having the lowest AOS_{Mn} (Fig. go. 5).

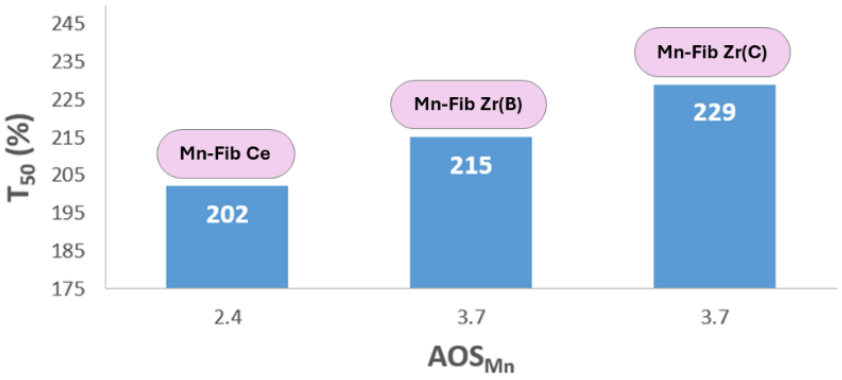

Fig. go. 6 - Mn average oxidation state (AOS_{Mn}) vs Temperature at 50% CO conversion (T_{50}) for all Mn-supported catalysts.

Best performing catalysts and comparisons with the literature

The following table (Table go. 1) reports the main properties of the best performing catalysts in all three oxidation reactions tested in this work.

Table go. 1 - Properties of the best performing catalysts in all oxidation reactions.

Target reaction	Best catalyst	Properties
Soot	Mn-Fib Ce	Good distribution (MnO_x) ↓ Particle size (MnO_x) AOS_{Mn} = 2.5 O_{ads} ≈ Fib Ce ↓ Ce^{3+}
CO		
Benzene	Fib Ce-12Mn	Solid solution Good distribution (MnO_x) AOS_{Mn} = 2.7 ↑ O_v ↑ O_{latt} & Ce^{3+}

Finally, to conclude, the best performing catalysts from this work (Table go. 1) are compared to different catalysts from the literature for the reactions of soot (Table go. 2), benzene (Table go. 3) and CO (Table go. 4) oxidation reactions.

Table go. 2 - Soot combustion: comparison of activity of the best performing catalyst with others reported in the literature.

Catalysts [Reference]	**Feed composition**	**Soot-catalyst wt. ratio Type of soot Type of contact**	**T_M (°C) [T_{50} (°C)]**
Mn-Fib Ce [This thesis]	3.3% O_2, 33% Ar, He balance	1:20 Printex U Wet contact	386 [384]
K/MnO_2 [226]	10% O_2, N_2 balance	1:10 Printex U Loose contact	nr [478]
Pt/$LaCoO_3$ [227]	Air atmosphere, N_2 balance	1:10 Printex U Loose contact	nr [437]
CeO_2 (fibers) [92]	10% O_2, N_2 balance	1:9 Printex U Loose contact	553 [533]
Mn_3O_4 [23]	0.05% NO, 5% O_2, He balance	1:4 Printex U Loose contact	nr [510]
12Co/CeO_2 (fibers) [123]	0.1% NO, 18% O_2, He balance	1:20 Real soot Wet contact	375 nr
MnO_x-CeO_2 [228]	0.1% NO, 10% O_2, N_2 balance	1:20 Real soot Loose contact	460 nr

nr = not reported.

From this table (Table go. 2), it can be observed that the best performing catalyst here reported exhibit a good activity in comparison to different formulations from the literature. However, it is important to note that the screening of catalysts in the reaction of soot combustion is difficult since there are many variables affected the T_M/T_{50} values such as feed composition, type of soot, soot-to-catalyst ratio and soot-to-catalyst contact.

Regarding benzene oxidation, Table go. 3 shows a comparison of different formulations from the literature with Fib Ce-12 Mn catalyst (Chapter I). It can be noted that the activity of the latter is comparable to that of non-noble metal catalysts.

Table go. 3 - Benzene oxidation: comparison of activity of the best performing catalyst with others reported in the literature.

Catalysts [Reference]	**Feed composition [Space velocity (mL. $g^{-1}.h^{-1}$)]**	**T_{90} (°C)**	**Reaction rate at 190 °C (µmol Bz/g cat. s)**
Fib Ce-12Mn [This thesis]	200 ppm benzene, 10% O_2, He balance. [60000]	288	0.022
0.25Pt/Fe_2O_3 [229]	1000 ppm benzene, 20% O_2, N_2 balance. [20000]	198	0.125
6.5Au/Co_3O_4 [230]	1000 ppm benzene, 40% O_2, N_2 balance. [20000]	189	0.206
$CoMn_2AlO$ [231]	100 ppm benzene, 20% O_2, N_2 balance. [60000]	208	0.038
CeO_2/$LaCoO_3$ [232]	500 ppm benzene, air. [96000]	410	nr
10Mn/$Ce_{0.75}Zr_{0.25}O_2$ [35]	2000 ppm benzene, air. [72000]	340	nr
Mn_3O_4 [38]	1000 ppm benzene, 20% O_2, N_2 balance. [60000]	360	nr

nr = not reported.

With respect to CO oxidation, a comparison of Mn-Fib Ce performance (Chapter III) with different catalysts from the literature is presented in Table go. 4.

Table go. 4 - CO oxidation: activity comparison to catalysts from the literature.

Catalysts [Reference]	Feed composition	T_{50} (°C)
Mn-Fib Ce [This thesis]	1% CO, 2% O_2, He balance.	202
$Ce_{80}Zr_{10}Pr_{10}$ [233]	0.1% CO, 50% air in N_2.	239
12Co/CeO_2 (fibers) [234]	1% CO, 2% O_2, He balance.	201
Ce-Zr-O [235]	0.1% CO, 10% O_2, He balance.	250
MnO_x-CeO_2 [236]	1.5% CO, 10% O_2, N_2 balance.	225
Cu-CeO_2 [237]	1.5% CO, 2.5% O_2, N_2 balance.	250
Ce-ZrO_2 [238]	1% CO, 4% O_2, N_2 balance.	180

GENERAL CONCLUSIONS - FUTURE WORK

General conclusions

Synthesis of supported catalytic fibers

The biomorphic method of synthesis allowed the obtention of oxides with fibrous morphology. Although starting from the same biotemplate (cotton), different fibers were obtained when using different precursor solutions. In the case of Ce and Co precursors, the impregnated cotton fibers, after the elimination of cellulose by calcination, formed cylindrical and helicoidal fibers with a variety of sizes. Some of them appeared as hollow fibers while others were closed at both ends, all of them having a foamy texture. On the other hand, when a Zr precursor was used, the biofibers obtained presented more open helicoidal fibers being more regular in size and shape. These results prove that the kind of fibers (shape, size and textural properties) obtained with this method using cotton as biotemplate, highly depend on the type of metal precursors used. This is directly related to the mechanism involved during the incipient wetness impregnation process in which the interaction between the precursor and the cellulosic fibers through terminal OH groups of the latter occur. This process implies both chemical and physical adsorption phenomena, for which any precursor solution will behave differently and will consequently produce distinct biomorphic fibers. Additionally, intrinsic characteristics like thermal and chemical stability of the oxide being formed, will impact on the outcome achieved.

The use of a conventional deposition method (wet impregnation) permitted the preparation of supported catalysts using biofibers. The composition of the catalysts could be easily tuned as different amounts of Mn, Co or Ce oxides were added to CeO_2 or Co_3O_4 biofibers. The formation of these oxides originates from the precursors deposited on fibers (after the solvent is completed eliminated) through the calcination process. The added oxides appeared heterogeneously distributed on the biofibers. By this technique, the formation of solid solutions apparently occurred for supported CeO_2 fibers, which did not happen for Co_3O_4 biofibers.

On the other hand, the glidarc plasma technique allowed the obtention of oxide precipitates from precursor solutions, either with or without the presence of a support. Metal oxides of Mn or Fe were obtained in this way, and the deposition of these oxides on biomorphic fibers was attained as well. Different Mn oxides were formed when using CeO_2 or ZrO_2 biofibers as supports, which indicates that the nucleation and

growing processes are affected by the type of surface and sites available on the support. This was not the case for the Fe precursor, as the same crystalline phase was detected for both supports. For plasma-supported catalysts, no evidence was seen of the formation of solid solutions, which is expected since the precipitates initially formed as oxides.

The use of this technique provoked a heterogeneous distribution of the precipitated oxides on the fibrous supports. It should be considered that the precipitation of metal oxides by means of the glidarc technique can occur both in the homogeneous liquid phase and on the support as well. As biofibers possess irregularities and defects on their surfaces, it is expected that the nucleation may occur in preferential sites throughout the fibrous structure (heterogenous nucleation). The latter situation is kinetically favored due to its lower activation energy, in comparison to the homogeneous nucleation.

Soot combustion

Soot-to-catalyst contact is a key issue in the solid-solid-gas reaction of soot combustion. Bare CeO_2 or Co_3O_4 biofibers showed the following pattern of activity after a contact study: tight > wet > loose. However, bare ZrO_2 biofibers behaved similarly for the three types of contact and close to that of the blank. From this, it can be concluded that the intrinsic activity of the sample, whether it is an active or inert support/catalyst, is directly correlated to the performance in reaction. In order to preserve the advantage of the morphology of the catalysts, wet contact is the most promising approach.

The best performing catalysts in soot combustion, prepared by wet impregnation, were those of Co supported on Fib Ce, exhibiting a maximum combustion rate temperature of 416 and 414 °C for the samples containing 5 and 12 wt.%, respectively. The formation of a Co-Ce solid solution along with the Co_3O_4 segregation and high surface concentration of O_{latt} and Ce^{3+}, were among the main features that positively impacted on the catalytic performance. Indeed, these catalysts were tested without NO in the feed (O_2-assisted) which means that under real conditions where NO is present the activity would be even better.

Among the formulations prepared via the glidarc method, Mn-supported on Fib Ce showed a promising activity, with a maximum combustion rate temperature of 386 °C both with and without feeding NO. It is worth noting that this catalyst has only 3.3 wt.% of Mn. The main characteristics of this catalyst are a good distribution of MnO_x on CeO_2 fibers, a low particle size, and the presence of the couple Mn^{2+}/Mn^{3+}. Also, the surface

concentration of O_{latt} and Ce^{3+} are similar to those of the best catalyst prepared by wet impregnation.

As previously stated, the best catalysts for the combustion of soot were those supported on CeO_2 fibers, whether being prepared by wet impregnation (Fib Ce-Co) or glidarc plasma (Mn-Fib Ce). This proves that besides the good intrinsic properties of CeO_2 towards oxidation reactions, it also constitutes a suitable platform for the development of supported catalysts. Moreover, bare CeO_2 fibers exhibited a selectivity of 100 % towards CO_2 while for all other bare supports it was lower. The good activity and selectivity shown by these formulations would allow the use of these catalysts in a real case scenario such as the DPF system in a car.

Benzene and CO oxidation

Regarding the activity of bare supports for the oxidation of benzene, Co_3O_4 biofibers were the best one having a T_{50} value of 304 °C, highlighting the good properties of the Co_3O_4 spinel towards this reaction. However, the supported formulations (Fib Co-Mn,Ce) could not bring a considerable improvement in activity as it was the case of supported Fib Ce (Fib Ce-Mn,Co). The most active catalyst resulted to be Fib Ce-12Mn showing a remarkable T_{50} value of 235 °C. This formulation exhibited the presence of a Mn-Ce solid solution, a good distribution of MnO_x over Fib Ce, the presence of surface oxygen vacancies, a Mn average oxidation state of 2.7, and a high concentration of surface lattice oxygen. Despite bare CeO_2 fibers having a lower activity than that of Co_3O_4 biofibers, the addition of active phases enhanced notably its performance, showing again that CeO_2 fibers are a great option as support.

Concerning the oxidation of CO, the incorporation by glidarc of Mn to CeO_2 biofibers (Mn-Fib Ce), markedly decreased the T_{50} from 305 to 202 °C. This same sample was also the best tested catalyst for soot combustion, as previously mentioned.

Despite being both gaseous reactants, benzene and CO are naturally two different compounds. The former is an aromatic compound with six carbon atoms whereas the latter is a smaller linear molecule. This was evidenced in the thesis in the catalytic evaluations, since the activity patterns shown by different catalyst formulations in CO oxidation were different to those of benzene oxidation. This could be connected to a different process of adsorption on active sites based on their sizes. In this thesis, it was seen that a higher concentration of O_{latt} helped in the oxidation of benzene which was not necessarily the case for CO

oxidation. This could mean that the MVK is primarily being followed for benzene oxidation, where lattice oxygen reacts with adsorbed benzene.

* * *

In summary, it can be concluded that many of the catalytic formulations studied in this thesis managed to transform, through oxidation reactions, hazardous contaminants into more environmentally friendly compounds, thus achieving the objectives initially proposed in this thesis work.

Future work

Biomorphic synthesis

Considering that the biomorphic synthesis proved to be successful, this method could be extended to using other biotemplates from organic wastes. Furthermore, an attractive approach could be applying this method to obtain mixed oxides biofibers, e.g. CeO_2-ZrO_2, aiming at improving the properties of bare CeO_2 (reducibility, oxygen storage capacity and thermal stability). Moreover, other combinations such as CeO_2-Co_3O_4 or Al_2O_3-ZrO_2 could be attempted as well. The addition of additives to the precursor solution might help in the retention of the template morphology.

Deposition techniques

Other types of deposition methods could be tried on the biomorphic fibers, such as atomic layer deposition or chemical vapor deposition, to prepare supported catalysts with the aim of enhancing the distribution of the supported species.

Regarding the failed trials with ceramic papers exposed to glidarc plasma, a new reactor design that allows to stir the solution without being in contact with the ceramic paper (isolated compartment) could be helpful, so that the migration of plasma generated species would be favored, and the support structure preserved. The same concept would apply for the wet impregnation method so as to not cause any damage to the fibrous supports.

The glidarc technique could be optimized in order to control the amount of precipitate generated varying the exposure time and the concentration of the target solutions.

It could be interesting to study why different Mn phases are obtained for different supports exposed to glidarc plasma, as well as the presence of potassium in the precipitates formed.

Other precursors solutions could be exposed to the glidarc plasma in order to keep studying different oxides and their activity in oxidation or other reactions of interest.

Structured catalysts

Both wet-impregnated and plasma-deposited catalytic fibers could be potentially used in the synthesis of ceramic papers by replacing partially or totally the cellulosic fibers, or by simply adding them as an extra ingredient in the paper-making technique. Also, other alternatives could be attempted to produce structured catalysts from supported biofibers such as their deposition on monoliths via washcoating.

Target reactions

Even though some formulations prepared in this thesis did not perform well for some reactions, they could be explored in other situations. For example, ZrO_2 fibers could be tested in reactions of hydrogenation, isomerization and transesterification, where their intrinsic properties can play a role. For Fe-supported fibers, water-gas shift reaction, dehydrogenation and Fenton process are attractive options.

For the best formulations of catalysts synthesized here, other oxidation reactions could be attempted as well.

REFERENCES

[1] G. Ertl, H. Knözinger, F. Schüth, J. (Jens) Weitkamp, Handbook of heterogeneous catalysis, Second, Completely Revised and Enlarged Edition, Volume 1, Wiley-VCH (2008).

[2] I. Chorkendorff, J.W. Niemantsverdriet, Concepts of Modern Catalysis and Kinetics Third, Completely Revised and Enlarged Edition, Wiley-VCH (2017).

[3] S. Wacławek, V.V.T. Padil, M. Černík, Major Advances and Challenges in Heterogeneous Catalysis for Environmental Applications: A Review, Ecological Chemistry and Engineering S 25 (2018) 9–34. https://doi.org/10.1515/eces-2018-0001.

[4] R. Chatterjee, P. Bhanja, A. Bhaumik, The design and synthesis of heterogeneous catalysts for environmental applications, Dalton Transactions 50 (2021) 4765–4771. https://doi.org/10.1039/d1dt00544h.

[5] World Health Organization (WHO), Paris Agreement. https://ec.europa.eu/clima/eu-action/international-action-climate-change/climate-negotiations/paris-agreement_en (accessed in 2022).

[6] Continental Automotive, Worldwide Emission Standards and Related Regulations, 2019. www.continental-automotive.com (accessed in 2022).

[7] WHO (World Health Organization), Ambient (outdoor) air pollution. https://www.who.int/news-room/fact-sheets/detail/ambient-(outdoor)-air-quality-and-health (accessed in 2022).

[8] K. Vohra, A. Vodonos, J. Schwartz, E.A. Marais, M.P. Sulprizio, L.J. Mickley, Global mortality from outdoor fine particle pollution generated by fossil fuel combustion: Results from GEOS-Chem, Environ Res 195 (2021). https://doi.org/10.1016/j.envres.2021.110754.

[9] WHO (World Health Organization), Billions of people still breathe unhealthy air: new WHO data, (n.d.). https://www.who.int/news/item/04-04-2022-billions-of-people-still-breathe-unhealthy-air-new-who-data (accessed in 2022).

[10] Primary and secondary pollutants: these are the most dangerous, Envira.Global (accessed in 2022).

[11] S. Trivedi, R. Prasad, A four-way catalytic system for control of emissions from diesel engine, Sādhanā (2018) 43–130. https://doi.org/10.1007/s12046-018-0884-0S.

REFERENCES

[12] United States Environmental Protection Agency, Particulate Matter (PM) Basics | US EPA, (n.d.). https://www.epa.gov/pm-pollution/particulate-matter-pm-basics#PM (accessed in 2022).

[13] L. Zhang, C. Ou, D. Magana-Arachchi, M. Vithanage, K.S. Vanka, T. Palanisami, K. Masakorala, H. Wijesekara, Y. Yan, N. Bolan, M.B. Kirkham, Indoor particulate matter in urban households: Sources, pathways, characteristics, health effects, and exposure mitigation, Int J Environ Res Public Health 18 (2021). https://doi.org/10.3390/ijerph182111055.

[14] H. Reis, C. Reis, A. Sharip, W. Reis, Y. Zhao, R. Sinclair, L. Beeson, Diesel exhaust exposure, its multi-system effects, and the effect of new technology diesel exhaust, Environ Int 114 (2018) 252–265. https://doi.org/10.1016/j.envint.2018.02.042.

[15] S.M. Platt, I. El Haddad, S.M. Pieber, A.A. Zardini, R. Suarez-Bertoa, M. Clairotte, K.R. Daellenbach, R.J. Huang, J.G. Slowik, S. Hellebust, B. Temime-Roussel, N. Marchand, J. De Gouw, J.L. Jimenez, P.L. Hayes, A.L. Robinson, U. Baltensperger, C. Astorga, A.S.H. Prévôt, Gasoline cars produce more carbonaceous particulate matter than modern filter-equipped diesel cars, Sci Rep 7 (2017). https://doi.org/10.1038/s41598-017-03714-9.

[16] A. Kontses, G. Triantafyllopoulos, L. Ntziachristos, Z. Samaras, Particle number (PN) emissions from gasoline, diesel, LPG, CNG and hybrid-electric light-duty vehicles under real-world driving conditions, Atmos Environ 222 (2020). https://doi.org/10.1016/j.atmosenv.2019.117126.

[17] B. Guan, R. Zhan, H. Lin, Z. Huang, Review of the state-of-the-art of exhaust particulate filter technology in internal combustion engines, J Environ Manage 154 (2015) 225–258. https://doi.org/10.1016/j.jenvman.2015.02.027.

[18] S. Mohankumar, P. Senthilkumar, Particulate matter formation and its control methodologies for diesel engine: A comprehensive review, Renewable and Sustainable Energy Reviews 80 (2017) 1227–1238. https://doi.org/10.1016/j.rser.2017.05.133.

[19] A. Beji, K. Deboudt, B. Muresan, S. Khardi, P. Flament, M. Fourmentin, L. Lumiere, Physical and chemical characteristics of particles emitted by a passenger vehicle at the tire-road contact, Chemosphere 340 (2023). https://doi.org/10.1016/j.chemosphere.2023.139874.

REFERENCES

[20] E.O. Semmens, C.W. Noonan, R.W. Allen, E.C. Weiler, T.J. Ward, Indoor particulate matter in rural, wood stove heated homes, Environ Res 138 (2015) 93–100. https://doi.org/10.1016/j.envres.2015.02.005.

[21] K. Adams, D.S. Greenbaum, R. Shaikh, A.M. van Erp, A.G. Russell, Particulate matter components, sources, and health: Systematic approaches to testing effects, J Air Waste Manage Assoc 65 (2015) 544–558. https://doi.org/10.1080/10962247.2014.1001884.

[22] Marco Piumetti, Samir Bensaid, Nanostructured Catalysts for Environmental Applications, Springer International Publishing (2021). https://doi.org/10.1007/978-3-030-58934-9.

[23] A. Bueno-López, Diesel soot combustion ceria catalysts, Appl Catal B 146 (2014) 1–11. https://doi.org/10.1016/j.apcatb.2013.02.033.

[24] A.M. Hernández-Giménez, D.L. Castelló, A. Bueno-López, Diesel soot combustion catalysts: Review of active phases, Chemical Papers 68 (2014) 1154–1168. https://doi.org/10.2478/s11696-013-0469-7.

[25] R. Prasad, Venkateswara Rao Bella, A Review on Diesel Soot Emission, its Effect and Control, Bulletin of Chemical Reaction Engineering & Catalysis 5 (2010) 69–86. https://doi.org/10.9767/bcrec.5.2.794.69-86.

[26] D. Fino, S. Bensaid, M. Piumetti, N. Russo, A review on the catalytic combustion of soot in Diesel particulate filters for automotive applications: From powder catalysts to structured reactors, Appl Catal A Gen 509 (2016) 75–96. https://doi.org/10.1016/j.apcata.2015.10.016.

[27] L. Castoldi, An overview on the catalytic materials proposed for the simultaneous removal of NO_x and soot, Materials 13 (2020). https://doi.org/10.3390/MA13163551.

[28] G.C. Dhal, S. Dey, D. Mohan, R. Prasad, Simultaneous abatement of diesel soot and NO_X emissions by effective catalysts at low temperature: An overview, Catal Rev Sci Eng 60 (2018) 437–496. https://doi.org/10.1080/01614940.2018.1457831.

[29] E.D. Bans, M.A. Ulla, E.E. Mir, V.G. Milt, Structured Catalysts for Soot Combustion for Diesel Engines, in: Diesel Engine - Combustion, Emissions and Condition Monitoring, InTech (2013). https://doi.org/10.5772/54516.

[30] C. Yang, G. Miao, Y. Pi, Q. Xia, J. Wu, Z. Li, J. Xiao, Abatement of various types of VOCs by adsorption/catalytic oxidation: A review, Chemical Engineering Journal 370 (2019) 1128–1153. https://doi.org/10.1016/j.cej.2019.03.232.

REFERENCES

[31] M.S. Kamal, S.A. Razzak, M.M. Hossain, Catalytic oxidation of volatile organic compounds (VOCs) - A review, Atmos Environ 140 (2016) 117–134. https://doi.org/10.1016/j.atmosenv.2016.05.031.

[32] Y. Guo, M. Wen, G. Li, T. An, Recent advances in VOC elimination by catalytic oxidation technology onto various nanoparticles catalysts: a critical review, Appl Catal B 281 (2021). https://doi.org/10.1016/j.apcatb.2020.119447.

[33] Medium.com, Global Strategies for Mitigating Air Pollution and Preserving Public Health, Medium.Com (2023).

[34] C. He, J. Cheng, X. Zhang, M. Douthwaite, S. Pattisson, Z. Hao, Recent Advances in the Catalytic Oxidation of Volatile Organic Compounds: A Review Based on Pollutant Sorts and Sources, Chem Rev 119 (2019) 4471–4568. https://doi.org/10.1021/acs.chemrev.8b00408.

[35] I.C. Sophiana, A. Topandi, F. Iskandar, H. Devianto, N. Nishiyama, Y.W. Budhi, Catalytic oxidation of benzene at low temperature over novel combination of metal oxide-based catalysts: CuO, MnO_2, NiO with $Ce_{0.75}Zr_{0.25}O_2$ as support, Mater Today Chem 17 (2020). https://doi.org/10.1016/j.mtchem.2020.100305.

[36] T.Y. Li, S.J. Chiang, B.J. Liaw, Y.Z. Chen, Catalytic oxidation of benzene over $CuO/Ce_{1-x}Mn_xO_2$ catalysts, Appl Catal B 103 (2011) 143–148. https://doi.org/10.1016/j.apcatb.2011.01.020.

[37] Y. Xiang, Y. Zhu, J. Lu, C. Zhu, M. Zhu, Q. Xie, T. Chen, Co_3O_4/α-Fe_2O_3 catalyzed oxidative degradation of gaseous benzene: Preparation, characterization and its catalytic properties, Solid State Sci 93 (2019) 79–86. https://doi.org/10.1016/j.solidstatesciences.2019.05.008.

[38] G. Liu, R. Yue, Y. Jia, Y. Ni, J. Yang, H. Liu, Z. Wang, X. Wu, Y. Chen, Catalytic oxidation of benzene over Ce-Mn oxides synthesized by flame spray pyrolysis, Particuology 11 (2013) 454–459. https://doi.org/10.1016/j.partic.2012.09.013.

[39] R.N. Colvile, E.J. Hutchinson, J.S. Mindell, R.F. Warren, The transport sector as a source of air pollution, Atmospheric Environment 35 (2001) 1537-1565.

[40] D.A. Vallero, Environmental Impacts of Energy Production, Distribution and Transport, in: Future Energy: Improved, Sustainable and Clean Options for Our Planet, Elsevier Inc., 2013: pp. 551–581. https://doi.org/10.1016/B978-0-08-099424-6.00025-9.

[41] Combustion of hydrocarbons, Nature 130 (1932) 440–441. https://doi.org/10.1016/b978-0-7506-8632-7.10010-6.

REFERENCES

[42] P. Li, X. Chen, Y. Li, J.W. Schwank, A review on oxygen storage capacity of CeO_2-based materials: Influence factors, measurement techniques, and applications in reactions related to catalytic automotive emissions control, Catal Today (2019) 90–115. https://doi.org/10.1016/j.cattod.2018.05.059.

[43] United States Environmental Protection Agency (EPA), Basic information about carbon monoxide outdoor air pollution. https://www.epa.gov/co-pollution/basic-information-about-carbon-monoxide-co-outdoor-air-pollution (accessed in 2024).

[44] S. Dey, G.C. Dhal, Materials progress in the control of CO and CO_2 emission at ambient conditions: An overview, Mater Sci Energy Technol 2 (2019) 607–623. https://doi.org/10.1016/j.mset.2019.06.004.

[45] United States Environmental Protection Agency, Air Quality. https://www.epa.gov/air-quality (accessed in 2024).

[46] World Health Organization, World Health Organization (WHO) air quality guidelines (AQGs). https://www.eea.europa.eu/publications/status-of-air-quality-in-Europe-2022/europes-air-quality-status-2022 (accessed in 2024).

[47] European Environment Agency, European Environment Agency (EEA) (2024). https://www.eea.europa.eu/en (accessed in 2024).

[48] EPA, NAAQS Table, www.epa.gov (2024). https://www.epa.gov/criteria-air-pollutants/naaqs-table (accessed in 2024).

[49] UL Solutions, Volatile Organic Compounds (VOCs): A Brief Regulatory Overview, www.ul.com (2018). https://www.ul.com/news/volatile-organic-compounds-vocs-brief-regulatory-overview (accessed in 2024).

[50] EIPIE, Air Quality, www.eipie.eu (24AD). https://eipie.eu/environmental-issues/air-quality (accessed in 2024).

[51] J.E. Vassallo, Status of Emission Control Science and Technology in Argentina, Emission Control Science and Technology 4 (2018) 73–77. https://doi.org/10.1007/s40825-018-0091-9.

[52] BASF, Mobile Emissions Control Catalysts | BASF Catalysts. https://catalysts.basf.com/industries/automotive-transportation/mobile-emissions-control-catalysts (accessed in 2022).

[53] ICCT (International Council on Clean Transportation), ICCT Euro 6/VI Briefing. https://theicct.org/ (accessed in 2024).

[54] European Council, Euro 7: Council adopts new rules on emission limits for cars, vans and trucks.

https://www.consilium.europa.eu/en/press/press-releases/2024/04/12/euro-7-council-adopts-new-rules-on-emission-limits-for-cars-vans-and-trucks/ (accessed in 2024).

[55] M. V. Twigg, Catalytic control of emissions from cars, Catal Today 163 (2011) 33–41. https://doi.org/10.1016/j.cattod.2010.12.044.

[56] B. Pereda-Ayo, J. R., NO_x Storage and Reduction for Diesel Engine Exhaust Aftertreatment, in: Diesel Engine - Combustion, Emissions and Condition Monitoring, InTech (2013). https://doi.org/10.5772/55729.

[57] A. Åberg, A. Widd, J. Abildskov, J.K. Huusom, Parameter estimation and analysis of an automotive heavy-duty SCR catalyst model, Chem Eng Sci 161 (2017) 167–177. https://doi.org/10.1016/j.ces.2016.12.024.

[58] I.A. Resitoglu, K. Altinişik, A. Keskin, The pollutant emissions from diesel-engine vehicles and exhaust aftertreatment systems, Clean Technol Environ Policy 17 (2015) 15–27. https://doi.org/10.1007/s10098-014-0793-9.

[59] P.C. Shukla, T. Gupta, A.K. Agarwal, Techniques to Control Emissions from a Diesel Engine, in: Energy, Environment, and Sustainability, Springer Nature, 2018: pp. 57–72. https://doi.org/10.1007/978-981-10-7185-0_4.

[60] Three Way Conversion (TWC) Catalyst, BASF. https://catalysts.basf.com/products/tri-metal-three-way-conversion-catalyst (accessed in 2024).

[61] S. Rood, S. Eslava, A. Manigrasso, C. Bannister, Recent advances in gasoline three-way catalyst formulation: A review, Proceedings of the Institution of Mechanical Engineers, Part D: Journal of Automobile Engineering 234 (2020) 936–949. https://doi.org/10.1177/0954407019859822.

[62] T. Montini, M. Melchionna, M. Monai, P. Fornasiero, Fundamentals and Catalytic Applications of CeO_2-Based Materials, Chem Rev 116 (2016) 5987–6041. https://doi.org/10.1021/acs.chemrev.5b00603.

[63] BASF, Four Way Conversion Catalyst (FWC). https://catalysts.basf.com/products/fwc-four-way-conversion-catalyst (accessed June 13, 2024).

[64] N.A. Sacco, J.P. Bortolozzi, V.G. Milt, E.E. Miró, E.D. Banús, One step citric acid-assisted synthesis of Mn-Ce mixed oxides and their application to diesel soot combustion, Fuel 322 (2022). https://doi.org/10.1016/j.fuel.2022.124201.

[65] S.A. Leonardi, M.A. Zanuttini, E.E. Miró, V.G. Milt, Catalytic paper made from ceramic fibres and natural ulexite. Application to diesel

particulate removal, Chemical Engineering Journal 317 (2017) 394–403. https://doi.org/10.1016/j.cej.2017.02.013.

[66] S. Wagloehner, S. Kureti, Study on the mechanism of the oxidation of soot on Fe_2O_3 catalyst, Appl Catal B 125 (2012) 158–165. https://doi.org/10.1016/j.apcatb.2012.05.032.

[67] J.P.A. Neeft, M. Makkee, J.A. Moulijn, Catalytic oxidation of carbon black – I. Activity of catalysts and classification of oxidation profiles, Fuel 77, 3, pp. 111-119 (1998).

[68] L. Hensgen, K. Stöwe, Soot-catalyst contact studies in combustion processes using nano-scaled ceria as test material, in: Catal Today (2011), pp. 100–107. https://doi.org/10.1016/j.cattod.2010.03.070.

[69] Y. Gao, X. Wu, S. Liu, D. Weng, R. Ran, MnO_x–CeO_2 mixed oxides for diesel soot oxidation: a review, Catalysis Surveys from Asia 22 (2018) 230–240. https://doi.org/10.1007/s10563-018-9255-4.

[70] A.I. Boronin, E.M. Slavinskaya, A. Figueroba, A.I. Stadnichenko, T.Y. Kardash, O.A. Stonkus, E.A. Fedorova, V. V. Muravev, V.A. Svetlichnyi, A. Bruix, K.M. Neyman, CO oxidation activity of Pt/CeO2 catalysts below 0 °C: platinum loading effects, Appl Catal B 286 (2021). https://doi.org/10.1016/j.apcatb.2021.119931.

[71] Z. Liu, J. Li, R. Wang, CeO_2 nanorods supported M–Co bimetallic oxides (M = Fe, Ni, Cu) for catalytic CO and C_3H_8 oxidation, J Colloid Interface Sci 560 (2020) 91–102. https://doi.org/10.1016/j.jcis.2019.10.046.

[72] E. Aneggi, C. de Leitenburg, M. Boaro, P. Fornasiero, A. Trovarelli, Catalytic applications of cerium dioxide, in: Cerium Oxide (CeO_2): Synthesis, Properties and Applications, Elsevier, 2020: pp. 45–108. https://doi.org/10.1016/b978-0-12-815661-2.00003-7.

[73] Z. Cuo, D. Wang, Y. Gong, F. Zhao, H. Liu, Y. Chen, A novel porous ceramic membrane supported monolithic Cu-doped Mn-Ce catalysts for benzene combustion, Catalysts 9 (2019). https://doi.org/10.3390/catal9080652.

[74] R. O'Donnell, K. Ralphs, M. Grolleau, H. Manyar, N. Artioli, Doping Manganese Oxides with Ceria and Ceria Zirconia Using a One-Pot Sol–Gel Method for Low Temperature Diesel Oxidation Catalysts, Top Catal 63 (2020) 351–362. https://doi.org/10.1007/s11244-020-01250-x.

[75] X. Tang, Y. Li, X. Huang, Y. Xu, H. Zhu, J. Wang, W. Shen, MnO_x-CeO_2 mixed oxide catalysts for complete oxidation of formaldehyde: Effect of preparation method and calcination temperature, Appl Catal B 62 (2006) 265–273. https://doi.org/10.1016/j.apcatb.2005.08.004.

[76] R. K.C, B. N.N, Cobalt doped ceria catalysts for the oxidative abatement of gaseous pollutants and colorimetric detection of H_2O_2, Mater Res Bull 139 (2021). https://doi.org/10.1016/j.materresbull.2021.111253.

[77] P. Venkataswamy, D. Jampaiah, K.N. Rao, B.M. Reddy, Nanostructured $Ce_{0.7}Mn_{0.3}O_{2-\delta}$ and $Ce_{0.7}Fe_{0.3}O_{2-\delta}$ solid solutions for diesel soot oxidation, Appl Catal A Gen 488 (2014) 1–10. https://doi.org/10.1016/j.apcata.2014.09.014.

[78] Y. Xie, C. Zhang, D. Wang, J. Lu, Y. Wang, J. Wang, L. Zhang, R. Zhang, Catalytic performance of a Bi_2O_3-Fe_2O_3 system in soot combustion, New Journal of Chemistry 43 (2019) 15368–15374. https://doi.org/10.1039/c9nj03419f.

[79] Q. Liu, A. Ma, C. Liu, Y. Li, D. Liu, J. Gui, Construction of urchin-structured Fe_2O_3 microspheres supported potassium for diesel soot catalytic elimination, Fuel 306 (2021). https://doi.org/10.1016/j.fuel.2021.121661.

[80] E. Reichelt, M.P. Heddrich, M. Jahn, A. Michaelis, Fiber based structured materials for catalytic applications, Appl Catal A Gen 476 (2014) 78–90. https://doi.org/10.1016/j.apcata.2014.02.021.

[81] Y. Matatov-Meytal, M. Sheintuch, Catalytic fibers and cloths (2002).

[82] T.F. Cooke, Fibers as supports for catalysts: a survey of the literature. TRI/Princeton, Vol. 9, Nº 1, 1990.

[83] A. Zagoruiko, S. Lopatin, Structured Glass-Fiber Catalysts (2020).

[84] M.L. Godoy, E.D. Banús, O. Sanz, M. Montes, E. Miró, V.G. Milt, Stacked wire mesh monoliths for the simultaneous abatement of VOCs and diesel soot, Catalysts 8 (2018). https://doi.org/10.3390/catal8010016.

[85] B. Xin, W. Gao, Z. Ji, S. Zhang, L. Xin, L. Zhao, H. Xue, Q. Wu, L. Zhang, C. Liu, J. Zhang, M. He, Carbon fiber-promoted activation of catalyst for efficient growth of single-walled carbon nanotubes, Carbon N Y 156 (2020) 410–415. https://doi.org/10.1016/j.carbon.2019.09.089.

[86] K. Ptaszyńska, A. Malaika, M. Kapska, M. Kozłowski, SO_3H-functionalized carbon fibers for the catalytic transformation of glycerol to glycerol tert-butyl ethers, Sci Rep 13 (2023). https://doi.org/10.1038/s41598-023-27432-7.

[87] F.M. Zoppas, T.F. Beltrame, F.A. Sosa, A.M. Bernardes, E. Miró, F.A. Marchesini, Superficial properties of activated carbon fiber catalysts produced by green synthesis and their application in water purification,

Environmental Science and Pollution Research 27 (2020) 40405–40420. https://doi.org/10.1007/s11356-020-10012-x.

[88] S.A. Leonardi, E.E. Miró, V.G. Milt, Activity of Catalytic Ceramic Papers to Remove Soot Particles - A Study of Different Types of Soot, Catalysts 12 (2022). https://doi.org/10.3390/catal12080855.

[89] K. Zhou, X. Wang, X. Sun, Q. Peng, Y. Li, Enhanced catalytic activity of ceria nanorods from well-defined reactive crystal planes, J Catal 229 (2005) 206–212. https://doi.org/10.1016/j.jcat.2004.11.004.

[90] P.A. Kumar, M.D. Tanwar, N. Russo, R. Pirone, D. Fino, Synthesis and catalytic properties of CeO 2 and Co/CeO 2 nanofibers for diesel soot combustion, in: Catal Today (2012), pp. 279–287. https://doi.org/10.1016/j.cattod.2011.12.025.

[91] E. Aneggi, D. Wiater, C. De Leitenburg, J. Llorca, A. Trovarelli, Shape-dependent activity of ceria in soot combustion, ACS Catal 4 (2014) 172–181. https://doi.org/10.1021/cs400850r.

[92] S. Bensaid, N. Russo, D. Fino, CeO_2 catalysts with fibrous morphology for soot oxidation: The importance of the soot-catalyst contact conditions, in: Catal Today (2013), pp. 57–63. https://doi.org/10.1016/j.cattod.2013.05.006.

[93] W. Zhang, X. Niu, L. Chen, F. Yuan, Y. Zhu, Soot Combustion over Nanostructured Ceria with Different Morphologies, Sci Rep 6 (2016). https://doi.org/10.1038/srep29062.

[94] W. Huang, Y. Gao, Morphology-dependent surface chemistry and catalysis of CeO_2 nanocrystals, Catal Sci Technol 4 (2014) 3772–3784. https://doi.org/10.1039/c4cy00679h.

[95] B.A. Marinho, S.M.A.G.U. de Souza, A.A.U. de Souza, D. Hotza, Electrospun TiO_2 nanofibers for water and wastewater treatment: a review, J Mater Sci 56 (2021) 5428–5448. https://doi.org/10.1007/s10853-020-05610-6.

[96] H. Esfahani, R. Jose, S. Ramakrishna, Electrospun ceramic nanofiber mats today: Synthesis, properties, and applications, Materials 10 (2017). https://doi.org/10.3390/ma10111238.

[97] M.Á. Stegmayer, V.G. Milt, N. Navascues, E. Gamez, S. Irusta, E.E. Miró, Cobalt deposited on micro and nanometric structures of ceria and zirconia applied in diesel soot combustion, Molecular Catalysis 481 (2020). https://doi.org/10.1016/j.mcat.2018.07.011.

[98] I. Moreno, N. Navascues, S. Irusta, J. Santamaria, Electrospun Au/CeO_2 nanofibers: A highly accessible low-pressure drop catalyst for

preferential CO oxidation, J Catal 329 (2015) 479–489. https://doi.org/10.1016/j.jcat.2015.06.011.

[99] T.V.S.L. Satyavani, A. Srinivas Kumar, P.S.V. Subba Rao, Methods of synthesis and performance improvement of lithium iron phosphate for high rate Li-ion batteries: A review, Engineering Science and Technology, an International Journal 19 (2016) 178–188. https://doi.org/10.1016/j.jestch.2015.06.002.

[100] L. Kumari, G.H. Du, W.Z. Li, R.S. Vennila, S.K. Saxena, D.Z. Wang, Synthesis, microstructure and optical characterization of zirconium oxide nanostructures, Ceram Int 35 (2009) 2401–2408. https://doi.org/10.1016/j.ceramint.2009.02.007.

[101] W. Liu, S. Wang, J. Wang, B. Zhang, L. Liu, H. Liu, J. Yang, Supercritical hydrothermal synthesis of nano-zinc oxide: Process and mechanism, Ceram Int 48 (2022) 22629–22646. https://doi.org/10.1016/j.ceramint.2022.05.094.

[102] S. Deuerling, S. Kugler, M. Klotz, C. Zollfrank, D. Van Opdenbosch, A Perspective on Bio-Mediated Material Structuring, Advanced Materials 30 (2018). https://doi.org/10.1002/adma.201703656.

[103] M.C. Herrera-Beurnio, J. Hidalgo-Carrillo, F.J. López-Tenllado, J. Martin-Gómez, R.C. Estévez, F.J. Urbano, A. Marinas, Bio-templating: An emerging synthetic technique for catalysts. A review, Catalysts 11 (2021). https://doi.org/10.3390/catal11111364.

[104] J. Qian, F. Chen, F. Wang, X. Zhao, Z. Chen, Daylight photocatalysis performance of biomorphic CeO_2 hollow fibers prepared with lens cleaning paper as biotemplate, Mater Res Bull 47 (2012) 1845–1848. https://doi.org/10.1016/j.materresbull.2012.04.066.

[105] T. Wang, Q. Yu, J. Kong, Preparation and heat-insulating properties of biomorphic ZrO_2 hollow fibers derived from a cotton template, Int J Appl Ceram Technol 15 (2018) 472–478. https://doi.org/10.1111/ijac.12797.

[106] T. Fan, B. Sun, J. Gu, D. Zhang, L.W.M. Lau, Biomorphic Al_2O_3 fibers synthesized using cotton as bio-templates, Scr Mater 53 (2005) 893–897. https://doi.org/10.1016/j.scriptamat.2005.06.036.

[107] V. Singh, S.K. Chakarvarti, Biotemplates and Their Uses in Nanomaterials Synthesis: A Review, American Journal of Bioengineering and Biotechnology (2016). https://doi.org/10.7726/ajbebt.2016.1001.

[108] N. Preda, A. Costas, M. Enculescu, I. Enculescu, Biomorphic 3D fibrous networks based on ZnO, CuO and ZnO–CuO composite

nanostructures prepared from eggshell membranes, Mater Chem Phys 240 (2020). https://doi.org/10.1016/j.matchemphys.2019.122205.

[109] M. Zhang, X.F. Zhang, Z.P. Deng, L.H. Huo, S. Gao, Synthesis and characterization of novel hierarchical metal oxide using scallion root as biotemplate, Mater Lett 223 (2018) 61–64. https://doi.org/10.1016/j.matlet.2018.03.166.

[110] B.A.T. Mehrabadi, S. Eskandari, U. Khan, R.D. White, J.R. Regalbuto, A Review of Preparation Methods for Supported Metal Catalysts, in: Advances in Catalysis, Academic Press Inc. (2017), pp. 1–35. https://doi.org/10.1016/bs.acat.2017.10.001.

[111] C.J. Zhong, J.R. Regalbuto, Metal Nanoparticle Synthesis, in: Comprehensive Inorganic Chemistry II (Second Edition): From Elements to Applications, Elsevier Ltd (2013), pp. 75–102. https://doi.org/10.1016/B978-0-08-097774-4.00711-7.

[112] Irving Langmuir, Oscillations in ionized gases, Physics 14 (1928).

[113] R.J. Goldston, P.H. Rutherford, Introduction to plasma physics, Institute of Physics Pub (1995).

[114] A.A. Fridman, Plasma chemistry, Cambridge University Press (2008).

[115] R. Suchentrunk, G. Staudigl, D. Jonke, H.J. Fuesser, Industrial applications for plasma processes-examples and trends, Surface and Coatings Technology 97 (1997), 1-9.

[116] R.C. Sanito, S.J. You, Y.F. Wang, Application of plasma technology for treating e-waste: A review, J Environ Manage 288 (2021). https://doi.org/10.1016/j.jenvman.2021.112380.

[117] J.L. Brisset, D. Moussa, A. Doubla, E. Hnatiuc, B. Hnatiuc, G. Kamgang Youbi, J.M. Herry, M. Naïtali, M.N. Bellon-Fontaine, Chemical Reactivity of Discharges and Temporal Post-Discharges in Plasma Treatment of Aqueous Media: Examples of Gliding Discharge Treated Solutions, Ind Eng Chem Res 47 (2008) 5761–5781. https://doi.org/10.1021/ie701759y.

[118] A. Czemichowski, Gliding arc. Applications to engineering and environment control, Pure and Applied Chemistry 66, 6, pp. 1201-1310 (1994).

[119] F.W.B. Tatchemo, S. Nzali, G. Kamgang Youbi, A. Tiya Djowe, D.K. Saa, E. Acayanka, S. Laminsi, E.M. Gaigneaux, Gliding Arc Plasma Synthesis of MnO_2 Nanorods for the Plasma-Catalytic Bleaching of Azoïc Amaranth Red Dye, Top Catal 60 (2017) 962–972. https://doi.org/10.1007/s11244-017-0761-9.

REFERENCES

[120] B. Benstaali, P. Boubert, B.G. Cheron, A. Addou, J.L. Brisset, Density and Rotational Temperature Measurements of the OH° and NO° Radicals Produced by a Gliding Arc in Humid Air, Plasma Chemistry and Plasma Processing 22, 4 (2002).

[121] A. Tiya-Djowe, E. Acayanka, A.P. Mbouopda, W. Boyom-Tatchemo, S. Laminsi, E.M. Gaigneaux, Producing oxide catalysts by exploiting the chemistry of gliding arc atmospheric plasma in humid air, Catal Today 334 (2019) 104–112. https://doi.org/10.1016/j.cattod.2019.01.008.

[122] A. Tiya-Djowe, S. Laminsi, G.L. Noupeyi, E.M. Gaigneaux, Non-thermal plasma synthesis of sea-urchin like α-FeOOH for the catalytic oxidation of Orange II in aqueous solution, Appl Catal B 176–177 (2015) 99–106. https://doi.org/10.1016/j.apcatb.2015.03.053.

[123] M.Á. Stegmayer, V.G. Milt, E.E. Miró, Biomorphic synthesis of cobalt oxide and ceria microfibers. Their application in diesel soot oxidation, Catal Commun 139 (2020). https://doi.org/10.1016/j.catcom.2020.105984.

[124] S.A. Leonardi, F.E. Tuler, E.M. Gaigneaux, D.P. Debecker, E.E. Miró, V.G. Milt, Novel ceramic paper structures for diesel exhaust purification, Environmental Science and Pollution Research 25 (2018) 35276–35286. https://doi.org/10.1007/s11356-018-3439-3.

[125] F.E. Tuler, E.D. Banús, M.A. Zanuttini, E.E. Miró, V.G. Milt, Ceramic papers as flexible structures for the development of novel diesel soot combustion catalysts, Chemical Engineering Journal 246 (2014) 287–298. https://doi.org/10.1016/j.cej.2014.02.083.

[126] S.A. Leonardi, PhD. Thesis: “Desarrollo de papeles cerámicos catalíticos aplicados a catálisis ambiental” (2019).

[127] S. Liu, X. Wu, D. Weng, R. Ran, Ceria-based catalysts for soot oxidation: A review, Journal of Rare Earths 33 (2015) 567–590. https://doi.org/10.1016/S1002-0721(14)60457-9.

[128] M. Thommes, K. Kaneko, A. V. Neimark, J.P. Olivier, F. Rodriguez-Reinoso, J. Rouquerol, K.S.W. Sing, Physisorption of gases, with special reference to the evaluation of surface area and pore size distribution (IUPAC Technical Report), Pure and Applied Chemistry 87 (2015) 1051–1069. https://doi.org/10.1515/pac-2014-1117.

[129] H. Liang, B. Jin, M. Li, X. Yuan, J. Wan, W. Liu, X. Wu, S. Liu, Highly reactive and thermally stable Ag/YSZ catalysts with macroporous fiber-like morphology for soot combustion, Appl Catal B 294 (2021). https://doi.org/10.1016/j.apcatb.2021.120271.

REFERENCES

[130] T. Luo, S. Liu, M. Li, W. Liu, X. Wu, S. Liu, Ozone-assisted diesel soot combustion over Mn_2O_3 catalysts: A tandem work of different reactive phases, J Catal 408 (2022) 56–63. https://doi.org/10.1016/j.jcat.2022.02.022.

[131] R.J. Gorte, Ceria in catalysis: From automotive applications to the water-gas shift reaction, AIChE Journal 56 (2010) 1126–1135. https://doi.org/10.1002/aic.12234.

[132] A. Trovarelli, C. De Leitenburg, M. Boaro, G. Dolcetti, The utilization of ceria in industrial catalysis, Cat Today 50 (1999) 353-367.

[133] S. Zhang, J. Lee, D.H. Kim, T. Kim, NO reduction by CO over CoO_x/CeO_2 catalysts: Effect of support calcination temperature on activity, Molecular Catalysis 482 (2020). https://doi.org/10.1016/j.mcat.2019.110703.

[134] Y. Gao, J. Xiao, J. Ye, X. Huo, Y. Shen, Catalytic oxidation of benzene over alumina-supported Cu-Mn-Ce mixed oxide catalysts, Korean Journal of Chemical Engineering 37 (2020) 54–64. https://doi.org/10.1007/s11814-019-0428-2.

[135] R. Mane, H. Kim, K. Han, K.J. Kim, S. Soo Lee, H.S. Roh, C. Lee, Y. Jeon, Pivotal role of MnOx physicochemical structure in soot oxidation activity, Fuel 346 (2023). https://doi.org/10.1016/j.fuel.2023.128287.

[136] Z. Ma, Cobalt Oxide Catalysts for Environmental Remediation, Current Catalysis 3 (2014) 15.

[137] J. Lei, S. Wang, J. Li, Mesoporous Co_3O_4 derived from Co-MOFs with different morphologies and ligands for toluene catalytic oxidation, Chem Eng Sci 220 (2020). https://doi.org/10.1016/j.ces.2020.115654.

[138] L.M. Martínez T, O.H. Laguna, C. López-Cartes, M.A. Centeno, Synthesis and characterization of Rh/MnO_2-CeO_2/Al_2O_3 catalysts for CO-PrOx reaction, Molecular Catalysis 440 (2017) 9–18. https://doi.org/10.1016/j.mcat.2017.06.018.

[139] P. Venkataswamy, D. Jampaiah, D. Mukherjee, C.U. Aniz, B.M. Reddy, Mn-doped Ceria Solid Solutions for CO Oxidation at Lower Temperatures, Catal Letters 146 (2016) 2105–2118. https://doi.org/10.1007/s10562-016-1811-9.

[140] Y. Gao, S. Teng, Z. Wang, B. Wang, W. Liu, W. Liu, L. Wang, Enhanced catalytic performance of cobalt and iron co-doped ceria catalysts for soot combustion, J Mater Sci 55 (2020) 283–297. https://doi.org/10.1007/s10853-019-03973-z.

[141] S. Andreoli, F.A. Deorsola, R. Pirone, MnO_x-CeO_2 catalysts synthesized by solution combustion synthesis for the low-temperature

NH_3-SCR, Catal Today 253 (2015) 199–206. https://doi.org/10.1016/j.cattod.2015.03.036.

[142] L. Zhu, J. Yao, G. Ma, P. Cao, S. Wu, Z. Li, NH_3-SCR performance and SO_2 resistance comparison of CeO_2 based catalysts with Fe/Mo additive surface decoration, Chemical Engineering Journal 428 (2022). https://doi.org/10.1016/j.cej.2021.131372.

[143] S. Agarwal, X. Zhu, E.J.M. Hensen, L. Lefferts, B.L. Mojet, Defect chemistry of ceria nanorods, Journal of Physical Chemistry C 118 (2014) 4131–4142. https://doi.org/10.1021/jp409989y.

[144] M.Y. Cui, X.Q. Yao, W.J. Dong, K. Tsukamoto, C.R. Li, Template-free synthesis of CuO-CeO_2 nanowires by hydrothermal technology, J Cryst Growth 312 (2010) 287–293. https://doi.org/10.1016/j.jcrysgro.2009.10.027.

[145] F. Li, J. Wu, Q. Qin, Z. Li, X. Huang, Facile synthesis of γ-MnOOH micro/nanorods and their conversion to β-MnO_2, Mn_3O_4, J Alloys Compd 492 (2010) 339–346. https://doi.org/10.1016/j.jallcom.2009.11.089.

[146] M.S. Yadav, Synthesis and characterization of Mn_2O_3–Mn_3O_4 nanoparticles and activated charcoal based nanocomposite for supercapacitor electrode application, J Energy Storage 27 (2020). https://doi.org/10.1016/j.est.2019.101079.

[147] Y. Luo, D. Lin, Y. Zheng, X. Feng, Q. Chen, K. Zhang, X. Wang, L. Jiang, MnO_2 nanoparticles encapsuled in spheres of Ce-Mn solid solution: Efficient catalyst and good water tolerance for low-temperature toluene oxidation, Appl Surf Sci 504 (2020). https://doi.org/10.1016/j.apsusc.2019.144481.

[148] N.A. Sacco, J.P. Bortolozzi, V.G. Milt, E.E. Miró, E.D. Banús, Ce-Mn oxides synthesized with citric acid on ceramic papers used as diesel particulate filters, Catal Today 383 (2021) 277–286. https://doi.org/10.1016/j.cattod.2021.03.023.

[149] S. Loridant, Raman spectroscopy as a powerful tool to characterize ceria-based catalysts, Cat Today (2021) 373, pp. 98-111. https://doi.org/10.1016/j.cattod.2020.03.044.

[150] A. Shourya, H.P. Dasari, Formation of nano-rod structures in manganese-rich ceria–manganese mixed oxides and their soot oxidation activity, Nano-Structures and Nano-Objects 34 (2023). https://doi.org/10.1016/j.nanoso.2023.100970.

[151] R. Najjar, R. Awad, A.M. Abdel-Gaber, Physical Properties of Mn_2O_3 Nanoparticles Synthesized by Co-precipitation Method at Different pH

REFERENCES

Values, J Supercond Nov Magn 32 (2019) 885–892. https://doi.org/10.1007/s10948-018-4765-x.

[152] G. Greczynski, L. Hultman, C 1s Peak of Adventitious Carbon Aligns to the Vacuum Level: Dire Consequences for Material's Bonding Assignment by Photoelectron Spectroscopy, ChemPhysChem Communications 18 (2017) 1507–1512. https://doi.org/10.1002/cphc.201700126.

[153] D. Puentes-Camacho, E.F. Velázquez, D.E. Rodríguez-Félix, M. Castillo-Ortega, R.R. Sotelo-Mundo, T. Del Castillo-Castro, Functionalization of multiwalled carbon nanotubes by microwave irradiation for lysozyme attachment: Comparison of covalent and adsorption methods by kinetics of thermal inactivation, Advances in Natural Sciences: Nanoscience and Nanotechnology 8 (2017). https://doi.org/10.1088/2043-6254/aa8b3c.

[154] J. Meng, H. Chen, H. Xie, Q. Zhang, C. Bu, X. Wang, J. Zhang, C. Liu, G. Piao, Plasma-catalytic benzene steam reforming over Ce doped Ni-HAP catalysts: Insights into enhanced oxygen activity, Chemical Engineering Journal 483 (2024). https://doi.org/10.1016/j.cej.2024.149141.

[155] J. Fan, X. Wu, L. Yang, D. Weng, The SMSI between supported platinum and CeO_2-ZrO_2-La_2O_3 mixed oxides in oxidative atmosphere, Catal Today 126 (2007) 303–312. https:/doi.org/10.1016/j.cattod.2007.06.005.

[156] F.F. Larachi, J. Pierre, A. Adnot, A. Bernis, Ce 3d XPS study of composite $Ce_xMn_{1-x}O_{2-y}$ wet oxidation catalysts, Applied Surface Science 195 (2002) 236-250. https://doi.org/https://doi.org/10.1016/S0169-4332(02)00559-7.

[157] F.W. Boyom-Tatchemo, F. Devred, G. Ndiffo-Yemeli, S. Laminsi, E.M. Gaigneaux, Plasma-induced redox reactions synthesis of nanosized α-, γ- and δ-MnO_2 catalysts for dye degradation, Appl Catal B 260 (2020). https://doi.org/10.1016/j.apcatb.2019.118159.

[158] J. Si, S. Xiao, Y. Wang, L. Zhu, X. Xia, Z. Huang, Y. Gao, Sub-nanometer Co_3O_4 clusters anchored on TiO_2(B) nano-sheets: Pt replaceable Co-catalysts for H_2 evolution, Nanoscale 10 (2018) 2596–2602. https://doi.org/10.1039/c7nr07336d.

[159] Y. Georgiou, M. Smyrnioti, T. Ioannides, Co_3O_4 Catalysts for Complete Toluene Oxidation: Review including Meta-Analysis of Catalyst Activity Data, Catalysts 13 (2023). https://doi.org/10.3390/catal13111454.

REFERENCES

[160] B. Jiang, M. Huang, D. Cai, K.B. Tan, G. Zhan, Fabrication of Pt/Co_3O_4 nanocatalysts based on pollen template for low-temperature CO oxidation, Catal Commun 174 (2023). https://doi.org/10.1016/j.catcom.2022.106597.

[161] H. Xu, N. Yan, Z. Qu, W. Liu, J. Mei, W. Huang, S. Zhao, Gaseous Heterogeneous Catalytic Reactions over Mn-Based Oxides for Environmental Applications: A Critical Review, Environ Sci Technol 51 (2017) 8879–8892. https://doi.org/10.1021/acs.est.6b06079.

[162] Z. Seidov, M. Açıkgöz, S. Kazan, F. Mikailzade, Magnetic properties of Co_3O_4 polycrystal powder, Ceram Int 42 (2016) 12928–12931. https://doi.org/10.1016/j.ceramint.2016.05.063.

[163] A. Diallo, A.C. Beye, T.B. Doyle, E. Park, M. Maaza, Green synthesis of Co_3O_4 nanoparticles via Aspalathus linearis: Physical properties, Green Chem Lett Rev 8 (2015) 30–36. https://doi.org/10.1080/17518253.2015.1082646.

[164] Y. Zheng, Y. Yu, H. Zhou, W. Huang, Z. Pu, Combustion of lean methane over Co_3O_4 catalysts prepared with different cobalt precursors, RSC Adv 10 (2020) 4490–4498. https://doi.org/10.1039/c9ra09544f.

[165] N. Sacco, E. Banús, V. Milt, E. Miró, J.P. Bortolozzi, Catalytic Paper Filters for Diesel Soot Abatement: Studies at Laboratory and Bench Scales, Emission Control Science and Technology 6 (2020) 450–461. https://doi.org/10.1007/s40825-020-00169-9.

[166] Y. Li, D. Li, S. Fan, T. Yang, Q. Zhou, Facile template synthesis of dumbbell-like Mn_2O_3 with oxygen vacancies for efficient degradation of organic pollutants by activating peroxymonosulfate, Catal Sci Technol 10 (2020) 864–875. https://doi.org/10.1039/c9cy01849b.

[167] Y. Wang, C. Hou, X. Lin, H. Jiang, C. Zhang, G. Liu, Dye degradation studies of hausmannite manganese oxide (Mn_3O_4) nanoparticles synthesized by chemical method, Appl Phys A Mater Sci Process 127 (2021). https://doi.org/10.1007/s00339-021-04428-6.

[168] W. Liu, L. Feng, C. Zhang, H. Yang, J. Guo, X. Liu, X. Zhang, Y. Yang, A facile hydrothermal synthesis of 3D flowerlike CeO_2 via a cerium oxalate precursor, J Mater Chem A Mater 1 (2013) 6942–6948. https://doi.org/10.1039/c3ta10487g.

[169] L. Song, H. Zhang, J. Xiong, Z. Chen, Y. Liu, H. Zhou, W. Yang, D. Cao, H. Huang, L. Chen, M. Fu, D. Ye, Doped Mn modulates the local charge distribution of cobalt-based spinel catalysts to promote the availability of ligand lattice oxygen for complete oxidation of methane, Appl Catal B 343 (2024). https://doi.org/10.1016/j.apcatb.2023.123547.

REFERENCES

[170] Y.H. Liu, J.C. Zuo, X.F. Ren, L. Yong, Synthesis and characterization of cerium oxide (CeO_2) by the precipitation method, Metalurgia 53 4 (2014) 463–465.

[171] S. Liu, B. Zhang, Y. Cao, H. Wang, Y. Zhang, S. Zhang, Y. Li, H. Gong, S. Liu, Z. Yang, J. Sun, Understanding the Effect of Nickel Doping in Cobalt Spinel Oxides on Regulating Spin State to Promote the Performance of the Oxygen Reduction Reaction and Zinc-Air Batteries, ACS Energy Lett 8 (2023) 159–168. https://doi.org/10.1021/acsenergylett.2c02457.

[172] R. Naeem, M. Ali Ehsan, R. Yahya, M. Sohail, H. Khaledi, M. Mazhar, Fabrication of pristine Mn_2O_3 and Ag-Mn_2O_3 composite thin films by AACVD for photoelectrochemical water splitting, Dalton Transactions 45 (2016) 14928–14939. https://doi.org/10.1039/c6dt02656g.

[173] K. Ramesh, L. Chen, F. Chen, Z. Zhong, J. Chin, H. Mook, Y.F. Han, Preparation and characterization of coral-like nanostructured α-Mn_2O_3 catalyst for catalytic combustion of methane, Catal Commun 8 (2007) 1421–1426. https://doi.org/10.1016/j.catcom.2006.12.008.

[174] B.P. Payne, M.C. Biesinger, N.S. McIntyre, Use of oxygen/nickel ratios in the XPS characterisation of oxide phases on nickel metal and nickel alloy surfaces, J Electron Spectros Relat Phenomena 185 (2012) 159–166. https://doi.org/10.1016/j.elspec.2012.06.008.

[175] P.J. Jodłowski, R.J. Jędrzejczyk, A. Rogulska, A. Wach, P. Kuśtrowski, M. Sitarz, T. Łojewski, A. Kołodziej, J. Łojewska, Spectroscopic characterization of Co_3O_4 catalyst doped with CeO_2 and PdO for methane catalytic combustion, Spectrochim Acta A Mol Biomol Spectrosc 131 (2014) 696–701. https://doi.org/10.1016/j.saa.2014.05.027.

[176] E. Beyreuther, S. Grafström, L.M. Eng, C. Thiele, K. Dörr, XPS investigation of Mn valence in lanthanum manganite thin films under variation of oxygen content, Phys Rev B Condens Matter Mater Phys 73 (2006). https://doi.org/10.1103/PhysRevB.73.155425.

[177] S. Soni, V.S. Vats, S. Kumar, B. Dalela, M. Mishra, R.S. Meena, G. Gupta, P.A. Alvi, S. Dalela, Structural, optical and magnetic properties of Fe-doped CeO_2 samples probed using X-ray photoelectron spectroscopy, Journal of Materials Science: Materials in Electronics 29 (2018) 10141–10153. https://doi.org/10.1007/s10854-018-9060-x.

[178] H. Zhao, X. Zhou, M. Wang, Z. Xie, H. Chen, J. Shi, Highly active MnO_x-CeO_2 catalyst for diesel soot combustion, RSC Adv 7 (2017) 3233–3239. https://doi.org/10.1039/c6ra25738k.

REFERENCES

[179] P. Hongmanorom, J. Ashok, P. Chirawatkul, S. Kawi, Interfacial synergistic catalysis over Ni nanoparticles encapsulated in mesoporous ceria for CO_2 methanation, Appl Catal B 297 (2021). https://doi.org/10.1016/j.apcatb.2021.120454.

[180] Z. Ni, X. Djitcheu, X. Gao, J. Wang, H. Liu, Q. Zhang, Effect of preparation methods of CeO_2 on the properties and performance of Ni/CeO_2 in CO_2 reforming of CH_4, Sci Rep 12 (2022). https://doi.org/10.1038/s41598-022-09291-w.

[181] A. Tiya-Djowe, N. Ruth, G. Kamgang-Youbi, E. Acayanka, S. Laminsi, E.M. Gaigneaux, FeO_x-kaolinite catalysts prepared via a plasma-assisted hydrolytic precipitation approach for Fenton-like reaction, Microporous and Mesoporous Materials 255 (2018) 148–155. https://doi.org/10.1016/j.micromeso.2017.07.036.

[182] A. Lassoued, B. Dkhil, A. Gadri, S. Ammar, Control of the shape and size of iron oxide (α-Fe_2O_3) nanoparticles synthesized through the chemical precipitation method, Results Phys 7 (2017) 3007–3015. https://doi.org/10.1016/j.rinp.2017.07.066.

[183] S. Liu, K. Yao, L.H. Fu, M.G. Ma, Selective synthesis of Fe_3O_4, γ-Fe_2O_3, and α-Fe_2O_3 using cellulose-based composites as precursors, RSC Adv 6 (2016) 2135–2140. https://doi.org/10.1039/c5ra22985e.

[184] M.Á. Stegmayer, M.L. Godoy, J.F. Múnera, E.E. Miró, V.G. Milt, In situ growth of ceria nanofibers on cordierite monoliths for diesel soot combustion, Surf Coat Technol 439 (2022). https://doi.org/10.1016/j.surfcoat.2022.128451.

[185] M. Aghazadeh, A. Bahrami-Samani, D. Gharailou, M.G. Maragheh, M.R. Ganjali, P. Norouzi, Mn_3O_4 nanorods with secondary plate-like nanostructures; preparation, characterization and application as high performance electrode material in supercapacitors, J Mater Sci: Materials in Electronics 27 (2016) 11192–11200. https://doi.org/10.1007/s10854-016-5239-1.

[186] L. Miñambres, E. Méndez, M.N. Sánchez, F. Castaño, F.J. Basterretxea, Water uptake of internally mixed ammonium sulfate and dicarboxylic acid particles probed by infrared spectroscopy, Atmos Environ 70 (2013) 108–116. https://doi.org/10.1016/j.atmosenv.2013.01.007.

[187] V.G. Milt, M.A. Peralta, M.A. Ulla, E.E. Miró, Soot oxidation on a catalytic NO_x trap: Beneficial effect of the Ba-K interaction on the sulfated Ba, K/CeO_2 catalyst, Catal Commun 8 (2007) 765–769. https://doi.org/10.1016/j.catcom.2006.09.011.

REFERENCES

[188] R.R. Koli, N.G. Deshpande, D.S. Kim, H.K. Cho, A synergistic strategy to remove hazardous water pollutants by mimicking burdock flower morphology structures of iron oxide phases, Chemosphere 286 (2022). https://doi.org/10.1016/j.chemosphere.2021.131789.

[189] D.M.D.M. Prabaharan, K. Sadaiyandi, M. Mahendran, S. Sagadevan, Structural, Optical, Morphological and Dielectric Properties of Cerium Oxide Nanoparticles, Materials Research 19 (2016) 478–482. https://doi.org/10.1590/1980-5373-MR-2015-0698.

[190] M.P. Araújo, M. Nunes, I.M. Rocha, M.F.R. Pereira, C. Freire, Electrocatalytic activity of new Mn_3O_4@oxidized graphene flakes nanocomposites toward oxygen reduction reaction, J Mater Sci 54 (2019) 8919–8940. https://doi.org/10.1007/s10853-019-03508-6.

[191] R. Zheng, R. Tan, Y. Lv, X. Mou, J. Qian, R. Lin, P. Fang, W. Kan, Oxygen-Vacancy-Rich Fe@Fe_3O_4 Boosting Fenton Chemistry, Catalysts 13 (2023) 1057. https://doi.org/10.3390/catal13071057.

[192] R. Liu, W. Huang, S. Pan, Y. Li, L. Yu, D. He, Covalent immobilization and characterization of penicillin G acylase on magnetic Fe_2O_3/Fe_3O_4 heterostructure nanoparticles prepared via a novel solution combustion and gel calcination process, Int J Biol Macromol 162 (2020) 1587–1596. https://doi.org/10.1016/j.ijbiomac.2020.07.283.

[193] M.C. Biesinger, B.P. Payne, A.P. Grosvenor, L.W.M. Lau, A.R. Gerson, R.S.C. Smart, Resolving surface chemical states in XPS analysis of first row transition metals, oxides and hydroxides: Cr, Mn, Fe, Co and Ni, Appl Surf Sci 257 (2011) 2717–2730. https://doi.org/10.1016/j.apsusc.2010.10.051.

[194] M. Claros, M. Setka, Y.P. Jimenez, S. Vallejos, AACVD Synthesis and Characterization of Iron and Copper Oxides Modified ZnO Structured Films, Nanomaterials 10 (2020). https://doi.org/10.3390/nano10030471.

[195] Z. Zhang, D. Han, S. Wei, Y. Zhang, Determination of active site densities and mechanisms for soot combustion with O_2 on Fe-doped CeO_2 mixed oxides, J Catal 276 (2010) 16–23. https://doi.org/10.1016/j.jcat.2010.08.017.

[196] J. Fan, X. Niu, W. Teng, P. Zhang, W.X. Zhang, D. Zhao, Highly dispersed Fe-Ce mixed oxide catalysts confined in mesochannels toward low-temperature oxidation of formaldehyde, J Mater Chem A Mater 8 (2020) 17174–17184. https://doi.org/10.1039/d0ta05473a.

[197] J.R.H. Ross, Heterogeneous Catalysis Fundamentals and Applications, Elsevier (2012).

REFERENCES

[198] A.K. Chitoria, A. Mir, M.A. Shah, A review of ZrO_2 nanoparticles applications and recent advancements, Ceram Int 49 (2023) 32343–32358. https://doi.org/10.1016/j.ceramint.2023.06.296.

[199] T. Yamaguchi, Application of ZrO_2 as a catalyst and a catalyst support, Cat Today 20 (1994) 199-218.

[200] G. Rajesh, S. Akilandeswari, D. Govindarajan, K. Thirumalai, Enhancement of photocatalytic activity of ZrO_2 nanoparticles by doping with Mg for UV light photocatalytic degradation of methyl violet and methyl blue dyes, Journal of Materials Science: Materials in Electronics 31 (2020) 4058–4072. https://doi.org/10.1007/s10854-020-02953-3.

[201] Y. Han, J. Zhu, Surface science studies on the zirconia-based model catalysts, Top Catal 56 (2013) 1525–1541. https://doi.org/10.1007/s11244-013-0156-5.

[202] I. Fatimah, I. Yanti, T.E. Suharto, S. Sagadevan, ZrO_2-based catalysts for biodiesel production: A review, Inorg Chem Commun 143 (2022). https://doi.org/10.1016/j.inoche.2022.109808.

[203] A.A. Vedyagin, A.M. Volodin, R.M. Kenzhin, V. V. Chesnokov, I. V. Mishakov, CO oxidation over Pd/ZrO_2 catalysts: Role of support's donor sites, Molecules 21 (2016). https://doi.org/10.3390/molecules21101289.

[204] A.H. Zapién, J.M.H. Enríquez, R.G. Alamilla, G.S. Robles, U.P. Garciá, L.A.G. Serrano, Influence of Molybdenum Content and MoO_x Species on the Textural and Structural ZrO_2 Properties, Advances in Materials Science and Engineering 2014 (2014). https://doi.org/10.1155/2014/432031.

[205] G.K. Sidhu, A.K. Kaushik, S. Rana, S. Bhansali, R. Kumar, Photoluminescence quenching of Zirconia nanoparticle by surface modification, Appl Surf Sci 334 (2015) 216–221. https://doi.org/10.1016/j.apsusc.2014.10.036.

[206] S. Ding, J. Zhao, Q. Yu, Effect of zirconia polymorph on vapor-phase ketonization of propionic acid, Catalysts 9 (2019). https://doi.org/10.3390/catal9090768.

[207] E. De la Rosa-Cruz, Evidence of non-radiative energy transfer from the host to the active ions in monoclinic ZrO_2 (2001). http://iopscience.iop.org/0022-3727/34/14/102.

[208] N.C. Horti, M.D Kamatagi, S.K. Nataraj, M.N. Wari, S.R. Inamdar, Structural and optical properties of zirconium oxide (ZrO2) nanoparticles: effect of calcination temperature, Nano Ex. 1 (2020).

REFERENCES

[209] I. Atribak, A. Bueno-López, A. García-García, P. Navarro, D. Frías, M. Montes, Catalytic activity for soot combustion of birnessite and cryptomelane, Appl Catal B 93 (2010) 267–273. https://doi.org/10.1016/j.apcatb.2009.09.038.

[210] S. Said, M. Riad, M. Helmy, S. Mikhail, L. Khalil, Preparation of nano-structured cryptomelane materials for catalytic oxidation reactions, J Nanostructure Chem 6 (2016) 171–182. https://doi.org/10.1007/s40097-016-0192-3.

[211] S.K. Ghosh, Diversity in the Family of Manganese Oxides at the Nanoscale: From Fundamentals to Applications, ACS Omega 5 (2020) 25493–25504. https://doi.org/10.1021/acsomega.0c03455.

[212] T. Kawai, K. Tsutsumi, Evaluation of the Secondary Pore Structure of Hydrothermally- and Acid-treated Faujasite Type Zeolites, n.d.

[213] M. Yi, Y. Zhang, J. Xu, D. Deng, Z. Mao, X. Meng, X. Shi, B. Zhao, Surface-enhanced raman scattering activity of ZrO_2 nanoparticles: Effect of tetragonal and monoclinic phases, Nanomaterials 11 (2021). https://doi.org/10.3390/nano11092162.

[214] M. Li, Z. Feng, G. Xiong, P. Ying, Q. Xin, C. Li, Phase transformation in the surface region of zirconia detected by UV Raman spectroscopy, Journal of Physical Chemistry B 105 (2001) 8107–8111. https://doi.org/10.1021/jp010526l.

[215] S.N. Basahel, T.T. Ali, M. Mokhtar, K. Narasimharao, Influence of crystal structure of nanosized ZrO_2 on photocatalytic degradation of methyl orange, Nanoscale Res Lett 10 (2015). https://doi.org/10.1186/s11671-015-0780-z.

[216] J. Podobiński, M. Śliwa, J. Datka, Determination of concentration of basic sites on oxides by IR spectroscopy, Spectrochim Acta A Mol Biomol Spectrosc 320 (2024). https://doi.org/10.1016/j.saa.2024.124548.

[217] M. Utami, W. Trisunaryanti, K. Shida, M. Tsushida, H. Kawakita, K. Ohto, K. Wijaya, M. Tominaga, Hydrothermal preparation of a platinum-loaded sulphated nanozirconia catalyst for the effective conversion of waste low density polyethylene into gasoline-range hydrocarbons, RSC Adv 9 (2019) 41392–41401. https://doi.org/10.1039/c9ra08834b.

[218] S. Sagadevan, J. Podder, I. Das, Hydrothermal synthesis of zirconium oxide nanoparticles and its characterization, Journal of Materials Science: Materials in Electronics 27 (2016) 5622–5627. https://doi.org/10.1007/s10854-016-4469-6.

[219] P. Khajuria, R. Mahajan, R. Prakash, Synthesis and luminescent properties of ZrO_2 and Dy^{3+}- activated ZrO_2 powders, Journal of Materials

Science: Materials in Electronics 32 (2021) 27441–27448. https://doi.org/10.1007/s10854-021-07120-w.

[220] S. Chen, Y. Yin, D. Wang, Y. Liu, X. Wang, Structures, growth modes and spectroscopic properties of small zirconia clusters, J Cryst Growth 282 (2005) 498–505. https://doi.org/10.1016/j.jcrysgro.2005.05.017.

[221] A.K. Bordbar, A.A. Rastegari, R. Amiri, E. Ranjbakhsh, M. Abbasi, A.R. Khosropour, Characterization of Modified Magnetite Nanoparticles for Albumin Immobilization, Biotechnol Res Int 2014 (2014) 1–6. https://doi.org/10.1155/2014/705068.

[222] R. Camposeco, S. Castillo, M. Hinojosa-Reyes, N. Nava, R. Zanella, Manganese promoted TiO_2 and ZrO_2 nanostructures for soot combustion with boosted eficiency, Surface & Coatings Technology 384 (2019) 125305. https://doi.org/10.1016/j.surcoat.2019.125305.

[223] F. Fang, N. Feng, P. Zhao, H. Wan, G. Guan, Potassium promoted macro-mesoporous Co_3O_4-$La_{0.88}Sr_{0.12}CoO_{3-\delta}$ nanotubes with large surface area: A high-performance catalyst for soot removal, J Colloid Interface Sci 582 (2021) 569–580. https://doi.org/10.1016/j.jcis.2020.08.070.

[224] A. Rinkenburger, T. Toriyama, K. Yasuda, R. Niessner, Catalytic Effect of Potassium Compounds in Soot Oxidation, ChemCatChem 9 (2017) 3513–3525. https://doi.org/10.1002/cctc.201700338.

[225] N. Feng, J. Meng, Y. Wu, C. Chen, L. Wang, L. Gao, H. Wan, G. Guan, KNO_3 supported on three-dimensionally ordered macroporous $La_{0.8}Ce_{0.2}Mn_{1-X}Fe_xO_3$ for soot removal, Catal Sci Technol 6 (2016) 2930–2941. https://doi.org/10.1039/c5cy02025e.

[226] C. Zheng, S. Bao, D. Mao, Z. Xu, S. Zheng, Insight into phase structure-dependent soot oxidation activity of K-MnO_2 catalyst, Journal of Environmental Sciences 126 (2023) 668-682. https://doi.org/10.1016/j.jes.2022.05.038.

[227] H. Xu, L. Zeng, L. Cui, W. Guo, C. Gong, G. Xue, In-situ generation of platinum nanoparticles on LaCoO3 matrix for soot oxidation, Journal of Rare Earths 40 (2022) 888-896. https://doi.org/10.1016/j.jre.2021.06.009.

[228] K. Tikhomirov, O. Kröcher, M. Elsener, A. Wokaun, MnO_x-CeO_2 mixed oxides for the low-temperature oxidation of diesel soot, Appl Cat B: Environmental 64 (2006) 72-78. doi:10.1016/j.apcatb.2005.11.003.

[229] K. Yang, Y. Liu, J. Deng, X. Zhao, J. Yang, Z. Han, Z. Hou, H. Dai, Three-dimensionally ordered mesoporous iron oxide-supported single-atom platinum: Highly active catalysts for benzene combustion, Appl Cat

B: Environmental 244 (2019) 650-659. https://doi.org/10.1016/j.apcatb.2018.11.077.

[230] Y. Liu, H. Dai, J. Deng, S. Xie, H. Yang, W. Tan, W. Han, Y. Jiang, G. Guo, Mesoporous Co_3O_4-supported gold nanocatalysts: Highly active for the oxidation of carbon monoxide, benzene, toluene, and o-xylene, Journal of Catalysis 309 (2014) 408-418. https://doi.org/10.1016/j.jcat.2013.10.019.

[231] S. Mo, S. Li, W. Li, J. Li, J. Chen, Y. Chen, Excellent low temperature performance for total benzene oxidation over mesoporous CoMnAl composited oxides from hydrotalcites, J Mater Chem A 4 (2016) 8113-8122. https://doi.org/10.1039/c6ta02593e.

[232] X. Wang, J. Zuo, Y. Luo, L. Jiang, New route to CeO_2-$LaCoO_3$ with high oxygen mobility for total benzene oxidation, Appl Surf Sci 396 (2017) 95-101. https://doi.org/10.1016/j.apsusc.2016.11.033.

[233] T. Andana, M. Piumetti, S. Bensaid, N. Russo, D. Fino, R. Pirone, CO and Soot Oxidation over Ce-Zr-Pr Oxide Catalysts, Nano Res Letters (2016) 11:278. DOI 10.1186/s11671-016-1494-6.

[234] M.A. Stegmayer, Ph.D. Thesis: "Síntesis, caracterización y evaluación de catalizadores basados en fibras para reacciones de oxidación" (2021).

[235] M. Piumetti, S. Bensaid, D. Fino, N. Russo, Nanostructured ceria-zirconia Catalysts for CO oxidation: Study on surface properties and reactivity, Appl Cat B: Environmental 197 (2016) 35-46. https://doi.org/10.1016/j.apcatb.2016.02.023.

[236] X. Li, J. Lu, K. Qian, W. Huang, M. Luo, A comparative study of formaldehyde and carbon monoxide complete oxidation on MnO_x-CeO_2 catalysts, J Rare Earths 27 (2009) 418-424. https://doi.org/10.1016/S1002-0721(08)60263-X.

[237] D. Jeong, H. Na, J. Shim, W. Jang, H. Roh, U. Jung, W. Yoon, Hydrogen production from low temperature WGS reaction on co-precipitated Cu-CeO2 catalysts: An optimization of Cu loading, Int J Hydrogen Energy 39 (2014) 9135-9142. https://doi.org/10.1016/j.ijhydene.2014.04.005.

[238] R. Saada, S. Kellici, T. Heil, D. Morgan, B. Saha, Greener synthesis of dimethyl carbonate using a novel ceria-zirconia oxide-graphene nanocomposite catalyst, Appl Cat B: Environmental 168-169 (2015) 353-362. https://doi.org/10.1016/j.apcatb.2014.12.013.

ARTICLES AND COMMUNICATIONS

Articles

- M. Rodriguez, S.A. Leonardi, F. Hanon, E.E. Miró, V.G. Milt, E.M. Gaigneaux, “Plasma-assisted deposition of Mn and Fe phases on CeO2 biomorphic fibers for soot combustion and CO oxidation”, Catalysis Today 431 (2024). https://doi.org/10.1016/j.cattod.2023.114457.
- M. Rodriguez, F. Hanon, F. Devred, E.M. Gaigneaux, E.E. Miró and V.G. Milt, “Mn and Co decorated biomorphic ceria fibers catalysts for soot and benzene total oxidation”, Chemosphere 359 (2024) 142247. https://doi.org/10.1016/j.chemosphere.2024.142247.
- M. Rodriguez, S.A. Leonardi, E.M. Gaigneaux, E.E. Miró, V.G. Milt, “Plasma-supported zirconia fibers for soot and CO/Bz oxidation“, to be sent by April 2025 (invitation accepted) to Applied Catalysis A: General, special edition titled “Catalysis in the Americas”.

Oral communications

- M. Rodriguez, V.G. Milt, E.E. Miró, E.M. Gaigneuax, “Template synthesis of fibrous catalysts for environmental application”, CRF ChemCYS 2022. Blankenberge, Belgium. October 2022.
- M. Rodriguez, V.G. Milt, E.E. Miró, E.M. Gaigneuax, “Biomorphic fibrous catalysts for the oxidation of soot and VOCs”, 9th World Congress on Oxidation Catalysis: Oxidation for a Sustainable Future and Clean Environment. Cardiff, Wales. September 2022.

Poster communications

- M. Rodriguez, S. Leonardi, V.G. Milt, E.E. Miró, “Estudio de resistencia en condiciones húmedas de papeles cerámicos y determinación de su actividad como catalizadores en la combustión de hollín diésel”, XXII Congreso Argentino de fisicoquímica y química inorgánica. La Plata, Argentina, 2021. April 2021.
- M. Rodriguez, S. Leonardi, V.G. Milt, E.E. Miró, E.M. Gaigneaux, “Biomorphic fibers for soot combustion”, Winter School - “A road map for catalysis to support a society powered by renewable energies”. Aussois, France. March 2022.
- M. Rodriguez, V.G. Milt, E.E. Miró, E.M. Gaigneuax, “Template synthesis of fibrous catalysts for environmental application”, CRF ChemCYS 2022. Blankenberge, Belgium. October 2022.
- M. Rodriguez, V.G. Milt, E.E. Miró, E.M. Gaigneuax, “Ce-based biomorphic fibers for the oxidation of soot and VOCs”, French-Argentinean Workshop on Heterogeneous Catalysis. Santa Fe, Argentina. April 2023.
- M. Rodriguez, V.G. Milt, E.E. Miró, E.M. Gaigneuax, “Fibras catalíticas biomórficas para oxidación de hollín y COVs”. V Congreso Nacional de Ciencia y Tecnología Ambiental. San Luis, Argentina. May 2023.
- M. Rodriguez, V.G. Milt, E.E. Miró, E.M. Gaigneuax, “Deposition of catalytic Fe and Mn on biomorphic fibers by plasma glidarc”, 13th International Symposium PREPA13. Louvain-la-Neuve, Belgium. July 2023.
- M. Rodriguez, V.G. Milt, E.E. Miró, E.M. Gaigneuax, “Fe and Mn phases deposited on ceria biomorphic fibers by glidarc plasma”, EUROCAT 2023. August 2023.
- S. Leonardi, M. Rodriguez, E.M. Gaigneaux, E.E. Miró, V.G Milt, “Síntesis de fibras biomórficas catalíticas para la oxidación de hollín diésel”, IV Simposio Internacional en catálisis ambiental y energías renovables (IV SICAMER 2024). Medellín, Colombia. October 2024.